Title
Mechanical and Structural Behavior of Compressed and Stabilized Earth Block Masonry Systems

Author
Kumar, Nitin

Publication Date
2022

Mechanical and Structural Behavior
of
Compressed and Stabilized Earth Block Masonry Systems

By

NITIN KUMAR
DISSERTATION

Submitted in partial satisfaction of the requirements for the degree of

Doctor of Philosophy

in

Civil and Environmental Engineering

in the

OFFICE OF GRADUATE STUDIES

of the

UNIVERSITY OF CALIFORNIA

DAVIS

Approved:

Michele Barbato, Chair

Sashi Kunnath

Mark M. Rashid

Committee in Charge

2022

DEDICATION

Dedicated to

My Mausi, Sushila Chauhan

and

My Family

(Mother, Father, Anamika, and Avyaan)

ACKNOWLEDGEMENT

Throughout the writing of this dissertation, I have received a great deal of support and assistance.

First, I would like to convey my special thanks to my thesis advisor, Professor Michele Barbato, for all his faith and confidence in me. He believed in me and has given me such an awesome research topic. Working with him and being a part of his research group has been a privilege for me. It would have been impossible for me to move forward without his motivation and well-organized guidance. His encouragement and technical guidance made my research work worthful and interesting. Working with him was indeed a fantastic, fruitful, and an unforgettable experience in my life.

Second, I gratefully acknowledge the invaluable advice and guidance received from Dr. Fabio Matta (University of South Carolina, Columbia, SC), which was fundamental to choose the right direction and successfully complete my dissertation. I would like to acknowledge my colleague Ms. Erika L. Rengifo-López (Ph.D. student at University of South Carolina, Columbia, SC) for their wonderful research collaboration throughout my Ph.D.

Third, I would like to thank my committee members, Professor Sashi Kunnath, and Professor Mark M. Rashid for their advice and taking the time to be active part of my Ph.D. Committee. Special thanks are extended to Dr. Ashok Mishra, Dr. Mirsardar Esmaeili (former Ph.D. student at UC Davis) and undergraduate research assistants, at Louisiana State University, Chris Doiron and James Babin for their assistance in performing the feasibility study presented in presented in this dissertation. In addition, I would like to acknowledge the help received during the production and experimental testing of sugarcane bagasse fiber reinforced earth blocks from Ms. Lucy C

Farrar, Mr. Alex E Ramirez, Mr. Neal Wright, and Mr. Matthew Gordon (undergraduate students at Louisiana State University). I would also like to thank Dr. James Fettinger and Mr. Christopher Perez (at UC Davis) for helping with the X-ray diffraction analysis. Lastly, I would like to say special thanks to several peoples, who have knowingly or unknowingly helped me during my Ph.D.

The research presented in this dissertation is based upon work partial supported by (1) the Louisiana Board of Regents through the Economic Development Assistantship Program, (2) the Louisiana State University's Coastal Sustainability Studio through the 2014-2015 New Projects Fund Program, (3) the U.S. National Science Foundation through award CMMI #1537078, and (4) the University of California Office of the President Laboratory Fees program through award LFR-20-651032.

Last but not the least, I owe a great deal of appreciation to my father and mother who gifted me this life and to my wife, Anamika, and my son, Avyaan for their love and understanding toward the completion of my research work.

ABSTRACT

Earthen structures are buildings and structures primarily made from soil. Since soil is a widely available and inexpensive material, it has been used in construction since prehistoric times. In the modern era of concrete and steel, earthen structures have seen a significantly reduced usage, due to their relatively low strength and lack of standardization. However, they are once again getting attention because of their low cost, low carbon footprint, energy efficiency, use of indigenous materials, and inherent simplicity. In particular, compressed and stabilized earth block (CSEB) construction is appealing as a viable response to the lack of affordable housing in the US and all around the world. CSEBs can be easily engineered to improve their properties, and CSEB construction shares many similarities with ordinary masonry, for which extensive experience and a vast engineering literature are available. Currently, US is facing a shortage of nearly 3.3 million affordable homes, and over two billion new houses will be needed worldwide in the next 80 years to address the predicted world population increase and expected improvements of living standards. CSEB construction can address this rapidly growing housing demand in the US and all around the world in an innovative, sustainable, and affordable manner.

Despite the advantages of CSEB structures over other industrial materials, only few building codes adopted in the US allow the use of CSEB construction through an empirical/prescriptive approach adapted from ordinary and concrete block masonry, without properly taking advantage of the specific characteristics of the CSEB materials and construction techniques. As a consequence, earthen buildings represent only a small fraction of the building inventory in the US, even in places where this type of construction is historically established and culturally appreciated (e.g., NM, CO, AZ, TX, CA). Furthermore, CSEB construction is even rarer in locations with humid and rainy climates such as the US Gulf Coast, because of the poor resistance to degradation experienced by earthen construction in these climate conditions and the widespread perception of earthen construction as a substandard choice for resistance to extreme wind loads.

The present research aims to: (1) demonstrate the feasibility of earthen masonry housing in the US Gulf Coast region to endure humid climate and hurricane winds, (2) enhance the strength and deformability of CSEBs using sugarcane bagasse fibers (SCBFs) that can be used for the construction of affordable eco-friendly low-rise dwellings, and (3) develop a finite element (FE) micro-modeling technique to understand the behavior of CSEB masonry at the structural level.

A structural, architectural, and economic feasibility study for CSEB structural systems in the US Gulf Coast was performed. The structural feasibility study concluded that CSEBs fabricated with local soil and protected with a soil-cement plaster can provide sufficient resistance against weathering and hurricane wind loads. The architectural feasibility study investigated the use of CSEB systems in vernacular housing typologies in Southern Louisiana. Finally, the economic feasibility study compared the cost of a reference house built using CSEBs and other ordinary construction materials. The results suggest that CSEB systems have the potential to provide a modern, cost-effective, sustainable, hurricane-resistant housing construction system as an alternative to more commonly used constructions systems in the US Gulf Coast region.

The effect of SCBFs on the mechanical strength and durability properties of CSEBs was also examined. A total of nine different soil mix compositions containing different amounts of SCBFs (0%, 0.5%, and 1.0% in weight) and Type II Portland cement (0%, 6%, and 12%) were considered. The flexural, dry compressive, and wet compressive strengths of the different CSEBs were evaluated experimentally. The CSEB durability was also examined by measuring mass loss, dry

density, water absorption, and wet compressive strength after 12 wetting and drying cycles. The morphology and chemical composition of the CSEBs were investigated via scanning electron microscopy and energy-dispersive X-ray spectroscopy, whereas the mineralogical characteristics were evaluated using X-ray crystallography. The results show that including 0.5% to 1.0% by weight of SCBFs in CSEBs stabilized with 12% by weight of cement can significantly improve the CSEB mechanical properties without compromising their durability properties. The use of CSEBs in conjunction with SCBFs represents a promising solution for the construction of affordable, eco-friendly, low-rise dwellings.

A new interface element's constitutive model was proposed for modeling masonry structure. The newly-developed model can simulate tension cracking, shear slipping, and compression failure and is defined by a convex composite failure surface comprising a tension-shear and a compression cap failure criterion. The proposed model removes the singularity in the tension-shear region but not in the compression-shear region and is based on the hypothesis of strain hardening. The robustness and computational cost of the proposed model were compared, through a series of one-element tests and through the comparison of FE response of an unreinforced masonry shear wall, to different existing constitutive models that have been widely used in the literature to describe masonry behavior and that are based on three-, two-, and single-surface failure criteria. The FE response results show that the proposed constitutive model is more efficient than and at least as accurate as the other existing constitutive models for simulating the mechanical behavior of masonry structures.

Using the newly-developed interface element's constitutive model for masonry structures, the capabilities and limitations of different FE simplified micro-modeling techniques were investigated for fired-clay brick (FCB) and CSEB masonry walls, for which well-documented experimental results are available in the literature. The FCB unreinforced masonry wall showed inelastic behavior and cracks limited to the masonry joints (i.e., mortar and unit-mortar interfaces), whereas the CSEB masonry showed inelastic behavior and cracks spread over the different masonry constituents. Three different simplified micro-model were developed for each benchmark example, based on the different material constitutive models used for the masonry units, i.e., rigid, elastic, and elasto-plastic constitutive models. The FE responses of the different simplified micro-model considered were compared with experimental results in terms of predicted load-displacement response, strength, initial stiffness, collapse mechanism, computational efficiency, and output information. The results show that simplified micro-models can properly simulate the FE behavior for the FCB masonry shear walls. However, this technique is not suitable for the CSEB masonry since the simplified micro-models does not allow free crack propagations.

Based on the investigation of capabilities and limitation of simplified FE micro-modeling techniques, it was concluded that a FE detailed micro-modeling approach is required to simulate the mechanical behavior of CSEB masonry systems, for which the inelastic behavior is not necessarily concentrated at the masonry joints but can spread to the masonry units. Therefore, a FE detailed micro-model was developed specifically tailored for earth block masonry systems. Through a series of FE simulations of representative volume elements of masonry, it is shown that the detailed micro-model and the simplified micro-models provide consistent predictions of the mechanical behavior of masonry systems only under specific conditions depending on the relative strength and stiffness of masonry units and mortar, as well as on the loading conditions. However, the proposed detailed micro-model is able to accurately simulate the experimentally-measured mechanical response of earth block wallettes subject to diagonal load testing, for which simplified micro-models were demonstrated to be inaccurate. The results of this research provide a new tool for accurate prediction and simulation of masonry systems in which the masonry units have strength and stiffness that are similar or lower than those of the mortar and the mortar-unit interfaces.

TABLE OF CONTENTS

LIST OF FIGURES

LIST OF TABLES

CHAPTER 1. INTRODUCTION

1.1. Background

Earthen structures are buildings and structures primarily made from soil [1]. Since soil is a widely available and inexpensive material, it has been used in construction since prehistoric times [2]. When compared to other traditional construction methods (e.g., reinforced concrete, fired masonry, concrete masonry, and wood construction), earthen structures: (1) can be more affordable [2–7]; (2) are environmentally friendly, with an embodied energy that can be up to 85% lower than concrete masonry units and fired clay bricks [8–12]; (3) require lower operational energy due to advanced thermal efficiency and high volumetric heat capacity, which reduces energy consumption for heating and cooling [13–18]; (4) are able to passively maintain a healthy indoor relative humidity between 40-60% [2,12,19], which represents an ideal range for healthy indoor relative humidity [18]; (5) have a longer useful life [12]; (6) are naturally resistant to mold, fungi, rot, insects, and pests [18]; (7) are extremely efficient for noise reduction [20]; (8) are built using almost exclusively locally available materials [13,14,21]; (9) are fire-resistance [22–24]; and (10) are equitable, community engaging, and inherently recyclable [25], which significantly reduces their carbon footprint compared to traditional structures.

Earthen construction is one of the most ancient and sustainable approaches to building structures, as evidenced by construction remains dating back thousands of years ago, e.g., in Italy, Iran, and China [2]. Soil can be combined with water to make mud, can be improved with straws or some form of stabilizing material such as lime and/or cement, and can be compacted to increase its strength [12,26]. Different traditional earthen structure systems were developed over the centuries, such as [12,27–31]:

1. Cob structures: cob, sometimes referred to as "monolithic adobe", is a natural building material composed by a soil mixture, which includes clay, sand or small stones, fibrous organic material such as straw, and water [30,31]. Cob walls are usually built up in courses, have no mortar joints and need 30% or more clay in the soil.
2. Rammed earth structures: rammed earth is a technique for building walls using natural raw materials such as earth, chalk, lime, and/or gravel [27,28]. A rammed earth wall is built by placing damp soil in a temporary form. The soil is manually or mechanically compacted and then the form is removed. Rammed earth is made using relatively small amounts of water, thus requiring shorter drying times than other earthen construction techniques.


(a) (b) (c)

Figure 1.1. Traditionally earthen structure systems: (a) 'cob stitch' repair on old traditional cob cottage in Devon, England; (b) Taipa section of the Great Wall of China; (c) adobe brick house under construction in Kyrgyzstan (courtesy: https://en.wikipedia.org/wiki/).

3. Adobe (earth block) structures: adobe structures are masonry constructions made of unfired bricks (adobe) produced using a mixture of sand, clay, water, and some kind of fibrous material (sticks, straw, or manure) [28]. Adobe bricks are fabricated with the help of molds and are dried in the sun. Then, these bricks are used to build walls (with or without mortar) as ordinary masonry. The word “adobe” has existed for around 4,000 years, as it can be traced to the Middle Egyptian era (about 2000 BC) before being introduced in Arabic, in Old Spanish, and later in English [29] in the early 18th century.

Traditionally-built earthen structures (i.e., non-engineered earthen constructions) are often not capable of resisting extreme loads from natural hazards such as earthquakes and strong winds, due to the inherent brittleness of the material [32–36]. However, in the last few decades, significant research has been devoted to develop engineered earthen structures as a more affordable and ecologically-friendly alternative to structures built using other construction methods based on industrial materials (e.g., reinforced concrete, fired-brick masonry, concrete masonry, and wood construction) [37–40]. Consequently, engineered earthen construction has emerged as a viable modern construction technique due to its eco-efficiency and extreme affordability [12,41]. Among the different typologies of earthen structures, adobe or earth block structures have been used more frequently in industrialized society due to their advantages, i.e., (1) the individual components (i.e., earth block and mortar) of the earth block structures can be easily engineered to improve their strength and durability [37,42,43], and (2) the earth block construction technique shared many similarities with ordinary masonry [42], for which extensive experience and a vast engineering literature are available. The modern adobe or earth blocks can be categorized into three different broad categories:

1. <u>Compressed earth blocks (CEB):</u> CEBs are bricks produced using a mix of dry inorganic subsoil, non-expansive clay, and aggregates compressed at high pressure [44,45]. Generally, a hydraulic or a manual press is used to mechanically compress the soil mix into strong blocks. The binding of the material is provided by the mechanical compression.
2. <u>Stabilized earth blocks (SEB):</u> the soil mix is stabilized with a chemical binder such as Portland cement or lime to form SEB [46]. These blocks are not compressed like CEBs; however, the stabilizer binds the mix, and provides strength and durability to the blocks.

3. Compressed and stabilized earth blocks (CSEB): a soil mix is first stabilized with a chemical binder and then compressed at high pressure to form CSEBs [43,47]. CSEBs use both mechanisms of CEBs and SEBs to form strong and durable earth blocks, which are more suitable for modern construction.

Earthen buildings represent only a small fraction of the building inventory in U.S., even in places where this type of construction is historically established and culturally appreciated (e.g., in NM, CO, AZ, TX, and CA). Earthen construction is viewed with hesitation by the construction industry and its use is negatively affected by the widespread perception of it as a substandard choice for construction [18]. In addition, earthen construction is even less common in humid and rainy climates such as those of the U.S. Gulf Coast [48], because traditional earthen construction exhibits a poor resistance to degradation in such climates [43] and to extreme wind loads [18]. These issues are related to the inherent brittleness of traditional non-engineered structures, as well as to the lack of engineering knowledge needed to model and predict the mechanical behavior of CSEB masonry at the structural level.

Because of the limited understanding, material-specific design standards for CSEB masonry construction are also lacking. In fact, despite the potential advantages of CSEB structures over other construction techniques, the international acceptance of this type of construction [3,20,42,49–54], and the availability of an ASTM standard for the design of earth block masonry systems [55], only few building codes in the U.S. allow the use of earth block construction, generally through an empirical/prescriptive approach adapted from ordinary and concrete block masonry [56–59], which does not properly take advantage of the specific characteristics of the CSEB materials and construction techniques. Similarly, earthen building codes from around the world, e.g., those developed by the International Code Council [57,58], Standards New Zealand [51,60], and Indian Standard [61], depend heavily on established methods for ordinary masonry and reinforced concrete structures when providing guidance on engineering analysis of earthen structure [62,63]. In recent years, most of the research studies focused on understanding the engineering characteristics of the CSEB components [22,23,69–78,24,79–83,26,43,64–68]. Only few studies have been performed to investigate the mechanical behavior of CSEB masonry systems at the structure level [21,84–90]. In addition, numerical studies to simulate or understand the behavior of CSEB masonry have been limited [91–93], and these numerical studies generally used finite element (FE) modeling technique originally developed for ordinary masonry. To the author's knowledge, no attempt has been made to develop FE modeling techniques that are specifically tailored to CSEB masonry. As a result, there is a significant gap between the current state of knowledge and the engineering understanding that is necessary for developing material-specific design standards of CSEB masonry systems.

1.2. Objectives

This dissertation focuses on CSEB construction by investigating the feasibility of using earthen masonry for building house in a humid climate, improving the mechanical properties of CSEBs to reduce their inherent brittleness, and advancing the engineering knowledge needed to understand the mechanical behavior of CSEB masonry at the material, component, and system level. The specific objectives are:

1. Investigating the structural, architectural, and economic feasibility of CSEB systems as a hurricane-resistant, affordable, and durable housing typology that can be reliably used even in the U.S. Gulf Coast's humid climate.

2. Investigating the effects of sugarcane bagasse fiber (SCBF) on the mechanical (i.e., toughness and ductility) and durability properties of CSEBs fabricated using different levels of cement stabilization and SCBF amounts.
3. Developing a computationally efficient and robust interface element's constitutive model that can simulate tension cracking, shear slipping, and compression failure for simulating and analyzing the mechanical behavior of masonry.
4. Investigating the capabilities and limitations of the FE simplified micro-modeling techniques that are frequently used for simulating the behavior of ordinary masonry by comparing experimentally measured and numerically simulated responses of fired-clay brick masonry and CSEB masonry.
5. Developing a FE detailed micro-modeling technique for simulating and analyzing the behavior of CSEB masonry systems and identifying the specific conditions under which simplified micro-modeling techniques can predict the mechanical behavior of masonry systems depends on the relative strength of masonry units and mortar, as well as on the loading conditions, through a series of FE simulations of representative volume elements of masonry subjected to three points bending and shear loading.

1.3. Motivation

In the modern era of industrial materials such as concrete, steel, and engineered timber, earthen structures have seen a significantly reduced usage, due to their relatively low strength and lack of standardization. However, they are once again getting attention because of their low cost, low carbon footprint, energy efficiency, use of indigenous materials, and inherent simplicity [1,94]. In particular, earth block construction is appealing as a viable response to the lack of affordable housing in the U.S. and all around the world. Currently, U.S. is facing a shortage of nearly 3.3

million economical affordable homes [95]. In addition, it is expected that over two billion new houses will be needed worldwide in the next 80 years [96] to address the predicted world population increase [97,98] and expected improvements of living standards [99]. If properly engineered, earth block construction has the potential to address this rapidly growing housing demand in the U.S. and all around the world in an innovative, sustainable, and economical affordable manner.

1.4. Research Novelty and Significance

The research presented in this study provides several novel contributions to engineering knowledge of earthen structures. The following specific contributions are noteworthy:

1. This study demonstrates for the first time that CSEB structures are feasible from a structural, architectural, and economic point of view even for affordable hurricane-resistant housing in the U.S. Gulf coast, which represents a very challenging environment for earthen construction.
2. The inclusion of SCBF in the production of reinforced CSEBs is shown to radically improve the mechanical and durability properties of CSEBs. The presented results suggest that SCBF-reinforced CSEBs potentially represent a more sustainable alternative to other conventional modern construction techniques, such as light-framed wooden construction, ordinary masonry, and concrete block masonry. The use of SCBFs in the fabrication of CSEBs can also address the waste disposal problems associated with excess production of SCBFs.
3. A novel mechanical constitutive model for interface elements is introduced in the context of the FE simplified micro-modeling approach for masonry structures. It is shown that the newly proposed constitutive model is more efficient than and at least as accurate as the other existing constitutive models for modeling masonry structures.

4. This study clearly demonstrates for the first time the capabilities and limitations of existing FE simplified micro-modeling techniques for ordinary and CSEB unreinforced masonry. In particular, this study shows that FE simplified micro-models (SMMs) of unreinforced masonry walls can provide accurate response results when the inelastic behavior is concentrated in the masonry joints (as it is usually the case for fired-brick and concrete block masonry), but it can produce very inaccurate response results when the inelastic behavior is spread across both masonry joints and masonry units, which is typical for CSEB unreinforced masonry because masonry units and mortar have often similar mechanical properties.
5. This investigation extends the use of FE detailed micro-modeling to analyze the mechanical behavior of earth block masonry systems for the first time. It also identifies the range of validity for SMMs of masonry walls as a function of the relative strength and stiffness of mortar and masonry units, and of the type of loading conditions. The new knowledge presented in this dissertation advances the FE modeling of unreinforced masonry, particularly for systems characterized by masonry units that are very weak or very strong when compared to the associated mortar. These results and the FE detailed micro-modeling approach developed in this study are critical to promote the practical use of earth block masonry, as they provide the structural engineering community with an accurate tool for the numerical modeling of the structural behavior of unreinforced masonry.

The results of this research represent an advancement in the engineering knowledge necessary for: (1) promoting CSEB construction that can endure humid climate and hurricane wind, and (2) understanding the structural behavior of CSEB masonry, which will ultimately be required for developing material-specific design standards of CSEB masonry system.

1.5. Outline of Dissertation

The research presented in this dissertation is the collection of several papers that have been published in, are under review by, or are in preparation for submission to peer-reviewed journals publishing research in the field of Structural Engineering. The complete list of these papers is provided in Section 1.6 of this introductory chapter.

Chapter 2 presents the structural, architectural, and economic feasibility study for CSEB structural systems in the U.S. Gulf Coast. The structural feasibility study presented in this chapter included the identification of locally available soils for CSEB fabrication, the experimental investigation of the mechanical properties of CSEBs and mortar as functions of their composition; a durability study for a CSEB wall with and without protective plastering, and the calculation of the wind resistance for a representative CSEB house. The architectural feasibility study investigated the use of CSEB systems in vernacular housing typologies of Southern Louisiana. Finally, the economic feasibility study compared the cost of a reference house built using CSEBs and other construction materials that are more commonly used in Southern Louisiana.

Chapter 3 investigates the effects of SCBFs on the mechanical strength and durability properties of CSEBs. CSEBs were fabricated using natural soil and SCBFs collected from Lakeland, LA, with a manually operated compression machine. Nine different soil mix compositions containing different amounts of sugarcane bagasse fiber (0%, 0.5%, and 1.0% by weight) and Type II Portland cement (0%, 6%, and 12% by weight) were considered. The flexural, dry compressive, and wet compressive strengths of the different CSEBs were evaluated experimentally. Durability was also examined by measuring mass loss, dry density, water absorption, and wet compressive strength after 12 wetting and drying cycles. The morphology and chemical composition of the CSEBs were investigated via scanning electron microscopy and energy-dispersive X-ray spectroscopy, whereas the mineralogical characteristics were evaluated using X-ray crystallography.

In chapter 4, a new interface element's constitutive model is proposed for analyzing masonry using the simplified micro-modeling approach, in which the mortar layer and the two adjacent unit-mortar interfaces are lumped into a zero-thickness joint (modeled using an interface element) between expanded masonry units. The new model is capable of simulating tension cracking, shear slipping, and compression failure and is defined by a convex composite failure surface consisting of a tension-shear and a compression cap failure criterion. It removes the singularity in the tension-shear region but not in the compression-shear region. In addition, the proposed model is based on the hypothesis of strain hardening. The robustness and computational cost of the proposed model are compared to different constitutive models (which are based on three, two and single failure criterion) that have been widely used in the literature to describe masonry behavior through a series of one-element tests and through the comparison of FE response simulation of an unreinforced masonry shear wall.

Chapter 5 of this dissertation highlights the capabilities and limitations of different SMMs by comparing their relative performance for two different types of masonry, i.e., fired-clay brick and CSEB masonry, for which well-documented experimental results are available in the literature. This chapter presents existing FE simplified micro-modeling techniques that have been widely used for simulating the mechanical behavior of ordinary masonry. It then provides recommendations on constitutive models, FE solvers, and discretization requirements for FE simplified micro-modeling of unreinforced masonry. Finally, two benchmark examples corresponding to fired-clay brick and CSEB masonry are investigated by comparing the FE responses numerically obtained from the different SMMs with experimental results in terms of predicted load-displacement response, strength, initial stiffness, collapse mechanism, computational efficiency, and output information.

Chapter 6 presents presents a detailed micro-model (DMM) specifically tailored to model earth block masonry systems. Then, through a series of FE simulations of representative volume elements of masonry subjected to three-point bending and to shear loading, this study identifies the conditions (in terms of relative strength of masonry units and mortar, and of loading conditions) under which the structural response results obtained using different SMMs and the DMM are consistent. Finally, the new DMM is validated through a comparison of its FE response with existing experimental results for earth block masonry wallettes subject to diagonal compression, for which SMMs were demonstrated to provide inaccurate results in the Chapter 5.

Finally, Chapter 7 provides a summary of the research performed, identifies the conclusions achieved in this study, and suggests future research directions. Six appendices provide additional material and data that did not find space in the journal articles, but that are complementary to the core material of this dissertation.

1.6. Journal publications derived from this dissertation

Journal article based on chapter 2 (published):

- Kumar, N.[1], Barbato, M.[2], Holton, R.[3] (2018). "Feasibility Study of Affordable Earth Masonry Housing in the U.S. Gulf Coast Region." *Journal of Architectural Engineering*, ASCE, 24(2): 04018009. https://doi.org/10.1061/(ASCE)AE.1943-5568.0000311

Journal article based on chapter 3 (published):

- Kumar, N.[1], Barbato, M.[2] (2022). “Effect of Sugarcane Bagasse Fiber on the Properties of Compressed and Stabilized Earth Blocks.” *Construction and Building Materials*, Elsevier, 315: 125552. https://doi.org/10.1016/j.conbuildmat.2021.125552

Journal article based on chapter 4 (published):

- Kumar, N.[1], Barbato, M.[2] (2019). “Interface Element Constitutive Model for Finite Element Modeling of Masonry.” *Journal of Engineering Mechanics*, ASCE, 145(5): 04019022. https://doi.org/10.1061/(ASCE)EM.1943-7889.0001592

Journal article based on chapter 5 (submitted):

- Kumar, N.[1], Barbato, M.[2], Rengifo-López, E. L.[4], Matta, F.[5], (2022). “Capabilities and Limitations of Existing Finite Element Simplified Micro-Modeling Techniques for Unreinforced Masonry: General Considerations and Case Studies.” *Research on Engineering Structures & Materials.*

Journal article based on chapter 6 (in preparation):

- Kumar, N.[1], Rengifo-López, E. L.[4], Barbato, M.[2], Matta, F.[5], (2022). “Finite Element Detailed Micro-modeling of Unreinforced Earth Block Masonry System.” *Journal of Structural Engineering*, ASCE.

---

[1] Ph.D. student, Department of Civil & Environmental Engineering, University of California, Davis; Email: ntnkumar@ucdavis.edu; ORCID: https://orcid.org/0000-0002-4045-300X

[2] Professor, Department of Civil & Environmental Engineering, University of California Davis; E-mail: mbarbato@ucdavis.edu; ORCID: https://orcid.org/0000-0003-0484-8191

[3] Associate Professor, School of Architecture, Louisiana State University, Baton Rouge, LA, USA; E-mail: rholton@lsu.edu

[4] Ph.D. student, Department of Civil & Environmental Engineering, University of South Carolina, Columbia; Email: rengifol@email.sc.edu; ORCID: https://orcid.org/0000-0002-2136-2639

[5] Associate Professor, Department of Civil & Environmental Engineering, University of South Carolina, Columbia; Email: fmatta@sc.edu; ORCID: https://orcid.org/0000-0001-7018-6611

CHAPTER 2. FEASIBILITY STUDY OF AFFORDABLE EARTH MASONRY HOUSING IN THE U.S. GULF COAST

2.1. Introduction

A significant portion of the world's population currently lives in earth-based dwellings [100]. Earth construction provides several advantages over other traditional construction methods (e.g., reinforced concrete, fired masonry, and wood construction). In particular, earth construction is: (1) affordable and locally appropriate, since inexpensive and locally available soils are used as the primary structural materials [2,101]; (2) energy and humidity efficient, due to its relatively high volumetric heat capacity and excellent ability to passively maintain a healthy indoor relative humidity [2,12]; and (3) environmentally friendly, with an embodied energy that can be over 80% lower than that of concrete masonry units and fired clay bricks [12,101].

Earth construction is also one of the most ancient and sustainable approaches for building construction, dating back over 9000 years ago [2], and with examples found all over the world [102]. Different earth construction techniques were developed over the centuries, the most prominent of which are cob construction, rammed earth construction, and earth block or adobe construction [12,30]. These traditionally built earthen structures (i.e., non-engineered constructions) are not capable of resisting extreme loads from natural hazards such as earthquakes and strong winds, due to the inherent brittleness of the material [32–36]; therefore, they are inadequate for mainstream modern construction. However, in the last few decades, significant research has been devoted to develop engineered earth blocks as a more affordable and ecologically friendly alternative to other masonry elements, e.g., fired bricks and concrete blocks [37–40]. Consequently, engineered earth block construction has emerged as a viable modern construction technique due to its eco-efficiency and extreme affordability [12,41]. In particular, earth block construction is a promising technique because: (1) its individual components (i.e., earth block and mortar) can be engineered to improve their strength and durability [37,42,43], and (2) the construction technique has many commonalities with ordinary masonry [42], for which extensive experience and a vast engineering literature are available. Modern earth blocks can be categorized into three different broad categories: (1) compressed earth blocks (CEBs), which are produced by compressing an appropriate soil mix with the help of a hydraulic or a manual press [12,44,45]; (2) stabilized earth blocks (SEBs), which are made from a soil mix that is stabilized using a chemical binder such as Portland cement or lime [46]; and (3) compressed and stabilized earth blocks (CSEBs), which are fabricated by mechanically compressing a stabilized soil mix [43,47]. CSEBs use both mechanisms of CEBs and SEBs to form strong and durable earth blocks, which are more suitable than other earth blocks to satisfy modern construction requirements.

Currently, earth construction in the USA is mainly used in dry and arid regions, e.g., New Mexico, Colorado, Arizona, California, and West Texas [15]. New Mexico has also incorporated the use of earth blocks for non-hurricane prone areas into the state's building code [56]. However, CSEB construction has rarely been used in the U.S. Gulf Coast [48] because of the poor resistance to degradation generally experienced by earth construction in a humid and rainy climate [43], and the widespread perception of earth construction as a substandard choice for resistance to extreme wind loads. By contrast, recent research based on structural analysis results and controlled laboratory experiments has demonstrated that earth masonry can safely withstand extreme wind loads [21] and windborne debris impacts [89,103] due to hurricanes or tornadoes.

The goal of this study is to investigate the feasibility of CSEB systems as a hurricane-resistant, affordable, and durable housing typology that can be reliably used even in the U.S. Gulf Coast's humid climate. This study includes the investigation of structural, architectural, and economic feasibility of a typical earth block house compared with one of a similar size built with common construction techniques. A preliminary investigation of the use of a soil-cement plaster protection for CSEB walls is also presented as part of the structural feasibility study.

2.2. Motivation and Significance

A significant portion of the U.S. population (including a significant number of underrepresented and underprivileged groups) live in rural and remote areas, particularly in Louisiana. In these rural areas, affordable housing is key to reducing homelessness, creating jobs, and fostering economic development. According to data published by the U.S. Department of Housing and Urban Development in 2010, 386,000 low-income households in Louisiana are in need of affordable housing [104]. The National Association of Home Builders [105] estimates that, for each newly built house, three full-time equivalent new jobs are created, particularly in the construction and manufacturing industry, and $111,000 in government revenue (including income taxes, government social insurance, permit and license fees, and sales taxes) is generated ($74,400 in federal taxes and $36,600 in state and local taxes). This estimate does not include the indirect economic impact of the new house, e.g., due to the relocation and future earnings of the building owners, which is generated over a prolonged period of time. The critical demand for low-cost housing in the U.S. Gulf Coast is exacerbated by recurring tropical storm, flooding events, subsidence, and water level rising, as recently documented by Davenport and Robertson [106], in which thousands of residents across southern Louisiana were displaced by the land loss induced by coastal erosion and climate change effects.

In our current period of rising global temperatures, unpredictable events have and will continue to displace thousands of residents in the coastal region of Louisiana. This historic unseating of entire communities necessitates a reconsideration of standard housing solutions. Constructed primarily of materials accessible from the building site, CSEB design and building techniques offer an economical and sustainable approach to the current increase in demand for affordable weather resistant housing. The research presented in this chapter proposes the novel use of CSEBs in a hot wet environment and provides the preliminary engineering basis needed to offer affordable, resilient, and sustainable housing for the many individuals in need in the U.S. Gulf Coast region.

2.3. Structural Feasibility Study

The structural feasibility of CSEB housing in the U.S. Gulf Coast depends on the mechanical properties of CSEB elements (i.e., blocks and mortar) and CSEB systems (e.g., walls and pillars). These properties need to satisfy several minimum standard requirements to ensure sufficient resistance of the construction to extreme winds as those associated with hurricanes. In addition, the CSEB walls need to achieve a sufficient durability when exposed to the humid weather typical of this region of the U.S. The CSEB mechanical properties depend mainly on the properties and composition of the available soil, the fabrication process, and the amount of stabilizer used in the soil mix. This section presents: (1) the identification of appropriate soil in the East Baton Rouge area, (2) the description of the CSEB fabrication process adopted in this study, (3) the investigation of the mechanical properties of CSEBs as a function of the amount of cement used as stabilizer, (4) the investigation of the mechanical properties of soil-based mortar as a function of cement and sand content, (5) a durability study of an actual CSEB wall subject to the humid weather in Baton Rouge, and (6) the estimation of the resistance of the main wind-force resisting system for a hypothetical house built using locally produced CSEBs. It is noted here that Portland cement was used as the stabilizer material and as an ingredient of the weather protection plaster. This preliminary selection was made based on the wide availability of this material and on existing literature, which suggests that cement is highly efficient in increasing the mechanical strength and durability of CSEBs [43,46]. However, other more sustainable solutions could also be considered in future studies, e.g., using lime as stabilizer [48], or modifying foundations, roofing, and building geometry to minimize the weather effects in rainy environments [53], and/or investigate other rendering solutions to protect the building envelopes (e.g., earthen plasters stabilized with lime, acrylic emulsions, polymers, asphalt emulsions, agave juice, see [107,108].

2.3.1. *Soil Identification*

Production of high-quality CSEBs requires soils with specific compositions, i.e., the appropriate proportions of sand, silt, and clay contents. Existing literature provides recommended soil composition ranges for fabrication of CEBs [12,38,42,44]. These soil compositions can be obtained through a particle size analysis and can be classified using the Unified Soil Classification System (USCS) [109]. **Figure 2.1(a)** shows the United State Department of Agriculture [110] soil texture triangle, which provides a graphical representation of the composition of a soil. In this figure, the thick blue line identifies the optimal soil compositions for fabricating CEBs, the thick magenta dashed line identifies sub-optimal soil compositions that can still be used for CEBs, and the region outside the above lines represents soil compositions that are generally considered inappropriate for CEB fabrication, according to the existing literature. Additional criteria have been suggested in terms of Atterberg limits ASTM D4318-17e1 [111], e.g., with optimal liquid limits (LL) ranging from 25 to 50, and optimal plasticity indexes (PI) ranging from 2.5 to 29 [12,44]. It is noted here that only scarce information is available in the literature for optimal soil compositions and Atterberg limits for fabrication of CSEBs. However, it is reasonable to expect that a wider range of soil compositions and values of Atterberg limits can be considered acceptable when compared to those for CEB fabrication, since the soil can be partially ameliorated by using appropriate stabilizers.

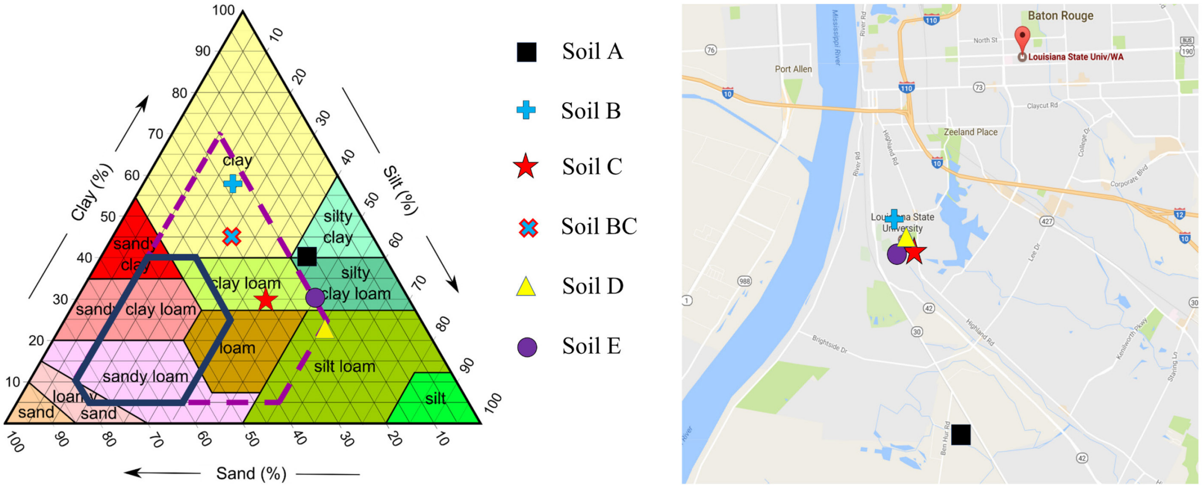

(a)

(b)

Figure 2.1. Tested soils: (a) USDA soil texture triangle with optimal soil grading region and composition of tested soils from Baton Rouge, LA; and (b) map of Baton Rouge with site locations of different soils.

Soil samples were taken from five different locations (A, B, C, D and E) in Baton Rouge from the layer between 1 and 2 m below the surface, as shown in **Figure 2.1(b)**). Simple preliminary in-situ tests (i.e., “cigar” and jar tests) were used to verify if these soils were appropriate for CSEB fabrication based on suggestions provided in the literature [42]. The average “cigar” lengths were in the range between 12-15 cm (see **Figure 2.2(a)**), which is considered an acceptable range for CEB fabrication [42]. In the jar test, only one layer of soil particle was observed for all soils, as shown in **Figure 2.2(b)**, which indicates that these soils contain almost exclusively fine particles (i.e., silt and clay).

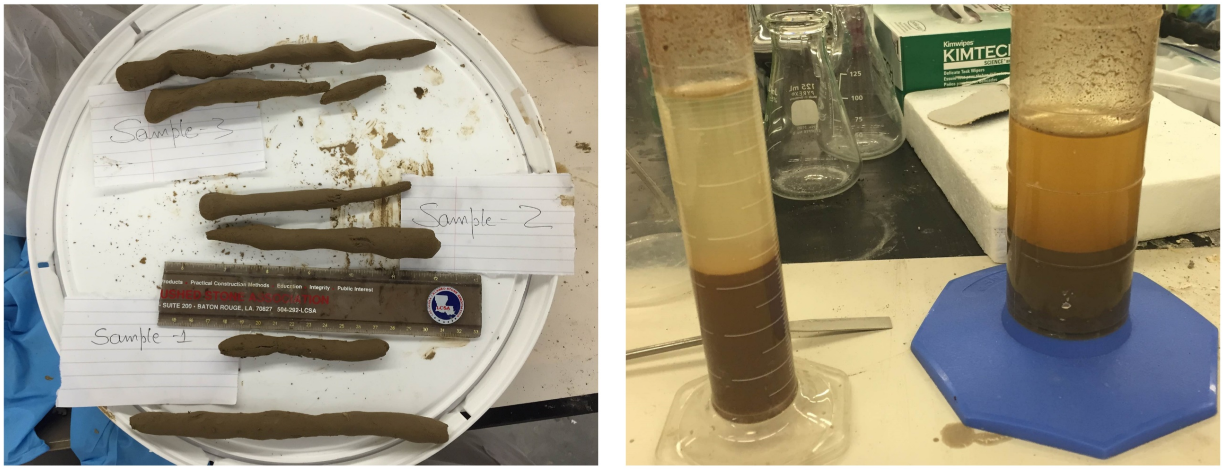

(a) (b)

Figure 2.2. In-situ soil identification tests: (a) cigar test; (b) jar test.

After performing in-situ tests, the granulometry and Atterberg limits of the soil samples were obtained by performing standard laboratory tests. The results of the particle size analysis, performed according to ASTM D6913-17 [112] and ASTM D7928-17 [113], are presented in **Figure 2.3** and were used to classify the different soils on the USDA soil texture triangle presented in **Figure 2.1(a)**. The Atterberg limits were measured according to ASTM D4318-17e1 [111]. The LL were 35.5%, 30%, 28%, 27.5%, and 26.5% for soil A, B, C, D, and E respectively, whereas the PI were 12.5%, 8.0%, 11.5%, and 12% for soil A, B, C, D, and E, respectively. The results of the laboratory test indicate that the used soils: (1) have LL and PI values within the optimal ranges, and (2) lay within the sub-optimal composition region (soil B and C) or immediately outside this region as identified on the USDA soil texture triangle (see Fig. 1). The soils used in this study are representative of the soil available in the East Baton Rouge area.

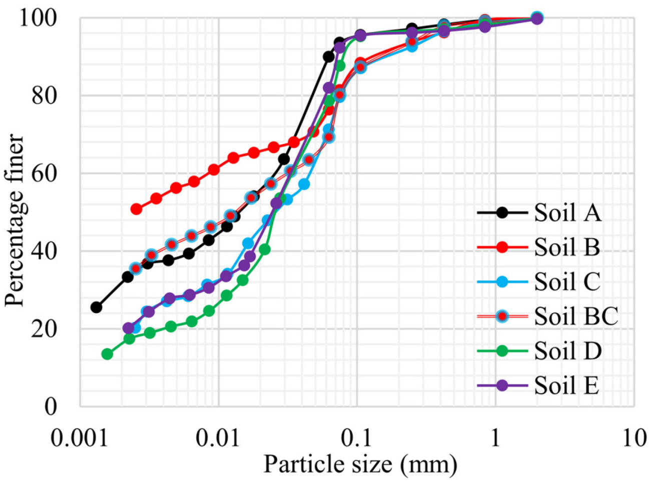

Figure 2.3. Grain size analysis of soils collected from different locations in Baton Rouge, LA.

2.3.2. *Fabrication Process of CSEBs*

The fabrication process of CSEBs, and in particular the compaction process, can significantly affect the CSEB mechanical and physical properties [38,114]. CSEBs can be fabricated using: (1) quasi-static compaction, through a slowly applied pressure in single-side compaction, double-side compaction, or extrusion [38,115]; or (2) dynamic compaction, through impact or vibration [116]. Quasi-static compaction is most commonly applied by using manually operated or hydraulic compression machines. A single-stroke manual one-side compaction machine made of steel was fabricated purposely for this study and is shown in **Figure 2.4**.

The CSEB fabrication was performed by: (1) extracting, drying, and pulverizing of the soil; (2) sieving the pulverized soil to remove any organic and course particle; (3) weighing the soil, cement, and water to obtain the desired amounts; (4) mixing soil and cement thoroughly with the help of a power-driven mixer for at least 10 min; (5) adding the water to the soil-cement blend in multiple steps while mixing it; and (6) compressing the wet soil-cement blend by using the compaction machine to form blocks. The production time between material mixing and fabrication of all blocks was maintained below 45 minutes for all batches, in order to avoid excessive curing of the cement. Each batch consisted of five to eight blocks. After fabrication, the blocks were cured for 28 days by wet-and-dry curing [42], i.e., the blocks were wrapped in a plastic sheet inside the laboratory for the first 14 days to maintain a high humidity environment, and avoid rapid evaporation and formation of shrinkage cracks, then they were left to dry for 14 additional days without being directly exposed to sun and wind.

Figure 2.4. Single-stroke manually operated one-side compaction machine.

2.3.3. *Mechanical Properties of CSEBs*

This study investigated the effects of different amounts of cement used as a stabilizer on the compressive and flexural strength of earth blocks made with soil from East Baton Rouge, LA. Compressed earth blocks of dimension 290 x 145 x 75 mm3 were fabricated with soil A and different percentages in weight (wt.%) of type II Portland cement (PC), namely 0 wt.% (CEB), 3 wt.% (CSEB03), 6 wt.% (CSEB06), 9 wt.% (CSEB09), and 12 wt.% (CSEB12). Five equally-built specimens for each cement content of CSEBs were tested using an MTS universal testing machine with a 50 kN load cell capacity to determine the block's average dry compressive strength, f_{bd} , wet compressive strength, f_{bw}, and modulus of rupture (MOR). The specimens were loaded in displacement-control mode at the rate of 2 mm/min.

First, a three-point bending flexure test was performed on the full-size blocks [56]. The displacement was applied at the middle of the block with a 20 mm distance between edge and support, giving a 250 mm clear span, as shown in **Figure 2.5(b)**. **Figure 2.6** plots the applied load-midspan deflection curves for all tested specimens. The results of the flexure test in terms of sample means, minimum/maximum values, and coefficients of variation for MOR and modulus of elasticity (MOE) are reported in **Table 2.1**. The flexure test resulted in the formation of a well-defined large crack in the middle of the earth blocks. The two halves of each tested specimen, produced by the fracture of the block in the flexure test, were trimmed using masonry cutting tools to produce two specimens of dimension 100 x 100 x 75 mm^3 to be used in a direct compression test [117]. For each cement content, five half-block specimens (one from each original earth block) were tested for dry compression tests, whereas the remaining five specimens were immersed in water for 24 hours before being tested for wet compressive strength. Neoprene pads were placed between the steel plates and test specimens during each compression test.

Figure 2.7(a) and **(b)** plot the stress-strain curves for all tested specimens corresponding to the dry and wet compression tests, respectively. The results of the dry and wet compression tests in terms of sample means, minimum/maximum values, and coefficients of variation for compressive strength and MOE are reported in **Table 2.1**, which also reports the estimate of the characteristic uniaxial dry and wet compressive strengths, f_{bkd} and f_{bkw} respectively, accounting for shape and aspect ratio corrections [118]. The failure mode observed during wet and dry compression tests corresponded to the development of an hour-glass shape following the spalling of the vertical sides of the tested specimen, as shown in **Figure 2.6(b)**. This failure mode is similar to that commonly observed in compression tests of typical concrete cubic specimens.

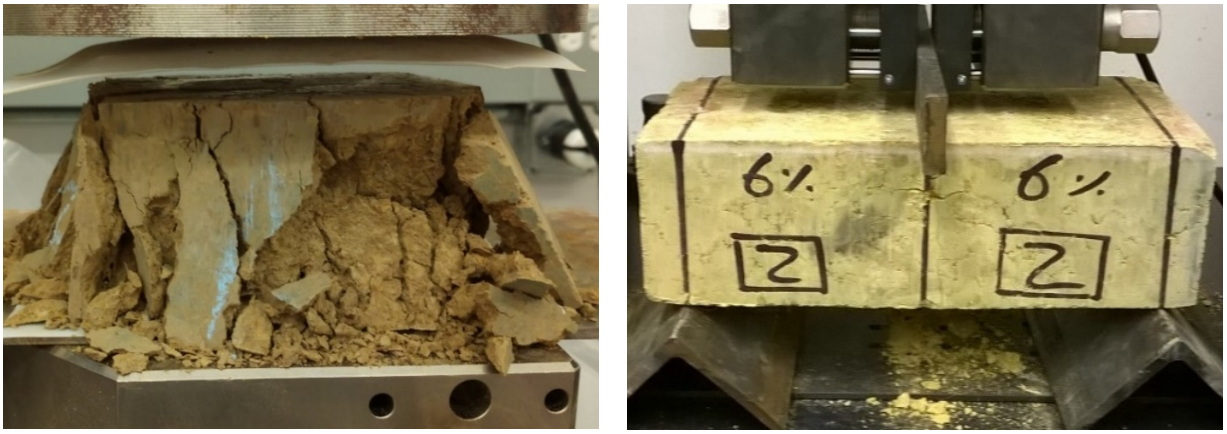
(a) (b)

Figure 2.5. Experimental mechanical tests: (a) specimen after flexure test; (b) specimen after compression test.

Table 2.1. Mechanical properties of CSEBs for different cement content.

Test	Cement content (%)	Strength*				MOE				f_{bk}** (MPa)
		Min. (MPa)	Max. (MPa)	Avg. (MPa)	COV (%)	Min. (MPa)	Max. (MPa)	Avg. (MPa)	COV (%)	
Flexure	0	0.29	0.36	0.33	9.50	56.40	82.86	67.00	17.10	-
	3	0.34	0.44	0.39	11.40	71.18	97.63	86.26	12.36	-
	6	0.50	0.58	0.53	6.38	109.90	130.29	118.84	6.38	-
	9	0.63	0.71	0.66	4.87	131.33	180.78	154.47	12.49	-
	12	0.75	0.82	0.78	4.17	170.49	241.86	194.90	14.39	-
Dry Compression	0	1.15	1.33	1.22	6.38	19.42	25.93	23.28	11.40	0.74
	3	1.51	1.86	1.66	8.74	29.90	50.20	38.53	20.49	0.96
	6	1.83	2.16	2.01	6.13	36.95	51.33	44.82	11.47	1.23
	9	2.70	3.27	2.97	7.19	59.05	62.27	60.45	2.34	1.78
	12	3.73	4.24	3.89	5.47	62.28	88.96	74.20	13.41	2.42
Wet Compression	0	-	-	-	-	-	-	-	-	-
	3	0.72	0.81	0.75	4.91	17.26	25.48	22.07	14.53	0.47
	6	0.88	1.11	0.97	9.91	22.17	27.76	24.33	8.97	0.54
	9	1.51	1.68	1.58	4.32	37.03	54.05	44.63	15.46	1.01
	12	1.98	2.33	2.16	5.84	48.00	58.19	52.21	7.26	1.34

* Strength = MOR for flexure test, f_{bd} for dry compression test, and f_{bw} for wet compression test.

** $f_{bk} = f_{bkd}$ for dry compression test, and f_{bkw} for wet compression test.

The average MOR of CSEBs is 18% to 136% higher than the average MOR of CEB by increasing the cement content from 3 wt.% to 12 wt.%. The average dry compressive strength of CSEBs is 36% to 219% higher than the average dry compressive strength of CEB by increasing the cement content from 3 wt.% to 12 wt.%. For the wet compressive strength, CEBs shows a strength equal to zero since the blocks dissolved after 24 hours of water submersion. The average wet compressive strength of CSEBs increases by 29%, 111%, and 188% for the CSEB06, CSEB09, and CSEB12, respectively, when compared to the strength of the CSEB03. The wet compressive strength is significantly lower than the dry compressive strength for equal amounts of cement content. In particular, the average wet compressive strength of CSEB03, CSEB06, CSEB09, and CSEB12 are 55%, 52%, 47%, and 44% lower when compared to the corresponding dry compressive strength. This reduction in the compressive strength can be attributed to the development of pore water pressures and a decrease in soil cohesion. As expected, for all three sets of tests performed, the strength of CSEBs increases with increasing cement content. In addition, it is observed that the MOE measured in all tests also follows the same trend as the corresponding strength, i.e., it increases with increasing cement content.

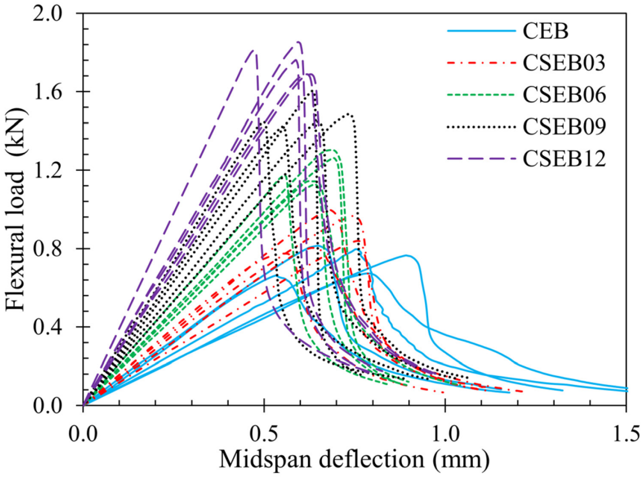

Figure 2.6. Load-displacement curves from flexure test of CSEBs.

These experimental results were compared to the minimum requirements suggested in current design codes and existing literature. In particular, the New Mexico Administrative Code [56] recommends a minimum average dry compressive strength of 2.07 MPa (300 psi), a minimum sample dry compression strength of 1.72 MPa (250 psi), and minimum average MOR of 0.35 MPa (50 psi) for compressed earth blocks. In addition, in humid environments, CSEBs should also have a minimum average wet compressive strength of 1.5 MPa [37,114] or a minimum unconfined characteristic wet compressive strength of 1.0 MPa [66]. From the results obtained in this study, it is observed that CSEB09 and CSEB12 satisfy these strength requirements.

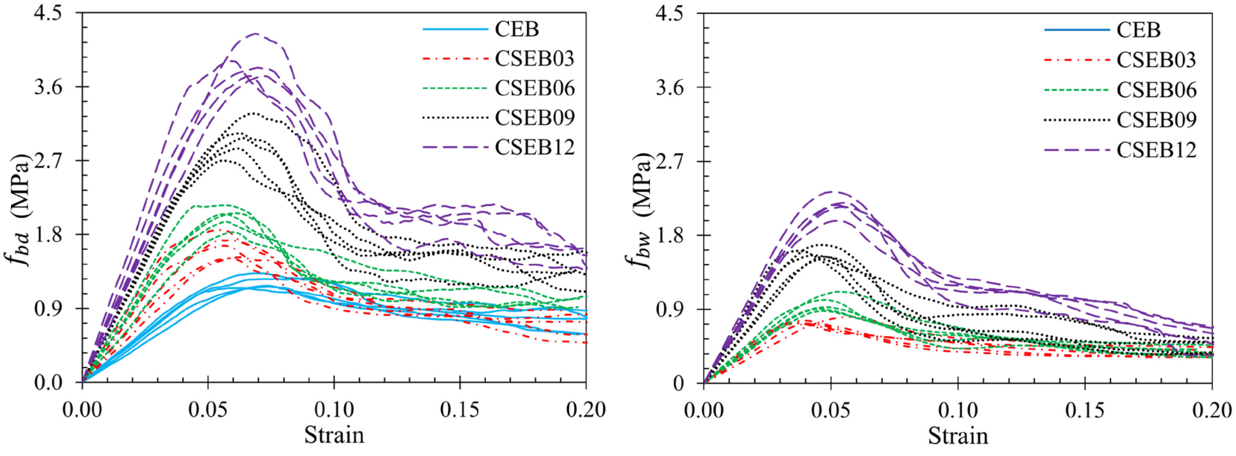

(a)

(b)

Figure 2.7. Stress-strain curves of CSEBs: (a) dry compression test; and (b) wet compression test.

2.3.4. *Mechanical Properties of Soil-Based Mortar*

The mechanical properties of cement-soil mortars produced with the same soil used for CSEBs were investigated to identify mortars that are compatible with the earth blocks for the construction of CSEB structures. It is noteworthy that the New Mexico Administrative Code allows the use of both soil-cement mortar and conventional mortars for CSEB walls [56]; however, Venkatarama Reddy and Gupta [119,120] suggested that soil-cement mortars can provide better bond strength, higher initial stiffness, and lower cost than conventional cement-based mortar. In particular, the effects on the compressive strength of soil-based mortar were investigated for: (1) different amounts of cement used as a stabilizer (soil-cement mortar), and (2) different amount of sand used to ameliorate the soil for a fixed 15 wt% cement content (soil-sand-cement mortar). Mortar cubes with a side dimension equal to 50 mm were fabricated by adding: (1) different amounts of Type II PC (varying between 3 wt% and 30 wt%, with increment intervals of 3 wt%) to soil A; and (2) different amounts of sand (varying between 10 wt% and 50 wt%, with increment intervals of 10 wt%) to a mix of soil A and 15 wt% cement. The samples were tested after being cured for 28 days (using the same curing procedure used for the CSEBs) to obtain the average dry compressive strength of the mortar, f_m [121]. The results of the compression tests in terms of sample means and coefficients of variation for the dry compressive strength and MOE as functions of the cement and sand contents are reported in **Table 2.2** together with the estimates of the unconfined characteristic compressive strength of the mortar, f_{mk} [122].

The results indicate that the soil-cement mortar compressive strength increases with increasing cement content. However, a significantly larger cement content is required to achieve a compressive strength that is comparable to that of the CSEBs. In particular, a soil-cement mortar with at least 24 wt% and 30 wt% cement contents should be used with CSEB09 and CSEB12 blocks, respectively. This result is most likely due to the high clay content (35-40 wt%) in the soil, which is significantly higher than the amount recommended for soil-cement mortar in CSEB masonry, i.e., up to 10-20 wt% of clay [64,119,120]. As expected, the addition of sand increases the mortar compressive strength for a given amount of cement. It is observed that soil-sand-cement mortars with 15 wt% cement and 30 or 40 wt% sand have a similar compressive strength to that of CSEB09 and CSEB12 blocks, respectively. Thus, these soil-sand-cement mortars can be used in conjunction with CSEB09 and CSEB12.

Table 2.2. Dry compressive strength and MOE of mortar cubes.

Cement content (%)	Sand content (%)	f_m		MOE		f_{mk} (MPa)
		Avg. (MPa)	COV (%)	Avg. (MPa)	COV (%)	
3	0	0.38	7.47	5.44	17.55	0.23
6	0	0.55	17.89	11.44	27.50	0.25
9	0	0.94	2.19	18.24	45.98	0.63
12	0	1.33	7.28	27.06	15.26	0.79
15	0	1.74	4.89	34.32	14.52	1.10
18	0	1.94	9.43	39.94	18.58	1.10
21	0	2.38	9.06	44.88	24.12	1.36
24	0	2.88	6.87	51.78	24.70	1.74
27	0	3.40	4.10	57.50	23.18	2.18
30	0	3.89	8.39	61.18	13.38	2.26
15	20	2.22	2.17	53.76	30.78	1.49
15	30	3.01	6.92	68.54	10.79	1.81
15	40	3.91	9.21	77.84	15.47	2.23
15	50	4.41	10.83	86.02	20.48	2.41

2.3.5. *Durability Investigation of CSEB Wall*

The performance of a plaster protection for a CSEB masonry wall exposed to the humid weather in Baton Rouge was investigated. A single-wythe 1220 x 920 mm2 (4 x 3 ft2) wall was constructed with CSEBs of dimensions 290 x 150 x 75 mm3 on June 6, 2015, outside Atkinson Hall, at the LSU School of Architecture in Baton Rouge, LA. Soils B and C were mixed in equal parts into soil BC to produce CSEBs with 6 wt.% type II PC. The particle size distribution of the reconstituted soil BC is reported in **Figure 2.3**. Five of these earth blocks were tested after 28 days curing to determine their flexural and dry compressive strength, which are reported in Table 2.3 in terms of sample means and coefficients of variation. These specimens are identified as CSEB^I hereinafter to indicate that they were tested before the construction of the wall.

Table 2.3. Mechanical properties of CBEBs before construction and after demolition of the wall.

	Flexure test				Compression test			
	MOR		MOE		f_{bd}		MOE	
Tested specimens	Avg. (MPa)	COV (%)	Avg. (MPa)	COV (%)	Avg. (MPa)	COV (%)	Avg. (MPa)	COV (%)
CSEB^{I}	0.57	11.28	164.32	22.00	1.38	6.40	31.22	16.98
CSEB^{P}	0.64	22.68	279.51	17.11	1.79	5.55	55.61	20.21
CSEB^{U}	0.37	21.82	143.33	31.60	1.50	13.80	44.78	26.82

The wall was divided into two parts: a protected side (side P) and an unprotected side (side U). The plaster protection of side P comprised two layers: a 12-mm-thick layer of soil-cement stucco made with soil BC and 6 wt% PC covered by a thin layer of cement paste paint, as shown in **Figure 2.8**. The wall was left exposed to outdoor weather conditions for six months and was visually inspected twice a week to observe and document the condition of the wall. After one-month of the exposure, the initiation of erosion was observed on the surface of the CSEBs on the unprotected side of the wall. This erosion progressed with time on the unprotected side, as shown in **Figure 2.8(b)**. After three months, the CSEBs at the top corner of the unprotected side of the wall lost their bond with the wall due to degradation of the blocks and the mortar in the top two courses, as shown in **Figure 2.8(c)**. **Figure 2.8(d)** shows the wall on December 10, 2015, before it was carefully dismantled. Two blocks at the top corner of the unprotected side were slightly dislodged, and one of them was cracked in the middle. By contrast, the protected side of the wall did not show any sign of distress after six months of weather exposure. The blocks from both the protected (CSEB^{P}) and unprotected (CSEB^{U}) side were recovered and carefully moved to the structural laboratory. Among the recovered blocks that were undamaged under visual inspection, five specimens from each side of the wall were subjected to flexure and compression testing using the same procedure previously described. The results of these experimental tests are reported in **Table**

2.3 in terms of sample means and coefficients of variation for the flexural and dry compressive strengths and the corresponding MOE.

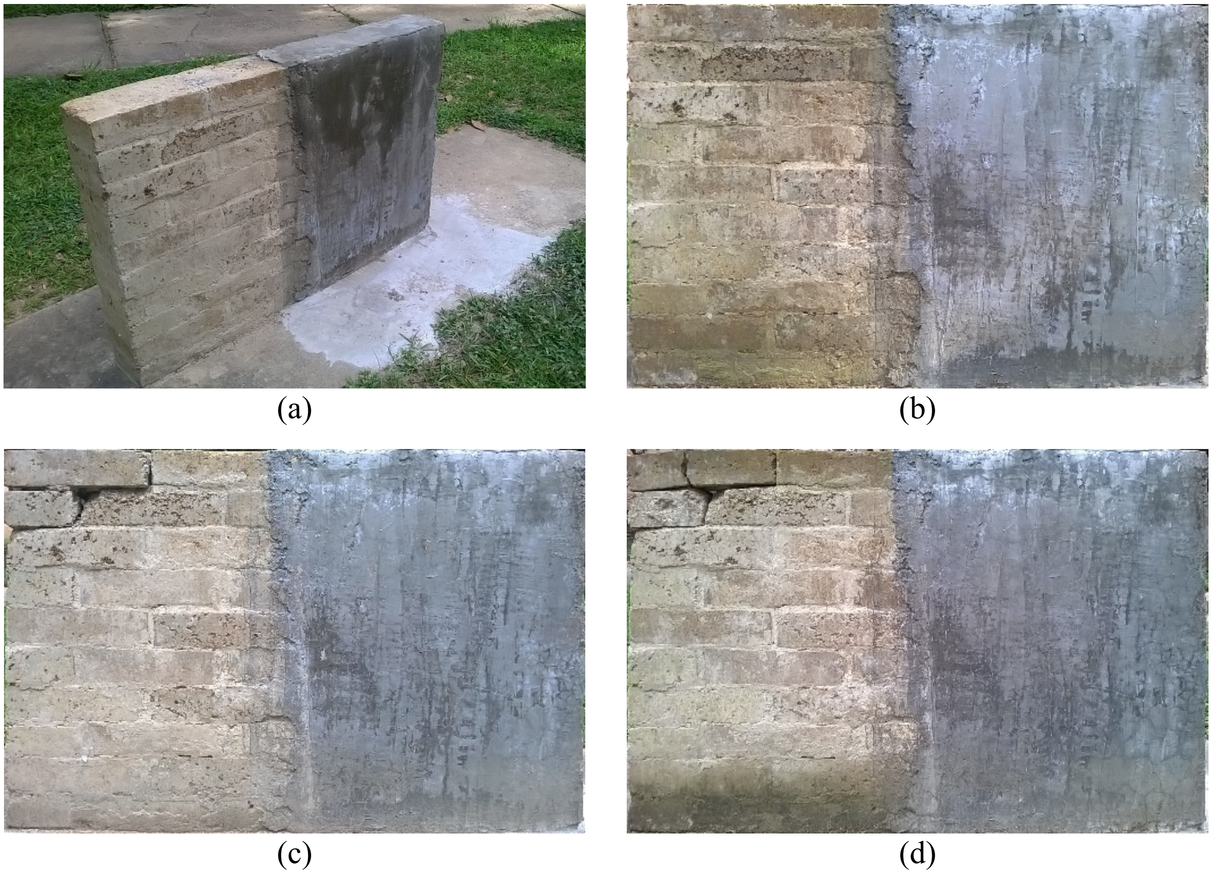
(a) (b)

(c) (d)

Figure 2.8. Durability study of CSEB masonry wall at LSU: (a) wall after construction; (b) wall after one month; (c) wall after three months; (d) wall after six months of exposure to Baton Rouge weather.

The average MOR and dry compressive strength of the CSEB^P are 72% and 19% higher than those of the CSEB^U, respectively, which demonstrates the effectiveness of the double layer plaster in protecting the wall from deterioration due to weather action. In addition, the average MOR and dry compressive strength of the CSEB^P are 11% and 23% higher than those of the CSEB^I. This phenomenon may be due to the progress of cement hydration under the high humidity conditions experienced by the wall. It is also observed that the average compressive strength of the CSEB^U is slightly higher than that of the CSEB^{I}, whereas the average MOR is significantly lower. This phenomenon may be due to the counteracting effects of cement hydration (which tends to increase the block strength and seems to be dominant for compressive strength) and superficial erosion (which tends to produce imperfections and cracks and seems to be dominant for flexural strength).

The results of this durability investigation confirm that humid weather produces very demanding conditions for CSEBs and that an exterior coating is needed to mitigate erosion and degradation induced by severe weather conditions. The proposed dual layer plaster consisting of a soil-cement stucco with a coat of cement paste was effective in protecting a CSEB wall from the humid climate that is typical of the U.S. Gulf Coast. However, further investigation is needed to determine an optimal, cost-effective option for protection of CSEB structures.

2.3.6. ***Hurricane Wind Resistance of CSEB Systems***

The hurricane wind resistance of CSEB systems built using local soil was investigated by using the parametric strength demand curves developed by Matta et al. [21] to identify the minimum acceptable wall thickness for the main wind-force resisting system of one-story single-family dwellings made of CSEB masonry and located in exposure zone C [123]. These parametric curves for CSEB structures with flat roofs are shown in **Figure 2.9**. The horizontal axis represents the basic wind speed (defined as the 3-s gust speed at 10 m above ground in exposure zone C), the vertical axis indicates the compressive strength of earth block masonry, and the different curves with markers identify the masonry strength required at any given wind speed for CSEB systems with walls of different thickness. The horizontal dashed lines labeled as M09 and M12 identify the characteristic masonry strength for earth block masonry built with: (1) CSEB09 blocks and soil-sand-cement mortar with 15 wt.% cement and 30 wt.% sand, and (2) CSEB12 blocks soil-sand-cement mortar with 15 wt.% cement and 40 wt.% sand, respectively. The characteristic compressive strength of the masonry walls was determined as f_c = 1.64 MPa for M09 and f_c = 2.14 MPa for M12, respectively, by using the following equation recommended in Eurocode 6 [124]

$$f_c = 0.55 f_{bd}^{0.7} f_m^{0.3} \tag{2.1}$$

where f_c denotes the characteristic compressive strength of the masonry. This equation was preferred to other expressions available in the literature and in other design codes [125–128] because it applies to the strength ranges considered in this study and it is the most conservative relations among those available in the literature [129]. The vertical solid lines identify the design wind speeds [123] for some of the major cities in Louisiana, i.e., Shreveport, Lafayette, Baton Rouge, New Orleans, and Houma.

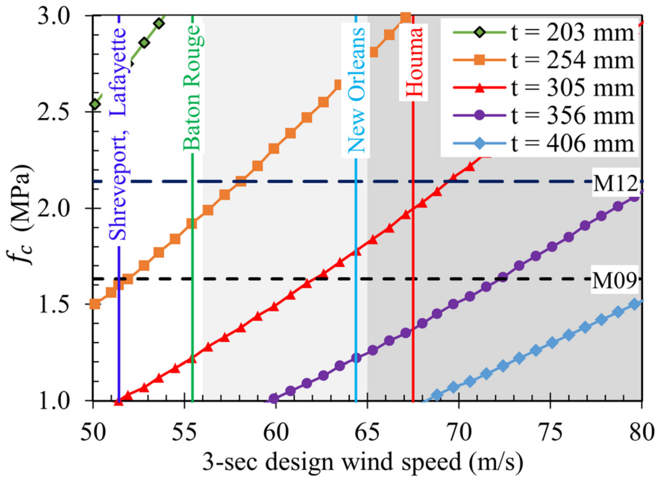

Figure 2.9. Parametric design curves for main wind-force resisting system of CSEB single-story houses with flat roof.

The results reported in **Figure 2.9** indicate that: (1) in Shreveport and Lafayette, a wall thickness *t* = 254 mm is sufficient for both M09 and M12; (2) in Baton Rouge, a wall thickness *t*

= 305 mm and 254 mm are needed for M09 and M12, respectively; and (3) in New Orleans and Houma, the minimum wall thickness for M09 and M12 increases to t = 356 mm and 305 mm respectively. Considering the dimension of the blocks, an earth block wall with t = 254 mm can be built using a single-wythe configuration [53,130], whereas larger wall thicknesses would require a double-wythe configuration. It is noted here that the required wall thickness could be further reduced, e.g., by using steel reinforcement [21], or a different set of optimized block sizes could be used [42,53,130].

2.4. Architectural Feasibility Study

In response to the need for affordable and climate responsive housing in coastal Louisiana, single-family prototype designs were developed using CSEBs as the primary construction element. In appreciation of the rich cultural heritage and environmental context of the Gulf Coast, the proposed prototype housing designs embrace many qualities inherent to local vernacular architecture, which includes Creole and Acadian influences and presents a heritage of building types composed of common elements that evolved from living in a hot wet climate [131]. Fundamental aspects, incorporated into the housing designs, include deep porches, high ceilings, and floor to ceiling openings, raised ground floors, and program specific room volumes, which all help to facilitate air movement by means of passive cross ventilation.

Two significant housing types, i.e., the shotgun and the dogtrot [131], were considered in the design of two single-family prototypes. Each prototype was based on a single-family program of around 1000 square feet on one level with an interior volume of 10 to 12 feet in height. They are composed of a main living area, kitchen, bathroom, two bedrooms, and outdoor porches. Beyond these equivalent features, unique characteristics of the housing designs were developed based on specific contextual qualities. The shotgun prototype, based on customs of the Creole who migrated from Haiti, represents an urban house and has a long thin linear arrangement of rooms for efficient cross ventilation and minimal frontage following the organization of dense inner-city land allotment (see **Figure 2.10**). A covered exterior porch faces the street and is open on the sides to promote social interaction with adjacent neighbors. The dogtrot prototype, based on customs of the Acadian who stemmed from Nova Scotia, represents a rural house and has an organization based on a central porch (which provides ventilation for adjacent rooms), flanked by public living spaces on one side and private on the other (see **Figure 2.11**). The mass of the dogtrot house has a recessed, inward facing porch that functions as an entry way and a private social space in less dense rural communities.

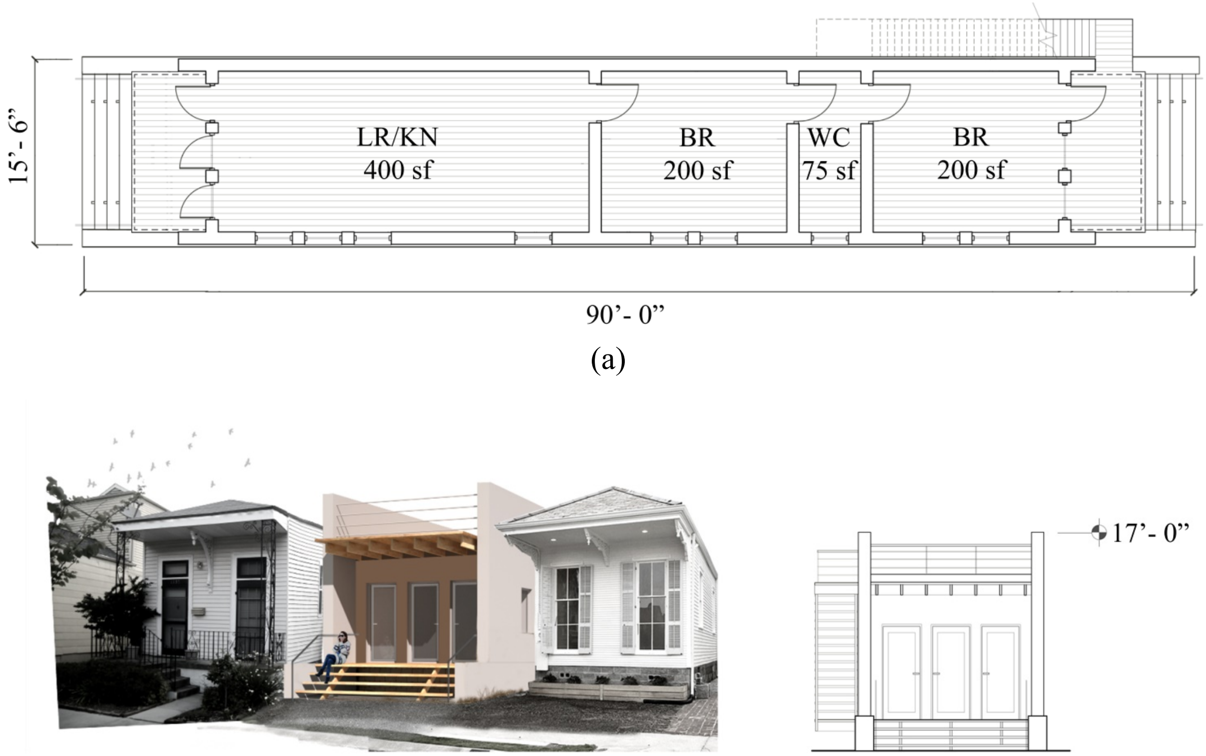

(a)

(b)

(c)

Figure 2.10. Drawings of the shotgun prototypes house: (a) floor plan, (b) front perspective (rendering), and (c) front elevation (1’ = 30.48 cm, 1” = 2.54 cm, and 1 sf = 0.093 m^2).

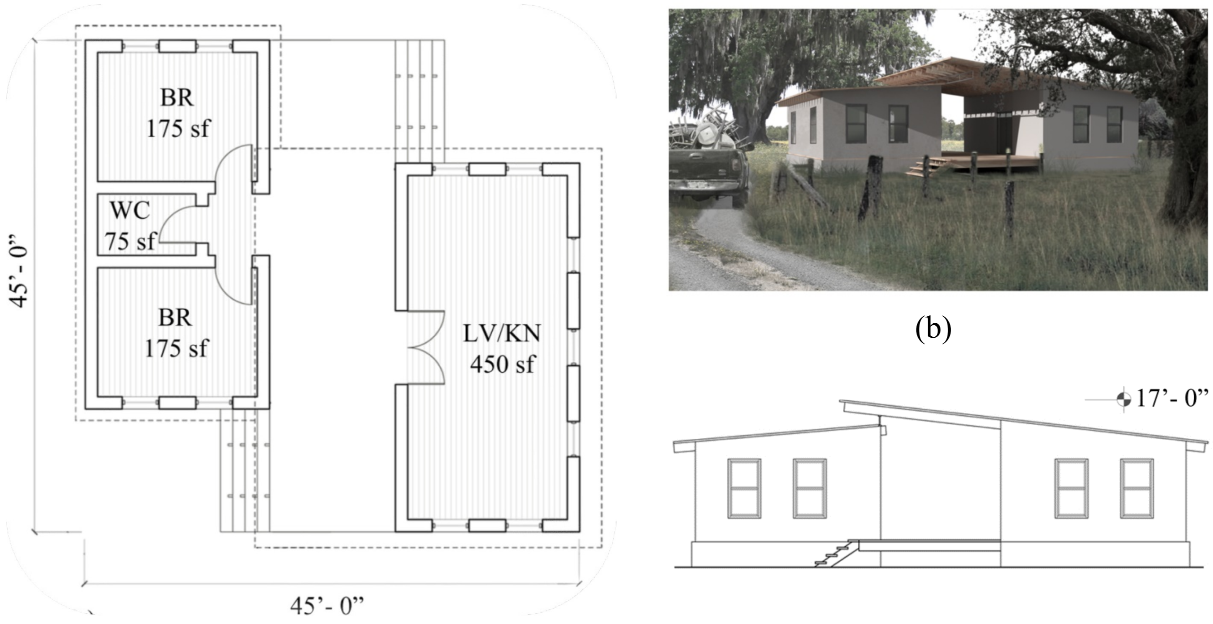

(a) (b) (c)

Figure 2.11. Drawings of the dogtrot prototypes house: (a) floor plan, (b) front perspective (rendering), and (c) front elevation (1' = 30.48 cm, 1" = 2.54 cm, and 1 sf = 0.093 m^2).

The proposed designs were developed around an architectural logic based on the 10"x6"x3" (25.4 cm x 15.2 cm x 7.6 cm) module of the CSEB. On top of the foundation, a 2'-6"-high (76.2 cm) stem wall (made of a triple layer of earth blocks) supports an elevated floor to promote improved air circulation and ventilation. For the shotgun prototype, the load bearing exterior wall continues vertically from the stem wall and is reinforced by a series of transverse walls that function as buttress bracing for lateral loads, with a maximum span between transverse walls of 30' (9.14 m). The exterior wall is finished with the proposed dual layer plaster to provide weather protection. Doors and windows openings are supported by wood box frames. All components, details, and connections were kept intentionally simple to help achieve the goal of affordable materials and labor that are readily available. An exploded axonometric illustration of the different assemblies for the shotgun prototype house is presented in **Figure 2.12**. Roof, foundations, and their connections with the walls were dimensioned to resist the wind lateral and uplift forces, which were calculated based on the envelope procedure for enclosed simple diaphragm low-rise buildings given in ASCE 7-10 [123]. The roof joists are connected to the walls through steel hurricane ties.

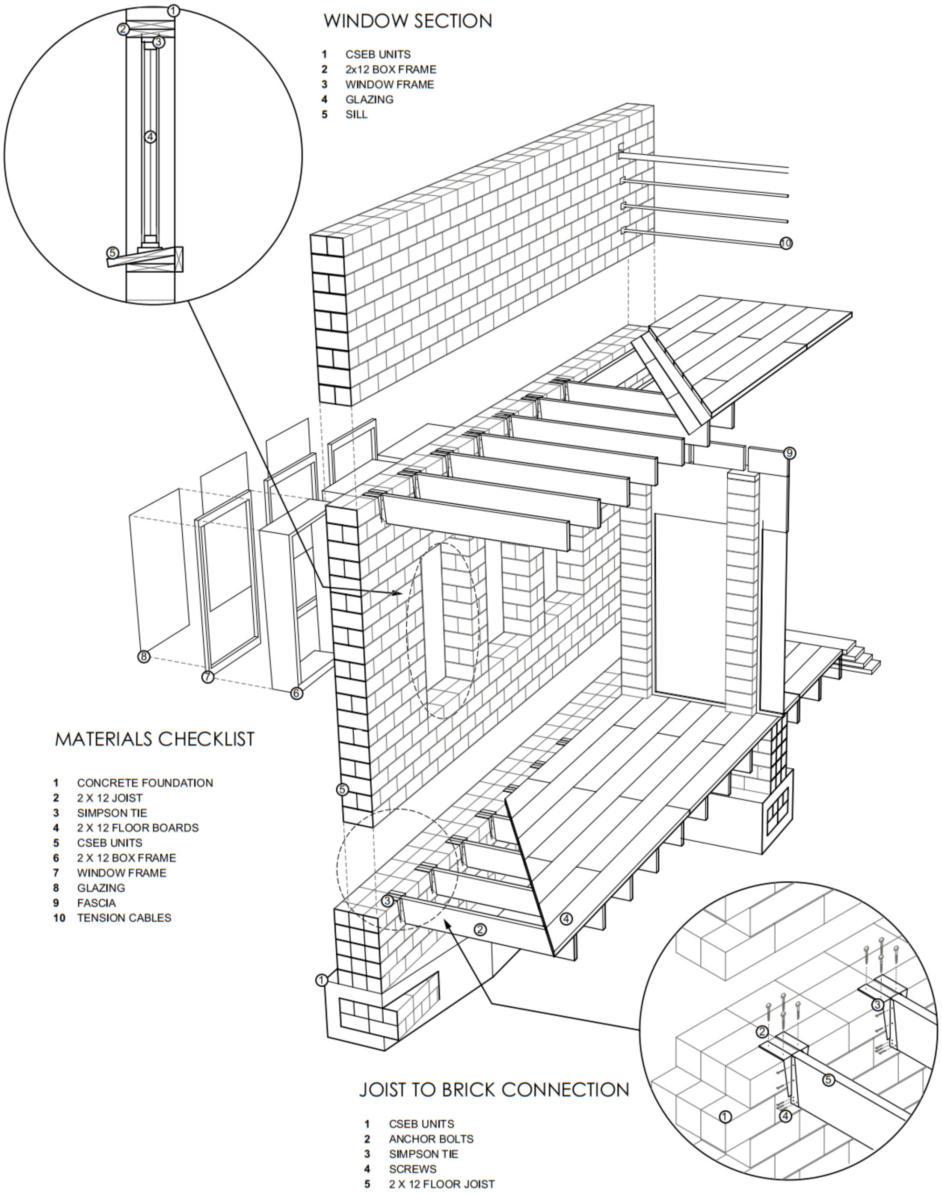

Figure 2.12. Exploded axonometric illustrations of the different assemblies in the shotgun prototype house.

It is concluded that CSEB systems can be adapted to design and build simple houses based on local vernacular architecture. Thus, CSEB houses can have the same appearance of houses built using other more traditional construction techniques, which could promote their acceptance from the local population.

2.5. Economic Feasibility Study

An economic feasibility study was performed to determine if CSEB structures could represent a sustainable approach for affordable, safe, and weather resistant housing in the U.S. Gulf Coast region. Based on the mechanical properties identified in the structural feasibility study, the shotgun prototype with 1000 ft2 area was considered as reference single-family dwelling. The cost to build this house was compared to the costs of equivalent houses built using light-frame wood construction, fired brick masonry, and concrete block masonry. For the sake of comparison, components other than the walls (e.g., foundation, roof, and floor systems) were assumed to be equal and, thus, have the same costs for all houses compared here. It is noted here that this assumption is only an approximation, and that further study is needed to investigate if and how much the cost of these other components is affected by the usage of different wall systems. However, this investigation is outside the scope of this study.

Two construction options were considered for the CSEB walls, namely: (1) CSEB walls built using mortar layers of typical thickness to provide the bond between blocks [53], referred to as mortared CSEB wall hereinafter (**Figure 2.13**); and (2) CSEB walls built with interlocking CSEBs (ICSEBs) with thin layers of mortar slurry and grouted vertical steel reinforcement [132], referred to as mortarless ICSEB wall (**Figure 2.13**). In the mortarless ICSEB wall option, the reinforcement consisted of #4 steel reinforcing bars at 406.4 mm center-to-center spacing and was used to speed up the construction process. The detailed cost estimates for all components of these two CSEB wall options are reported in **Table 2.4.**

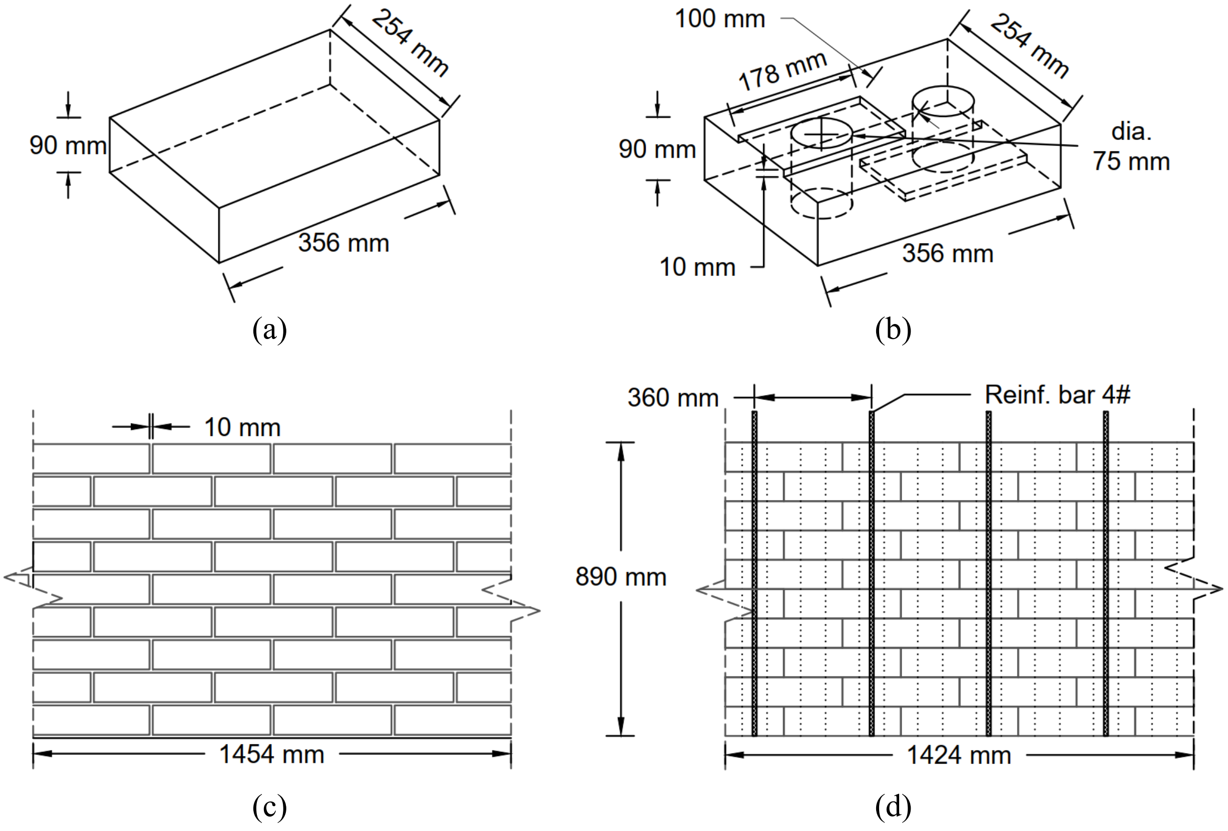

Figure 2.13. CSEB wall systems: (a) ordinary CSEB element, (b) ICSEB element, (c) mortared CSEB wall system, and (d) mortarless ICSEB wall system.

The total number of blocks needed for construction was estimated at 9680 for the mortared CSEB wall and 10938 for the mortarless ICSEB wall. All costs were determined using the average national costs of material and labor and applying the appropriate city cost index for Baton Rouge, LA [133]. The labor cost for the CSEB walls includes block fabrication, construction, stucco installation (only on exterior walls), and masonry painting. The number of man-hours hour required for building a unit area of mortared CSEB wall was assumed equal to those required to build ordinary fired clay masonry walls when using skilled labor [133]. A 50% reduction of labor hours was considered for building mortarless ICSEB wall walls when compared to the labor needed for mortared CSEB wall [134]. In addition, it was assumed that semi-skilled workers could build mortarless ICSEB wall walls under the supervision of a skilled mason [134]. These two assumptions were based on existing literature on dry stack mortarless masonry [135,136] and on information obtained by conducting a survey among active U.S. earth block builders (De Jong B., Dwell Earth, personal communication).

Table 2.4. Detailed cost estimates of CSEB walls for reference prototype house

		Mortarless ICSEB Wall			Mortared CSEB Wall		
Components	Items	Quantity	Unit	Cost ($)	Quantity	Unit	Cost ($)
Blocks	Soil	133.3	Ton	-	132.6	Ton	-
	Cement	40,055	lbs.	3,676	39,851	lbs.	3,651
	Labor	584	Hours	4,234	528	Hours	3,828
	Machine	73	Hours	2,555	66	Hours	2,310
Reinforcement	Material	1,610	lbs.	483	-	lbs.	-
	Labor	29	Hour	580	-	Hour	-
Mortar & grout	Soil	10.6	Ton	-	10.6	Ton	-
	Cement	7,806	lbs.	720	7,806	lbs.	720
	Sand	10.6	Ton	531	10.6	Ton	530
Masonry Work	Stem walls	113	Hours	2,250	225	Hours	5,721
	Long walls	288	Hours	5,766	577	Hours	14,755
	Short walls	92	Hours	1,830	183	Hours	4,683
Rendering	Soil	2.7	Ton	-	2.7	Ton	-
	Cement	2,938	lbs.	271	2,938	lbs.	271
	Sand	2.7	Ton	133	2.7	Ton	133
	Masonry paint	5,964	ft2	1,372	5,964	ft2	1,372
	Plastering	87	Hours	2,185	87	Hours	2,185
	Painting	48	Hours	1,193	48	Hours	1,193
	Total cost			**27,779**			**41,352**

The costs of light-frame wood, fired brick, and concrete block walls for the same reference prototype house were also determined by considering national average costs adjusted by the city cost index for Baton Rouge, LA [133,137], as shown in **Table 2.5**. In addition to the costs of materials and labor, the overhead for general contractors and the costs associated with other components of the house (i.e., concrete footing, light-frame wooden floor, light-frame wooden roof, interior ceiling, doors and windows, kitchen, bathroom, and electric system) were estimated and reported in **Table 2.5**. Finally, **Table 2.5** reports the relative costs of the wall systems and entire houses built using the different materials and considering the mortarless ICSEB wall system as reference.

Table 2.5. Cost comparison of different wall systems for reference prototype house.

Items	Mortarless ICSEB	Mortared CSEB	Light frame Wood	Bricks	Concrete Blocks
Material	7,186	6,676	15,638	19,533	12,844
Labor	20,593	34,674	13,068	27,625	20,255
Overheads	11,112	16,540	12,264	19,840	13,882
Total wall cost	38,891	57,890	40,970	66,997	46,981
Total cost of assemblies	65,110	65,110	65,110	65,110	65,110
Total cost of house	104,001	123,000	106,080	132,107	112,091
Wall cost ratio (wcr)	1.000	1.489	1.053	1.723	1.208
House cost ratio (hcr)	1.000	1.183	1.020	1.270	1.078

It is observed that, among the solutions considered in this study, the mortarless ICSEB wall system is the least expensive option with a wall cost ratio (wcr) equal to 1.00, followed by the light-frame wood (wcr = 1.053), concrete block (wcr = 1.208), mortared CSEB (wcr = 1.489), and fired brick (wcr = 1.723) wall systems. The cost of the mortarless ICSEB system is very similar to that of a light-frame wood wall system, which is the most commonly used construction technique for housing construction in the region [138]. On the contrary, the cost of the mortared CSEB wall system is significantly higher than that of wooden frame walls. This result makes the mortared CSEB wall system economically unfeasible unless the owners of the house can also be its builders. It is noteworthy that this circumstance is quite common in rural settings and in developing countries, where this type of construction is often adopted by low-income families that can provide the labor [37,139].

2.6. Conclusion

This chapter presented the results of a feasibility study for compressed and stabilized earth block (CSEB) construction in the U.S. Gulf Coast, which included structural, architectural, and economic components. Based on the results of the structural component of this feasibility study, the following conclusions are drawn: (1) the soil available in the East Baton Rouge area is suitable for fabricating CSEBs; (2) the CSEBs fabricated with at least 9% in weight (wt.%) of cement content satisfy the minimum strength requirements for building single-story dwellings; (3) soil-sand-cement mortars with 15 wt.% cement and at least 30 wt.% sand can be used in conjunction with CSEBs; (4) exterior CSEB walls need a protection from the weather conditions in a humid climate, and a dual layer plaster consisting of a soil-cement stucco with a coat of cement paste seems to provide a sufficient protection; and (5) hurricane-resistant earthen dwellings can be built using single- or double-wythe earth block masonry walls. The architectural feasibility investigation indicates that CSEB systems can be adapted to design based on local vernacular architecture, which could promote their acceptance from the local population. Finally, the economic feasibility study suggests that mortarless ICSEB wall can be built at a lower cost than other traditional wall systems, i.e. (in order of increasing average cost), light-frame wood, concrete block, and fired clay brick wall systems; whereas mortared CSEB wall system is less expensive than only fired clay brick walls, due to the high labor required for their construction.

The feasibility study presented in this chapter shows that earthen dwellings built using mortarless ICSEB wall systems can be an attractive choice for low-cost hurricane-resistant housing in the U.S. Gulf Coast region. However, further detailed investigations are required to understand the performance of earthen dwellings and to provide guidance in the design and code development for this type of structures. In particular, both experimental and numerical investigations are needed to determine the structural resistance and reliability of CSEB systems against extreme loads due to natural hazards (e.g., high winds and earthquakes), the appropriate dimensioning and performance of different type of reinforcements, the effects of different stabilizers and fabrication procedures on the performance of CSEBs and CSEB masonry, as well as the proper configurations of architectural and structural details (e.g., taller foundation walls to separate the wall from the wet soil, alternative wall coating and/or rendering surfaces, shading/shielding elements, specific roofing and grading details, connections between walls and foundation and/or between walls and roof, details of window and door openings).

CHAPTER 3. EFFECTS OF SUGARCANE BAGASSE FIBERS ON THE PROPERTIES OF COMPRESSED AND STABILIZED EARTH BLOCKS

3.1. Introduction

Earthen structures represent one of the most ancient construction techniques, dating back over 9000 years ago [102]. Even today, a significant portion of the world's population lives in earthen dwellings [140]. Traditional earthen constructions are generally non-engineered buildings made using cob, rammed earth, or adobe; whereas modern earthen constructions are often built using engineering principles in conjunction with rammed earth and compressed earth blocks [12]. More recently, compressed and stabilized earth block (CSEB) construction (in which soil is mixed with a chemical stabilizer and then compressed) has seen a rapid development [141]. In the last few decades, significant research has been devoted to developing CSEBs as a more affordable and eco-friendly alternative to other more common construction elements, e.g., fired clay bricks and concrete blocks [41]. CSEBs are emerging as a viable modern construction technique for low-rise buildings due to their eco-efficiency and extreme affordability [12]. However, CSEBs have some inherent limitations, such as low tensile strength, brittle behavior, and poor durability against humidity [12,43]. Over the centuries, various natural fibers have been used for improving the mechanical (e.g., shrinkage, tensile strength, and ductility) and durability properties of traditional earthen structures [12]. Recently, considerable effort has been directed to develop reinforced compressed earth blocks using agricultural waste fibers [26]. The use of these fibers is often shown to improve the mechanical and durability properties of earthen materials while addressing sustainability issues [26,142].

Sugarcane bagasse fibers (SCBF) have received particular attention for their use in earthen construction because of their abundance worldwide [26,142]. Bock-Hyeng et al. [143] and Lertwattanaruk and Choksiriwanna [144] observed improvement in the compressive strength, shrinkage, and moisture absorption of adobe bricks with the inclusion of SCBFs. Eko and Riskowski [145] observed that it is unnecessary to remove sugar from SCBF for fabricating reinforced CSEBs, as the sugar present in SCBFs forms polysaccharides, which are known to bind soil particles together. By investigating the effects of cement content (i.e., 5%, 10%, and 15% by weight) and SCBF content (i.e., 10%, 20%, and 30% by volume) on the compressive strength of SCBF-reinforced CSEBs, they concluded that the compressive strength of SCBF-reinforced CSEBs increases for increasing cement content and constant fiber content and decreases for increasing SCBF levels and constant cement content. Danso [26] investigated SCBF-reinforced compressed earth blocks (CEBs) fabricated using different soil types and fiber contents, and concluded that: (1) the density, shrinkage, and water absorption rate of CEBs improve for increasing SCBF content; (2) the inclusion of SCBFs enhances the compressive and tensile properties of CEBs, with optimum performance achieved at 0.5 % by weight (wt. %) of SCBF content; and (3) the SCBF reinforcement in CEBs reduces the rate of erosion when the blocks are subjected to water spray test. The same study also observed that: (1) the SCBF reinforcement is randomly distributed in the soil matrix, with gaps between the fibers and soil matrix caused by fiber shrinkage; and (2) the SCBFs in the soil matrix can either fail by pull out or by fracture [26].

Previous studies on SCBF-reinforced CSEBs focused mainly on compressive and/or tensile peak strength. However, to the best of the authors' knowledge, mechanical properties associated with energy dissipation, such as toughness and ductility, have not been investigated for SCBF-reinforced CSEBs. These properties are crucial to assess the performance of CSEB constructions subjected to dynamic horizontal loading, such as seismic and wind excitations. Another aspect that has not been investigated in the previous studies is the durability of SCBF-reinforced CSEBs. The present study addresses this knowledge gap by investigating the effects of SCBF on the mechanical (i.e., toughness and ductility) and durability properties of CSEBs fabricated using different levels of cement stabilization and SCBF amounts.

3.2. Motivation and Significance

The study presented in this chapter has two major motivations. The first motivation is the increasing need for affordable housing worldwide, which incentivizes the development of sustainable construction solutions, such as engineered earthen building techniques. Based on 2018's data, the USA housing supply is about 2.5-4.0 million housing units below what is needed to match its long-term demand [146]. On a global scale, more than two billion new homes are expected to be needed in the next 80 years due to a combination of increasing world population and decreasing household size [96]. The second motivation is the abundance of residual SCBFs produced every year and the associated waste disposal issues, which promote the interest in valorizing this agricultural by-product material by identifying new beneficial applications. In fact, the juice extraction from sugarcane produces a large volume (32%) of SCBFs as a waste product [143,147]. In 2018 alone, Brazil produced 746.8 million metric tons of sugarcane, followed by India with 376.9 million metric tons, and China with 108.7 million metric tons, with an estimated production of more than 400 million metric tons of SCBFs [148]. In 2017, the USA produced 28.0 million metric tons of sugarcane, mostly in Florida, Louisiana, and Texas [149], yielding approximately 9 million metric tons of SCBFs. Only about half of the produced SCBF is used for energy generation in the sugar mills, whereas the remaining portion is disposed of in landfills, creating environmental issues and a potential fire hazard [143,150].

The research presented in this study could represent an important step toward the adoption of SCBF-reinforced CSEBs as a more sustainable alternative to other conventional modern construction techniques, such as light-framed wooden construction, ordinary masonry, and concrete block masonry. The usage of SCBFs in the fabrication of CSEBs has the potential to address both the waste disposal problems associated with excess production of SCBFs, and the need for improved mechanical and durability properties of CSEBs, which have been historically an impediment to the broad adoption of this construction technique, particularly in developed countries and in regions affected by extreme seismic and wind loading conditions. An additional potential benefit of this study could be the improvement of the living conditions for low-income, under-represented, and under-served populations around the world, both in developing and developed countries.

3.3. Materials and Methods

3.3.1. *Materials*

This study used natural soil collected in the East Baton Rouge Parish, LA, which was extracted from the layer contained between 1 m and 2 m below the ground surface to minimize the organic content. This soil was selected for this investigation because it is representative of local Southern Louisiana's soil and is most likely to be used in conjunction with SCBFs for the fabrication of CSEBs. Standard laboratory tests were performed to determine the physical properties of the soil. The results of these tests are summarized in **Table 3.1** and indicate that the used soil had a high content of fines (i.e., clay and silt were more than 89% of the soil), thus resulting in a composition that was within the sub-optimal region on the USDA soil texture triangle, see chapter 2. It is highlighted here that such compositions are generally inappropriate for use in the fabrication of

CEBs but can still be used for CSEBs. The values of the Atterberg limits measured for this soil were contained within the ranges considered appropriate for fabrication of earth blocks [12].

Table 3.1. Physical properties of soil.

Laboratory tests	Standards	Properties	Values
Particle-size analysis	ASTM D6913-04 [112] and D7928-16 [113]	Gravel (>2 mm) (%)	<1.00
		Sand (2–0.063 mm) (%)	9.85
		Silt (0.063–0.002 mm) (%)	58.03
		Clay (<0.002 mm) (%)	31.12
Atterberg limits	ASTM D4318-10 [111]	Liquid limit LL (%)	35.47
		Plastic limit PL (%)	22.94
		Plasticity index PI (%)	12.53
Soil compaction tests	ASTM D698-12 [151]	Optimum moisture content (%)	23.42
		Maximum dry density (kg/m^3)	1571.53
		Specific gravity of soil (-)	2.59

The SCBF used in this investigation was obtained from a sugarcane mill in Alma Plantation, Lakeland, LA. The average length and thickness of the SCBFs were obtained by using a Vernier caliper as 55 mm and 0.2 mm, respectively. The SCBF received from the sugarcane mill was soaked in cold water for one day to remove any impurities and white spruce sawdust before being used to fabricate the CSEBs. Type II ordinary Portland cement (PC), as per ASTM C150/C150M-17 [152], was used in this investigation to stabilize the earth blocks.

3.3.2. *Earth block fabrication*

The earth block specimens were manufactured using a manual single-stroke one-side compaction machine, which can apply a pressure of 2-4 MPa. The material for the CSEBs was prepared by mixing pulverized dry soil, saturated SCBF, and cement using a power-driven mixer for at least 10 min, and then gradually adding water to the soil-cement-SCBF blend while mixing it [153]. The optimum moisture content for each soil-cement mixture was obtained through a standard Proctor test [151], thus accounting also for the water demand of cement, and was used in the fabrication of the earth block specimens. In addition, the SCBFs were soaked in water for 24 h till saturation before being added to each mixture (in order to satisfy the water requirement of fibers). The production time between material mixing and fabrication of each batch of blocks was maintained below 45 minutes, to avoid excessive hardening of the cement. Each batch consisted of four blocks. After fabrication, the blocks were cured for 28 days by wet-and-dry curing at room temperature before further testing [153].

3.3.3. *Experimental test matrix*

The experimental test matrix considered two variable parameters: (1) the percent amount of cement by weight of the soil, with three different levels, i.e., 0 wt.%, 6 wt.%, and 12 wt.%; and (2) the percent amount of SCBF by weight of soil, with three different levels, i.e., 0.0 wt.%, 0.5 wt.%, and 1.0 wt.%. The water content for the soil-cement mixtures with 0 wt.%, 6 wt.%, and 12 wt.% cement was equal to 23.42%, 24.08%, and 24.88%, respectively, of the dry mass. Eight earth blocks of nominal dimensions 290 mm × 145 mm × 75 mm were fabricated for each of the nine soil-cement-SCBF compositions, yielding a total of 72 earth blocks. The dimension tolerance in the two major directions was ±0.1%, whereas the dimension tolerance in the thickness was ±4.0%. The soil-cement-SCBF compositions were identified as EB-X-Y, in which X = 00, 06, or 12 indicates the amount of cement, and Y = 00, 05, 10 indicates the amount of SCBF. Within each group, the eight CSEB specimens were identified as T1 through T5 and U1 through U3. The first five specimens (T1 through T5) were used for three-point flexure tests (hereinafter referred to as flexurally tested blocks), and the last three specimens (U1 through U3) were not tested in flexure (hereinafter referred to as pristine blocks). After the flexural test, each of the flexurally tested (T1 through T5) and pristine (U1 through U3) specimens were trimmed using masonry cutting tools to produce two specimens of dimensions 100 mm × 100 mm × 75 mm, which were then used in the dry compression test (T1b, T3a, T5b, U1b, and U2a), wet compression test (T1a, T2a, T4b, U1a, and U3b), and durability test (T2b, T3b, T4a, T5a, U2b, and U3a). This experimental matrix was designed to have at least five specimens for each test, as recommended in [65]. The specimens were randomly selected such that: (1) three flexurally tested and two pristine specimens were used for each compression test, and (2) four flexurally tested and two pristine specimens were used for the durability investigation (see **Figure 3.1** for the summary of the experimental test program). It is noted here that, originally, a total of 10 specimens was planned to be tested for each soil-cement-SCBF composition, i.e., the number of pristine blocks for each composition was also supposed to be equal to five, as for the flexurally tested specimens. However, only eight blocks for each soil-cement-SCBF composition were fabricated due to the limited availability of natural soil; thus, the initial experimental matrix was accordingly modified.

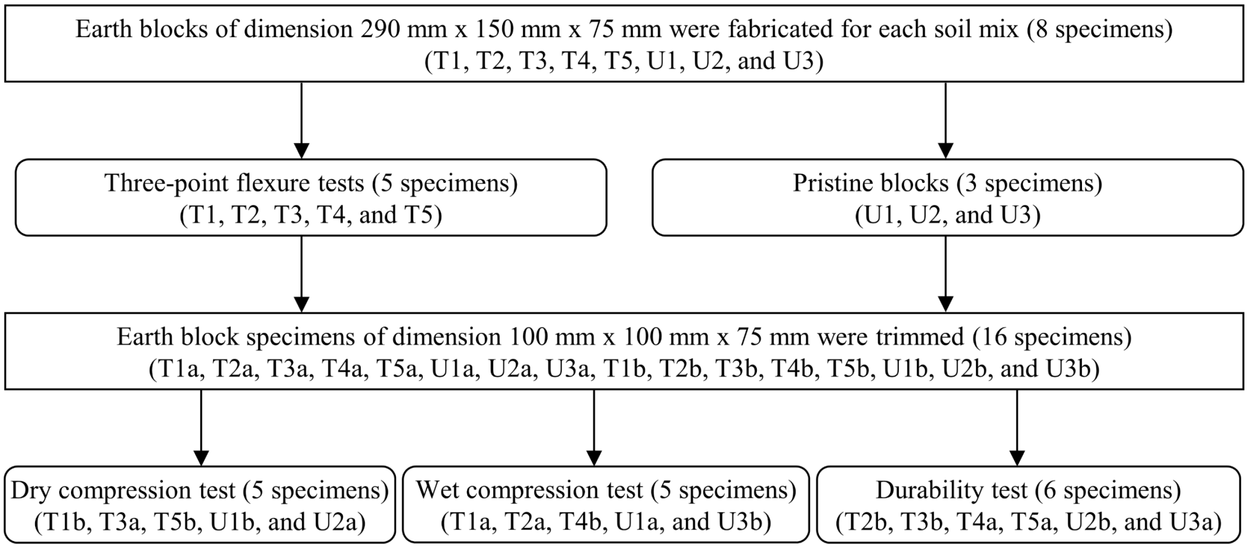

Figure 3.1. Experimental test program for all considered soil-cement-SCBF compositions.

3.3.4. *Scanning electron microscopy-energy dispersive X-ray spectroscopy (SEM-EDS)*

A Quanta™ 3D Dual Beam™ FEG FIB-SEM, with EDAX Pegasus EDS/EBSD detectors, was utilized to evaluate the morphology and chemical composition of natural soil, SCBFs, and earth blocks via scanning electron microscopy (SEM) and energy-dispersive X-ray spectroscopy (EDS), respectively. The EDS was used to collect spectra via area mode with a 20kV accelerating voltage and a 4pA current.

3.3.5. ***X-ray diffraction (XRD)***

The mineralogical characteristics of the natural soil and earth blocks (corresponding to each soil-cement mix) were evaluated utilizing a Panalytical Empyrean X-ray Diffractometer. The XRD technique was conducted using Cu$k\alpha$ radiation at 40 mA and 45 kV. The scan ranged between 5°-70° 2θ, where θ denotes the Bragg's angle, with a step size of 0.026°. The quantitative XRD analysis was performed on GSAS-II [154], based on the Rietveld method with an estimated error smaller than or equal to ± 8%. In addition, the crystalline phase identification was performed by using the DIFFRAC.SUITE EVA Version 4.1 [155].

3.3.6. ***Experimental strength testing***

A TestResources 313 Family universal testing machine with a 50 kN load cell capacity in both tension and compression (with an accuracy of ± 0.5% for the load measurement) was used for the experimental strength testing of the earth block specimens. This universal testing machine was equipped with two internal displacement transducers, which were used to measure the displacements at the moving crosshead of the equipment during both flexure and compression tests. All tests were performed in displacement-control mode at a loading rate of 2 mm/min. A three-point flexure test was performed on five full-block specimens for each soil-cement-SCBF mixture, as per the New Mexico Administrative Code [56]. The displacement was applied in the middle of the blocks with a 250 mm clear span and a 20 mm clearance between edges and supports. This test was used to determine the modulus of rupture (MOR), flexural modulus of elasticity

(MOE_f), flexural displacement ductility factor (δ), and flexural toughness index corresponding to a mid-span flexural displacement equal to 3 times the first crack-deflection (FT-I_5). The flexural displacement ductility factor δ was defined as the ratio of mid-span deflection at failure and the mid-span deflection at the peak load. The FT-I_5 was determined according to ASTM C1018-97 [156]. The flexure test resulted in the formation of a well-defined large crack in the middle of the earth block specimens. The resulting two halves of each flexurally tested specimen were trimmed using masonry cutting tools to produce two specimens, which were then used in the direct compression test [117] and for the durability investigation. Five of these trimmed specimens were tested for dry compression after being left for 48 hours at room conditions (i.e., 22 ± 1 °C and 60 ± 5% relative humidity), and the other five specimens were immersed in water for 24 hours, then tested to obtain their wet compressive strength. In addition, neoprene pads were placed between the steel plates and test specimens during each compression test to minimize the confinement effects due to friction. The dry compression test was used to determine the dry compressive strength (f_{bd}), dry compressive modulus of elasticity (MOE_d), and dry compressive toughness index (DCT-I_5); whereas the wet compression test provided the wet compressive strength (f_{bw}), wet compressive modulus of elasticity (MOE_w), and wet compressive toughness index (WCT-I_5). In addition, the characteristic uniaxial dry compressive strengths (f_{bkd}) and characteristic uniaxial wet compressive strengths (f_{bkw}) were also calculated by accounting for shape and aspect ratio corrections as follows

$$f_{bk} = s_x \cdot \left(\mu_{f_b} - t_{0.05,n-1} \cdot \sigma_{f_b} \right) \tag{3.1}$$

where $f_{bk} = f_{bkd}$ or f_{bkw}, s_x = shape and aspect ratio correction factor [118], μ_{f_b} = sample mean of the (dry or wet) compressive strength, $t_{0.05,n-1}$ = one-side Student's t-distribution factor corresponding to a probability equal to 0.05 and n - 1 degrees of freedom [157], n = number of samples for each batch, σ_{f_b} = sample standard deviation of the (dry or wet) compressive strength. Eq. (3.1) is valid for n > 3.

3.3.7. *Durability test*

The dry density (ρ) and water absorption (ω) of the specimens were determined according to ASTM C67-14 [158] during the first cycle of the durability test. Then, a wetting and drying test was carried out on six half-block specimens for each soil-cement-SCBF mixture as per the ASTM D559-03 standard [159], as described in **Figure 3.1**. This durability test was selected because it is appropriate to assess the performance of CSEBs in hot and humid weather conditions such as those typically encountered in Southern Louisiana. The specimens were submerged in water at room temperature (22 ± 1 °C) for 5 hours, and then they were dried in an oven at 71± 1 °C for 42 hours. After each wetting and drying cycle, two vertical wire scratch brushstrokes were applied to all the surface areas of the specimens using a 13.3 N force for each stroke. A total of 12 wetting and drying cycles were performed, and the percentage loss in mass (LIM) was recorded for each specimen. The ρ and ω of the eroded specimens were also determined at the end of the wetting and drying cycles, to find the change in dry density (Δ_ρ) and water absorption (Δ_ω) due to the 12 cycles of wetting and drying. Finally, a wet compression test was performed on the eroded specimens using the same procedure previously described.

3.3.8. *Statistical analysis of experimental data*

A series of one-way analysis of variance (ANOVA) [160] was conducted on the experimental data to evaluate the statistical significance of the differences among the sample groups for each of the investigated properties of the CSEBs made with different soil-cement-SCBF compositions. A significance level value α = 0.05 was used to decide rejection of the null hypothesis (i.e., that properties measured from different groups of specimens could be drawn from the same probability distribution). The corresponding p-values were compared with the assumed α-value. If the p-values of any statistical tests were lower than 0.05, then, the test was considered to reject the null hypothesis. The statistical analysis was performed using the commercial software MATLAB R2019b [161]. Three different sample groups were considered for each given cement amount, i.e., 0-0.5 wt.% SCBF, 0-1.0 wt.% SCBF, and 0.5-1.0 wt.% SCBF. The classical ANOVA assumes: (1) independence of observations, (2) normal distribution of residuals, and (3) homogeneity of data variances [160,162]. The first assumption was satisfied because the data samples used in the study were collected from randomly grouped specimens. The second assumption was not explicitly checked because the results from classical ANOVA are in general only weakly sensitive to departures from normality [162]. The third assumption was explicitly checked by employing Levene's test [163], since violating the variance homogeneity assumption can have a significant effect on the statistical results [162]. For the groups that failed to meet the assumption of variance homogeneity, a Welch's ANOVA test [164] was performed to identify if the differences between mean values were statistically significant. In the cases in which the (classical or Welch's) ANOVA tests rejected the null hypothesis, the Games-Howell post-hoc test [165] was used to determine the mean of which group(s) presented statistically significant differences from the means of the other groups. The Games-Howell test was selected among other possible post-hoc tests because it does not rely on equal variances and can accommodate different sample sizes.

3.4. Results and Discussion

3.4.1. *Morphology and chemical composition*

Figure 3.2 presents the SEM micrographs of typical SCBFs, EB-00-05, EB-06-05, EB-12-05 and matrix-fiber interfaces for EB-12-05. **Figure 3.2**(a) shows the SEM micrograph at 500 μm scale of the SCBFs used for fabricating the reinforced earth blocks, which reveals the typical morphological features on the surface of the SCBFs [166], i.e., fiber structures and surface residual pith. **Figure 3.2**(b) and (c) show the SEM micrographs at 100 μm scale of the fiber surface (which is characterized by parallel stripes) and of the pith (which is a fragmented structure containing small pores), respectively. **Figure 3.2**(d) through (f) presents the SEM micrographs of the soil-cement matrix for the EB-00-05, EB-06-05, and EB-12-05 specimens, respectively, at 500 μm scale. Only earth blocks reinforced with 0.5% SCBF were selected for SEM micrographs since the soil-cement matrix of earth blocks having different fiber content was assumed to be similar. **Figure 3.2**(d) shows that the matrix of the EB-00-05 specimen presents discontinuities of different sizes and shapes, with prevalent grain-like particles. By contrast, the surface of the EB-06-05 specimen shown in **Figure 3.2**(e) appears more uniform, with a prevalence of compacted fine particles with only a few grain-like particles. The micrograph of the EB-12-05 specimen reported in **Figure 3.2**(f) shows that the soil-cement matrix features well-distributed pores that are typically 10 μm or less in diameter, thus relatively small compared to those seen in the EB-00-05 and EB-06-05 specimens. The visual evidence indicates that increasing the cement content in the earth block leads to a denser and more homogeneous soil-cement matrix, with smaller and more uniformly distributed voids. These results are consistent with the finding reported by other researchers for CSEBs [167,168]. **Figure 3.2**(g-i) shows three different SEM images of matrix-fiber interfaces for the EB-12-05 specimen. In **Figure 3.2**(g), the SCBF is mostly covered under the soil-cement matrix, whereas **Figure 3.2**(h) shows a fiber that is not entirely embedded inside the soil-cement matrix. **Figure 3.2**(i) shows the different textures of soil-cement matrix (A1), matrix-fiber interface (A2), and fibers (A3).

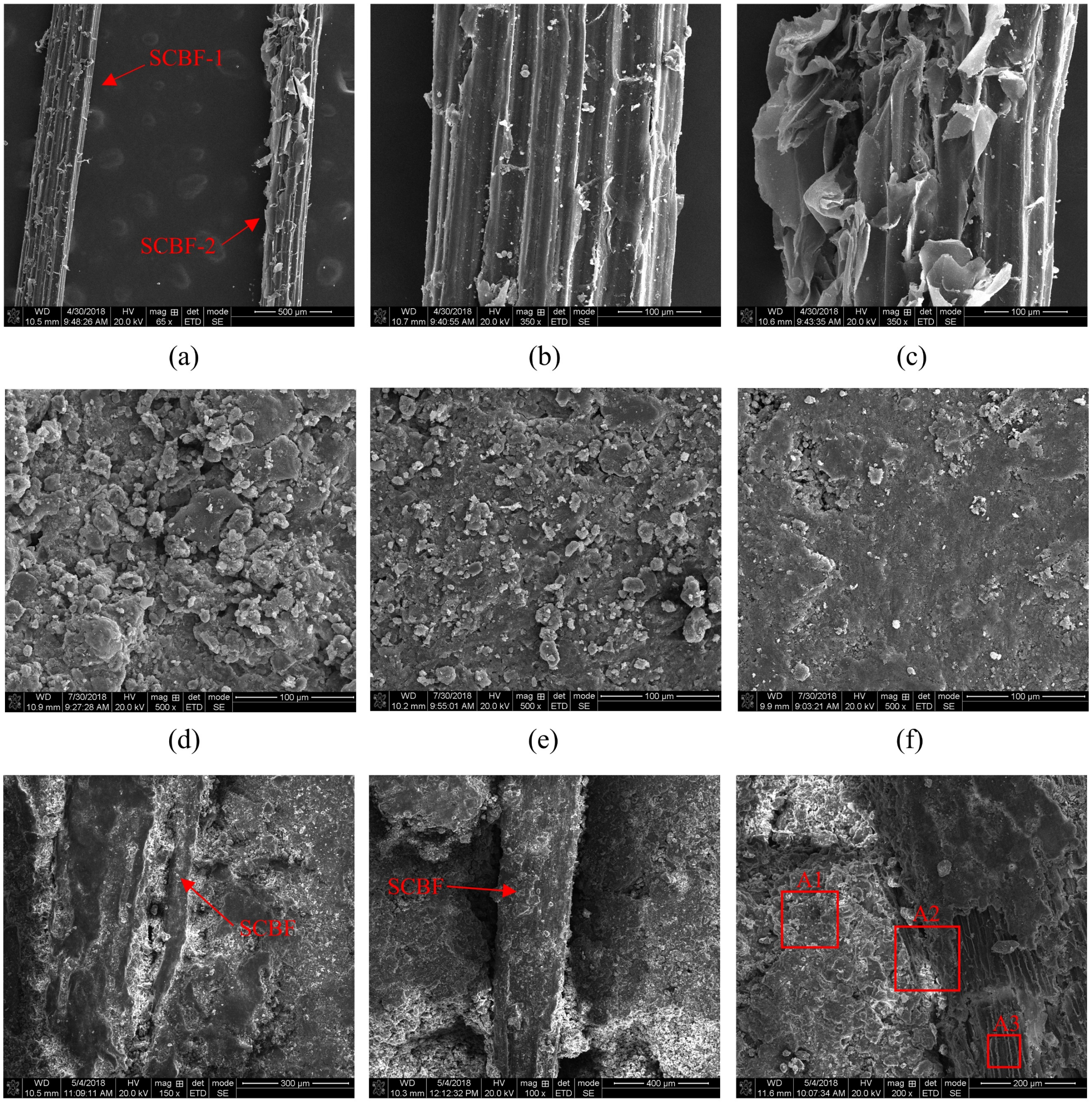

(a) (b) (c)

(d) (e) (f)

(g) (h) (i)

Figure 3.2. SEM micrographs: (a) SCBFs at 500 µm scale; (b) fiber surface of SCBF-1 at 100 µm scale; (c) residual pith of SCBF-2 at 100 µm scale; (d) EB-00-05; (e) EB-06-05; (f) EB-12-05; and (g) through (i) matrix-fiber interfaces for EB-12-05.

Table 3.2 reports the results of the EDS microanalysis (in terms of percentage mass of chemical elements) for the soil, SCBF-1, SCBF-2, and the different regions identified in the EB-12-05 specimen. **Figure 3.3**(a) presents the EDS spectra corresponding to natural soil and the SCBFs. The natural soil mainly contains silicon (Si) and oxygen (O), with lesser amounts of aluminum (Al), iron (Fe), calcium (Ca), potassium (K), magnesium (Mg), sulfur (S), and phosphorus (P). The carbon (C) content was found to be negligible. As expected, the SCBFs predominantly contain C and O, with lesser amounts of Si, Al, Fe, Ca, K, and other minor elements. **Figure 3.3**(b) shows the EDS spectra for the three different regions identified in **Figure 3.2**(i), i.e., soil-cement matrix (A1), matrix-fiber interface (A2), and fiber (A3). Region A1 has a higher percentage of O, Si, Ca, Al, and Fe elements when compared to region A3, which contains a very high portion of C, confirming that A1 corresponds to the soil-cement matrix, whereas region A3 corresponds to SCBFs. As expected, the composition of region A2, which corresponds to the matrix-fiber interface, is somewhere in between the compositions of A1 and A3.

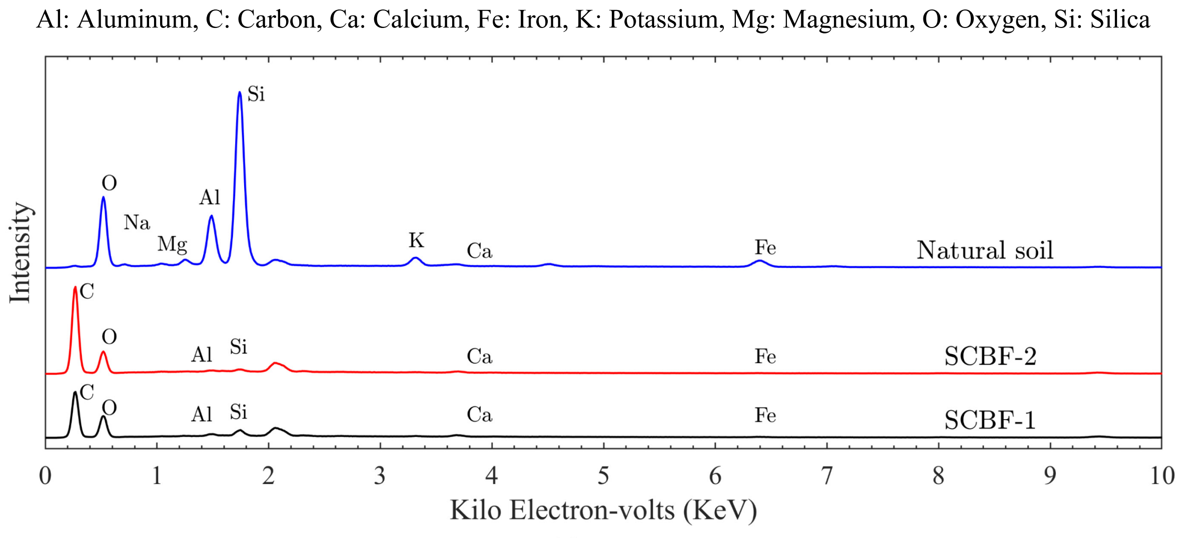

(a)

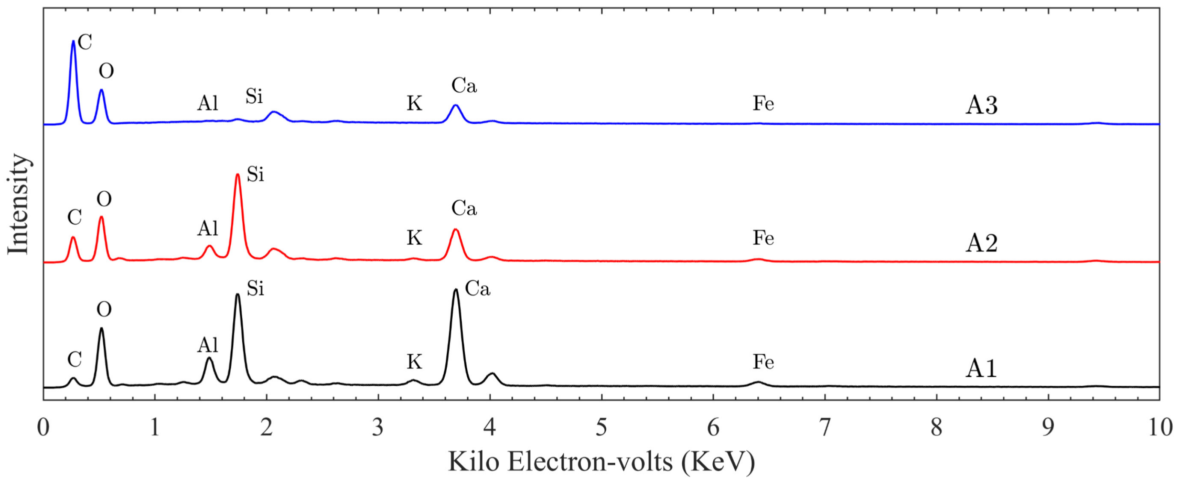

(b)

Figure 3.3. EDS spectra: (a) natural soil and SCBFs; and (b) different regions of EB-12-05.

Table 3.2. EDS microanalysis results (wt.% of chemical elements) of different materials.

Materials	Regions	C	O	Si	Ca	Al	Fe	K	Mg	Na	*Other
Soil	-	-	43.1	35.5	0.6	9.7	5.8	2.6	1.0	0.6	1.1
SCBF-1	-	57.9	38.2	1.3	0.7	0.3	0.4	0.1	-	-	1.3
SCBF-2	-	67.8	30.1	0.4	0.4	0.2	0.1	-	-	-	1.0
EB-12-05	A1	8.5	48.1	11.9	24.9	3.2	2.9	0.5	0.0	0.0	<0.1
EB-12-05	A2	29.9	40.0	12.7	9.5	1.9	1.8	0.2	0.0	0.0	4.0
EB-12-05	A3	54.1	39.3	0.4	5.9	0.0	0.0	0.0	0.0	0.0	0.3

3.4.2. *Mineralogical characteristics*

The XRD was conducted on natural soil, EB-00-05, EB-06-05, and EB-12-05 specimens. The XRD results of these specimens are expected to be representative of all CSEBs with a given amount of cement and different SCBF content considered in this study, since the XRD was performed on the soil-cement matrix of the specimens. The X-ray diffraction pattern of the natural soil, EB-00-05, EB-06-05, and EB-12-05 are presented in **Figure 3.4**, and the XRD quantitative analysis in terms of the percentage weight of the different phases identified are reported in **Table 3.3**.

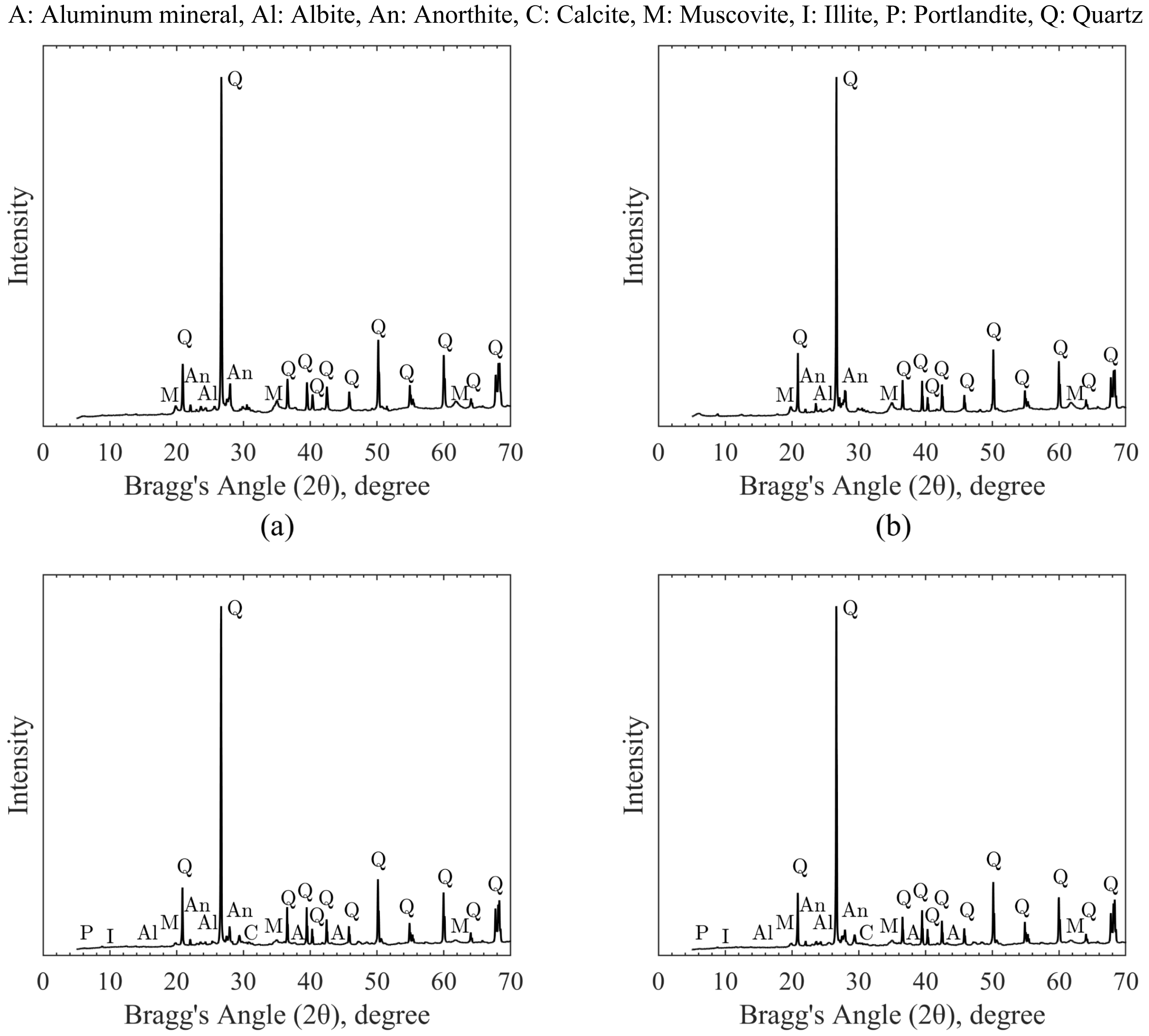

(a)

(b)

(c)

(d)

Figure 3.4. X-ray diffraction patterns: (a) natural soil, (b) EB-00-05, (c) EB-06-05, and (d) EB-12-05.

As expected, a significant amount of quartz was observed in both the natural soil and the earth blocks. The percentage amount of quartz decreases with increasing cement content in the earth blocks. In addition to the quartz, a significant amount of anorthite, albite, and muscovite was also found in the natural soil and the EB-00-05 specimen. By contrast, illite, ettringite, portlandite, were identified only in the EB-06-05 and EB-12-05 specimens. Furthermore, an increase in the amount of Ca-bearing minerals (i.e., anorthite, rankinite, ettringite, and portlandite) was observed for increasing cement content in the earth blocks. It is hypothesized that these Ca-bearing minerals and the cement hydration products may be responsible for making the soil-cement matrix of earth blocks denser and more homogeneous for increasing cement content. It is also observed that the amounts of feldspar minerals, i.e., anorthite, orthoclase, and albite, are comparatively higher than the amount of portlandite.

Table 3.3. XRD mineralogy results (% weight) of soil and earth blocks.

Minerals	Chemical Formula	Soil	EB-00-05	EB-06-05	EB-12-05
Quartz	SiO_2	64.4	65.1	60.8	57.5
Portlandite	$Ca(OH)_2$	-	-	0.2	0.5
Anorthite*	$CaAl_2Si_2O_8$	6.1	6.4	7.9	8.2
Albite*	$NaAlSi_3O_8$	12.4	11.6	11.4	7.8
Orthoclase*	$KAlO_8Si_3$	0.4	0.5	0.9	1.5
Illite	$(K,H_3O)(Al,Mg,Fe)_2(Si,Al)_4O_{10}[(OH)_2,(H_2O)]$	-	-	1.9	2.9
Ettringite	$(CaO)_6(Al_2O_3)(SO_3)_3.32\ H_2O$	-	-	0.3	0.4
Calcite	$CaCO_3$	0.5	0.4	1.1	1.9
Muscovite	$(KF)_2(Al_2O_3)_3(SiO_2)_6(H_2O)$	10.4	10.3	9.0	10.1
Rankinite	$Ca_3(Si_2O_7)$	2.3	2.2	2.5	4.9
Andalusite	Al_2O_5Si	1.9	1.8	2.5	3.1
Almandine	$Fe_3Al_2(SiO_4)_3$	1.6	1.7	1.5	1.2
	Total	100.0	100.0	100.0	100.0

* Feldspar mineral

3.4.3. *Physical properties*

The specimens selected for the durability test were used for determining the physical properties of the earth blocks before the wetting and drying cycles. The measured dry density, ρ, and water absorption, ω, of the earth blocks are reported in **Table 3.4** in terms of sample means and coefficients of variation (COV). The results of the statistical investigation are given in **Table 3.5**. All EB-00-Y specimens lost their integrity after submersion in water for the durability test. Therefore, ρ and ω for EB-00-Y specimens could not be determined. The differences among the dry densities of earth block specimens and the maximum dry density of the raw soil obtained from the standard Proctor compaction test are small, i.e., they are contained between +3.6% and -5.5%

of the maximum dry density of the raw soil. The average ρ values for the EB-06-05 and EB-06-10 specimens are 2.9% higher and 3.0% lower, respectively, than those for the EB-06-00 specimens, whereas the corresponding average ω values are 13.5% and 6.9% lower, respectively than the EB-06-00 specimens. The statistical study shows that the difference between the average ρ value for the EB-06-05 specimens and the EB-06-00 and EB-06-10 specimens is statistically significant. Moreover, the difference between the average value of ω for the EB-06-00 specimens and those for the EB-06-05 and EB-06-10 specimens is also statistically significant. Among the EB-12-Y compositions, the average ρ values of the EB-12-05 and EB-12-10 specimens are 4.5% and 1.9% higher than that for the EB-12-00 specimens. In addition, their average ω values are 6.2% and 11.4% lower than that for the EB-12-00 specimens. A statistical significance in the differences between the average ρ values is observed for EB-12-00 and EB-12-05 specimens, whereas the differences between the average ω values for the different EB-12-Y compositions are not statistically significant. These results show that the earth blocks achieved the maximum dry density and resistance to water absorption when the blocks were reinforced with 0.5 wt.% SCBF.

Table 3.4. Physical properties.

Earth block specimens	Dry density (ρ)		Water absorption (ω)	
	Mean (kg/m^3)	COV (%)	Mean (%)	COV (%)
EB-06-00	1531	1.70	24.35	2.73
EB-06-05	1575	1.45	21.07	4.12
EB-06-10	1485	2.79	22.68	5.29
EB-12-00	1558	0.51	20.22	3.34
EB-12-05	1628	1.61	18.97	8.07
EB-12-10	1588	3.87	17.91	12.55

The obtained results on reinforced CSEBs are in disagreement with those reported by Danso et al. [83] on reinforced CEBs, in which a monotonic decrease in density and an increase in water absorption (obtained by capillary testing performed per BS EN772-11 [169]) were observed for increasing SCBF content. It is noteworthy that three major differences exist between the specimens used in the present study and those used in [83]: (1) the total content of clay and silt in the present study was significantly higher (i.e., more than 89%, versus less than or equal to 46%); (2) the present specimens were fabricated using soil stabilized with cement, whereas those in [83] were fabricated using only soil with no stabilization; and (3) the present specimens were manufactured using a single-stroke manual one-side compaction machine with a pressure approximately equal to 2-4 MPa, whereas those in [83] were fabricated using a hydraulic compaction machine with pressures as high as 10 MPa. However, further investigation is needed to identify how each of these differences affects the changes in the trend for the dry density and water absorption with increasing SCBF content observed in this investigation when compared to those reported in Danso et al. [83].

Table 3.5. Statistical tests and corresponding p-values for the physical properties.

Parameters	Earth block specimens	Levene's test	ANOVA/Welch test	Games-Howell post-hoc tests		
				0-0.5 wt.%	0-1.0 wt.%	0.5-1.0 wt.%
Dry density (ρ)	EB-06-Y	0.13	< 0.01	0.03	0.11	< 0.01
	EB-12-Y	0.04	< 0.01	< 0.01	0.50	0.36
Water absorption (ω)	EB-06-Y	0.21	< 0.01	< 0.01	0.04	0.06
	EB-12-Y	0.08	0.08	-	-	-

* indicates rejection of the null hypothesis by the statistical test.

The comparison of physical properties for earth blocks having different cement content indicates that ρ increases and ω decreases for increasing cement content and given SCBF reinforcement level. This observed trend is consistent with the SEM micrographs and the results of the XRD quantitative analysis. The changes in the physical properties of earth blocks for increasing cement content can be attributed to the increase in Ca-bearing minerals, which are primarily responsible for making the earth block's soil-cement matrix denser and more homogeneous.

The measured COV < 4% for the dry density and < 13% for the water absorption of all groups of earth block specimens. It is observed that, in general, the COVs of both dry density and water absorption increase (1) for a given amount of cement and increasing SCBF content, and (2) for a given amount of SCBFs and increasing cement content, with the exception of the COV for the dry density of the EB-06-00 specimens. The increase in COV for dry density with increasing SCBF content may be caused by the fabrication method used in this research, which is unable to fully remove all voids around the SCBFs through the relatively small compaction pressure produced by manual compaction. The increase in the COV of the water absorption may be produced by the random distribution and orientation of the SCBFs near the surface of the specimens, which can increase the variability of the capillarity effect. However, these hypotheses need further testing in future investigations.

3.4.4. *Flexure test*

The flexure test results for MOR, MOE_f, δ, and FT-I_5 are reported in **Table 3.6** in terms of sample means and COV. **Figure 3.5** plots representative load-displacement curves obtained from the flexure tests of EB-12-Y and EB-X-05 specimens. The results of the statistical analysis performed on the flexure test results are reported in **Table 3.7**. All the EB-X-00 specimens (i.e., the unreinforced earth block specimens) failed immediately after reaching the peak strength and significantly before reaching the flexural displacement needed to estimate FT-I_5, which was assumed to be deterministic and equal to one.

It is observed that the mean value of MOR for the EB-00-Y specimens increases by 34.5% when the SCBF content increases from 0 to 0.5 wt.% and decreases by 12.8% when the SCBF content is further increased from 0.5 to 1.0 wt.%. However, only the mean MOR of the EB-00-05 specimens is statistically different from the mean MOR of the EB-00-00 specimens, whereas the difference in the mean MOR values of other sample groups is not statistically significant. The mean values of MOR for the EB-06-Y and EB-12-Y specimens increase with increasing SCBF content (with increments ranging from 12.8% to 21.3%, and from 9.9% to 25.4%, respectively, when compared to the corresponding unreinforced CSEB specimens), which is consistent with the results reported in Bouhicha et al. [170] for CSEBs reinforced with barley straw. The statistical study shows that the increase in the mean value of MOR for the EB-06-Y specimens are not statistically significant, whereas the mean MOR for the EB-12-10 specimens is statistically different from those of the EB-12-00 and EB-12-05 specimens. The mean values of MOE_f consistently decrease with increasing SCBF content for any given cement content. These decreases range from 13.7% to 55.0%, 9.7% to 19.4%, and 21.8% to 47.4% for EB-00-Y, EB-06-Y, and EB-12-Y specimens, respectively, when compared to the corresponding unreinforced CSEB specimens. This observed trend is similar to that obtained from tensile tests reported in [83] for CEBs reinforced with SCBFs and from flexure tests reported in [171] for CSEBs reinforced with banana fibers. The range of MOE_f values obtained in the present study for the EB-06-Y specimens (i.e., 80.8-100.4 MPa) is also consistent with the range reported in [171] for CSEBs with similar compositions (i.e., 63-175 MPa). The decrease in MOE_f with increasing SCBFs is statistically significant only when the reinforcement in CSEBs is increased to 1.0 wt.% from 0 or 0.5 wt.%, except for the EB-06-Y specimens, for which only the sample groups of 0-1.0 wt.% SCBF content have a statistically significant difference in the mean value of MOE_f.

The mean values of δ for the EB-00-Y specimens increase by 338.9% when the SCBF content increases from 0 to 0.5 wt.% and decrease by 46.8% when the SCBF content is further increased from 0.5 to 1.0 wt.%. The statistical results show that only the mean values of δ for the EB-00-00 specimens differ significantly from those of the EB-00-05 and EB-00-10 specimens. The mean values of δ for the EB-06-Y and EB-12-Y specimens increase with increasing SCBF content (with increments ranging from 222.6% to 278.8%, and from 124.1% to 259.3%, respectively, when compared to the corresponding unreinforced CSEB specimens), which is in agreement with the findings of other studies on natural fiber-reinforced earth blocks [26,170]. The increase in the mean values of δ with increasing SCBFs is statistically significant, except for the sample groups of 0.5-1.0 wt.% SCBF content. The mean values of FT-I_5 for reinforced CSEB specimens are significantly higher than for the corresponding unreinforced CSEBs, with increases contained between 75% and 198%. The mean value of FT-I_5 for the EB-00-10 specimens is 3.4% lower than that for the EB-00-05 specimens; however, this decrease is not statistically significant. By contrast, the mean values of FT-I_5 for the EB-06-10 and EB-12-10 specimens are 21.8% and 54.9% higher than those for the EB-06-05 and EB-12-05 specimens, respectively, and these increases are statistically significant.

Table 3.6. Flexure test results.

Earth block specimens	MOR		MOE_f		δ		FT-I_5	
	Mean (MPa)	COV (%)	Mean (MPa)	COV (%)	Mean (-)	COV (%)	Mean (-)	COV (%)
EB-00-00	0.29	17.86	67.2	17.6	1.85	14.24	1.00	-
EB-00-05	0.39	5.66	57.98	14.89	8.12	29.12	2.98	4.93
EB-00-10	0.34	7.96	30.27	11.42	4.32	62.00	2.88	10.64
EB-06-00	0.47	10.06	100.36	8.17	1.37	11.22	1.00	-
EB-06-05	0.53	16.70	90.65	17.69	4.42	21.96	2.20	11.24
EB-06-10	0.57	4.64	80.84	8.47	5.19	17.42	2.68	9.17
EB-12-00	0.71	4.17	195.12	14.31	1.45	8.59	1.00	-
EB-12-05	0.78	6.19	152.64	14.61	3.25	28.72	1.75	58.02
EB-12-10	0.89	4.55	102.73	5.49	5.21	28.82	2.71	10.78

For any given SCBF reinforcement level, the mean values of the MOR and MOE_f consistently increase for increasing cement content. When compared to the corresponding EB-00-Y specimens, these increases range between 35.9% and 161.8% for the MOR, and between 49.3% and 239.4% for the MOE$_f$. The mean value of δ reaches its minimum value at 6 wt.% cement for the EB-X-00 specimens, and it monotonically decreases with increasing cement content for the EB-X-05 and EB-X-10 specimens (although the change between the EB-06-10 and EB-12-10 is negligible, i.e., less than 0.4%, and not statistically significant). The mean values of FT-I$_5$ decrease with increasing cement content for the EB-X-05 specimens, by 26.2% for EB-06-05 specimens and by 41.3% for the EB-12-05 specimens when compared to the EB-00-05 specimens. By contrast, for the EB-X-10 specimens, the mean values of FT-I$_5$ reach their lowest value at 6 wt.% cement contents, i.e., 6.9% lower that the corresponding value for the EB-00-10 (although, also in this case, the change between the EB-06-10 and EB-12-10 is negligible, i.e., less than 1.1% and not statistically significant).

Table 3.7. Statistical tests and corresponding p-values for the flexure test results.

Parameters	Earth block specimens	Levene's test	ANOVA/Welch test	Games-Howell post-hoc tests		
				0-0.5 wt.%	0-1.0 wt.%	0.5-1.0 wt.%
MOR	EB-00-Y	0.04	0.01	0.03	0.26	0.05
	EB-06-Y	0.23	0.08	-	-	-
	EB-12-Y	0.66	<0.01	0.08	<0.01	0.01
MOE$_f$	EB-00-Y	0.02	0.00	0.39	<0.01	<0.01
	EB-06-Y	0.02	0.02	0.49	0.01	0.47
	EB-12-Y	0.33	<0.01	0.07	<0.01	0.01
δ	EB-00-Y	0.01	<0.01	0.01	0.01	0.20
	EB-06-Y	0.29	<0.01	<0.01	<0.01	0.44
	EB-12-Y	0.02	<0.01	0.03	0.01	0.10
FT-I$_5$	EB-00-Y	0.11	<0.01	<0.01	<0.01	0.80
	EB-06-Y	0.35	<0.01	<0.01	<0.01	0.04
	EB-12-Y	0.17	<0.01	<0.01	<0.01	0.04

* indicates rejection of the null hypothesis by the statistical test.

The observed behavior is due to contrasting and interacting effects produced by the increase of cement and SCBF contents: the increase in cement content generally has a positive effect on flexural strength and stiffness, but a negative effect on the ductility of the specimens; whereas the addition of SCBF generally has a negative effect on stiffness, but a positive effect on flexural strength and ductility up to a critical fiber content, the value of which depends on the cement content (i.e., 0.5 wt.% for EB-00-Y specimens). For increasing SCBF content and constant cement content, the CSEB's MOE_f decreases because the SCBFs are significantly less stiff than the soil-cement matrix, they induce discontinuities and micro-cracks in the soil-cement matrix, and there is some slip between the fibers and the soil-cement matrix at their interfaces. The observed increase in MOR and FT-I_5 with increasing SCBF content can be attributed to the fiber-bridging effect of SCBF, which prevents and resists the opening of cracks in the earth blocks until failure of the fibers through pull out or rupture. The failure mechanism (i.e., pull-out or rupture of the fiber) depends on the relative values of the fiber's tensile strength and the bond strength (due to friction and cohesion) between the fiber and the soil-cement matrix [26,82]. In this study, the critical fiber content was identified only for the EB-00-Y specimens; however, it is expected that a similar but higher critical fiber content exists also for CSEB specimens with higher cement content. In fact, increasing the SCBF content increases the formation of micro-cracks in the soil-cement matrix at the matrix-fiber interface, as also observed in adobe blocks reinforced with Hibiscus cannabinus fibers [172]. These micro-cracks limit the fiber-bridging effect of the SCBFs by weakening the soil-cement matrix and thus reducing the pull-out strength of the fiber. At the same time, increasing cement content strengthen the soil-cement matrix (due to the increase in Ca-bearing materials, which make the matrix denser and more homogeneous, as shown in **Figure 3.2**), thus increasing the pull-out strength of the fiber and the critical fiber content. A theoretical upper limit for the fiber-bridging effect of SCBF is given by the condition in which the fiber failure mechanism is only fiber rupture, which is fully controlled by the tensile strength of the individual fiber and by the amount of SCBF. It is observed that, for 1.0 wt.% SCBF, FT-I_5 is practically independent on the cement amount, i.e., within the investigated ranges of SCBF and cement contents, the increase in ductility provided by the SCBFs at 1.0 wt.% counterbalances the decrease in ductility produced by increasing the cement content from 0 wt.% to 12 wt.%. Further studies are needed to better understand and quantify the interaction between soil properties, fiber properties, cement amount, and SCBF amount under different conditions and, ideally, to develop a mechanistic model that can be used to select the optimal amounts of cement and SCBF for a given soil and predict the mechanical properties of the corresponding CSEBs.

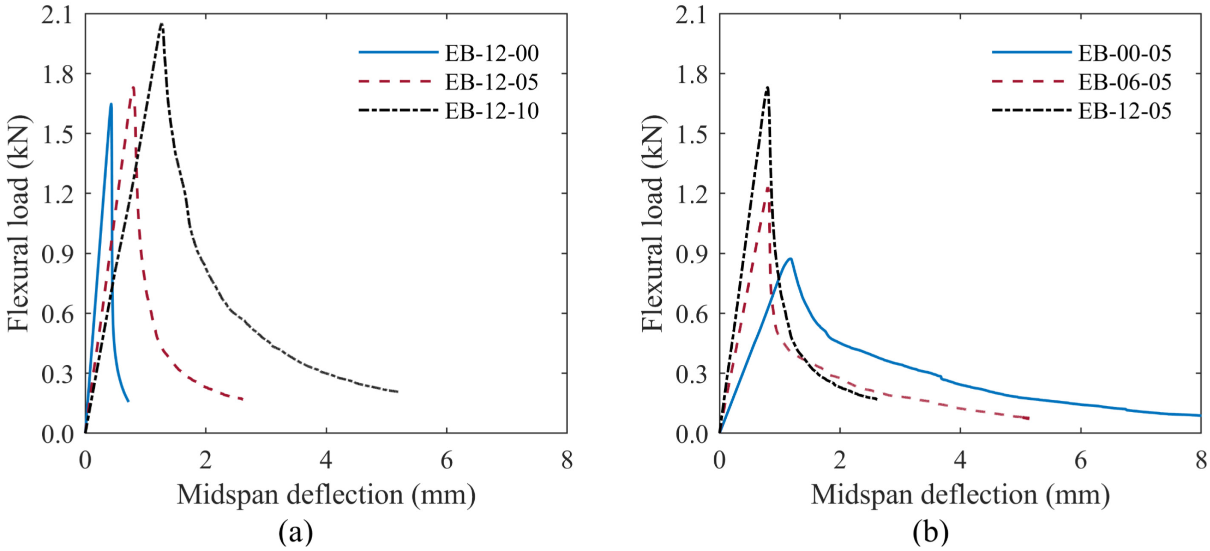

Figure 3.5. Representative load-displacement curve from flexure test: (a) EB-12-Ys, and (b) EB-X-05s.

The flexure tests resulted in the formation of a well-defined large crack in the middle of the earth blocks, as shown in **Figure 3.6**(a) and **Figure 3.6**(c) for an EB-00-00 specimen, and in **Figure 3.6**(b) and **Figure 3.6**(d) for an EB-12-10 specimen. The failure of the unreinforced blocks was sudden (brittle) and corresponded to a significant reduction in the sustained load at small levels of deformation, whereas the failure of the SCBF-reinforced blocks was more gradual (ductile), with larger deformations, larger crack openings, and higher residual strength after the formation of the middle cracks. These results are consistent with the behavior observed for other fiber-reinforced earth blocks [26]. By visual (naked eye) inspection, it was observed that some SCBFs were pulled out from the soil-cement matrix, whereas other fibers fractured, similar to what was observed in Danso et al. [82].

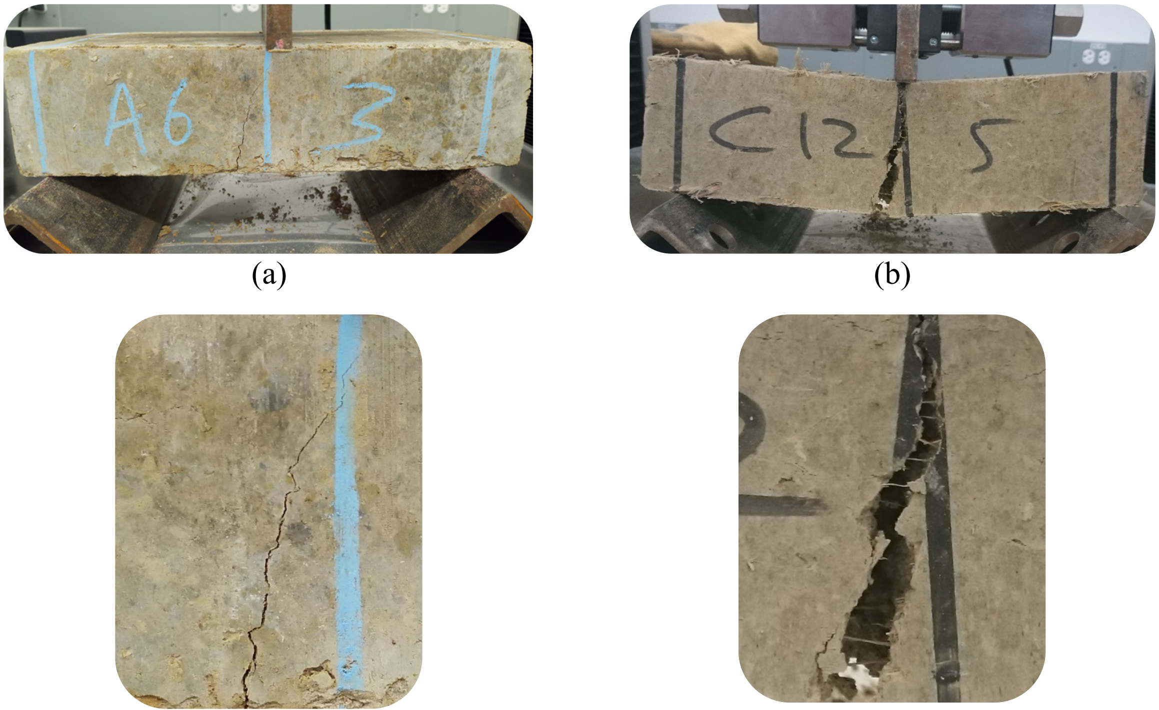
(a) (b) (c) (d)

Figure 3.6. Failure and crack pattern of earth blocks under three-point flexure test: (a) global view of EB-00-00, (b) global view of EB-12-05, (c) zoom view of the crack in EB-06-00, and (d) zoom view of the crack in EB-12-05.

It is noteworthy that, with the exception of the EB-00-00 and EB-00-10 specimens, all CSEB groups satisfied the minimum requirement by the New Mexico Administrative Code [56] of an average MOR ≥ 0.35 MPa (50 psi).

3.4.5. *Compression test*

The results of the dry and wet compression tests in terms of sample means and COV for f_{bd}, MOE$_{d}$, DCT-I$_{5}$, f_{bw}, MOE$_{w}$, and WCT-I$_{5}$ are reported in **Table 3.8**, which reports also the estimated values of the characteristic compressive strengths f_{bkd} and f_{bkw}. **Figure 3.7** show representative axial load-displacement curves of EB-12-Y and EB-X-05 specimens obtained from the dry and wet compression tests. It is noted that the force-displacement response is preferred over stress-strain curve for representing the compressive behavior of CSEB specimens in the present study. In fact, the stress-strain curve obtained from this test do not represent the uniaxial compressive behavior (particularly after peak load) of the CSEB material because of the effects associated with the specimens' aspect ratio and the potential confinement at the platen restraints (i.e., friction along the interface between the platen and test specimens can confine the lateral expansion of the specimens) [65]. To obtain, the compressive stress-strain curve of CSEBs, the Digital Image Correlation (DIC) testing procedure proposed in [79,173] can be used. The results of the statistical tests are tabulated in **Table 3.9**.

Table 3.8. Compression test results.

		Strength*		MOE**		CT-I_5		
Tests	Earth block specimens	Mean (MPa)	COV (%)	Mean (MPa)	COV (%)	Mean (-)	COV (%)	f_{bk}^{***} (MPa)
Dry compression	EB-00-00	1.22	6.38	22.92	11.01	5.46	7.22	0.74
	EB-00-05	1.57	12.47	18.07	17.15	6.34	8.18	0.81
	EB-00-10	1.38	13.80	14.04	19.80	6.16	3.22	0.68
	EB-06-00	1.95	12.70	37.79	15.28	4.89	16.31	1.00
	EB-06-05	2.34	7.57	34.85	10.78	5.33	10.03	1.37
	EB-06-10	2.28	8.63	30.96	8.49	5.62	2.13	1.30
	EB-12-00	3.70	5.47	75.29	10.97	4.69	14.53	2.28
	EB-12-05	4.50	6.26	69.07	7.30	5.01	4.78	2.73
	EB-12-10	4.48	7.09	65.20	10.64	5.37	8.32	2.66
Wet compression	EB-00-00	-	-	-	-	-	-	-
	EB-00-05	-	-	-	-	-	-	-
	EB-00-10	-	-	-	-	-	-	-
	EB-06-00	0.97	9.91	24.37	8.55	4.81	6.30	0.53
	EB-06-05	1.36	6.76	20.73	13.63	5.10	3.45	0.82
	EB-06-10	0.92	9.45	17.51	13.61	5.30	6.56	0.52
	EB-12-00	2.16	5.84	52.38	6.61	5.12	11.83	1.33
	EB-12-05	2.39	7.67	48.82	7.70	5.11	7.16	1.40
	EB-12-10	2.28	7.74	45.50	8.54	5.39	9.18	1.33

* Strength = f_{bd} for dry compression test or f_{bw} for wet compression test; ** MOE = MOE$_d$ for dry compression test or MOE$_w$ wet compression test; and *** f_{bk} = f_{bkd} for dry compression test or f_{bkw} for wet compression test.

The experimental results show that, for a fixed cement content, the average f_{bd} reaches its peak value for 0.5 wt.% SCBF, which is 28.6%, 19.9%, and 21.7% higher for EB-00-05, EB-06-05, and EB-12-05 specimens, respectively, when compared to the corresponding unreinforced CSEB specimens. This observation is consistent with previous studies on earth blocks reinforced with other natural fibers, which also reported an initial increase in strength at low fiber contents followed by a subsequent decline at higher fiber contents [26,142,170]. The statistical study shows that the differences in mean f_{bd} between EB-X-00 and EB-X-05 specimens, as well as between EB-12-00 and EB-12-10 specimens, are statistically significant. However, these differences are not statistically significant for other sample groups. The mean values of MOE_d consistently decrease with increasing SCBF content and constant cement content, with increments ranging from 21.2% to 38.7%, 7.8% to 18.1%, and 8.3% to 13.4% for EB-00-Y, EB-06-Y, and EB-12-Y specimens, respectively, when compared to the corresponding unreinforced CSEB specimens. The statistical significance is only observed for the EB-00-00 specimen when compared with the EB-00-05 and EB-00-10 specimens. The average DCT-I_5 of the EB-00-Y specimens reaches its maximum value for 0.5 wt.% SCBF content, which is 16.0% higher than that for the EB-00-00 specimens. However, the statistical study indicates that the only statistically significant differences in mean DCT-I_5 are those between the EB-00-00 specimens and other EB-00-Y specimens. By contrast, the mean values of DCT-I_5 for the EB-06-Y and EB-12-Y specimens monotonically increase with increasing SCBF content, with increments ranging from 9.0% to 14.9% and from 6.9% to 14.5%, respectively, when compared with the values for the corresponding unreinforced CSEB specimens. However, the differences in mean DCT-I_5 are not statistically significant. For any given amount of SCBF reinforcement and increasing cement content, the dry compressive strength and stiffness of CSEBs significantly increase, whereas the DCT-I_5 slightly decreases.

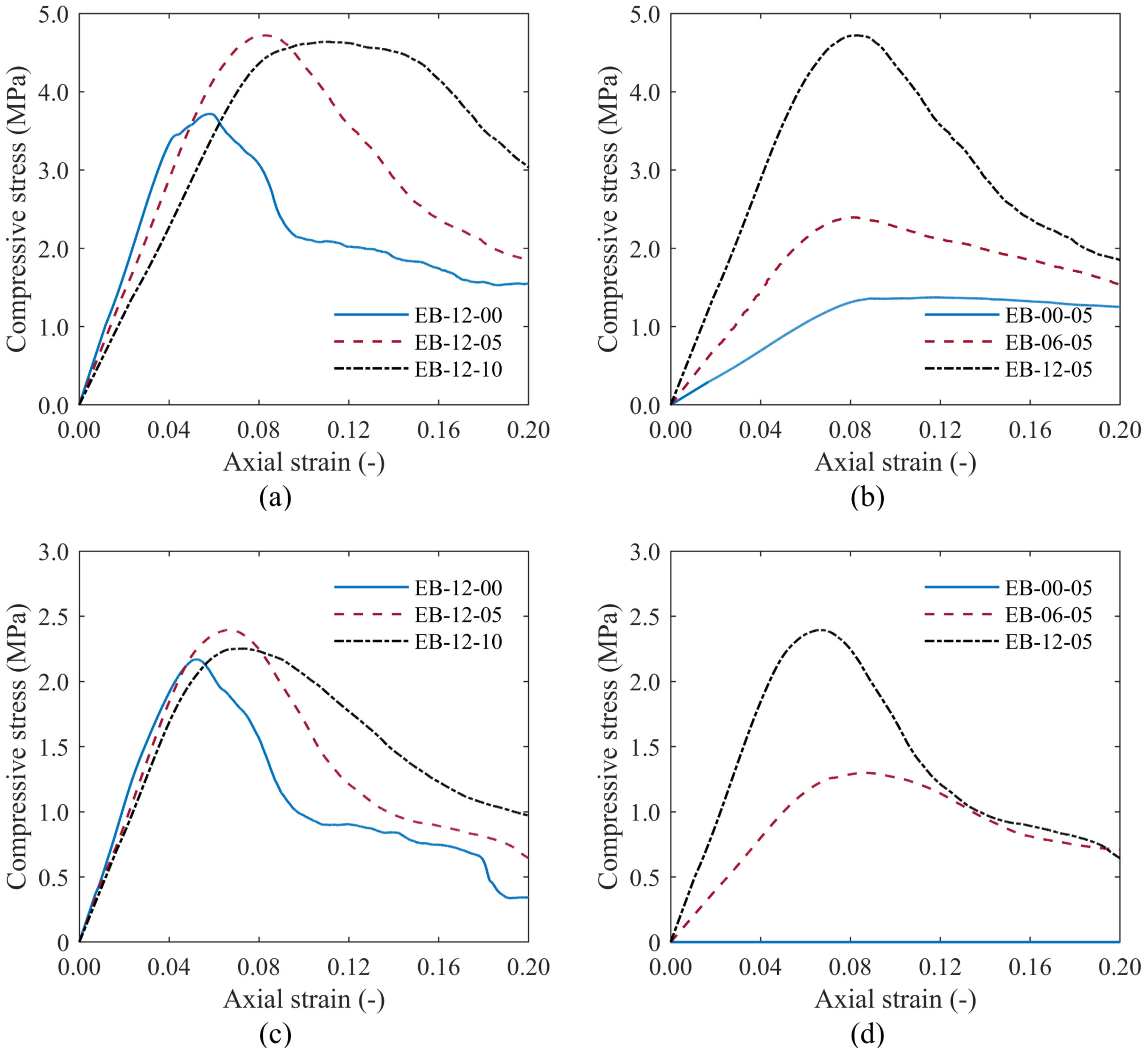

Figure 3.7. Representative load-displacement curves for compression test: (a) EB-12-Y from dry compression test and (b) EB-X-05 from dry compression test, (c) EB-12-Y from wet compression test, and (d) EB-X-05 from wet compression test.

It is noteworthy that all EB-00-Y specimens lost their integrity after 24 hours of immersion in water; thus, the average f_{bw} for these specimens is considered equal to zero. The average f_{bw} values of the EB-06-Y and EB-12-Y specimens follow a trend that is similar to that observed for f_{bd} (i.e., they reach a peak for 0.5 wt.% SCBF content). In particular, the average f_{bw} values for the EB-06-05 and EB-12-05 specimens are 40.8% and 10.3% higher, respectively, than those of the corresponding EB-X-00 specimens. The average f_{bw} values are approximately 41.4% to 59.5% lower than the corresponding f_{bd}. This reduction in the compressive strength can be attributed to the development of pore water pressures and a decrease in clay cohesion [66,174]. The differences in the mean value of f_{bw} between the EB-06-05 and other EB-06-Y specimens are statistically significant; however, all other differences are not statistically significant. For any given cement content, the MOE_w mean values monotonically decrease with increasing SCBF content, similar to the trend observed for MOE_d. In particular, the increments in the MOE_w mean values for the EB-06Y and EB-12-Y specimens range from 14.9% to 28.1%, and from 6.8% to 13.1%, respectively, when compared to the values for the corresponding unreinforced CSEB specimens. However, statistical significance is found only for the differences between the mean MOE_w of the EB-X-00 and EB-X-10 specimens. The MOE_w mean values are approximately 29.3% to 43.4% lower than those of the corresponding MOE_d. The average WCT-I_5 values for the EB-06-Y and EB-12-Y specimens increase with increasing SCBF content, but these differences are not statistically significant. For any given SCBF content, the mean values of f_{bw}, MOE_w, and WCT-I_5 increase for increasing cement content. In particular, the mean values of f_{bw} increase by 122.7%, 75.7%, and 147.8% going from 6 wt.% to 12 wt.% cement for 0.0, 0.5, and 1.0 wt.% SCBF, whereas the mean values of MOE_w increase by 114.9%, 135.5%, and 159.9% going from 6 wt.% to 12 wt.% cement for 0.0, 0.5, and 1.0 wt.% SCBF. By contrast, the differences in WCT-I_5 between EB-06-Y and EB-12-Y specimens are very small for 0 wt.% cement and negligible for 0.5 wt.% and 1.0wt.% cement. From the results reported in **Table 3.8**, it is observed that both the MOE_d and MOE_w values are relatively low. However, these values are consistent with results presented in the literature for earth blocks with similar density and soil composition [175].

Table 3.9. Statistical tests and corresponding p-values for the compressive test results.

Parameters	Earth block specimens	Levene's test	ANOVA/Welch test	Games-Howell post-hoc tests		
				0-0.5 wt.%	0-1.0 wt.%	0.5-1.0 wt.%
f_{bd}	EB-00-Y	0.37	0.02	0.03	0.28	0.32
	EB-06-Y	0.70	0.03	0.04	0.11	0.88
	EB-12-Y	0.60	< 0.01	< 0.01	< 0.01	1.00
MOE_d	EB-00-Y	0.80	< 0.01	0.04	< 0.01	0.14
	EB-06-Y	0.44	0.08	-	-	-
	EB-12-Y	0.28	0.10	-	-	-
DCT- I_5	EB-00-Y	0.13	< 0.01	0.04	0.03	0.77
	EB-06-Y	0.26	0.16	-	-	-
	EB-12-Y	0.13	0.13	-	-	-
f_{bw}	EB-00-Y	-	-	-	-	-
	EB-06-Y	0.96	< 0.01	< 0.01	0.74	< 0.01
	EB-12-Y	0.74	0.14	-	-	-
MOE_w	EB-00-Y	-	-	-	-	-
	EB-06-Y	0.66	< 0.01	0.11	< 0.01	0.19
	EB-12-Y	0.96	0.04	0.32	0.04	0.40
WCT- I_5	EB-00-Y	-	-	-	-	-
	EB-06-Y	0.47	0.05	-	-	-
	EB-12-Y	0.63	0.62	-	-	-

* indicates rejection of the null hypothesis by the statistical test.

Similar to the behavior observed for the flexural properties, increasing amounts of cement were generally associated with increases in strength, stiffness, and brittleness of the CSEB specimens. However, cement content had a significantly smaller effect on the CSEB toughness in compression than of that in flexure. Also in this case, these results can be explained by the increase in Ca-bearing materials, which made the soil-cement matrix denser and more homogeneous. This study identified a critical fiber content of 0.5 wt.% for the three considered cement content levels, beyond which the CSEB compressive behavior started degrading (0 wt.% and 6 wt.% cement) or not improving (12 wt.% cement). It is hypothesized that the increase in compressive strength and toughness observed for increasing SCBF content below the critical fiber content may be due to a confinement effect produced by the SCBF fibers on the soil-cement matrix. Under these conditions, the fibers oppose the formation of vertical cracks and more uniformly distribute the tension stresses within the material by acting as a structural mesh, as it has been observed in adobe bricks reinforced with SCBFs [143]. However, for SCBF reinforcement amounts higher than the critical value, several combined effects tend to reduce the strength and toughness of the material e.g.: (1) it becomes more difficult to ensure a uniform distribution of the fibers, with potential formation of knots and lumps of SCBF [176], (2) some of the fibers are unable to properly bond with the soil-cement matrix [177], and (3) increasing fiber amounts produce an increase in the micro-cracks and pores within the soil-cement matrix and at the matrix-fiber interface [26,172].

The failure mode observed during the compression tests of the unreinforced CSEB specimens corresponded to the development of an hour-glass shape following the spalling of the vertical sides, as shown in **Figure 3.8**(a) for an EB-12-00 specimen. This failure mode is typical of brittle material behavior and is commonly observed in compression tests of ordinary concrete cubic specimens [178]. For the reinforced CSEB specimens, the SCBFs prevent the spread of large cracks in the CSEBs through friction and chemical bonds between the SCBFs and the soil-cement matrix. Because of this phenomenon, the CSEB specimens maintain their integrity even after their failure, as shown in **Figure 3.8**(b) for an EB-12-05 specimen.

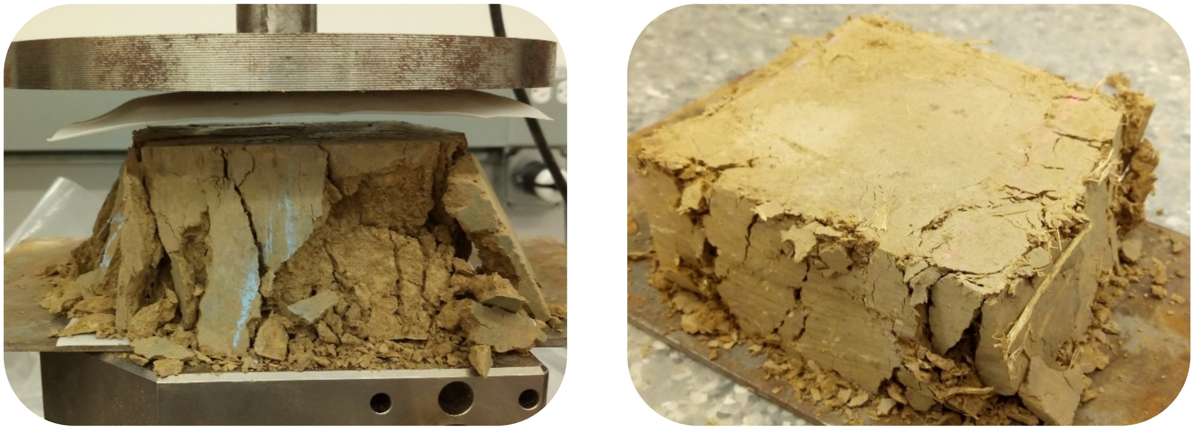

(a) (b)

Figure 3.8. Failure under direct dry compression test: (a) EB-12-00 and (b) EB-12-05.

It is observed that the New Mexico Administrative Code requires a minimum average dry compressive strength of 2.07 MPa, and a minimum sample dry compressive strength of 1.72 MPa for CEBs and CSEBs [56]. A minimum average wet compressive strength of 1.96 MPa [179] or a minimum unconfined characteristic wet compressive strength of 1.00 MPa [66] are also recommended in the literature. The obtained experimental results obtained indicate that, among the specimens considered in this study, only the EB-12-Y specimens satisfy all of these strength requirements.

3.4.6. *Durability test*

The results of the durability test after 12 cycles of wetting and drying are reported in **Table 3.10** in terms of sample means and COVs for LIM, Δ_ρ, and Δ_ω. The EB-00-Y specimens lost their integrity after a five-hour water immersion; thus, their corresponding results are not reported in the table. The results of the statistical study are reported in **Table 3.11**. **Figure 3.9** shows one specimen for each group that survived the twelve wetting-and-drying cycles of the durability tests.

Table 3.10. Wetting-and-drying durability test results.

Earth block specimens	Loss in mass (LIM)		Change in dry density (Δ_ρ)		Change in water absorption (Δ_ω)	
	Mean (%)	COV (%)	Mean (%)	COV (%)	Mean (%)	COV (%)
EB-06-00	13.07	33.33	-2.04	52.71	-2.09	57.97
EB-06-05	15.13	25.45	-4.76	28.32	3.76	59.99
EB-06-10	19.63	24.57	-3.81	52.83	2.43	28.08
EB-12-00	1.40	53.29	-1.43	92.52	1.60	51.47
EB-12-05	2.34	25.92	-3.70	70.28	1.29	36.10
EB-12-10	5.29	30.35	-4.35	38.66	3.84	35.49

When considering only the specimens that survived the durability test, the average LIM of the EB-06-Y and EB-12-Y specimens increases from 13.07% to 19.63% and from 1.40% to 5.29%, respectively, with increasing SCBF content from 0.0 wt.% to 1.0 wt.%., see the **Figure 3.9**. For EB-06-Y specimens, the differences in mean LIM values for different SCBF contents are not statistically significant. For EB-12-Y specimens, only the mean LIM for the EB-12-10 specimen is statistically significantly different from those of the EB-12-00 and EB-12-05 specimens. Overall, the LIM of CSEBs slightly increases with increasing SCBF content and a given cement content, and significantly decreases with increasing cement content at a given SCBF content. These results are consistent with the SEM results in the **Figure 3.2**(d) through (f), which show that the soil-cement matrix becomes more compact and homogeneous with increasing cement content. The increase in LIM for increasing SCBF content can be explained by the corresponding increase in micro-cracks and pores [26,172], which make the CSEBs more vulnerable to water penetration and, thus, less durable. These trends are also similar to those observed in Gowda [142] for reinforcement of CSEBs with guayule plant fibers. However, Danso [26] observed a rapid reduction in the LIM of CEBs with increasing SCBF content up to 0.5 wt.%, after which the LIM levelled off or increased slightly with further fiber inclusion. This different behavior could be because in Danso [26] a modified version of the durability test described in the ASTM D559-03 standard [159] was used, where the CEBs specimens were exposed to water through capillary action for only 2 minutes (instead of submersion in water for 5 hours) during the wetting and drying cycles. Recommendations found in the literature for acceptable LIM's limits suggest LIM smaller than 10% [141,142]. The experimental results obtained in this study show that, among the specimens considered in this study, only the EB-12-Y specimens satisfy this durability requirement.

A decrease in dry density (ranging from 1.43% to 4.76%) and an increase in water absorption (ranging from 1.29% to 3.84%) is observed for all specimens between before and after the durability test, except for the water absorption of the EB-06-00 specimens, which decreases by 2.09%. The average Δ_ρ values of the EB-06-Y specimens reach their minimum for 0.5 wt.% SCBF content (i.e., -4.76%), whereas they decrease monotonically with increasing SCBF content for EB-12-Y specimens (ranging from -1.43% to -4.35%). However, the observed differences are statistically significant only between EB-06-00 and EB-06-05 specimens and between EB-12-00 and EB-12-10 specimens. At 0.5 wt.% SCBF content, the average Δ_ω values reach their maximum for the EB-06-Y specimens (i.e., 3.76%) and their minimum for the EB-12-Y specimens (i.e., 1.29%). The observed differences are statistically significant only between EB-06-00 and the other EB-06-Y specimens, and between the EB-12-10 and the other EB-12-Y specimens.

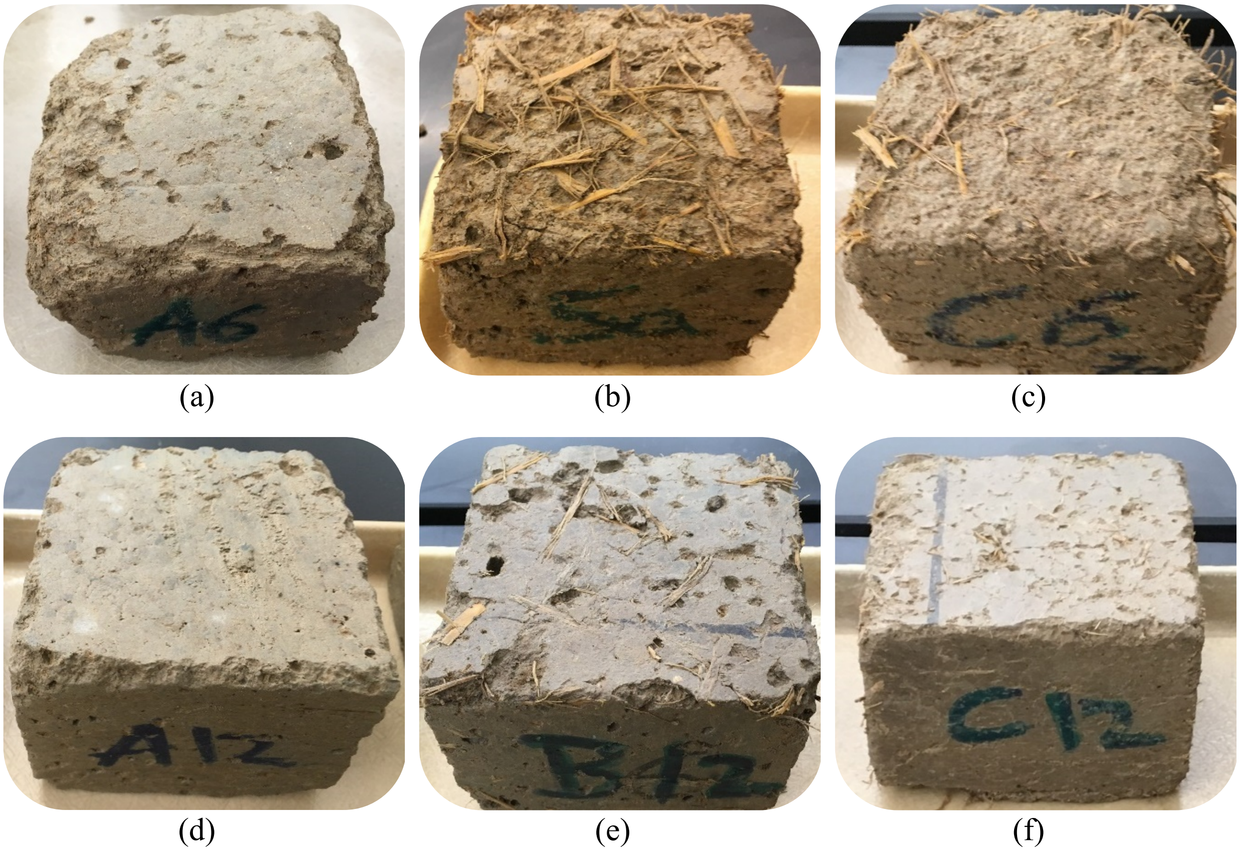

(a) (b) (c)

(d) (e) (f)

Figure 3.9. Specimens after 12 cycles of wetting and drying: (a) EB-06-00, (b) EB-06-05, (c) EB-06-10, (d) EB-12-00, (e) EB-12-05, and (f) EB-12-10.

Table 3.11. Statistical tests and corresponding p-values for the durability test results.

Parameters	Earth block specimens	Levene's test	ANOVA/Welch test	Games-Howell post-hoc tests		
				0-0.5 wt.%	0-1.0 wt.%	0.5-1.0 wt.%
LIM	EB-06-Y	0.82	0.05	-	-	-
	EB-12-Y	0.02	< 0.01	0.09	< 0.01	0.01
Δ_ρ	EB-06-Y	0.27	0.02	< 0.01	0.20	0.62
	EB-12-Y	0.31	0.04	0.20	0.02	0.87
Δ_ω	EB-06-Y	0.13	< 0.01	< 0.01	< 0.01	0.41
	EB-12-Y	0.16	< 0.01	0.71	0.02	0.01

* indicates rejection of the null hypothesis by the statistical test.

A wet compression test was performed on the CSEBs that survived the durability test (i.e., EB-06-Y and EB-12-Y specimens). **Table 3.12** reports the sample means and COV for f_{bw}, MOE$_w$, and WCT-I$_5$, as well as the estimates of f_{bkw}. **Figure 3.10** shows some representative axial load-displacement curves for EB-12-Y and EB-X-05 specimens. The corresponding statistical analysis results are reported in **Table 3.13**.

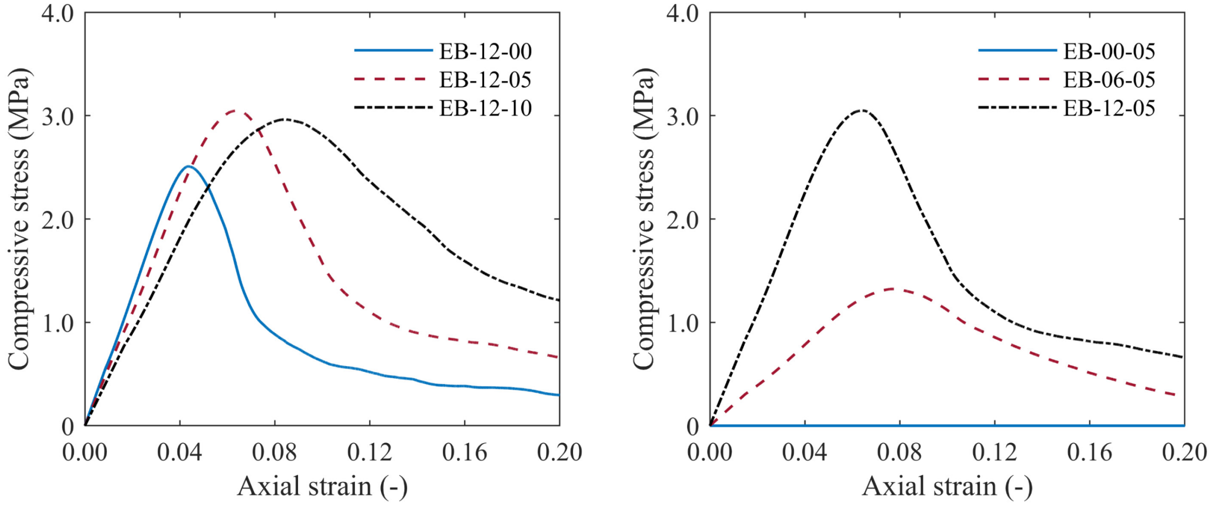

(a) (b)

Figure 3.10. Representative load-displacement curves from wet compression test performed after durability investigation: (a) EB-12-Y and (b) EB-X-05.

The EB-06-Y specimens show a 29.4% to 60.9% reduction in the average f_{bw} compared to the corresponding CSEBs tested before subjecting them to the durability test. By contrast, the EB-12-Y specimens exhibit an 11.2% to 25.6% increase in the average f_{bw} after the durability test. This observed increase in strength may be due to the progress of cement hydration during the wet cycle of the durability test, as the high content of clay and silt combined with the relatively high cement content may have prevented full hydration of the cement during the 28-day curing period after which the specimens not subjected to the durability test were originally tested. This result is consistent with the findings of the chapter 2 of this dissertation, where the mechanical properties of CSEBs were found to improve after exposure to wet climate conditions. However, further investigation is needed to fully test this hypothesis. The average f_{bw} of the EB-06-Y and EB-12-Y specimens reach their maximum values at 0.5 wt.% SCBF content, with the mean f_{bw} values for the EB-06-05 and EB-12-05 specimens 154.3%, and 19.0% higher, respectively, than the corresponding values for the EB-06-00 and EB-12-00 specimens. This trend is identical to that observed for the wet compressive strength of CSEBs before the durability test. The statistical analysis indicates that only the differences in the f_{bw} mean values between EB-06-00 specimens and other EB-06-Y specimens are statistically significant. The average MOE_w after the durability test are 23.5% to 61.7% lower for the EB-06-Y specimens and 11.4% to 17.3% higher for the EB-12-Y specimens, when compared to the corresponding values before the durability test. The average MOE_w reaches its maximum value at 0.5 wt.% SCBF content for the EB-06-Y specimens (i.e., 70.2% and 68.3% higher than for EB-06-00 and EB-06-12 specimens, respectively), whereas it slightly decreases with increasing SCBF content for EB-12-Y specimens (i.e., 4.0% and 8.5% lower for EB-12-05 and EB-12-10 specimens than for EB-12-00 specimens). However, the differences in MOE_w mean values are statistically significant only between EB-06-05 and EB-06-10 specimens. It is also observed that the average WCT-I_5 after the durability test is between 1.0% and 23.1% lower than the corresponding value obtained before the durability test, except for the EB-06-00 specimens, for which the average WCT-I_5 increases by 16.7% after the durability test.

For increasing SCBF content, the mean value of WCT-I$_5$ decreases for EB-06-Y specimens (with reductions equal to 9.9% and 11.7% for EB-06-05 and EB-06-10 specimens, respectively, when compared to EB-06-00 specimens) and increases for EB-12-Y specimens (with increments equal to 9.7% and 32.1% for EB-12-05 and EB-12-10 specimens, respectively, when compared to EB-12-00 specimens). However, the differences in average WCT-I$_5$ are statistically significant only between EB-12-00 and other EB-12-Y specimens.

Table 3.12. Compression test results after the durability test.

Earth block specimens	Wet compressive strength Mean (MPa)	Wet compressive strength COV (%)	MOE$_w$ Mean (MPa)	MOE$_w$ COV (%)	WCT- I$_5$ Mean (MPa)	WCT- I$_5$ COV (%)	f_{bkw} (MPa)
EB-06-00	0.38	42.29	9.32	48.12	5.61	28.59	0.04
EB-06-05	0.96	32.89	15.86	32.27	5.05	24.21	0.23
EB-06-10	0.60	15.26	9.42	14.67	4.95	9.65	0.29
EB-12-00	2.41	10.51	58.34	13.54	3.94	13.21	1.33
EB-12-05	2.86	22.69	55.99	29.34	4.32	9.83	1.08
EB-12-10	2.84	12.10	53.39	20.16	5.20	10.37	1.52

For a given SCBF reinforcement level, the mean values of f_{bw} and MOE$_w$ obtained after the durability test monotonically increase with increasing cement content. The mean f_{bw} values for the EB-12-00, EB-12-05, and EB-12-10 specimens are 535.7%, 195.4%, and 374.3% higher, respectively, than those for the corresponding EB-06-Y specimens, whereas the mean MOE$_w$ values for EB-12-00, EB-12-05, and EB-12-10 specimens are 525.9%, 252.9%, and 466.5% higher, respectively, than those for the corresponding EB-06-Y specimens. In addition, for increasing cement content, the mean values of WCT-I$_5$ for EB-12-00 and EB-12-05 specimens decrease by 29.7% and 14.4%, respectively, when compared to the corresponding EB-06-Y specimens, whereas the average WCT-I$_5$ increases by 5.1% from the EB-06-10 to the EB-12-10 specimens. These trends for the compressive behavior of CSEBs after the durability test are identical to the trends observed for their flexural behavior, i.e., for increasing cement content, the

EB-X-00 and EB-X-05 specimens become stronger and more brittle, whereas the EB-X-10 specimens become stronger without losing ductility. It is also observed that only the EB-12-Y specimens satisfy the wet compressive strength requirements recommended in the Indian Standard [179] (i.e., minimum average wet compressive strength of 1.96 MPa) and in Walker and Stace [66] (i.e., minimum unconfined characteristic wet compressive strength of 1.00 MPa) after the durability test.

Table 3.13. Statistical tests and corresponding p-values for the compressive properties of the earth blocks subjecting to durability test.

Parameters	Earth block specimens	Levene's test	ANOVA/Welch test	Games-Howell post-hoc tests		
				0-0.5 wt.%	0-1.0 wt.%	0.5-1.0 wt.%
f_{bw}	EB-00-Y	-	-	-	-	-
	EB-06-Y	0.96	< 0.01	0.01	0.04	0.08
	EB-12-Y	0.74	0.17	-	-	-
MOE_w	EB-00-Y	-	-	-	-	-
	EB-06-Y	0.96	0.02	0.09	1.00	0.04
	EB-12-Y	0.74	0.78	-	-	-
WCT- I_5	EB-00-Y	-	-	-	-	-
	EB-06-Y	0.96	0.60	-	-	-
	EB-12-Y	0.74	< 0.01	0.38	< 0.01	0.03

* indicates rejection of the null hypothesis by the statistical test.

3.4.7. *Comparison of flexurally tested and pristine specimens*

Figure 3.11 presents the comparison of dry and wet compressive strength for the flexurally tested and pristine specimens. It is observed that the results from different flexurally tested and pristine specimens are overall very similar. Comparable results were also obtained by comparing MOE_d, MOE_w, DCT-I_5, WCT-I_5, ρ, ω, LIM, Δ_ρ, and Δ_ω. Albeit the number of specimens belonging to the two different groups was insufficient to perform a rigorous statistical analysis, these results seem to suggest that the mechanical and physical properties of flexurally tested and pristine specimens with the same soil-cement-SCBF composition can be considered as describing the same group of specimens, i.e., it is hypothesized that the flexure test induces only insignificant damage, if any, in the trimmed specimens. Further investigations are recommended to rigorously test this hypothesis.

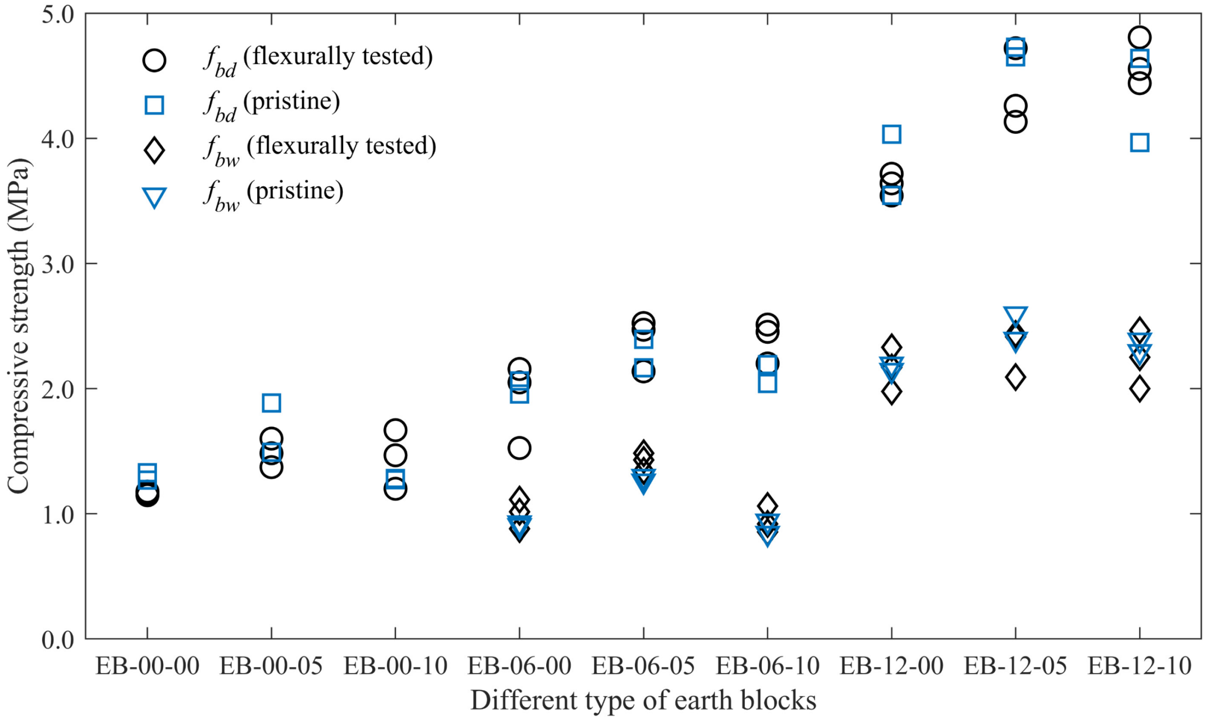

Figure 3.11. Comparison of dry and wet compressive strength for flexurally tested and pristine specimens.

3.5. Conclusions

This study presents the properties of compressed and stabilized earth blocks (CSEBs) reinforced with different amounts (i.e., 0%, 0.5% and 1.0% by weight, or wt.%) of sugarcane bagasse fibers (SCBF) and containing different amounts (i.e., 0 wt.%, 6 wt.%, and 12 wt.%) of type II ordinary Portland cement. The CSEBs were fabricated using a single-stroke manual compaction machine. Based on the experimental test results and the statistical analysis of the experimental data, the following conclusions are drawn:

1. The scanning electron microscopy results show that increasing the cement content in the CSEBs led to a denser and more homogeneous soil-cement matrix. The X-ray crystallography

results suggest that the formation of Ca-bearing minerals (e.g., anorthite, rankinite, ettringite, and portlandite) were responsible for making the soil-cement matrix denser and stronger.

2. The modulus of rupture (MOR) and the flexural modulus of elasticity (MOE_f) of CSEBs improved with increasing cement content and given SCBF content; however, the flexural toughness index (FT-I_5) decreased. The effect of the SCBF content for a given cement content was dependent on the amount of cement, with positive effects on both MOR and FT-I_5 up to a critical fiber content due to fiber-bridging of the cracks. The critical fiber content was identified as 0.5 wt.% for CSEBs without cement. It is hypothesized that the value of the critical fiber content increases with the cement content until the failure mechanism is controlled by fiber fracture. Increasing SCBF content always corresponded to a decrease in MOE_f for any constant cement content.
3. For a constant SCBF content, the dry compressive strength (f_{bd}) and modulus of elasticity (MOE_d) increased, whereas the dry compressive toughness index (DCT-I_5) showed only a small decrease for increasing cement content. For any given cement content, the f_{bd} reached their maximum values at 0.5 wt.% SCBF content, the MOE_d decreased, and the DCT-I_5 behavior was dependent on the cement amount. In particular, the DCT-I5 reached a peak value for 0.5 wt.% SCBF content at 0.0 wt.% cement, whereas it monotonically increased for increasing SCBF content at both 6 wt.% and 12 wt.% cement contents. Similar to the flexural properties, it is hypothesized that a critical fiber content exists for different cement contents; however, the compressive behavior is controlled by a confinement effect produced by the fibers on the soil-cement matrix.

4. The earth blocks fabricated without stabilization (i.e., without cement addition) did not survive the wet compression test nor the wetting and drying cycles of the durability test. Therefore, stabilization is necessary to produce durable earth blocks.
5. For the CSEBs that maintained their integrity after 24 hours submersion in water, the mechanical properties under wet conditions followed trends similar to those of the corresponding dry mechanical properties. The wet compressive strength and wet modulus of elasticity were 41-59% and 29-43% lower, respectively, than their dry counterparts, whereas the wet compressive toughness index values are very similar to their dry counterparts.
6. Higher amounts of cement corresponded to better durability for any given SCBF amount. The CSEBs that survived the durability test showed an increase in loss in mass and water absorption with increasing SCBF content and constant cement content; however, variations of SCBF amount did not affect the dry density of CSEBs.
7. Among the CSEBs that survived the durability test, by comparing the wet mechanical properties before and after the 12 cycles of the wetting and drying, the CSEBs stabilized with 6 wt.% cement showed a reduction in wet compressive strength (between 29% and 61%) and modulus of elasticity (between 23% and 62%); whereas the wet compressive toughness index showed changes between 17% increase and 7% decrease. By contrast, the CSEBs stabilized with 12 wt.% cement had an 11-26% increase in wet compressive strength, an 11-17% increase in wet modulus of elasticity, and a 3-23% reduction in wet compressive toughness index.

It is concluded that, among the CSEBs considered in this study, the CSEBs with 0.5 wt.% or 1.0 wt.% SCBF and 12 wt.% cement contents provided the best compromise between strength and durability and satisfied the corresponding recommendations available in design standards and the literature.

CHAPTER 4. NEW CONSTITUTIVE MODEL FOR INTERFACE ELEMENTS IN FINITE-ELEMENT MODELING OF MASONRY

4.1. Introduction

Finite element (FE) modeling of masonry structures is a very complex problem in computational mechanics, which continues to attract the interest of the research community after several decades of investigations. Several FE approaches have been proposed, with different levels of accuracy, computational cost, and information details [180,181]. The highest level of accuracy and detail on the mechanical behavior of masonry could be achieved using the FE micro-modeling approach, in which different masonry components, i.e., masonry units (bricks/blocks) and mortar, are distinctly represented through continuum elements, and the unit-mortar interface is represented by interface elements [180]. Thus, micro-modeling explicitly addresses the intrinsic discontinuity and heterogeneity of masonry elements. However, it is also computationally very intensive and, thus, rarely employed for analyzing masonry. The computational cost can be reduced by lumping mortar and two unit-mortar interfaces into a zero-thickness joint (generally modeled using an interface element) between expanded masonry units [180,182]. This modelling approach is referred to as simplified micro-modeling (SMM) and has been widely employed to investigate the local behavior of masonry [180,182–188].

The capability of the SMM approach to simulate the mechanical response of masonry properly relies upon the accuracy and robustness of the employed interface element, which relates the traction vector with the relative displacement vector. In fact, in most SMM approaches, the nonlinearity of the system is often concentrated in the interface element, and masonry units are assumed to be elastic in nature [180,182–184,189,190]. Hence, interface elements should be able to describe all major failure mechanisms of masonry under multi-axial stress conditions [167,180,191–193] which include: (a) cracking of masonry units in direct tension, (b) cracking of mortar joints, (c) bed or head joint failure due to sliding under normal stress, (d) diagonal tension cracking of masonry units, and (e) masonry crushing.

Zero-thickness interface elements formulated in terms of traction-separation relationships were originally introduced by Goodman, Taylor and Brekke [194] to model discontinuity in rock mechanics. Page [182] introduced the use of interface elements between elastic continuum elements (representing expanded masonry units) in failure analysis of masonry. The non-linear behavior of masonry was simulated through the interface behavior, which was modeled through a constitutive model that included a brittle failure in tension and hardening in shear/compression. However, compression (crushing) failure was not included in the interface elements [182,190,195,196], until an appropriate constitutive model for analysis of masonry shear walls was developed by Lourenco and Rots [197] to simulate/predict the ultimate strength and post-peak behavior of masonry. The Lourenco and Rots' model is a multi-surface composite interface model (CIM) that consists of three different failure criteria (failure surfaces), i.e., a Rankine failure criterion (tension cut-off criterion) for mode-I failure (opening in tension), a Mohr-Coulomb failure criterion for mode-II failure (in plane shearing or sliding), and a compression cap failure criterion for compression failure. The Rankine and the Mohr-Coulomb failure surfaces are coupled through internal softening parameters, whereas the Mohr-Coulomb and the compression cap failure surfaces are uncoupled. This multi-surface CIM has been used by many researchers to investigate the behavior of masonry structures [91,183,198–200].

Numerous interface element's constitutive models (based on numbers of failure surfaces, different failure criteria, and softening/hardening hypotheses) have been proposed to investigate the behavior of masonry by using the SMM approach. The simplest approach in defining an interface element's constitutive model is to adopt one failure surface to describe each of the three major failure mechanisms, i.e., tension, shear, and compression, [180,189,198,201]. However, the use of multiple failure surfaces leads to singularity problems at the intersections between two of these surfaces [202]. Therefore, several constitutive models were developed with failure surfaces representing two [184,203] or three [186,204,205] failure mechanisms at a time. The usage of these more complex failure surfaces can introduce issues of robustness and may increase the computational cost of the constitutive model [203].

This chapter proposes a new interface element's constitutive model that is capable of simulating tension cracking, shear slipping, and compression failure for masonry analysis using the SMM approach. The proposed constitutive model is developed within the framework of non-associative elastoplastic materials with softening. It is noted here that other approaches could be used to improve the efficiency and robustness of masonry modeling based on the SMM approach, e.g., the plasticity-damage approach [201,206,207], the variational approach [208], the damage approach [209], and the elasto-viscoplastic modeling approach [210,211]. However, the consideration of these alternative approaches is beyond the scope of this study. The robustness and computational cost of the proposed constitutive model are compared to those of different constitutive models that have been widely used in the literature to describe masonry behavior through a one-element test. In addition, the performance of the different constitutive models is investigated in terms of accuracy and computational cost by simulating an unreinforced masonry shear wall for which well-documented experimental results are available in the literature. Finally, conclusions are made based on the results obtained in the present study.

4.2. Research significance

This chapter introduces a novel mechanical constitutive model for interface elements used in the context of the SMM approach for masonry structures. The proposed constitutive model achieves robustness, computational efficiency, and accuracy in modeling masonry structures under multi-axial stress conditions by (1) overcoming the singularity problem that arises from the interaction between the Mohr-Coulomb failure criterion and the Rankine failure criterion, and (2) using the strain hardening/softening hypothesis to improve the numerical robustness of the solution during the evolution of the yield surfaces. In addition, the proposed constitutive model is easily extendable to cyclic/hysteretic behavior. Therefore, the constitutive model developed here for interface elements can extend the usage of the SMM approach to investigate the behavior of masonry components and structures.

This chapter also investigates the advantages and disadvantages of different constitutive models for interface elements when using the same integration scheme. This comparison provides useful information for further development of interface element's constitutive models to simulate the mechanical behavior of masonry and other quasi-brittle materials.

4.3. Proposed coupled tension-shear interface model (CTSIM)

Interface elements permit discontinuities in the displacement field, and their behavior can be described in terms of a relation between the traction, $\boldsymbol{\sigma}$, and relative displacements, $\boldsymbol{u}$, across the interface. Thus, the generalized elastic behavior of the interface element's constitutive model can be written in standard form as

$$\boldsymbol{\sigma} = \boldsymbol{k} \cdot \boldsymbol{u} \tag{4.1}$$

where, for a 3D configuration, $\boldsymbol{\sigma} = \{\sigma, \tau_s, \tau_t\}^T$, $\boldsymbol{u} = \{u_n, u_s, u_t\}^T$, and $\boldsymbol{k} = \text{diag}[k_n, k_s, k_t]$, $\text{diag}[\bullet]$ denotes the diagonal matrix operator, n denotes the normal components, and s and t denote the shear components in two orthogonal directions. The component of the elastic stiffness matrix, k, for the constitutive model in the SMM approach can be obtained from the properties of the masonry components (i.e., masonry units and mortar), and can be written as follows (Rots and Picavet, 1997):

$$\frac{1}{k_n} = \left(\frac{h_m}{E_m} - \frac{h_m}{E_b}\right), \frac{1}{k_s} = \frac{1}{k_t} = \left(\frac{h_m}{G_m} - \frac{h_m}{G_b}\right) \tag{4.2}$$

where E_m and E_u are Young's modulus for mortar and masonry units, respectively; G_m and G_u denote the shear modulus for mortar and masonry units, respectively; and h_m is the thickness of the mortar joints. It is noted that Eq. (4.2) may significantly overestimate the elastic stiffness of the masonry joint's interface, particularly when the masonry units are weaker than the mortar or when the bond surface between mortar and units presents gaps [212,213]. Thus, several approaches have been proposed to obtain a better representation of the actual response of unreinforced masonry, e.g., by introducing a reduction factor in the calculation of the elastic stiffness based on Eq. (4.2) [189,212,214], or by proposing more refined model parameter calibration strategies [215].

The inelastic behavior of the proposed constitutive model for interface elements, referred to as coupled tension-shear interface model (CTSIM) hereafter, is defined by a convex composite failure surface (shown in **Figure 4.1**), which consists of a tension-shear failure criterion $F_1(\boldsymbol{\sigma}, \kappa_1, \kappa_2)$ and a compression cap failure criterion $F_2(\boldsymbol{\sigma},\kappa_3)$, where κ_1, κ_2, and κ_3 are the scalar softening/hardening parameters. The selection of this composite failure surface, which removes the singularity in the tension-shear region but not in the compression-shear region, is based on the fact the shear and tensile behaviors of masonry are coupled while the compression and shear behaviors can be considered as uncoupled [180]. Thus, removing the singularity in the tension-shear region can reduce the computational cost of the interface element, whereas removing the singularity in the compression-shear region is not effective in reducing the computational cost of the interface element [203]. It is noteworthy that the specific form of $F_1(\boldsymbol{\sigma},\kappa_1,\kappa_2)$ used in this study presents several novel characteristics when compared to other existing models and has been used here for the first time in the context of interface elements for masonry modeled using the SMM approach.

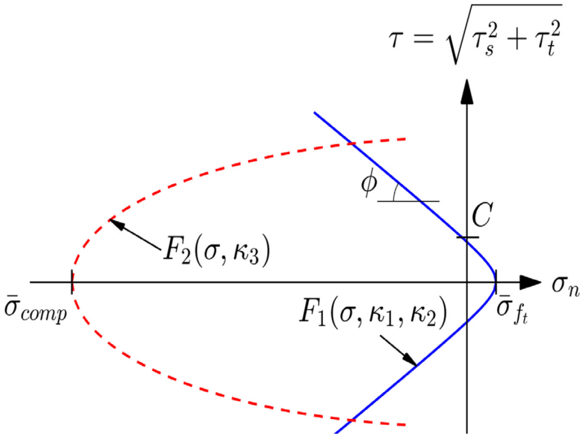

Figure 4.1. Typical composite failure surface for the proposed CTSIM in stress space.

4.3.1. *Tension-shear failure criterion*

A single hyperbolic surface is used for representing pressure-dependent shear failure and tensile cracking. The usage of this surface overcomes the singularity problem that occurs in multi-surfaces failure criteria, i.e., in the combination of the Mohr-Coulomb and Rankine failure criterion [202] and it enables the proposed interface element's constitutive model to converge faster for larger load steps at the Gauss point level. The failure criterion originally proposed by [216] for concrete fracture problem is adopted here for the first time to describe the tension-shear yield surface, which is given as:

$$F_1(\boldsymbol{\sigma},\kappa_1,\kappa_2) = -[C(\kappa_1,\kappa_2) - \sigma \cdot \tan\phi(\kappa_1,\kappa_2)] + \sqrt{\tau^2 + [C(\kappa_1,\kappa_2) - \bar{\sigma}_{f_t}(\kappa_1,\kappa_2)\cdot \tan\phi(\kappa_1,\kappa_2)]^2} \qquad (4.3)$$

where $\tau^2 = \tau_s^2 + \tau_t^2$, ϕ is the frictional angle, $\bar{\sigma}_{f_t}(\kappa_1,\kappa_2)$ is the tensile yield stress, and $C(\kappa_1,\kappa_2)$ is the cohesive yield stress. This hyperbolic failure criterion represents an improvement with respect to other criteria described by quadratic terms [184,204,217], which consist of two hyperbolic branches, only one of which has physical meaning. Therefore, this modified yield function relaxes the requirement for small load steps at the Gauss point level, which otherwise would be needed to guarantee that the computed stress is associated with the correct branch of the hyperbolic surface [216]. A strain-softening hypothesis is considered for this failure criterion, in which the normal and shear plastic relative displacements jointly control the softening of both tensile and cohesive yield stresses. The tensile and cohesive yield stresses are implicitly coupled and softening in the tensile yield stress produces a proportional softening in the cohesive yield stress and vice versa. Thus, the rates of the scalar softening parameters are defined as follows by adapting the expressions originally derived in Lourenco [180] to satisfy simultaneously the Mohr-Coulomb and Rankine failure criteria at their singularity point:

$$\dot{\kappa}_1 = \langle \dot{u}_n^p \rangle + \frac{G_f^I}{G_f^{II}} \cdot \frac{C_0}{f_t} \cdot \sqrt{\left|\dot{u}_s^p\right|^2 + \left|\dot{u}_t^p\right|^2} \qquad (4.4)$$

$$\dot{\kappa}_2 = \frac{G_f^{II}}{G_f^I} \cdot \frac{f_t}{C_0} \cdot \langle \dot{u}_n^p \rangle + \sqrt{\left|\dot{u}_s^p\right|^2 + \left|\dot{u}_t^p\right|^2} \qquad (4.5)$$

respectively, where f_t is the tensile strength; C_0 is the initial cohesion; G_f^I is the mode-I fracture energy; G_f^{II} is the mode-II fracture energy; u_n^p, u_s^p, and u_t^p denote the plastic relative displacements in the n, s, and t directions, respectively; $\langle \bullet \rangle$ denotes the Macaulay brackets; and a superposed dot indicates differentiation with respect to (pseudo-)time. This form of the rates of the softening parameters allows their efficient computation when using a single smooth yield surface. In fact, the usage of the Macaulay brackets ensures that the softening parameters are affected by tensile stresses in the shear-tension region, whereas they are not affected by compression stresses in the shear-compression region, consistently with the typical behavior of masonry joints (which are damaged by tension and shear stresses, but not by low compression stresses). The tensile yield stress $\bar{\sigma}_{f_t}(\kappa_1,\kappa_2)$ and cohesive yield stress $C(\kappa_1,\kappa_2)$ are defined as

$$\bar{\sigma}_{f_t}(\kappa_1,\kappa_2) = f_t \cdot \exp\left[-\sqrt{\left(\frac{f_t}{G_f^I} \cdot \kappa_1 \right)^2 + \left(\frac{C_0}{G_f^{II}} \cdot \kappa_2 \right)^2} \right] \tag{4.6}$$

$$C(\kappa_1,\kappa_2) = C_0 \cdot \exp\left[-\sqrt{\left(\frac{f_t}{G_f^I} \cdot \kappa_1 \right)^2 + \left(\frac{C_0}{G_f^{II}} \cdot \kappa_2 \right)^2} \right] \tag{4.7}$$

respectively. The exponential terms are defined so to ensure that the tensile and cohesive yield stresses evolve in a proportional fashion (i.e., the shape of the yield function remains the same during the analysis) and include the effects of both softening parameters. The softening of the friction angle is assumed proportional to the softening of the cohesive yield stress, i.e.

$$\tan\phi(\kappa_1,\kappa_2) = \tan\phi_r + \left(\tan\phi_0 - \tan\phi_r \right) \cdot \frac{C(\kappa_1,\kappa_2)}{C_0} \tag{4.8}$$

where ϕ_0 is the initial friction angle and ϕ_r is the residual friction angle. A non-associative formulation is assumed for the tension-shear failure criterion because the friction angle, ϕ, and the dilatancy angle, ψ, are generally considerably different for masonry [218,219]. The plastic potential function $Q_1(\boldsymbol{\sigma},\kappa_1,\kappa_2)$ is defined as [217]:

$$Q_1(\boldsymbol{\sigma},\kappa_1,\kappa_2)=-[C_Q(\kappa_1,\kappa_2)-\sigma\cdot\tan\psi(\kappa_1,\kappa_2)]^2+\tau^2+[C_Q(\kappa_1,\kappa_2)-\bar{\sigma}_{f_t}(\kappa_1,\kappa_2)\cdot\tan\psi(\kappa_1,\kappa_2)]^2 \quad (4.9)$$

where $C_Q(\kappa_1,\kappa_2)$ is the apparent cohesive yield stress. The behavior of parameters C_Q and ψ are obtained by substituting C_Q and C_{Q0} to C and C_0, respectively, in Eq. (4.7), and, ψ_0 and ψ_r to ϕ, ϕ_0, and ϕ_r respectively, in Eq. (4.8). The plastic potential function in Eq. (4.9) consists of quadratic terms and, thus, of two hyperbolic branches, similar to the failure yield criterion used, e.g., in Caballero [217], Macorini and Izzuddin [184], and Citto [204], in which the same functional form was employed for both yield criterion and plastic potential function. However, since for the proposed CTSIM the yield criterion functional form is different from that of the plastic potential function, the existence of a non-physically meaningful branch does not introduce convergence issues, because only the physically meaningful branch is actually used due to the constraints imposed by the consistency condition during the plastic-corrector step of the CTSIM's return mapping algorithm [220]. The plastic potential function defined by Eq. (4.9) presents several computational advantages when compared to other existing expressions, e.g., the derivatives of the plastic potential function with respect to stress are simpler than those for the plastic potential function proposed in Caballero, Willam and Carol [216].

4.3.2. *Compression cap failure criterion*

The compression cap model used in the proposed constitutive model used here is described by an elliptical yield function originally introduced for orthotropic plasticity of soil materials [221], which is given by

$$F_2(\boldsymbol{\sigma},\kappa_3) = C_{nn}\cdot\sigma^2 + C_{ss}\cdot\tau^2 + C_n\cdot\sigma - \bar{\sigma}^2_{comp}(\kappa_3) \tag{4.10}$$

where C_{nn} and C_n are parameters that control the coordinates of the center of the compression cap failure surface, C_{ss} is a parameter that controls the width of the cap failure surface in the shear stress axis, and $\bar{\sigma}^2_{comp}(\kappa_3)$ is the compressive yield stress, which determines the width of the cap failure surface in the compressive stress axis. In the present study, the center of the cap failure surface is assumed to coincide with the origin of the $\sigma-\tau$ plane with $C_{nn}=1$ and $C_n=0$, in order to avoid the activation of this surface in the tension-shear region, which is controlled by the tension-shear failure criterion described in the previous subsection. A strain hardening/softening hypothesis is introduced for the compressive yield stress, which describes the rate of the corresponding scalar softening parameter as

$$\dot{\kappa}_3 = \sqrt{\left(\dot{u}_n^p\right)^2 + \left(\dot{u}_s^p\right)^2 + \left(\dot{u}_t^p\right)^2} \tag{4.11}$$

and the compressive yield stress is defined as

$$\bar{\sigma}_{comp}(\kappa_3) = \begin{cases} \bar{\sigma}_0 + \left(\bar{\sigma}_p - \bar{\sigma}_0\right)\cdot\left(\dfrac{2\kappa_3}{\kappa_p} - \dfrac{\kappa_3^2}{\kappa_p^2}\right) & \text{if } \kappa_3 \le \kappa_p \\ \bar{\sigma}_p + \left(\bar{\sigma}_m - \bar{\sigma}_p\right)\cdot\left(\dfrac{\kappa_3 - \kappa_p}{\kappa_m - \kappa_p}\right)^2 & \text{if } \kappa_p < \kappa_3 \le \kappa_m \\ \bar{\sigma}_r + \left(\bar{\sigma}_m - \bar{\sigma}_r\right)\cdot\exp\left(m\cdot\dfrac{\kappa_3 - \kappa_m}{\bar{\sigma}_m - \bar{\sigma}_r}\right) & \text{if } \kappa_3 > \kappa_m \end{cases} \tag{4.12}$$

where $m = 2(\bar{\sigma}_m - \bar{\sigma}_p)/(\kappa_m - \kappa_p)$; $\bar{\sigma}_0$, $\bar{\sigma}_p$, $\bar{\sigma}_m$, and $\bar{\sigma}_r$ are initial (i.e., corresponding to the transition from linear to nonlinear behavior), peak, intermediate (i.e., corresponding to the inflection point in the softening branch), and residual compressive yield stress, respectively; and κ_p and κ_m denote the total plastic strain at peak and intermediate compressive yield stress. **Figure 4.2** illustrates the evolution of the compressive yield stress, $\bar{\sigma}_{comp}$, as a function of the parameter κ_3. In Eq. (4.12), the first branch was taken from Lotfi and Shing [222], whereas the second and third branches were taken from Lourenço [180]. An associative flow rule is assumed for the compression cap failure criterion, thus, $Q_2(\boldsymbol{\sigma}, \kappa_3) = F_2(\boldsymbol{\sigma}, \kappa_3)$.

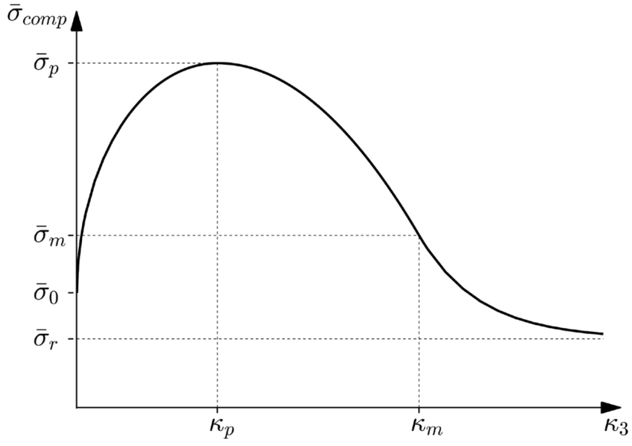

Figure 4.2. Hardening/softening law for compression cap failure criterion.

The CTSIM has been implemented in the commercial finite element software package ABAQUS [223] through an user-defined material subroutine (UMAT) written in FORTRAN [224] for an implicit integration scheme [225]. The implicit backward Euler integration method [220] is used to integrate the different constitutive equations of the CTSIM, which leads to a system of nonlinear algebraic equations. These nonlinear equations are solved monolithically with the local/global Newton-Raphson technique as described in Ottosen and Ristinmaa [226], Caballero et al. [216], and Macorini and Izzuddin [184] which leads to a combined local and global solution strategy. In addition, the CTSIM is combined with an adaptive sub-stepping strategy to ensure convergence and accuracy of the final solution at both local and global levels [184,216,227].

4.4. Comparison of constitutive models using one-element test

In this section, the robustness, computational cost, and accuracy of the CTSIM are compared with three interface element's constitutive models that are available in the literature, namely the constitutive models proposed by Lourenco and Rots [197], Macorini and Izzuddin [184] and Citto [204]. **Figure 4.3** shows the typical failure surfaces corresponding to each of these constitutive models and compares them with the failure surface corresponding to the CTSIM.

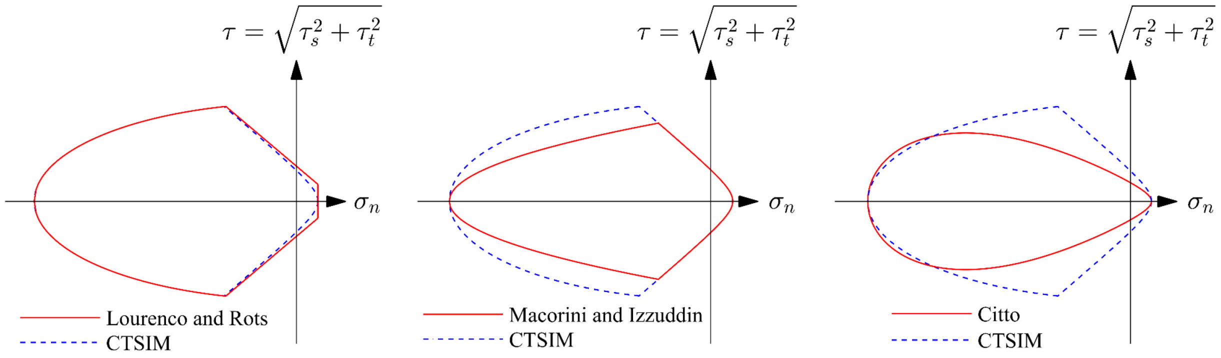

(a) (b) (c)

Figure 4.3. Typical failure surface in stress space for: (a) Lourenco's model, (b) Macorini's model, and (c) Citto's model.

These failure surfaces are plotted using the following values of the material parameters: $C = 0.35$ MPa, $\bar{\sigma}_{f_t} = 0.25$ MPa, $\bar{\sigma}_{comp} = 3.50$ MPa, and $\tan\phi = 0.65$. The Lourenco's model consists of three failure surfaces, as previously described in the section 4.1 (i.e. in the Introduction of this chapter). The Macorini's model is defined by two hyperbolic failure surfaces (failure criteria), i.e., a tension-shear failure surface that represents Mode-I and Mode-II fracture, and a compression failure surface. Both failure surfaces shrink when the plastic work (which drives the softening of the material parameters) increases. The Citto's model is comprised of a single failure surface (failure criteria), which represents all three failure mechanisms of the interface element, i.e., Mode-I, Mode-II, and compression failure. The evolution of the hardening parameters is governed by a set of work hardening/softening rules and the rate of plastic work [204]. It is also observed that the CTSIM and Lourenco's model use the hypothesis of strain hardening for the evolution of the hardening/softening parameters, whereas, the Macorini's and Citto's models use the hypothesis of work hardening. All these constitutive models were also implemented in the FE software ABAQUS [223] by using a UMAT subroutine, similar to the implementation of the CTSIM, in order to provide a common platform for the comparison of these models with the CTSIM by removing the bias that could arise from the usage of different integration schemes.

4.4.1. *One-element test*

In the following section, the performance of the different models is assessed through a one-element test. A single zero-thickness interface element is subjected to thirteen different load paths defined by the angle $\theta = \arctan\left(u_\tau / u_n\right)$, where $u_\tau = \sqrt{u_s^2 + u_t^2}$ (as shown in **Figure 4.4**), i.e., by considering a proportional increase of axial and shear relative displacements corresponding to θ = 0°, 15°, 30°, 45°, 60°, 75°, 90°, 105°, 120°, 135°, 150°, 165°, and 180°. The relative displacement magnitude was incremented from $|\boldsymbol{u}| = 0$ mm to $|\boldsymbol{u}| = 0.2$ mm using a displacement control analysis. Four different load step sizes were considered by dividing the final relative displacements into 5, 10, 50, and 100 equal increments (designated as N5, N10, N50, and N100 respectively). The material parameters corresponding to the masonry joint and potential cracks of a shear wall described in Vermeltfoort and Raijmakers [228] and Raijmakers and Vermeltfoort [229] and given in **Table 4.1** were used in these one-element tests. In addition, an elastic modulus $E_b = 16700$ MPa and a Poisson ratio $\nu_b = 0.15$ are used for the masonry units.

Table 4.1. Inelastic properties for joints and potential cracks.

Properties		Joints	Potential cracks
k_n	(N/mm^3)	82.00	16700
k_s	(N/mm^3)	36.00	7260
f_t	(MPa)	0.250	2.0
C_0	(MPa)	0.362	2.9
C_{Q0}	(MPa)	18.125	2.9
$\tan\phi_0$	(-)	0.75	0.75
$\tan\phi_r$	(-)	0.75	0.75
$\tan\psi_0$	(-)	0.001	0.001
$\tan\psi_r$	(-)	0.0001	0.0001
G_f^I	(N/mm)	0.018	0.008
G_f^{II}	(N/mm)	0.125	0.050
$\bar{\sigma}_0$	(MPa)	3.5	-
$\bar{\sigma}_p$	(MPa)	10.5	-
$\bar{\sigma}_m$	(MPa)	5.25	-
$\bar{\sigma}_r$	(MPa)	1.5	-
κ_p	(-)	0.09	-
κ_m	(-)	0.49	-
C_{ss}	(-)	9.0	-

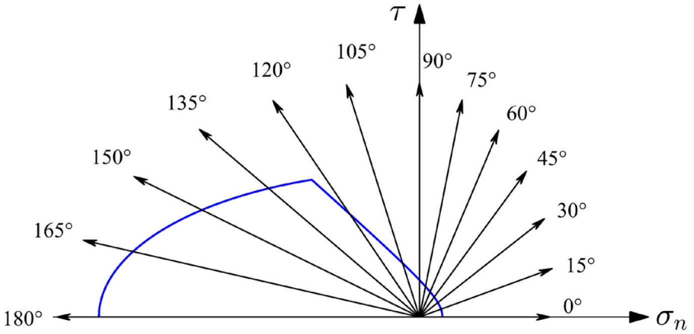

Figure 4.4. Load paths used in the one-element test of the different constitutive models.

The adaptive sub-stepping algorithm was not activated in any of the considered constitutive models during these analyses to ensure a consistent (i.e., fixed) load step size for all constitutive models during each set of analyses. A total of 52 finite element response simulations (corresponding to 13 load paths each with four load step sizes) were carried out for each constitutive model, and these simulations were performed in ABAQUS [223] with one CPU on a computer having an Intel(R) Core(TM) i5-2400S CPU @ 2.50 GHz processor and 12.0 GB RAM.

For determining the accuracy of the constitutive models, a base load step size corresponding to 1,000 relative displacement increments (i.e., N1000 with $|\Delta \boldsymbol{u}| = 2\times10^{-4}$ mm) is used to compare the results of the one-element tests. This load step size is considered sufficiently small to serve as an accurate reference solution for estimating the percentage error, δ, which is evaluated through the expression [230]:

$$\delta = \frac{\sqrt{\left(\boldsymbol{\sigma}_n - \boldsymbol{\sigma}_{exact}\right)^T \cdot \left(\boldsymbol{\sigma}_n - \boldsymbol{\sigma}_{exact}\right)}}{\sqrt{\boldsymbol{\sigma}_{exact}^T \cdot \boldsymbol{\sigma}_{exact}}} \times 100 \tag{4.13}$$

in which $\boldsymbol{\sigma}_n$ denotes the numerical traction response of the single interface element obtained by using different relative displacement increments, and $\boldsymbol{\sigma}_{exact}$ denotes the reference solution of the traction response corresponding to the same constitutive model used to evaluate $\boldsymbol{\sigma}_n$ with 1000 relative displacement increments (i.e., for N1000 load step sizes). The CPU time ratio (CTR) of the simulations for the different constitutive models with respect to the CPU time of the reference solution obtained using the CTSIM for each load path is also calculated. The results in terms of CTR and δ for the different constitutive models are reported in **Table 4.2** and **Table 4.3** for the tension-shear region (load paths θ = 0°, 15°, 30°, 45°, 60°, 75°, 90°) and compression-shear region (load paths θ = 105°, 120°, 135°, 150°, 165°, and 180°), respectively. Simulation results having percentage errors δ higher than 5% are identified by underlines in these tables. Some simulations did not converge to a solution for large (fixed) load step sizes and are identified by a hyphen. As expected, the presented results indicate that the δ increase for decreasing CTR along all load paths for all constitutive models.

4.4.2. *Tension-shear region*

In the tension-shear region, nine simulations (out of 28 simulations) did not converge for both Macorini's and Citto's models, whereas all simulations for the CTSIM and Lourenco's model reached convergence for all load step sizes. Among the converged simulations, 27 simulations converged with less than 5% errors for the CTSIM (i.e., only one simulation had δ larger than 5%), 25 simulations converged with less than 5% errors for the Lourenco's model (i.e., three simulations had δ larger than 5%), 17 simulations converged with less than 5% errors for the Macorini's model (i.e., two simulations had δ larger than 5% in addition to the nine simulations that did not converge), and 13 simulations converged with less than 5% errors for the Citto's model (i.e., six simulations had δ larger than 5% in addition to the nine simulations that did not converge). Considering only the converged cases, the CPU time used by the simulation based on the CTSIM is less than or equal to the CPU time corresponding to the Lourenco's, Macorini's, and Citto's models in 25 (out of 28), 17 (out of 19), and 12 (out of 19) simulations, respectively.

The results presented in **Table 4.2** for the tension-shear region indicate that the CTSIM is: (1) computationally robust for all load step sizes except for case N5 of load path $\delta = 90^{\circ}$, (2) generally more accurate and computationally robust than the other three constitutive models considered here, and (3) computationally efficient, since for all considered load paths it can provide accurate results with load step sizes that are larger than or equal to those needed for any other constitutive models. In order to understand better the mechanical differences among the different models, iso-error maps [230–232] were developed for all four constitutive models at the point on the yield surfaces corresponding to load path δ = 36.13° (see **Figure 4.5**). This point was selected as representative of the tension-shear region because it corresponds to the singularity point between the Rankine and Mohr-Coulomb failure criteria in the Lourenco's model and, thus, can be used to illustrate the advantages of using a single surface failure criterion by eliminating the singularity in the tension-shear region. The iso-error maps plot the error defined in Eq. (4.13) as a function of the normalized increment of relative displacement in the axial direction, u_n, and in the shear direction, u_τ. The normalization parameter for each of these relative displacement increments corresponds to the elastic relative displacement associated with the initial yielding in each of the two directions, respectively. **Figure 4.5(a)** through **Figure 4.5(d)** plot the iso-error maps for the CTSIM, Lourenco's, Macorini's, and Citto's models, respectively. The inset in each subfigure shows the location on the corresponding yield surface of the point selected as the origin of the iso-error map. The shaded region in each subfigure indicates the combinations of relative displacement increments for which the corresponding model cannot achieve convergence. It is observed that, within the range of normalized relative displacement increments considered here, the CTSIM is the only model that can always achieve convergence. The Lourenco's model does not converge within a region that corresponds approximately to $\Delta u_n / u_{ny} \geq 1$ and $\Delta u_\tau / u_{\tau y} \geq \Delta u_n / u_{ny}$. This result was first qualitatively observed in Lourenço and Rots [203] and is due both to the presence of a singularity in the yield surface and to the heuristic (i.e., trial-and-error) approach adopted in the Lourenco's model to identify the active yield surface(s), which cannot guarantee convergence of the analysis for large load step sizes [203]. The Macorini's and Citto's models also present a region of non-convergence, corresponding approximately to $\Delta u_n / u_{ny} \geq 2$ and $\Delta u_n / u_{ny} \geq 3$, respectively.

Table 4.2. CPU time ratio (CTR) vs percentage error (δ) for tension-shear region.

		CTSIM		Lourenco's model		Macorini's model		Citto's model	
θ	N	CTR	δ	CTR	δ	CTR	δ	CTR	δ
0	N100	0.093	<0.01	0.106	<0.01	0.106	2.62	0.087	96.45
	N50	0.050	<0.01	0.050	<0.01	0.050	5.58	0.043	>100
	N10	0.012	<0.01	0.012	<0.01	-	-	-	-
	N5	0.006	<0.01	0.006	<0.01	-	-	-	-
15	N100	0.099	<0.01	0.106	<0.01	0.113	2.26	0.134	1.67
	N50	0.042	<0.01	0.049	<0.01	0.049	4.81	0.056	>100
	N10	0.014	<0.01	0.021	<0.01	-	-	-	-
	N5	0.007	<0.01	0.007	0.02	-	-	-	-
30	N100	0.101	<0.01	0.101	<0.01	0.109	1.60	0.116	1.44
	N50	0.058	<0.01	0.051	<0.01	0.051	3.40	0.051	>100
	N10	0.014	<0.01	0.014	0.03	-	-	-	-
	N5	0.007	<0.01	0.007	0.04	-	-	-	-
45	N100	0.093	<0.01	0.099	<0.01	0.105	0.92	0.099	1.09
	N50	0.049	<0.01	0.062	<0.01	0.049	1.94	0.049	2.30
	N10	0.019	<0.01	0.019	<0.01	-	-	-	-
	N5	0.006	<0.01	0.006	67.70	-	-	-	-
60	N100	0.096	<0.01	0.110	<0.01	0.103	0.03	0.103	0.68
	N50	0.062	<0.01	0.062	<0.01	0.055	0.08	0.055	1.42
	N10	0.014	<0.01	0.021	<0.01	0.021	1.28	0.014	>100
	N5	0.007	<0.01	0.007	>100	-	-	-	-
75	N100	0.097	<0.01	0.090	<0.01	0.111	0.10	0.097	0.29
	N50	0.056	<0.01	0.049	<0.01	0.056	0.21	0.049	0.61
	N10	0.014	<0.01	0.014	<0.01	0.014	1.67	0.014	4.04
	N5	0.007	0.03	0.007	37.87	0.007	1.83	0.007	10.16
90	N100	0.097	0.42	0.103	0.02	0.109	0.35	0.085	0.22
	N50	0.048	0.87	0.048	0.04	0.055	0.72	0.042	0.46
	N10	0.012	3.42	0.012	0.33	0.018	3.50	0.018	2.60
	N5	0.006	5.90	0.006	1.46	0.012	8.37	0.006	4.58

This non-convergence region for these two models is due to the presence of a non-physically meaningful branch of the yield surface having a quadratic functional form, as previously discussed. In particular, the convergence of these models is impaired as soon as the imposed relative displacement increment intercepts the non-physically meaningful branch of the corresponding yield surface. It is observed that, when the models converge, the magnitude of the errors is smallest for the Lourenco's model (i.e., less than 0.01%), followed by the CTSIM (i.e., less than or equal to approximately 2%), and then by the Macorini's and Citto's models (i.e., less than 10%). These error's magnitudes increase with the complexity of the functional form used for the corresponding yield surfaces (i.e., the Lourenco's model is represented by linear yield functions, which correspond to the simplest functional form and the smallest percentage errors). The errors also depend on the hardening/softening hypothesis used in each model (i.e., the Macorini's and Citto's models use a work hardening/softening hypothesis, which negatively affects the accuracy of their solutions when compared with the results obtained using the CTSIM and Lourenco's model, which adopt a strain hardening/softening hypothesis). Finally, it is also observed that the percentage error for all models is more sensitive to the size of the relative displacement increments in the axial direction than to that of the relative displacement increments in the shear direction. Based on these results, it is concluded that the CTSIM provides the best compromise between accuracy and robustness in the tension-shear region among all models considered in this study.

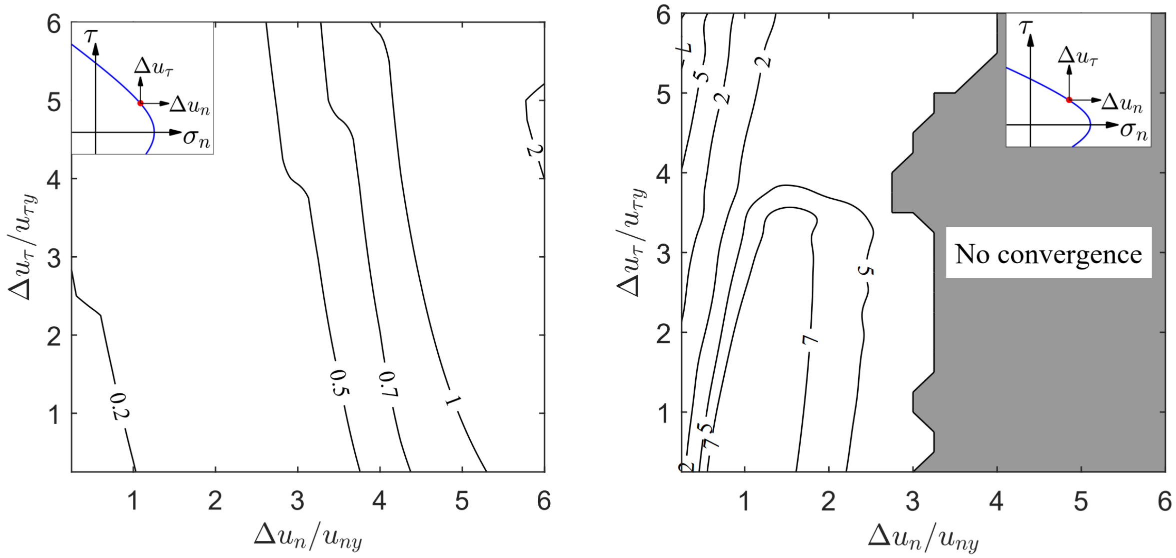

(a) (b)

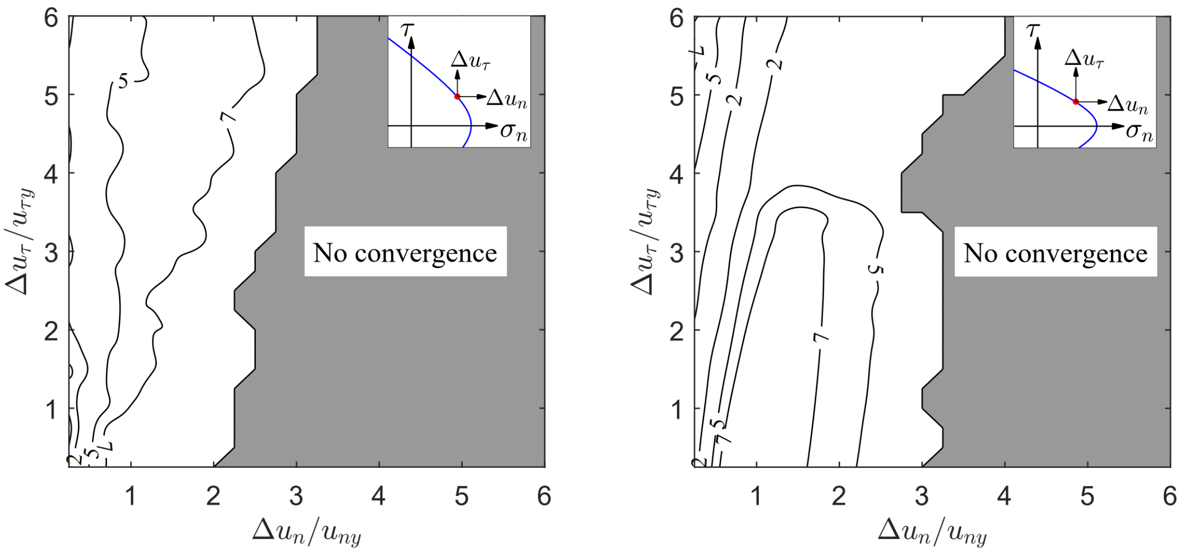

(c) (d)

Figure 4.5. Iso-error maps for the point on the yield surfaces at θ = 36.13°: (a) CTSIM, (b) Lourenco's model, (c) Macorini's model, and (d) Citto's model.

4.4.3. *Compression-shear region*

In the compression-shear region, two simulations (out of 24 simulations) did not converge for both Macorini's and Citto's models, whereas all simulations for the CTSIM and Lourenco's model reached convergence. Among the converged simulations, 19 simulations converged with less than 5% errors for the CTSIM and Lourenco's model (i.e., five simulations had δ larger than 5%), 18 simulations converged with less than 5% errors for the Macorini's model (i.e., four simulations had δ larger than 5% in addition to the two simulations that did not converge), and 12 simulations converged with less than 5% errors for the Citto's model (i.e., nine simulations had δ larger than 5% in addition to the three simulations that did not converge). Considering only the converged cases, the CPU time used by the simulation based on the CTSIM is less than or equal to the CPU time corresponding to the Lourenco's, Macorini's, and Citto's models in 21 (out of 24), 16 (out of 22), and 18 (out of 22).

Table 4.3. CPU time ratio (CTR) vs percentage error (δ) for compression-shear region.

	N	CTSIM		Lourenco’s model		Macorini’s model		Citto’s model	
θ		CTR	δ	CTR	δ	CTR	δ	CTR	δ
105	N100	0.105	0.02	0.105	0.01	0.112	0.03	0.112	0.12
	N50	0.049	0.05	0.056	0.02	0.042	0.31	0.042	0.29
	N10	0.014	0.39	0.014	0.33	0.014	3.53	0.014	1.09
	N5	0.007	0.76	0.007	0.45	0.007	10.39	0.007	1.72
120	N100	0.101	0.06	0.109	0.06	0.109	0.05	0.109	6.19
	N50	0.051	0.12	0.065	0.13	0.051	0.11	0.051	7.19
	N10	0.014	1.17	0.014	1.31	0.014	3.16	0.014	10.60
	N5	0.007	49.53	0.007	54.68	0.007	73.19	0.007	>100
135	N100	0.102	0.07	0.102	0.08	0.102	0.11	0.109	0.57
	N50	0.054	0.14	0.048	0.16	0.048	0.24	0.051	1.23
	N10	0.014	1.32	0.014	1.54	0.014	0.60	0.014	57.20
	N5	0.007	35.45	0.007	35.56	0.007	52.46	0.007	>100
150	N100	0.094	0.05	0.101	0.07	0.081	0.12	0.107	0.65
	N50	0.054	0.11	0.054	0.14	0.047	0.24	0.040	1.34
	N10	0.013	1.03	0.013	1.26	0.013	2.24	0.013	98.96
	N5	0.007	49.10	0.007	48.81	-	-	-	-
165	N100	0.104	0.02	0.090	0.03	0.097	0.02	0.111	0.14
	N50	0.056	0.05	0.042	0.06	0.049	0.05	0.049	0.20
	N10	0.014	0.81	0.014	0.57	0.014	0.32	0.021	11.19
	N5	0.007	55.63	0.007	54.73	0.007	61.02	-	-
180	N100	0.097	<0.01	0.097	<0.01	0.103	0.01	0.097	1.18
	N50	0.055	<0.01	0.055	<0.01	0.055	0.02	0.055	2.10
	N10	0.014	<0.01	0.014	<0.01	0.014	0.22	0.014	13.43
	N5	0.007	59.35	0.007	57.99	-	-	-	-

The results presented in **Table 4.3** indicate that the performance of CTSIM in the compression-shear region is practically identical to that of the Lourenco's model since both models use the same compression cap model for representing the compression failure. These models are: (1) computationally robust for all load step sizes except for the N5 (load paths θ = 120º, 135º, 150º, 165º, and 180º) and N10 (load paths θ = 150º and 165º); (2) more accurate and computationally robust than the Macorini’s, and Citto’s models; and (3) computationally efficient, since both models provide accurate results with load step sizes that are larger than or equal to those for the Macorini’s and Citto’s models.

4.4.4. *Discussion of one-element test results*

The different performance of the constitutive models considered here can be more easily interpreted by analyzing the properties of the integration algorithm (i.e., the elastic predictor-plastic corrector strategy with local/global Newton-Raphson integration) and its interaction with the constitutive models' equations. During the plastic-corrector step, different sets of equations are solved in the different constitutive models depending upon which failure surface(s) is(are) violated, leading to different sizes of the Jacobian matrix that needs to be inverted. The size of this Jacobian matrix and the complexity of each Jacobian component both contribute towards the computational cost and accuracy of the different constitutive models in the different regions (i.e., tension, shear, and compression cap regions). For the CTSIM, three different cases can be encountered during the plastic-corrector step: (1) violation of the tension-shear failure surface, which involves a 6×6 Jacobian matrix (see Eq. **(E.1)** in Appendix E); (2) violation of the compression cap failure surface, which involves a 5×5 Jacobian matrix (see Eq. **(E.2)** in Appendix E); and (3) violation of both failure surfaces, which involves an 8×8 Jacobian matrix (see Eq. **(E.3)** in Appendix E). **Figure 4.6** illustrates the size of the Jacobian matrix used in the different regions of the different constitutive models.

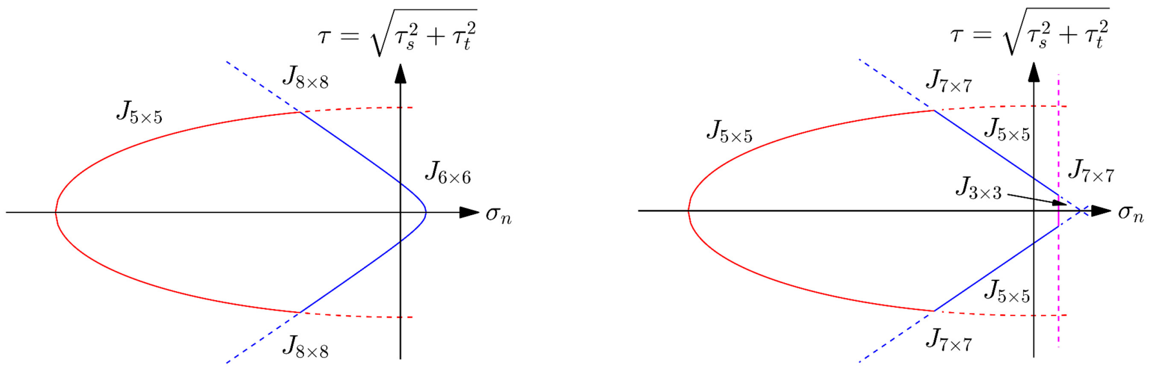

(a) (b)

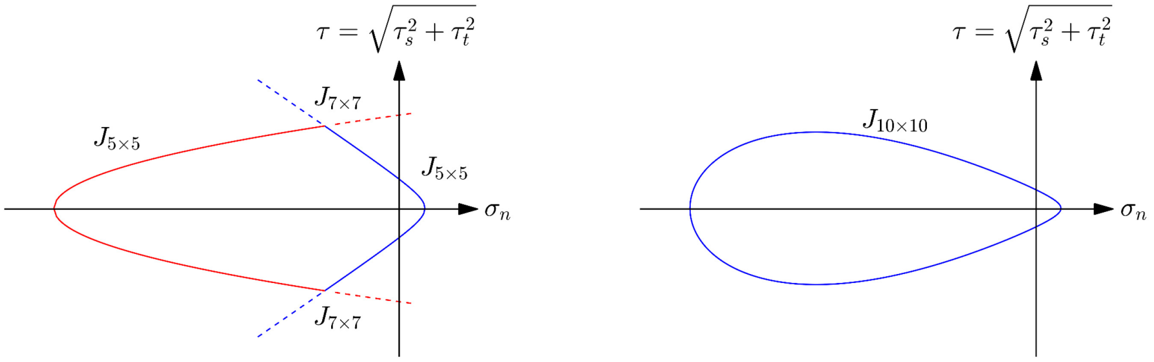

(c) (d)

Figure 4.6. Size of the Jacobian matrix for different regions of the constitutive models: (a) CTSIM, (b) Lourenco's model, (c) Macorini's model, and (d) Citto's model.

The CTSIM is at least as efficient as the Lourenco's model along load paths θ = 0º, 15º, 30º, 45º, and 60º. In this region, the return mapping algorithm for the Lourenco's model requires inverting a 3×3, 5×5, and/or 7×7 Jacobian matrix, depending on which failure surface(s) is(are) violated, whereas the the CTSIM requires the inversion of a 6×6 Jacobian matrix. However, the Jacobian matrix for the Lourenco's model mainly assumes a 7×7 dimension because, in most of the cases, both the Rankine and the Mohr-Coulomb failure surfaces are simultaneously violated, generally for large load steps or even for small load steps after the failure surfaces have experienced softening of their scalar parameters. The accuracy of the results obtained using the Lourenco's model is very similar or slightly lower than the accuracy of the CTSIM's results for load paths 15º, 30º, 45º, and 60º since the Lourenco's model requires the solution of a multi-surface plasticity problem (with a singularity located along the load path θ = 33.02º for the specific problem considered in this study), whereas the CTSIM uses a single surface in the same region. For load paths θ = 75º and 90º, the Lourenco's model is slightly more efficient than the CTSIM because the Jacobian matrix has dimensions 5×5 for the Lourenco's model and 6×6 for the CTSIM. However, the CTSIM is consistently more accurate than the Lourenco's model along these load paths, particularly for large load step sizes. In the shear-tension region, the Macorini's and the Citto's models are very similar, because they use the same equation to define the failure surface and the hypothesis of work hardening. When compared to the CTSIM, the Macorini's and Citto's model perform poorly for load paths with small angles, i.e., $\theta \leq 60^{\circ}$. These two models perform better for load paths $\theta = 75^{\circ}$ and 90º, and Citto's model is the most efficient and accurate model for $\theta = 90^{\circ}$.

In the compression-shear region, both the CTSIM and Lourenco's model have a similar efficient and accurate behavior, with the exception of cases corresponding to large load step sizes. This is due to the fact that in this region the two models use the same failure criteria. In the compression-shear region, the Macorini's and Citto's model are very different from each other and from the other constitutive models. In general, the Macorini's model is generally more efficient than the CTSIM and Lourenco's model for small load step sizes but is less accurate (or lacks convergence) for large load step sizes. The Citto's model generally performs poorly, both in terms of efficiency and accuracy. The efficiency of the Macorini's model for small load step sizes can be attributed to its evolution model for the compressive yield stress, which assumes a linear behavior up to the peak compressive yield stress, after which softening of the compressive yield stress takes place [184]. By contrast, the CTSIM and Lourenco's model assume a linear behavior only up to an initial compressive yield stress that is significantly lower than the peak compressive yield stress (e.g., approximately 1/3 of it for quasi-brittle materials [205]), which is followed by hardening till the peak compressive yield stress and by softening afterward (see **Figure 4.2** and Eq (4.12)). In addition, it appears that the lower accuracy of the Macorini's and Citto's models may be related to their use of the work hardening hypothesis, in contrast with the CTSIM and Lourenco's model that use the hypothesis of strain hardening. In particular, for the specific problem considered in this chapter of interface element's constitutive models for masonry analysis based on the SMM approach, the hypothesis of strain hardening/softening appears to improve the robustness of the numerical response for yield surfaces that evolve for increasing plastic deformation, as assumed by the softening plasticity framework adopted in this study.

4.5. Constitutive model comparison using masonry shear wall experimental data

The performance of the proposed CTSIM is compared with the other constitutive models considered in this study through the numerical response analysis of an unreinforced masonry shear wall for which experimental data are available in Vermeltfoort and Raijmakers [228] and Raijmakers and Vermeltfoort [229]. The numerical analyses were performed for all constitutive models using the FE software ABAQUS [223]. The masonry shear wall consisted of a pier with a width to height ratio approximately equal to one, i.e., with dimensions 990 mm × 1000 mm, as shown in **Figure 4.7(a)**.

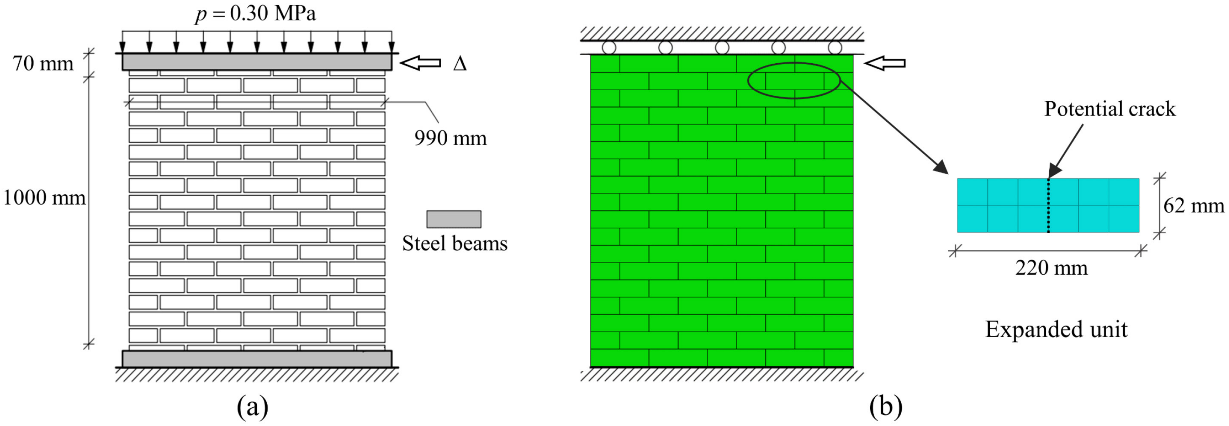

Figure 4.7. Masonry shear walls: (a) shear walls, and (b) SMM used for simulating the shear wall.

The wall was built using wire cut solid clay blocks of dimensions 210 mm × 52 mm × 100 mm and mortar layers of thickness equal to 10 mm, and consisted of 18 courses of blocks, two of which (the bottom and top ones) were clamped to steel beams that were used to transfer the lateral load to the system, as shown in **Figure 4.7(a)**. The mortar was prepared with one part of cement, two parts of lime, and nine parts of sand. The experimental test involved a uniformly distributed normal pressure $\left(p = 0.30 \text{ MPa}\right)$, followed by a monotonically increasing horizontal loading phase, in which a horizontal displacement Δ was applied quasi-statically to the top of the wall through a steel beam while keeping the bottom boundary fixed horizontally. The material properties of blocks and mortar were obtained from experimental results of tension, shear, and compression tests reported in the literature Vermeltfoort and Raijmakers [228] and Raijmakers and Vermeltfoort [229] and are the same as those reported in **Table 4.1**. In addition, an elastic modulus E_b = 16700 MPa and a Poisson ratio ν_b = 0.15 are used for the masonry units.

4.6. Definition of FE models for unreinforced masonry shear wall

The SMM approach with elastic masonry units and non-linear joints was adopted here for the FE modeling of the unreinforced masonry shear wall described above. Plane stress conditions were assumed, and geometric non-linearity (i.e., large strains and large displacements [223] was also included in the simulation of the FE models. The FE model consisted of a set of elastic masonry units bonded by potential crack, potential slip, and crushing planes at joints, see **Figure 4.7(b)**. For modelling cracking of the masonry units, a potential crack was placed vertically in the middle of each unit as shown in **Figure 4.7(b)**. All the degrees of freedoms are restrained at the bottom of the FE model, and a monotonically increasing horizontal displacement is applied on the side of the top course of the FE model while keeping the top edge of the FE model vertically fixed. A general procedure for static loading based on an incremental-iterative globally-convergent Newton-Raphson method with the line search technique was used in ABAQUS [223] for solving the nonlinear system of equilibrium equations for the different FE models [223]. In addition, an automatic load step increment technique was adopted for efficient and robust simulation of the response of the different FE models with initial, minimum, and maximum normalized increment sizes equal to 1×10^{-4}, 1×10^{-9}, 5×10^{-4}, respectively.

In the FE models of the masonry shear wall, the masonry units were modeled using a 4-node bilinear plane stress quadrilateral element with reduced integration and hourglass control (CPS4R element [223]), and the joints and potential cracks were modeled by using a 4-node two-dimensional cohesive element (COH2D4 element [223]). A mesh sensitivity analysis of the FE Model was performed to ensure a good compromise between accuracy and computational costs for all the constitutive models. The mesh used in this study consisted of six interface elements employed for each bed joints (i.e., three interface elements for the bed joint of each half masonry unit), two interface elements employed for each head joint and for potential vertical cracks, and six CPS4R elements for each half masonry unit. One FE model was built for each of the constitutive models considered in this study, i.e., CTSIM, Lourenco's, Macorini's, and Citto's models. The adaptive sub-stepping algorithm was activated for all considered constitutive models to achieve maximum computational efficiency in all FE analyses. It should be noted here that the behavior of the potential vertical cracks did not include the compression failure mechanism. Thus, the compression failure surface of the CTSIM, Lourenco's model, and Macorini's model was deactivated for the interface element of potential vertical cracks, and a high 'dummy' value in the Citto's model was used for the compressive yield stress to avoid activation of the failure surface in the compression region of this constitutive model.

4.6.1. *Comparison of FE responses and experimental data*

The comparison of the experimental load-displacement curves with their numerical counterparts for all constitutive models is shown in **Figure 4.8**. The FE response results obtained using any of the interface element's constitutive models considered in this study are in very good agreement with the experimental behavior, with a ratio of the numerically simulated peak load over the average experimental peak load equal to 1.04, 1.01, 1.10, and 0.98 for the CTSIM, Lourenco's, Macorini's, and Citto's models, respectively.

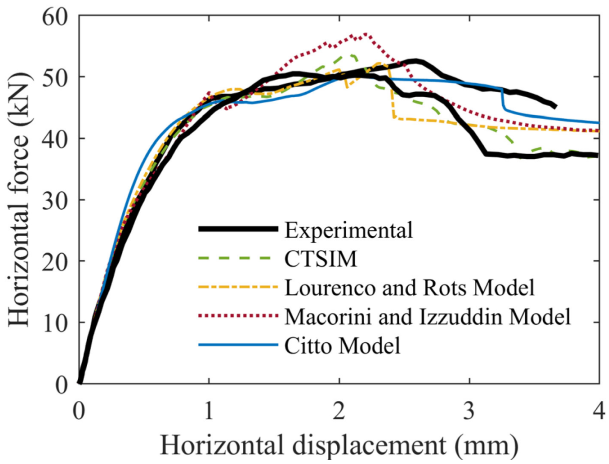

Figure 4.8. Comparison of experimental and numerical results in terms of load-displacement response of the shear wall.

The deformed shape and the minimum principal stress distribution (corresponding to the maximum compressive stress) at an applied top horizontal displacement $\Delta = 4\ mm$ (i.e., the maximum displacement recorded in the experimental tests) of the FE analyses using different constitutive models are presented in **Figure 4.9**. For the sake of visualization, the interface elements are represented by white empty spaces in this figure so that highly plasticized interface elements appear as openings between masonry units. The stress distributions of the shear wall FE models corresponding to the different constitutive models were very similar. In addition, the crack patterns were also similar to those observed experimentally for all FE models, except for that corresponding to the Citto’s model.

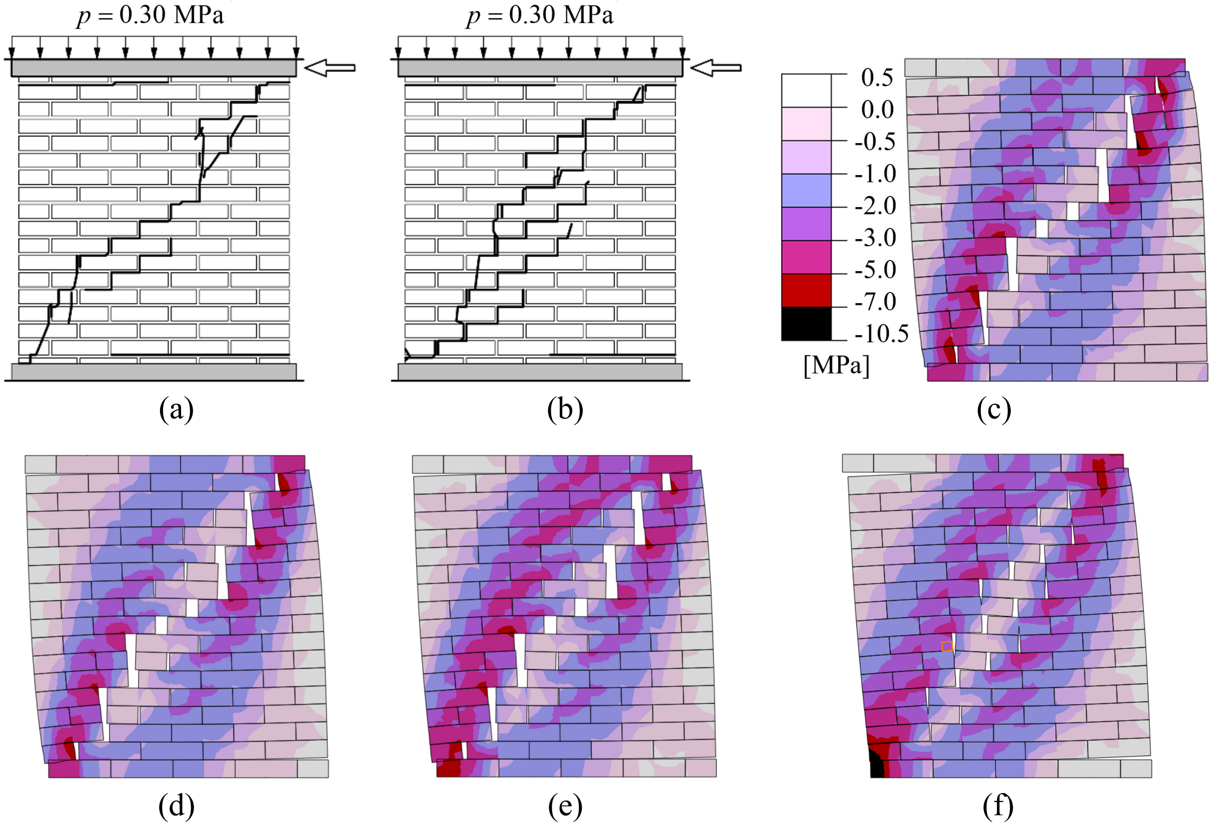

Figure 4.9. Comparison of experimental and numerical results: (a) and (b) experimental crack patterns for the two specimens; and deformed shaped and distribution of minimum principal stress for (c) CTSIM, (d) Lourenco’s model, (e) Macorini’s model, and (f) Citto’s model.

During the application of the monotonically increasing horizontal load, horizontal tensile cracks developed at the bottom and top of the wall, particularly in the bed joint at an early loading stage, followed by the formation of a diagonal stepped crack due to a combined tension-shear failure of the joints. For large horizontal load levels, the diagonal stepped crack was followed by crushing of the toes of the masonry and tensile cracking within the masonry units, leading to the overall failure of the masonry wall. The cracking of the masonry units is significant for all constitutive models except for the Citto’s model, in which the behavior of the potential vertical crack within a unit is more ductile than for the other constitutive models, leading to smaller crack's openings. This behavior is due to the use of a high 'dummy' value for the compressive yield stress of cracks within the masonry units, which is required to avoid the activation of the compressive failure surface in the Citto's model. In fact, while for the CTSIM, Lourenco's, and Macorini's models the compressive failure surface is independent of the tension-shear behavior, a change of the compressive yield stress in the Citto's model also affects the shape of the failure surface in the tension-shear region. This shape change deteriorates the capability of the Citto's model to simulate the brittle cracking of masonry units.

4.6.2. ***Assessment of computational cost***

The FE models corresponding to the different constitutive models were also compared in terms of computational cost. In particular, **Table 4.4** reports the number of increments, cutbacks (reduction of load/displacement increment size when the iterative global solution algorithm cannot converge within a specified number of iterations), and total iterations [223], as well as the CPU time ratios (CTR) corresponding to the FE analyses for each of the considered constitutive models. The CTRs were calculated with respect to the total CPU time corresponding to the FE analysis using the CTSIM, which was assumed as a reference with CTR = 1.00. The FE analysis based on the CTSIM took 9.53 hours of CPU time using an Intel(R) Core(TM) i5-2400S CPU @ 2.50 GHz processor and 12.0 GB RAM. It is noteworthy that the FE analysis using the CTSIM was found to be the least computationally expensive one among those considered in this study. The second most computationally efficient model was the Macorini's model with CTR = 1.22, followed by the Lourenco's model (CTR = 1.37) and the Citto's model (CTR = 1.48). Moreover, the CTSIM completed the simulation with the smallest numbers of increments, cutbacks, and total iterations. This result indicates that the CTSIM can allow FE simulation of the masonry shear wall with larger load steps than those corresponding to the other interface element's constitutive models, which explains the lower computational cost of the proposed constitutive model.

Table 4.4. Load increments and CPU time ratio for different constitutive models in the analysis of the benchmark masonry shear wall.

Item	CTSIM	Lourenco's model	Macorini's model	Citto's model
Increments	26,620	29,679	35,564	40,119
Cutback	6,796	7,861	9,538	11,137
Total iterations	106,567	114,378	136,680	170,495
CPU time ratio (CTR)	1.00	1.37	1.22	1.48

Table 4.5 reports the number of the local iterations corresponding to the different regions of constitutive models during the FE simulations of the benchmark masonry shear wall. It is observed that the CTSIM requires the least number of local iterations, i.e., 21.15 million, followed by the Macorini's (24.77 million), Lourenco's (27.68 million), and Citto's models (29.81 million). The FE simulation with the CTSIM requires 17.96 local iterations (out of 21.15 million) occurring in the tension and shear failure region, which corresponds to a 6×6 Jacobian matrix. For the Lourenco's model, 24.58 million local iterations (out of 27.68 million) occur in the failure region. These local iterations are associated with three different failure conditions, i.e.: (1) violation of the Rankine failure criterion that requires the inversion of a 3×3 Jacobian matrix (0.52 million iterations); (2) violation of the Mohr-Coulomb failure criterion that requires the inversion of a 5×5 Jacobian matrix (18.47 million iterations); and (3) violation of both failure criteria simultaneously (T-S corner), which requires the inversion of a 7×7 Jacobian matrix (5.59 million iterations). By contrast, Thus, by comparing the FE simulations with the CTSIM and the Lourenco's model, it is observed that the use of a smooth failure surface instead of the two different failure surfaces (the Rankine and Mohr-Coulomb failure surfaces) results in 6.62 million fewer local iterations. Even though the computational cost associated with each local iteration for the two constitutive models is different (generally lower for the Lourenco's model), the CTSIM results in lower CPU times

because of the significantly smaller number of iterations required. Therefore, it can be concluded that the use of smooth failure surface to describe the shear and tension failure region results in a more computationally efficient interface element's constitutive model. Furthermore, the FE simulation with the Macorini's model requires 24.42 million local iterations violating the tension and shear failure criterion, which is 6.46 million iterations more (approximately 35.97%) than the corresponding total local iterations for the CTSIM. In addition, the FE simulation with the Macorini's model required a comparatively higher number of global increments (approximately 33.60% higher) when compared with the CTSIM, as reported in **Table 4.4**. The higher number of local iteration and global increments may be since the Macorini's model requires smaller load step sizes to achieve the same accuracy of the CTSIM, as shown by the results reported for the one-element test.

Table 4.5. Number of iterations under different conditions for different models.

	CTSIM		Lourenco's model		Macorini's model		Citto's model	
Violation of failure criterion	Iteration (Millions)	%	Iteration (Millions)	%	Iteration (Millions)	%	Iteration (Millions)	%
Rankine	-	-	0.52	1.89	-	-	29.81	100
Mohr-Coulomb	-	-	18.47	66.74	-	-		
Tension-shear	17.96	82.60	-	-	24.42	98.58		
Compression cap	3. 01	16.58	2.93	10.58	0.32	1.31		
T-S corner*	-	-	5.59	20.19	-	-		
S-C corner**	0.18	0.82	0.17	0.60	0.03	0.11		
Total	**21.15**		**27.68**		**24.77**		**29.81**	

* Multi-surface singularity between Rankine and Mohr-Coulomb failure criterion

** Multi-surface singularity between Mohr-Coulomb or tension-shear and compression cap failure criterion

In the compression cap failure region, the FE simulations of the masonry shear wall with the CTSIM and Lourenco's model results in 3.19 million and 3.10 million local iterations, respectively, which require the inversion of a 5×5 Jacobian matrix. Thus, the Lourenco's model is slightly more efficient than the CTSIM in the compression cap failure region. The Macorini's model requires only 0.35 million local iterations that correspond to violating the compression failure surface. This difference in the number of local iterations when compared to the CTSIM and Lourenco's models is mainly due to the different assumptions for the evolution of the compressive yield stress and the different values for the initial compressive yield stress. In fact, these different assumptions result in the Macorini's model exhibiting linear elastic behavior for a much wider range of strains and stresses when compared to the CTSIM and Lourenco's model.

The FE simulation of the masonry shear wall with the Citto's model results in the largest number of local iterations, i.e., 26.81 million local iterations, compared to the other constitutive models. Thus, the Citto's model is the least efficient model among those considered in this study for simulating the response of this masonry shear wall. This result is due to: (1) the lower accuracy in normal and shear stress evaluations for a given load/displacement step size (as shown by the results reported for the one-element test); (2) the larger size of the Jacobian matrix (10×10) that needs to be inverted in the local iterations; (3) the more complex equation used for representation of the single failure surface. The comparison of the computational costs of the FE simulations corresponding to the different constitutive models considered in this study (i.e., the CTSIM, Lourenco's model, Macorini's model, and the Citto's model) indicate that the use of single failure surface for all failure modes decreases the overall computational efficiency of the interface element's constitutive model.

4.7. Conclusions

A new interface element's constitutive model, referred to as coupled tension-shear interface model (CTSIM), is proposed in this chapter for finite element (FE) analysis of masonry using the simplified micro-modeling approach. This new model is capable of simulating tension cracking, shear slipping, and compression failure and is defined by a convex composite failure surface consisting of a tension-shear failure criterion and a compression cap failure criterion. The constitutive model is implemented in the FE software ABAQUS through a user-defined material subroutine. The different constitutive equations of the CTSIM are integrated using the implicit backward Euler integration method, and the integrated equations are solved monolithically with the local/global Newton-Raphson technique, which leads to a combined local and global solution strategy. Moreover, the CTSIM is combined with an adaptive sub-stepping strategy to ensure convergence and accuracy of the final solution for larger load step sizes.

The performance of the CTSIM is assessed through a series of one-element tests and through the comparison of FE response simulation and experimental results for an unreinforced shear wall. Furthermore, the robustness, computational cost, and accuracy of the CTSIM are also compared with three constitutive models that are available in the literature, i.e., the Lourenco's, Macorini's and Citto's models. The comparison of one-element test's results shows that the CTSIM is at least as efficient as and generally more robust than the other constitutive models for varying load step sizes and load paths. The comparison of the FE results for the masonry shear wall indicates that the CTSIM is more efficient than and at least as accurate as the other constitutive models. Moreover, it is observed that: (1) the use of a single failure surface for mode-I and mode-II failure can improve the computational efficiency and robustness of the constitutive model when compared to constitutive models that use two separate failure surfaces; (2) the use of a single failure surface for all failure mechanisms has negative effects on the computational efficiency and robustness of the constitutive model when compared to constitutive models that use multi-surface criteria; and (3) constitutive models based on the hypothesis of strain hardening seem to be more efficient and robust than those based on the hypothesis of work hardening.

CHAPTER 5. LIMITATIONS OF EXISTING FINITE ELEMENT SIMPLIFIED MICRO-MODELING TECHNIQUES FOR UNREINFORCED MASONRY

5.1. Introduction

Over the last three decades, finite element (FE) simplified micro-modeling techniques have been commonly employed to investigate the local and global mechanical response of masonry structures [184,186,236,187,195,197,198,204,233–235]. Simplified micro-models (SMMs) have been used as a computationally efficient alternative to detailed micro-models, which require the FE discretization of all masonry constituents, i.e., masonry units (bricks or blocks), mortar layers, and unit-mortar interfaces, and have been used only for small masonry components due to their high computational cost [182,237–242]. In SMMs, the mortar joint and the two adjacent unit-mortar interfaces (referred to as masonry joints hereinafter) are lumped into zero-thickness interfaces (referred to as masonry joint interfaces hereinafter), which connect expanded masonry units (with dimensions equal to those of the masonry unit and half of the mortar thickness) [180]. The expanded masonry units are generally augmented with an additional zero-thickness interface (referred to as potential crack interface hereinafter), which is vertically placed in the middle of the expanded masonry units to model the potential crack that is often experimentally observed within the masonry units [180]. Based on the different constitutive models adopted for the expanded masonry units, three SMMs are commonly found in the literature, i.e., SMMs with rigid (referred to SMM-I hereinafter), elastic (referred to SMM-II hereinafter), and inelastic (referred to SMM-III hereinafter) constitutive models for the expanded masonry units.

Early uses of SMMs did not include potential-crack elements [182,243], which were introduced only later to better describe the experimental behavior of unreinforced masonry

[212,244]. Lourenço and Rots [197] proposed an SMM-II approach in which the response of the interface elements was described by a three-surface interface constitutive model based on softening plasticity. This constitutive model could simulate shear sliding, tensile cracking, and compressive crushing, and was later extended, based on plasticity theory, to simulate the cyclic response of masonry structures [198] in many different applications [91,183,199,200,245–248]. Macorini and Izzudin [184] proposed a three-dimensional two-surface interface constitutive model that used a co-rotational approach to account for geometric nonlinearity. This model has also been widely used for numerical modeling of masonry structures [213,215,249], and has been extended based on a damage-plasticity framework to simulate the cyclic behavior of masonry [201]. In addition, the chapter 4 of this dissertation proposed a new three-dimensional two-surface interface constitutive model with improved computational efficiency and robustness. Other SMM-II approaches available in literature are based on different interface constitutive models based on damage and friction [206,250–252], elasto-plasticity [186,187,204], damage-plasticity [201,209], softening fracture [189], and viscoplasticity [210]. More recently, SMM-I [183] and SMM-III approaches [185,253–255] have been developed to simulate the cyclic behavior of masonry systems. Bolhassani et al. [256] also used an SMM-III approach to model hollow and partially grouted concrete block masonry walls. The SMM-I was originally introduced to reduce the number of models' degrees-of-freedom and the corresponding computational time; however, subsequent developments of the SMM-I lead to its most common use within a discrete element method framework [257–261].

The major assumption of existing SMMs is that most of the inelastic behavior of a masonry wall is concentrated at known locations that can be modeled using interface elements, i.e., at the masonry joint and potential crack interfaces [197]. This basic assumption is valid only when (1) the geometry of masonry units and mortar joints is regular (i.e., the masonry units have a uniform cuboid shape and the mortar layers have uniform thickness), and (2) the masonry units are significantly stronger in compression and shear than the masonry joints (i.e., for masonry built with fired clay bricks, concrete blocks, or regularly shaped stones [236]). However, specific instances exist in which the compressive and shear strengths of masonry units is similar to or smaller than those of the masonry joints, e.g., in earth block masonry, for which significant cracking through the earth blocks has been experimentally observed [167]. To the authors' knowledge, the only study available in the literature that employed SMMs to reproduce the mechanical response of earth block masonry did not achieve an accurate match between experimental and numerical results when using the experimentally-measured modeling parameters [91]. The same study was able to numerically reproduce the experimental results only after modifying the modeling parameter values through a numerical parametric study.

This chapter investigates the capabilities and limitations of different SMMs by comparing their relative performance for two different types of masonry, i.e., fired-clay brick (FCB) and compressed and stabilized earth block (CSEB) masonry. After describing the different SMMs, this chapter provides recommendations on constitutive models, FE solvers, and discretization requirements for FE SMMs of unreinforced masonry. Appropriate error measures are suggested to facilitate this comparison. Two benchmark examples are investigated, which correspond to FCB walls and CSEB panels for which well-documented experimental results are available in the literature. The FE responses of the different SMMs considered in this study are compared with experimental results in terms of predicted load-displacement response, strength, initial stiffness, collapse mechanism, computational efficiency, and output information.

5.2. Research Novelty and Significance

This chapter fills several gaps in knowledge with regard to the use of SMMs to model the inelastic response behavior of unreinforced masonry walls. In particular, this study investigates the FE modeling of unreinforced masonry walls that do not satisfy the basic hypothesis of inelastic behavior concentrated at known locations by providing useful information for: (1) selecting constitutive models, FE solvers, and mesh discretization; (2) identifying under which conditions different SMMs can be used; and (3) suggesting potential development directions for more accurate, robust, and computationally efficient FE models of unreinforced masonry walls. To the authors' knowledge, this dissertation also represents the first rigorous investigation of the performance (in terms of accuracy and computational cost) of different SMMs in modeling the inelastic response of earth block masonry, which also acknowledges and identifies the inherent limitations of SMM approaches applied to earth block construction.

The present study aims to advance the FE modeling of unreinforced masonry with masonry units and masonry joints of similar mechanical properties, e.g., earth block masonry. Although this type of masonry is currently uncommon among new constructions, it is representative of many constructions with important historical value [262] and has the potential to expand into a significant portion of new low-rise buildings because of its sustainability, affordability, and safety advantages over other ordinary industrial construction materials [18,21].

5.3. Existing Simplified Micro-Modeling Techniques

The typical FE discretization of an unreinforced masonry wall using SMMs is shown in **Figure 5.1**. In general, the masonry joint and potential crack interfaces are represented by zero-thickness interface elements, the response of which is described by a relation between the traction vector and the relative displacement vector. By contrast, the expanded masonry units are modeled using continuum FE elements, the mechanical behavior of which can be described by different material constitutive models, i.e., rigid, elastic, and inelastic constitutive models, corresponding to SMM-I, SMM-II, and SMM-III, respectively.

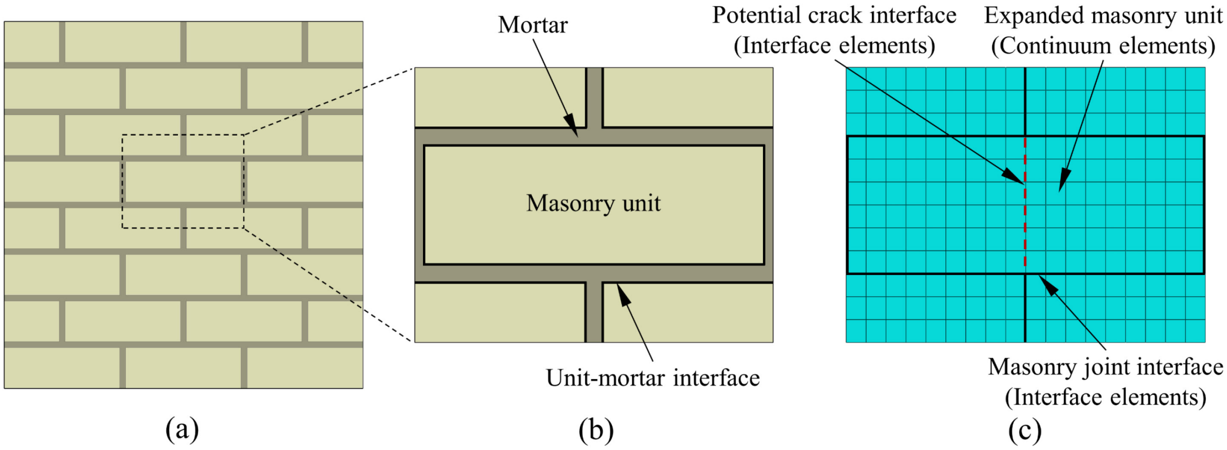

Figure 5.1. Simplified micro-modeling techniques for unreinforced masonry: (a) masonry wall, (b) representative volume element of masonry, and (c) SMM representation.

In order to accurately model the masonry's local and global mechanical behavior, SMMs need to account for all major failure mechanisms of masonry under multi-axial stress conditions [181,191,192,218,219,263–266], i.e.: (a) masonry crushing, (b) diagonal tension cracking of masonry units, (c) cracking of masonry joints, (d) failure of masonry joints due to sliding under combined normal and shear stress, and (e) cracking of masonry units in direct tension. In SMM-I and SMM-II, all failure mechanisms are modeled through the constitutive model of the interface elements used to describe the masonry joint and potential crack interfaces. In particular, failure mechanisms (a) through (d) are modeled via the masonry joint interface elements, and failure mechanism (e) is modeled via the potential crack interface elements. In SMM-III, failure mechanism (a) is modeled via the expanded masonry unit elements, failure mechanisms (b) through (d) are modeled via the masonry joint interface elements, and failure mechanism (e) is modeled via the potential crack interface elements. SMM-I also requires the addition of an auxiliary interface element between the rigid expanded masonry units and the interface elements to ensure compatibility under large relative displacements among the rigid components [183].

In this chapter, the capabilities and limitations of different SMMs were investigated using two benchmark examples representative of FCB and CSEB masonry, for which the SMMs were built using ABAQUS 6.14 [223], which is a general-purpose multiphysics commercial FE software widely used for unreinforced masonry modeling and simulation [183,185,186,204]. The accuracy, robustness, and computational efficiency of the different SMMs in simulating the structural response of masonry rely upon: (1) the material constitutive models used for the interface and expanded masonry unit element; (2) the FE solver; and (3) the FE mesh discretization. The selection of material constitutive models, FE solvers, and FE mesh discretization is discussed in the following sections.

5.3.1. ***Nonlinear material constitutive models***

SMMs employ nonlinear constitutive models for the interface elements corresponding to the masonry joint and potential crack interfaces in all SMMs and for the expanded masonry units in SMM-III. For SMM-I and SMM-II, rigid and elastic constitutive model, respectively, are used for the expanded masonry units. In this study, the coupled tension-shear interface model (CTSIM), presented in the chapter 4, is employed for the interface elements, whereas the concrete damaged plasticity model (CDPM) [267,268] is used for the expanded masonry units in SMM-III.

The CTSIM is based on a convex composite failure surface comprising a tension-shear and a compression cap failure criterion, and requires the following input parameters: tensile strength

$\left(f_{\mathrm{t}}\right)$; initial cohesion $\left(C_0\right)$; apparent initial cohesion $\left(C_{\mathrm{Q0}}\right)$; initial friction angle $\left(\phi_0\right)$; residual friction angle $\left(\phi_{\mathrm{r}}\right)$; initial dilatancy angle $\left(\psi_0\right)$; residual dilatancy angle $\left(\psi_{\mathrm{r}}\right)$; mode-I fracture energy $\left(G_{\mathrm{f}}^{\mathrm{I}}\right)$; mode-II fracture energy $\left(G_{\mathrm{f}}^{\mathrm{II}}\right)$; compressive stress at proportional limit $\left(\bar{\sigma}_0\right)$; peak compressive stress $\left(\bar{\sigma}_{\mathrm{p}}\right)$; intermediate compressive stress corresponding to the inflection point in the softening branch $\left(\bar{\sigma}_{\mathrm{m}}\right)$; residual compressive yield stresses $\left(\bar{\sigma}_{\mathrm{r}}\right)$; plastic strain at peak compressive stress $\left(\kappa_{\mathrm{p}}\right)$; total plastic strain at intermediate compressive stress $\left(\kappa_{\mathrm{m}}\right)$; and parameter that controls the width of the compression cap failure surface in the shear stress axis $\left(C_{\mathrm{ss}}\right)$. These input parameters are derived from the experimental testing of: (1) masonry couplet specimens under uniaxial tensile loading, which provide f_{t} and $G_{\mathrm{f}}^{\mathrm{I}}$; (2) masonry triplet specimens subjected to direct shear test with different pre-compression loads, which provide C_0, C_{Q0}, ϕ_0, ϕ_{r}, ψ_0, ψ_{r} and $G_{\mathrm{f}}^{\mathrm{II}}$; (3) masonry prism or wallette specimens subjected to compression load, which provide $\bar{\sigma}_0$, $\bar{\sigma}_{\mathrm{p}}$, $\bar{\sigma}_{\mathrm{m}}$, $\bar{\sigma}_{\mathrm{r}}$, κ_{p}, and κ_{m}; and (4) masonry wallettes subjected to biaxial compression loads, which provide C_{ss}. The compression cap failure criterion in the CTSIM can be easily disabled to better simulate the behavior of the potential crack interfaces, which cannot fail in compression in SMMs. Thus, when used in potential crack interfaces, the CSTIM requires only the following input parameters: f_{t}, C_0, C_{Q0}, ϕ_0, ϕ_{r}, ψ_0, ψ_{r}, $G_{\mathrm{f}}^{\mathrm{I}}$, and $G_{\mathrm{f}}^{\mathrm{II}}$. Of these parameters, f_{t} and $G_{\mathrm{f}}^{\mathrm{I}}$ are generally obtained from tensile test of masonry units; ϕ_0, ϕ_{r}, ψ_0 and ψ_{r} are assumed equal to 1; and other parameters are defined as functions of f_{t} and/or $G_{\mathrm{f}}^{\mathrm{I}}$ [184].

The CDPM is a continuum, plasticity-based, damage model for concrete and other quasi-brittle materials such as rocks, mortar, and ceramics [267,268]. This model requires the following input parameters: compressive stress-plastic strain curve, tensile stress-plastic strain curve, dilation angle (ψ_{c}), eccentricity (e_{c}), ratio of bi-axial compressive strength and uniaxial compressive strength (β_{bc}), ratio of the second stress invariant on the tensile meridian and on the compressive meridian (K_{c}), and viscosity parameter (η). These input parameters are derived from the experimental testing of: (1) masonry unit specimens under uniaxial tensile loading, which provide the tensile stress-plastic strain curve; (2) masonry prism or wallette subjected to compression load, which provide the compressive stress-plastic strain curve; (3) masonry wallette subjected to shear load, which provides ψ_{c}; and (4) masonry wallettes subjected to biaxial loads, which provide β_{bc} and K_{c}. Typically, the parameters e_{c} and η are obtained from calibration of the constitutive model to the experimental results used to obtain the other parameters.

5.3.2. *FE solver*

The FE solver represents the set of algorithms used to solve the system on nonlinear equilibrium equations corresponding to a given FE model [223,269,270]. Three different families of FE solvers have been commonly used to simulate the nonlinear structural response of masonry structures: (1) implicit static FE solvers [197,246], (2) implicit dynamic FE solvers [271,272], and (3) explicit dynamic FE solvers [183,184,253]. The implicit static FE solvers are based on an iterative method (e.g., the Newton-Raphson method [220,269]) to solve the system of nonlinear equilibrium equations corresponding to a quasi-static loading (i.e., without inertial effects) applied incrementally. The implicit dynamic FE solvers use the same type of iterative algorithms for the system of nonlinear equilibrium equations as the implicit static FE solvers in conjunction with a time-stepping scheme that accounts for inertial forces, e.g., the Newmark-beta family of algorithms [269,273]. The explicit dynamic FE solvers are based on an explicit integration algorithm (e.g., a central difference time integration or a predictor-corrector algorithm [274]) to extrapolate the nonlinear response of the structural model under consideration by using sufficiently small time increments to avoid instability (i.e., without using the equation of motion of the current time step to determine the current time step displacement) [223,270]. Implicit methods can be conditionally or unconditionally stable [223,269], whereas explicit methods are always conditionally stable with a maximum critical time step $\Delta t_{crit} = \min\left(L_e/C_d\right)$ [223,270], in which L_e denotes the characteristic length of any FE within the model, and C_d denotes the dilatational wave speed of the material in the given FE. In addition, static solvers can be used only for problems in which inertial effects can be neglected, whereas dynamic solvers can be used for problems in which inertial effects are significant or negligible. In fact, implicit static FE solvers used to simulate the mechanical behavior of masonry with SMMs could be affected by convergence issues due to the sudden release of elastic energy when cracks spread along the masonry joint interfaces and potential crack interface [184]. For these problems, dynamic FE solvers have been adopted to balance this sudden release of elastic energy through changes in the kinetic and viscous energy [184]. All three types of FE solvers are readily available in the FE software ABAQUS [223].

5.3.3. *FE discretization*

A general SMM requires the full three-dimensional discretization of expanded masonry units and interface elements, which in general is very computationally demanding. The computational cost of three-dimensional SMMs can be reduced when the loads are applied in the plane of a wall by assuming a two-dimensional plane stress condition [180,246]. This assumption can provide accurate results for structures with single-wythe masonry walls and moderate levels of compressions [246,275]. When this assumption is not satisfied, a generalized or kinematic-enriched plane state can be used with good approximation for nonlinear analysis of masonry subjected to high levels of compressions [275,276].

A mesh sensitivity analysis must also be performed to ensure a good compromise between accuracy (i.e., convergence of FE response to a unique solution) and computational cost for a given SMM. For unconditionally stable implicit (static and dynamic) FE solvers, the mesh sensitivity analysis alone is sufficient to determine an acceptable FE mesh size [223]. However, for explicit dynamic FE solvers that are only conditionally stable, the maximum stable time step depends on both the mesh size and the material properties of the FE model. Therefore, the mesh sensitivity and the determination of the stable time step must be performed simultaneously for SMMs developed using explicit dynamic FE solvers. The identification of the coarser converged mesh and the corresponding maximum stable time step is needed to ensure the best compromise between accuracy, computational costs, and stability of the FE model.

In this investigation, plane stress conditions were assumed for all the SMMs because the two benchmark examples considered in this study (i.e., FCB and CSEB masonry walls) were single-wythe walls and these walls were not subjected to extreme compression stress. Therefore, the two-dimensional plane stress assumption can provide reasonably accurate results while considerably reducing the computational cost [246].

5.4. Performance comparison of FE response analyses using SMMs

The performance of different SMMs can be expressed in terms of the comparison between the experimentally-measured and numerically-estimated force-displacement responses, deformed shapes, stress distributions, and strain distributions. Often, a few global response parameters such as peak strength and initial stiffness are sufficient for design purposes; however, these parameters need to be integrated at least with the information regarding the failure mode identified by the FE model. In this study, the FE response are compared with the experimental results by estimating the following point-wise relative error in the peak load $\left(P_{\max}\right)$, initial stiffness $\left(k\right)$, and displacement at failure $\left(\Delta_{\mathrm{f}}\right)$:

$$\varepsilon_X = \frac{X_{\mathrm{FE}} - X_{\exp}}{X_{\exp}} \tag{5.1}$$

where $X_{\mathrm{FE}} = P_{\max}$, k, or Δ_{f} obtained from a FE analysis. When multiple nominally-identical replicas are experimentally tested, $X_{\exp}$ is taken as the average of the corresponding experimentally-measured values. Furthermore, the accuracy of the different FE models in estimating the force-displacement response curve is evaluated using three different global relative errors, i.e., the mean error $\left(\varepsilon_{\mathrm{mean}}\right)$, root mean squared error $\left(\varepsilon_{\mathrm{RMS}}\right)$, and mean absolute error $\left(\varepsilon_{\mathrm{abs}}\right)$, which are defined as follows:

$$\varepsilon_{\mathrm{mean}} = \frac{1}{n_s} \sum_{j=1}^{n_s} \left[\frac{1}{n_j} \sum_{i=1}^{n_j} \frac{\left(P_{\mathrm{FE}}^{(i)} - P_{\exp,j}^{(i)}\right)}{P_{\exp,j}^{(i)}} \right] \tag{5.2}$$

$$\varepsilon_{\mathrm{RMS}} = \frac{1}{n_s} \sum_{j=1}^{n_s} \left[\sqrt{ \frac{1}{n_j} \sum_{i=1}^{n_j} \left[\frac{P_{\mathrm{FE}}^{(i)} - P_{\exp,j}^{(i)}}{P_{\exp,j}^{(i)}} \right]^2 } \right] \tag{5.3}$$

$$\varepsilon_{\text{abs}} = \frac{1}{n_s} \sum_{j=1}^{n_s} \left[\frac{1}{n_j} \sum_{i=1}^{n_j} \frac{\left| P_{\text{FE}}^{(i)} - P_{\exp,j}^{(i)} \right|}{P_{\exp,j}^{(i)}} \right] \tag{5.4}$$

in which $P_{\exp,j}^{(i)}$ and $P_{\text{FE}}^{(i)}$ denote the experimentally-measured and numerically-simulated values, respectively, of the reaction force for a given masonry wall measured at a given level of displacement, $\Delta^{(i)}$; n_j denotes the number of recorded displacement levels for the j-th experimental sample, in which the maximum displacement level corresponds to the experimental displacement at failure; and n_s denotes the number of experimental specimens.

Another comparison criterion is provided by the computational efficiency of FE models with similar accuracy in reproducing the experimental behavior of masonry. The computational efficiency of different SMMs is expressed hereinafter in terms of computational time ratio (CTR), which is defined as the ratio of the computational CPU time corresponding to two different models and obtained using the same computer for a given FE response simulation.

5.5. Benchmark Example #1: Fired-Clay Brick (FCB) Masonry

The first benchmark example considered in this study consists of a series of FCB unreinforced masonry shear walls, tested by Vermeltfoort and Raijmakers [228,229], in which the masonry units are considerably stronger than the mortar and the unit-mortar interfaces. For this type of masonry, most of the inelastic behavior is expected to be concentrated at the masonry joints.

5.5.1. *Description of experimental tests*

The considered masonry shear walls considered in this example had a width-to-height ratio approximately equal to one, with dimensions 990 mm (length) × 1000 mm (height) × 100 mm (thickness). The walls were single-wythe walls consisting of 18 courses, with the bottom and top courses clamped to steel beams, as shown in **Figure 5.2**(a). The masonry shear walls comprised wire-cut solid clay bricks with dimensions of 210 mm × 52 mm × 100 mm, and mortar layers of thickness equal to 10 mm. The experimental test involved a uniformly distributed normal pressure (p) applied vertically at the top of the walls, followed by a monotonically increasing horizontal displacement (Δ_H) applied to the top steel beam, while the bottom boundary was fixed.

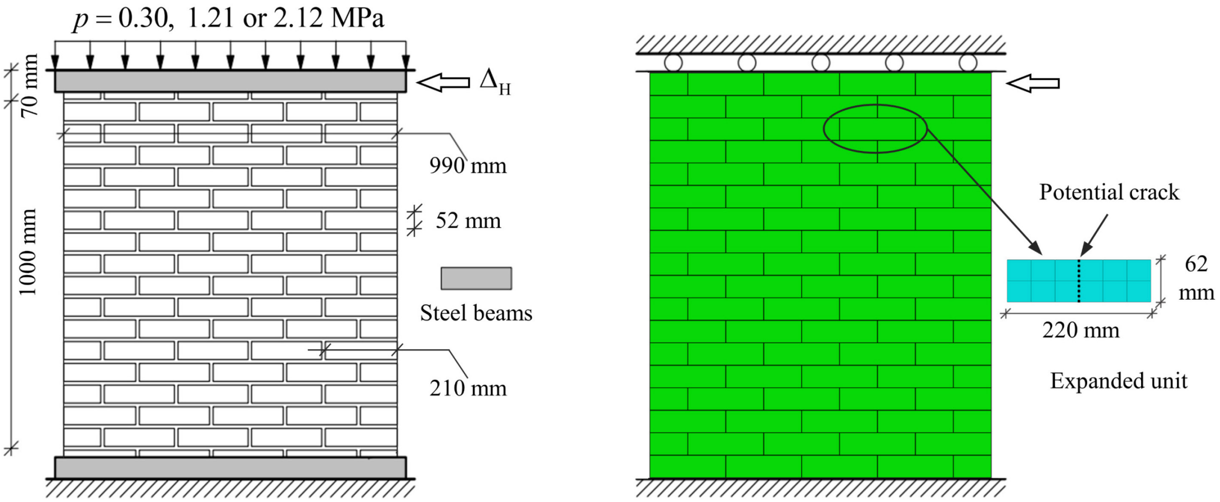

Figure 5.2. FCB masonry: (a) shear walls and (b) SMM discretization of the shear wall.

The FCB masonry shear walls were experimentally tested for three different vertical pressures, i.e., wall SW030 (with two specimens SW030a and SW030b) was subjected to a constant pressure equal to 0.30 MPa, wall SW121 to a constant pressure equal to 1.21 MPa, and wall SW212 to a constant pressure equal to 2.12 MPa. The experimental failure patterns for the different walls are shown in **Figure 5.3**. All the walls exhibited very similar failure mechanisms and, as expected, most of the cracking and inelastic behavior was concentrated at the masonry joints. During the application of the monotonically increasing horizontal displacement, horizontal tensile cracks developed first at the bottom and top of the wall in the bed joints at earlier loading stages, and were followed by diagonal stepped cracks. Finally, the crushing of the toes of the masonry and the tensile cracking in the middle of some masonry units led to the overall failure of each shear wall.

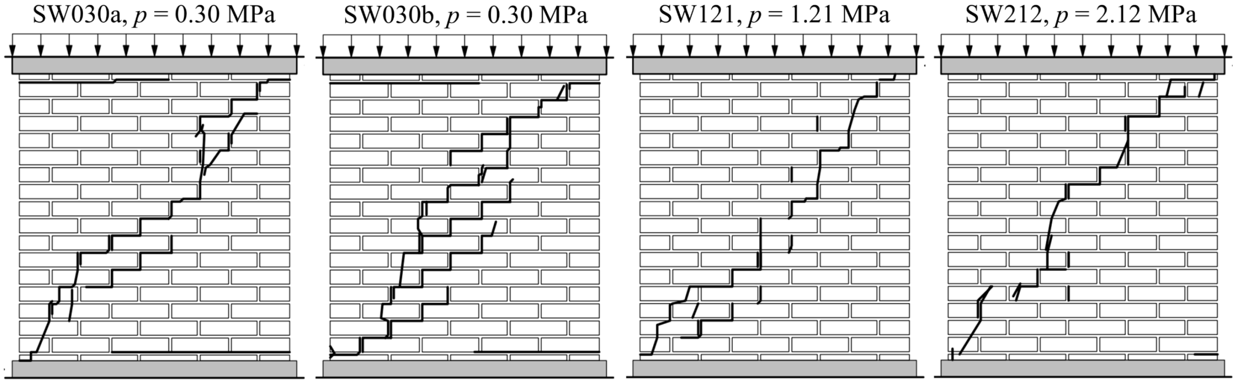

Figure 5.3. Experimental crack patterns of the different FCB unreinforced masonry shear walls.

5.5.2. *Description of SMMs developed for the FCB unreinforced masonry*

Figure 5.2(b) shows the SMM discretization of the FCB unreinforced masonry shear walls. The FE models were constructed using two-dimensional elements under the assumption of plane stress. The masonry joints and potential cracks interface were modeled by using a 4-node two-dimensional cohesive element, i.e., the COH2D4 element in ABAQUS 6.14 [223], and the expanded masonry units were modeled using a 4-node bilinear plane stress quadrilateral element with reduced integration and hourglass control, i.e., the CPS4R element in ABAQUS 6.14 [223]. Auxiliary interface elements were not needed in the SMM-I because the shear deformations in the masonry joints and potential crack interfaces were sufficiently small [183].

The material properties used for developing different SMMs were obtained from existing experimental results on tension, shear, and compression tests available in the literature [228,229]. An elastic modulus E_{b} =16,700 MPa and a Poisson ratio ν_{b} = 0.15 were used for the expanded masonry units in SMM-II and SMM-III. The elastic and inelastic properties of the masonry joint interface for the different SMMs are given in **Table 5.1**, where $k_{\mathrm{n}}^{\mathrm{b}}$ and $k_{\mathrm{s}}^{\mathrm{b}}$ denote the normal and shear stiffness, respectively, of the masonry joint interfaces corresponding to the bed masonry joints; and $k_{\mathrm{n}}^{\mathrm{h}}$ and $k_{\mathrm{s}}^{\mathrm{h}}$ denote the normal and shear stiffness, respectively, of the masonry joint interfaces corresponding to the head masonry joints. The compressive input parameters given in the **Table 5.1**, i.e., $\bar{\sigma}_0$, $\bar{\sigma}_{\mathrm{p}}$, $\bar{\sigma}_{\mathrm{m}}$, $\bar{\sigma}_{\mathrm{r}}$, κ_{p} and κ_{m}, were used to describe the stress-strain curve for the expanded masonry units in SMM-III based on a hardening/softening constitutive law used for the compression cap failure criterion of the CTSIM, see chapter 4. The other parameters needed to fully define the CDPM for the expanded masonry units in the SMM-III were taken from the literature [277–279] and are: $\psi_{\mathrm{c}} = 38°$, $e_{\mathrm{c}} = 0.1$, $\beta_{\mathrm{bc}} = 1.16$, $K_{\mathrm{c}} = 0.67$, $\eta = 8.5\times10^{-5}$.

Table 5.1. Properties of masonry joint interfaces (SMM-I, SMM-II, and SMM-III) and inelastic compressive properties for the expanded masonry units (SMM-III) of the FCB unreinforced masonry shear walls.

Properties		SMM-I			SMM-II			SMM-III		
		SW030	SW121	SW212	SW030	SW121	SW212	SW030	SW121	SW212
$k_{\mathrm{n}}^{\mathrm{b}}$	(N/mm^3)	62.9	78.1	62.9	82	110	82	82	110	82
$k_{\mathrm{s}}^{\mathrm{b}}$	(N/mm^3)	27.6	35.5	27.6	36	50	110	36	50	110
$k_{\mathrm{n}}^{\mathrm{h}}$	(N/mm^3)	39.4	63.8	39.4	82	110	82	82	110	82
$k_{\mathrm{s}}^{\mathrm{h}}$	(N/mm^3)	17.3	29.0	17.3	36	50	110	36	50	110
f_t	(MPa)	0.250	0.160	0.160	0.250	0.160	0.160	0.250	0.160	0.160
C_0	(MPa)	0.362	0.232	0.232	0.362	0.232	0.232	0.362	0.232	0.232
C_{Q0}	(MPa)	18.125	11.6	11.6	18.125	11.6	11.6	18.125	11.6	11.6
$\tan\phi_0$	(-)	0.75	0.75	0.75	0.75	0.75	0.75	0.75	0.75	0.75
$\tan\phi_r$	(-)	0.75	0.75	0.75	0.75	0.75	0.75	0.75	0.75	0.75
$\tan\psi_0$	(-)	0.001	0.001	0.001	0.001	0.001	0.001	0.001	0.001	0.001
$\tan\psi_r$	(-)	0.0001	0.0001	0.0001	0.0001	0.0001	0.0001	0.0001	0.0001	0.0001
G_f^I	(N/mm)	0.018	0.012	0.012	0.018	0.012	0.012	0.018	0.012	0.012
G_f^{II}	(N/mm)	0.125	0.050	0.050	0.125	0.050	0.050	0.125	0.050	0.050
$\bar{\sigma}_0$	(MPa)	3.50	3.83	3.83	3.50	3.83	3.83	3.50	3.83	3.83
$\bar{\sigma}_p$	(MPa)	10.50	11.50	11.50	10.50	11.50	11.50	10.50	11.50	11.50
$\bar{\sigma}_m$	(MPa)	5.25	5.75	5.75	5.25	5.75	5.75	5.25	5.75	5.75
$\bar{\sigma}_r$	(MPa)	1.50	1.64	1.64	1.50	1.64	1.64	1.50	1.64	1.64
κ_p	(-)	0.090	0.090	0.090	0.090	0.090	0.090	0.007	0.007	0.007
κ_m	(-)	0.490	0.490	0.490	0.490	0.490	0.490	0.033	0.033	0.033
C_{ss}	(-)	9.0	9.0	9.0	9.0	9.0	9.0	-	-	-

Note: underlined values are for expanded masonry units of SMM-III.

The properties of potential crack interfaces used in the different SMMs are given in **Table 5.2**, where k_n and k_s are the normal and shear stiffness, respectively, of the potential crack interfaces.

Table 5.2. Properties of potential cracks used in the SMMs of the FCB unreinforced masonry shear walls.

FE Model	k_n (N/mm^3)	k_s (N/mm^3)	f_t (MPa)	G_f^I (N/mm)	C_0 (MPa)	C_{Q0} (MPa)	$\tan\phi_0$ / $\tan\phi_r$ (-)	$\tan\psi_0$ / $\tan\psi_\mathrm{r}$ (-)	G_f^II (N/mm)
SMM-I	159	69	2.00	0.008	2.90	2.90	1.0/1.0	1.0/1.0	0.50
SMM-II	16700	7260	2.00	0.008	2.90	2.90	1.0/1.0	1.0/1.0	0.50
SMM-III	16700	7260	2.00	0.008	2.90	2.90	1.0/1.0	1.0/1.0	0.50

5.5.3. *Selection of FE solver and mesh size*

The implicit static, implicit dynamic, and explicit dynamic FE solvers, which are readily available in the FE software ABAQUS [223], were compared in terms of accuracy and computational effort for the SMM-IIs of the FCB masonry shear wall SW030. In the FE model based on the implicit static solver, all the degrees of freedoms were restrained at all the nodes at the top edge of the model, and a monotonically increasing horizontal displacement was applied on the side of the top course of the FE model while keeping the top edge of the FE model vertically fixed. A general procedure for static loading based on an incremental-iterative globally convergent Newton-Raphson method with the line search technique was used in ABAQUS [223]. In addition, an automatic load step increment technique was adopted for efficient and robust simulation of the response of the different FE models with initial, minimum, and maximum normalized increment sizes equal to 1×10^{-4}, 1×10^{-9}, 5×10^{-4}, respectively. In the FE model based on the implicit dynamic and explicit dynamic FE solvers, all the degrees of freedoms were restrained at the bottom edge of the model, and a fixed value of velocity $V = 0.1$ mm/s was applied at all nodes of the top edge of the wall. In addition, zero acceleration was assigned to the top edge of the model during the analysis to ensure a linear variation with time of the top wall displacements. A density ρ_b =

1.9×10^3 kg/m^3 and mass-proportional damping, corresponding to a damping ratio ζ = 5%, were used for the solid elements to represent inertia and damping effects. For the implicit dynamic FE solver, a general implicit dynamic procedure was used, which was based on an incremental-iterative version of the globally convergent Newton-Raphson method [223] and an automatic load step increment having minimum normalized increment sizes equal to 5×10^{-4}. For the explicit dynamic FE solver, an implicit dynamic procedure based on the central-difference time integration was employed, with the critical time step equal to 3.3×10^{-6} s.

Figure 5.4 shows the experimental and numerical load-displacement responses and the CTR of the SMM-II corresponding to the different FE solvers and same mesh discretization. **Table 5.3** reports the different error estimates. All the FE solvers were able to simulate the behavior of the FCB masonry shear wall SW030 up to failure, and the FE load-displacement responses corresponding to the different solvers are similar. The value of $\varepsilon_{\mathrm{RMS}}$ and $\varepsilon_{\mathrm{abs}}$ for the different FE solvers are almost identical, varying between 8.22% and 8.61% (approximately a 5.0% variation) and between 6.19% and 6.79% (approximately a 9.0% variation), respectively. The $\varepsilon_{\mathrm{mean}}$ values indicate that all solvers have a similar level of accuracy and slightly underestimate the FE response of the masonry wall, i.e., by 1.42%, 3.17% and 3.67% corresponding to implicit static, implicit dynamic, and explicit dynamic FE solvers. Also, the $\varepsilon_{P_{\mathrm{max}}}$ and ε_k corresponding to the different FE solvers are small, i.e., less than 4.0% and 6.0%, respectively, showing that the different FE solvers can very accurately predict the peak load, P_{max}, and initial stiffness, k, of FBC masonry walls. By contrast, the $\varepsilon_{\Delta_{\mathrm{f}}}$ is equal to 26.66%, 10.34%, and 15.43% for implicit static, implicit dynamic, and explicit dynamic FE solvers, respectively, which indicates that all FE solvers tend to overestimate the ultimate displacement of the masonry walls. This observation is not surprising, as it is known that the prediction of the structural response of unreinforced masonry walls after the peak strength has been reached is a very complex problem affected by significant uncertainties [128,280]. However, this discrepancy between experimental and numerical estimates of the displacement at failure could also be due to the fact that the criterion used to terminate the physical experiments is unknown (e.g., the experiments may have been interrupted before the complete collapse of the walls in order to protect the laboratory equipment); thus, the numerical results relative to the displacements at failure may or may not be representative of the experimental results.

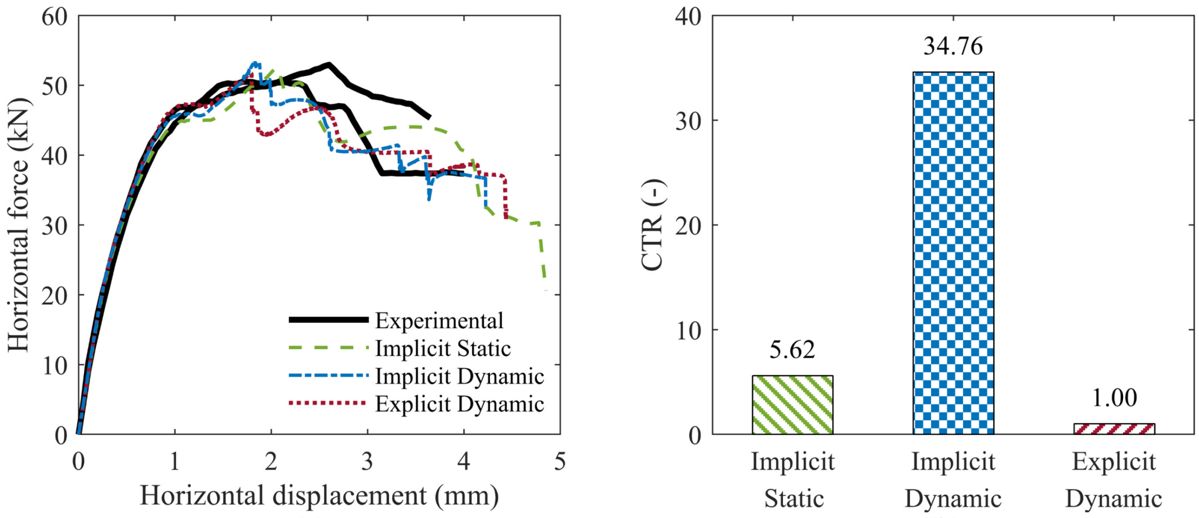

(a) (b)

Figure 5.4. FE results corresponding to different FE solvers: (a) comparison of experimental and FE load-displacement curves, and (b) comparison of CTR for different FE solvers.

Table 5.3. FE results of the FCB unreinforced masonry shear walls in term of errors between the experimental and FE load-displacement curve corresponding to different FE solvers.

FE Solver (-)	$\varepsilon_{P_{\max}}$ (%)	ε_k (%)	ε_{Δ_f} (%)	$\varepsilon_{\text{mean}}$ (%)	ε_{RMS} (%)	ε_{abs} (%)
Implicit Statics	1.89	3.05	26.66	-1.42	8.48	6.45
Implicit Dynamic	3.82	5.99	10.34	-3.17	8.22	6.19
Explicit Dynamic	0.31	4.01	15.43	-3.67	8.61	6.79

In **Figure 5.4**(b), the comparison of the different CTRs shows that the explicit dynamic solver is the most computationally efficient solver among those considered in this study, as it produces FE analysis results 5.62 and 34.76 times faster than the implicit static and implicit dynamic FE solver, respectively. Based on these results, the explicit dynamic solver seems to provide the best compromise between accuracy and computational cost in simulating the behavior of masonry among the three FE solvers considered in this study.

A mesh sensitivity analysis of the FE SMM-II model of masonry shear wall SW030 was performed. The FE models were analyzed by using the explicit dynamic FE solver and a maximum time increment equal to the critical time step. It was found that the critical time step of the SMMs depends only on the thickness of the interface elements, and the mesh size of the expanded masonry units does not affect the critical time step for any practical FE discretization. Thus, the thickness of the interface elements was set equal to 0.05 mm, giving a critical time step equal to 3.3×10^{-6} s, and the mesh sensitivity analysis was performed by developing SMM-IIs with four different mesh sizes for the expanded masonry units of the FCB masonry shear wall SW030. These meshes are identified by two numbers representing the number of elements used along the length and height of the expanded masonry units, respectively. The mesh sensitivity analysis was performed starting from a coarse 6×2 mesh, and progressively increasing the number of elements in each direction in a proportional manner until convergence was achieved. Convergence was verified by calculating the point-wise changes in peak load $\left(\delta_{P_{\max}}\right)$, initial stiffness $\left(\delta_k\right)$, and displacement at failure $\left(\delta_{\Delta_{\mathrm{f}}}\right)$, defined as:

$$\delta_X = \frac{X_{\mathrm{m2}} - X_{\mathrm{m1}}}{X_{\mathrm{m1}}} \tag{5.5}$$

in which X_{m_1} and X_{m_2} = $P_{\max}$, k, or Δ_{f} obtained from the FE analysis corresponding to the two mesh discretization being compared; as well as the global relative difference $\left(\delta_{\mathrm{abs}}\right)$, which is defined as:

$$\delta_{\mathrm{abs}} = \frac{1}{n_m} \sum_{i=1}^{n_m} \frac{\left| P_{\mathrm{m}_2}^{(i)} - P_{\mathrm{m}_1}^{(i)} \right|}{P_{\mathrm{m}_1}^{(i)}} \tag{5.6}$$

in which $P_{\mathrm{m}_1}^{(i)}$ and $P_{\mathrm{m}_2}^{(i)}$ denote the reaction forces at displacement $\Delta^{(i)}$ obtained from the FE analysis corresponding to the two mesh discretization being compared; and n_m denotes the minimum of the number of displacement levels before failure for the two meshes being compared. In particular, it was assumed the convergence was achieved when the four convergence measures reached an absolute value smaller than 1%. The following meshes were developed: 6×2, 12×4, 18×6, and 24×8. The horizontal load-displacement responses of the considered SMM-IIs are shown in **Figure 5.5**(a), and the corresponding CTRs are compared in **Figure 5.5**(b), in which mesh 18×6 is used as reference. It is observed that the FE load-displacement curves corresponding to meshes 18×6 and 24×8 are almost overlapped, whereas the other meshes provide significantly different response results. In addition, it is observed that the computational cost increases by a factor approximately equal to 3 going from one mesh size to the next finer mesh.

The values of the convergence measures are reported in Table 5.4. As expected, the convergence measures rapidly decrease in absolute value when refining the mesh, and they are all smaller than 1% in absolute value going from mesh 18×6 to mesh 24×8, which indicates that convergence has been achieved. Based on the results obtained in this mesh convergence analysis, mesh 18×6 was used for SMM-II and SMM-III hereinafter in conjunction with the FE explicit dynamic solver and a maximum time increment equal to 3.3 × 10-6 s.

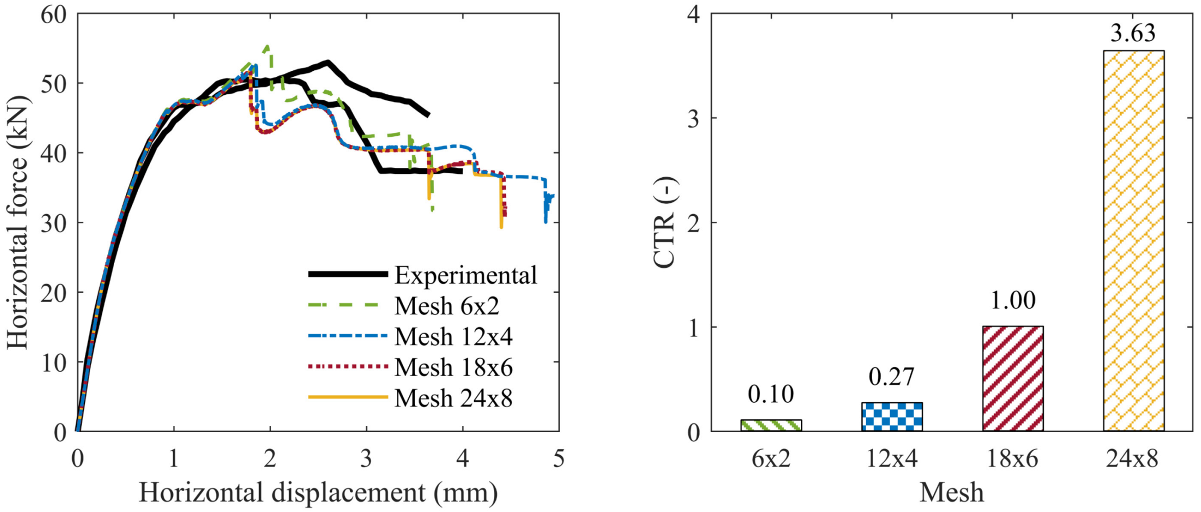

(a) (b)

Figure 5.5. Comparison of different mesh discretizations for the SMM-IIs: (a) load-displacement curves, and (b) CTRs with mesh 18x6 as reference mesh.

Table 5.4. FE response of the SMM-IIs corresponding to the four different meshes in term of relative difference among the FE load-displacement curve

Mesh		$\delta_{P_{\max}}$	δ_k	δ_{Δ_f}	δ_{abs}
m_I	m_I	(%)	(%)	(%)	(%)
6×2	12×4	-4.60	-0.39	34.15	3.27
12×4	18×6	-1.95	-0.22	-10.30	1.54
18×6	24×8	-0.01	-0.01	-0.68	0.21

5.5.4. *Comparison of the FE results obtained using different SMMs*

The FE results corresponding to the different SMMs of the FCB unreinforced masonry shear wall having different initial pressure, i.e., SW030, SW121, and SW212 are presented in **Figure 5.6**. **Figure 5.6**(a-c) compares the experimentally-measured horizontal force-horizontal displacement response of the shear walls with the corresponding numerically-estimated FE responses of the different SMMs considered in this investigation. The sudden load drops in the FE force-displacement responses are due to cracking of expanded masonry units at the potential crack locations. The FE results show that all SMMs can reproduce the complete load path of the FCB unreinforced masonry shear wall up to and beyond the peak strength. **Figure 5.6**(d) presents the CTRs corresponding to different FE models. All the FE simulations for the SMMs of the FCB unreinforced masonry shear wall were run on a Microsoft Windows-based personal computer having an Intel(R) Core (TM) i7-8700 CPU @ 3.19 GHz with 16.0 GB RAM, with only one CPU core used in each simulation. The CPU time for the SMM-II is used as reference (i.e., CTR = 1.0) for each FCB unreinforced masonry shear wall. As expected, the results show that the computation demand is lowest for SMM-I and highest for SMM-III for all modeled shear walls.

The different error measures for all models are reported in **Table 5.5**. For the SW030 shear wall, SMM-II provides the most accurate predictions for the peak load and the initial stiffness, SMM-I provides the best prediction of the displacement at failure, and SMM-III presents the lowest global relative errors (i.e., $\varepsilon_{\text{mean}}$ = 2.58%, ε_{RMS} = 8.33%, and ε_{abs} = 6.43%), although these errors are very similar to those for SMM-II ($\varepsilon_{\text{mean}}$ = -3.67%, ε_{RMS} = 8.61%, and ε_{abs} = 6.79%), whereas they are significantly (approximately two to four times) higher for SMM-I. For the SW121 shear wall, SMM-I provides the most accurate estimate of $P_{\max}$, SMM-II provides the most accurate estimate of k and Δ_{f}, and SMM-III has the lowest value for $\varepsilon_{\text{mean}}$, ε_{RMS}, and ε_{abs}, i.e., 1.32%, 4.15%, and 3.36%, respectively. For the SM212 shear wall, The SMM-II always provides the lowest errors between the experimental and numerical estimates, with the exception of $\varepsilon_{P_{\max}}$, for which SMM-I gives the lowest value, i.e., $\varepsilon_{P_{\max}}$ = 8.18%. SMM-I generally underestimate all response quantities for all walls considered in this study, with the exception of the peak strength of the SW212 wall, for which $\varepsilon_{P_{\max}} = 8.18\%$. The SMM-I also presents the largest ε_k, $\varepsilon_{\text{mean}}$, ε_{RMS}

, and ε_{abs} among all the SMMs, these errors increase in magnitude for increasing values of the initial vertical pressure applied to the shear wall. SMM-II always slightly overestimates the peak load (with $0.31\% \leq \varepsilon_{P_{\max}} \leq 15.26\%$) and initial stiffness (with $1.59\% \leq \varepsilon_k \leq 5.34\%$), with errors $\varepsilon_{P_{\max}}$, $\varepsilon_{\text{mean}}$, ε_{RMS}, and ε_{abs} increasing in magnitude for increasing values of the initial vertical pressure applied to the shear wall. SMM-III presents largest error in Δ_{f} for all the shear walls (with $24.43\% \leq \varepsilon_{\Delta_{\text{f}}} \leq 26.86\%$), always overestimating the displacement at failure. However, SMM-III has also the lowest global relative errors for the SW030 and SW121 walls. It is noted that $\varepsilon_{P_{\max}}$ for all SMMs increases for increasing levels of initial vertical pressure, whereas this phenomenon is not observed for ε_k or $\varepsilon_{\Delta_{\text{f}}}$. This phenomenon is likely due to the use of a single vertical potential crack interface at a prescribed location, which provides a proper representation of the cracking pattern observed for walls with lower initial vertical pressure. However, for higher values of initial vertical pressure, the experimental cracking pattern show diagonal cracks in the masonry units, which cannot be properly represented by the vertical potential crack interfaces in the expanded masonry units of the SMMs.

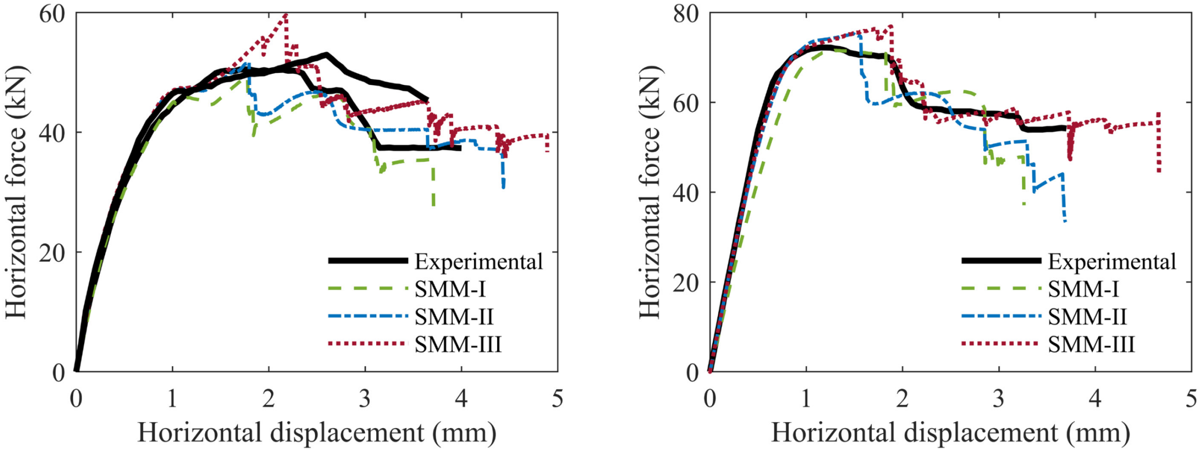

(a) (b)

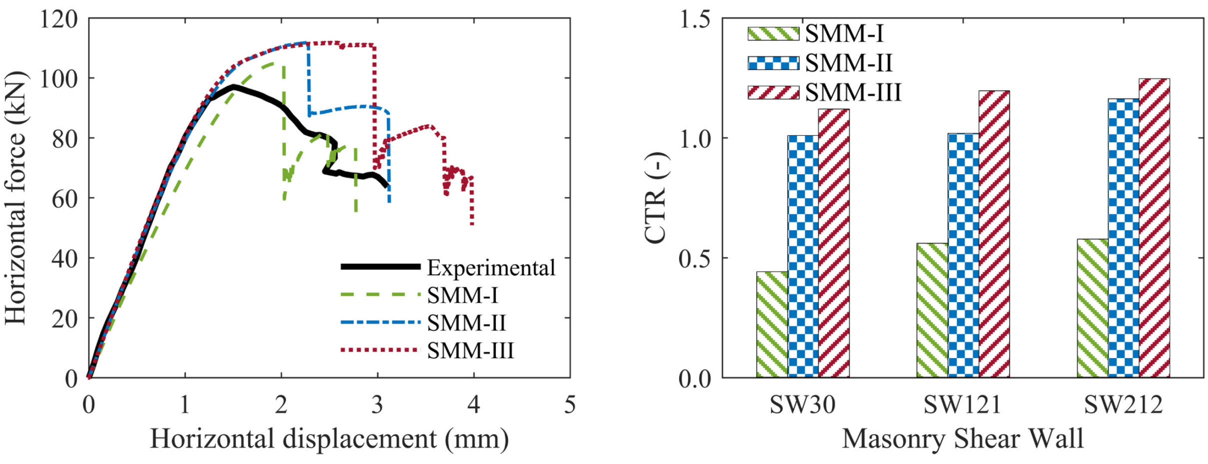

(c) (d)

Figure 5.6. Comparison of the experimentally-measured and numerically-simulated force-displacement response for the SMMs of the FCB unreinforced masonry shear walls: (a) SW030, (b) SW121, (c) SW212, and (d) CTR corresponding to different FE models.

Table 5.5. FE Simulation results for the SMMs of the FCB unreinforced masonry shear walls in term of errors between the experimental and FE load-displacement curve.

Shear Wall	FE Modal	$\varepsilon_{P_{\max}}$ (%)	ε_k (%)	ε_{Δ_f} (%)	$\varepsilon_{\text{mean}}$ (%)	ε_{RMS} (%)	ε_{abs} (%)
SW030	SMM-I	-4.08	-10.01	-3.24	-12.78	21.53	12.82
	SMM-II	0.31	4.01	15.43	-3.67	8.61	6.79
	SMM-III	14.95	5.13	27.71	2.58	8.33	6.42
SW121	SMM-I	-0.59	-10.56	-13.22	-17.02	35.31	19.48
	SMM-II	4.40	5.34	-2.27	-6.02	14.71	8.28
	SMM-III	6.70	6.29	24.43	1.32	4.15	3.36
SW212	SMM-I	8.18	-11.40	-11.49	-17.37	36.11	20.85
	SMM-II	15.20	1.59	-0.61	11.48	18.33	13.09
	SMM-III	15.26	1.80	26.86	16.70	28.23	18.96

The FE crack patterns and the distribution of the in-plane minimum principal stress for the SMMs of the FCB unreinforced masonry shear walls are presented in **Figure 5.7**(a-c) for SMM-I, **Figure 5.7**(d-f) for SMM-II, and **Figure 5.7**(g-i) are for SMM-III. In order to make the cracks visible, the deformed shape in the **Figure 5.7** is magnified by a factor 10. The numerically-simulated inelastic behavior of the shear wall is similar to the actual behavior observed in the experimental tests: horizontal tensile cracks start developing first at the bottom and top of the shear walls at approximately 1.0 mm of horizontal displacement, followed by a diagonal stepped crack in the shear wall. After approximately 2.5 mm of horizontal displacement, a combined shear and crushing mechanism develops at the toe of the shear wall, which leads to the failure of the model. All the different SMMs reproduce almost the same crack patterns for each of the walls, and these patterns are very similar to those observed experimentally. The distribution of the in-plane minimum principal stress in the SMM-II and SMM-III shows that small compressive struts, parallel to the diagonal line defined by the center of the bricks, form in all SMMs when horizontal cracks develop at the bottom and top of the shear wall. With further increase in the displacement, the formation of additional compressive struts is averted by the initiation of the diagonal crack in the SMMs. Finally, when the diagonal crack is fully open, two distinct struts are formed on each side of the diagonal crack, as shown in the **Figure 5.7**. The compressive stress in the struts increases with increasing levels of initial vertical pressure, i.e., the compressive stress is lowest in the SW030 walls and highest in the SW212 walls. The maximum compressive stress values in the SMM-II for the SW030 and SW121 shear walls remain below 8.0 and 10.0 MPa, respectively, which indicates that the assumption of linear elastic behavior in the expanded masonry units is reasonable. In SMM-III, the compressive stress values for the SW030 and SW121 shear walls are found to be slightly lower, i.e., approximately 7.5 and 9.5 MPa, respectively, than the corresponding compressive stress values in the SMM-II, with a negligible plastic strain in the expanded masonry units, i.e., less than 1.0×10^{-4}. The maximum compressive stress in the SMM-II for the SW212 wall reaches approximately 14.0 MPa, which is close to the compressive strength of the masonry units. In the SMM-III of the SW212 wall, the compressive stress is approximately equal to 12.5 MPa, and the plastic strain is approximately equal to 1.0×10^{-2}, indicating a significant plasticization of the expanded masonry units.

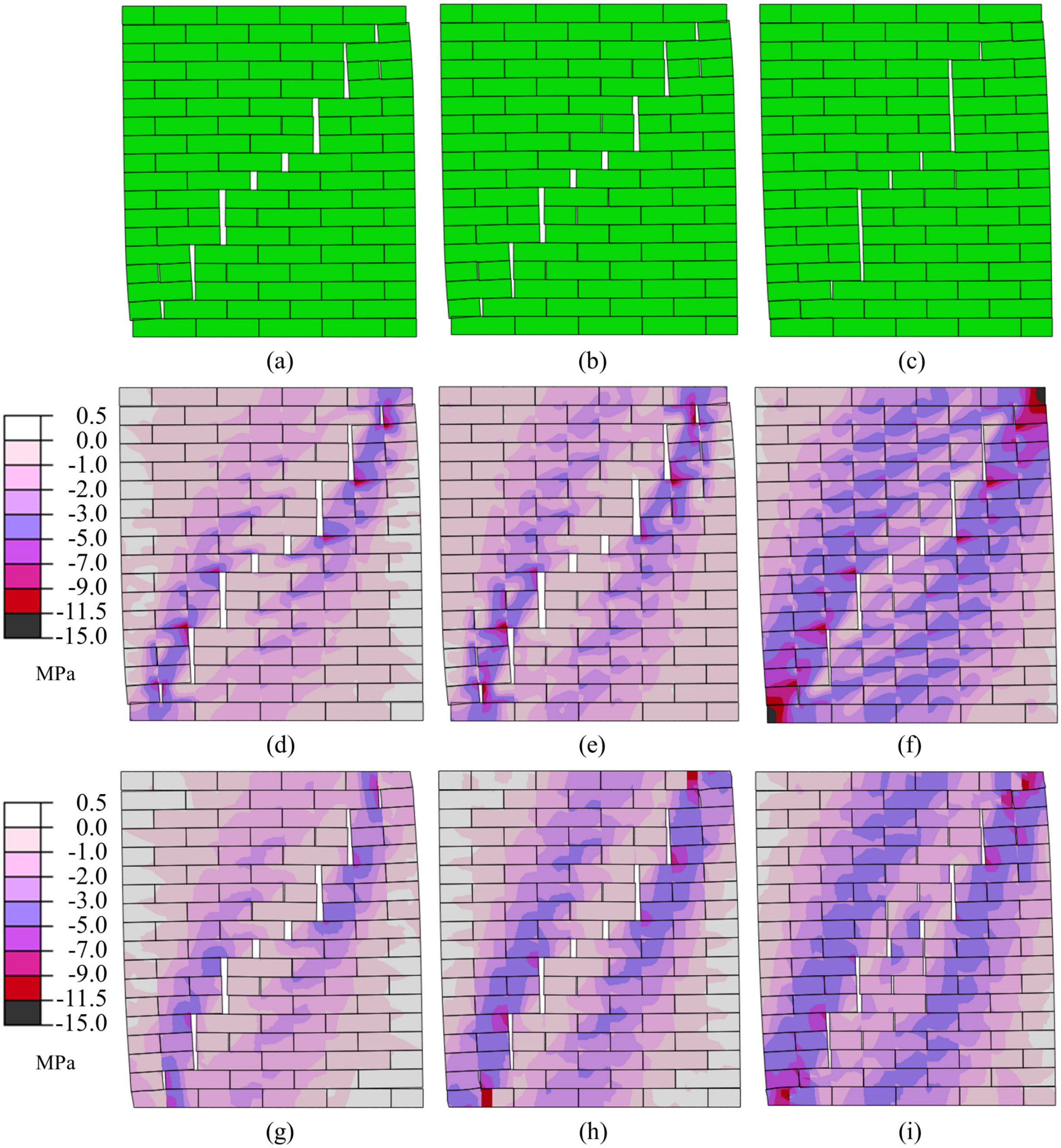

Figure 5.7. FE crack patterns and distribution of in-plane minimum principal stress for the SMMs of the FCB unreinforced masonry shear walls: (a-c) SW030, SW121 and SW212 for SMM-I; (d-f) SW030, SW121 and SW212 for SMM-II; and (g-i) SW030, SW121 and SW212 for SMM-III.

5.6. Benchmark Example #2: Compressed and Stabilized Earth Block (CSEB) Masonry

The second application example considered in this study is a CSEB unreinforced masonry wallette, in which cracking and inelastic behavior is spread across the different components (i.e., masonry units, mortar, and unit-mortar interfaces) of the masonry walls.

5.6.1. *Description of Experimental Tests*

A diagonal compression test performed on three replicate CSEB masonry wallettes (Wall-1, Wall-2 and Wall-3), reported in [55], was selected for this investigation. Each specimen consisted of a single-leaf, eight-course CSEB masonry wallette having dimensions of 864 mm (length) × 787 mm (height) × 178 mm (thickness), as shown in **Figure 5.8**. The specimens were built using: (1) CSEBs with dimensions equal to 254 mm × 178 mm × 89 mm and fabricated using silty loam soil and 6% cement; and (2) earthen mortar layers of thickness equal to 13 mm and mortar fabricated using a cement:soil:sand proportion by weight equal to 1:1:6 and water-to-cement ratio equal to 2.4. The CSEB masonry wallettes were tested under diagonal compression force that was imparted through steel shoes that were placed at the top and bottom corner of each specimen, as illustrated in the **Figure 5.8**. The experimental test involved a monotonically increasing horizontal displacement on the steel shoe at the top of the masonry wallettes, while keeping the boundaries of the steel shoe at bottom of the masonry wallette fixed. The horizontal extension and vertical contraction were recorded using two displacement transducers, which are labeled as “A” and “B”, respectively, in **Figure 5.8**(a).

Figure 5.9 shows the experimental crack patterns of the three wallettes at the end of the diagonal compression test. The specimens exhibited consistent failure modes with diagonal cracks parallel to the direction of the load and inclined by approximately 45° with respect to the bed joints.

As shown in **Figure 5.9**, the cracks at failure were observed mainly through the CSEBs and to a lesser extent along the head and bed joints and affected in a minor manner the mortar joints. This behavior is common for CSEB masonry and is fundamentally different from that of ordinary masonry, in which specimens typically fail mostly along the bed and head joints.

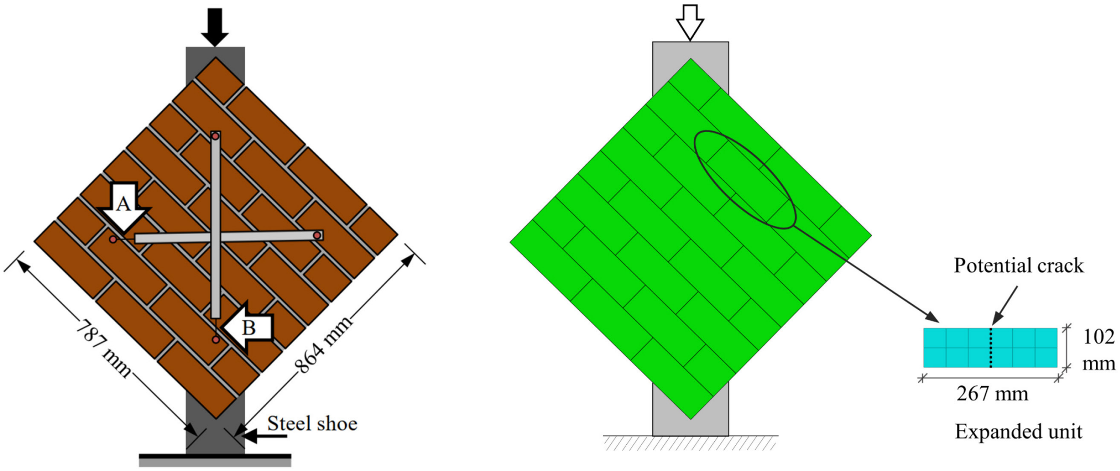

(a) (b)

Figure 5.8. CSEB masonry wallette: (a) test setup and (b) SMM discretization.

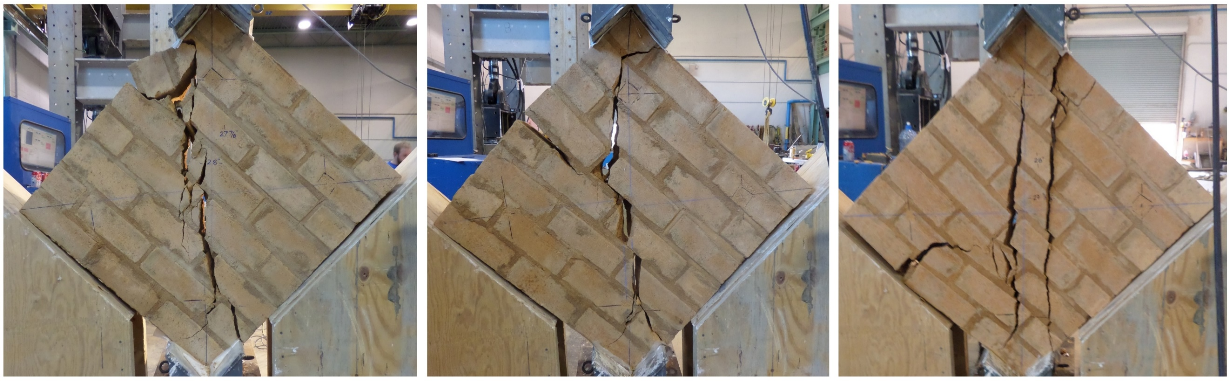

(a) (b) (c)

Figure 5.9. Experimental crack patterns of the CSEB masonry wallettes: (a) Wall-1, (b) Wall-2, and (c) Wall-3.

5.6.2. *Description of the SMMs for the CSEB masonry wallette*

Figure 5.9(b) presents a schematic of the FE models that were developed to simulate the response of the CSEB masonry wallettes. The models were constructed using the two-dimensional elements under the assumption of plane stress as those used for the FCB masonry walls, i.e., the CPS4R and COH2D4 elements in ABAQUS 6.14 [223]. Also in this case, auxiliary interface elements were not used in SMM-I. All FE models were analyzed using the explicit dynamic FE solver with time step equal to the critical time step of 2.5×10^{-6} s. All degrees of freedoms at the bottom edge of the bottom steel shoe were fixed in the FE models, and a constant vertical velocity of V = 0.1 mm/s (i.e., with zero acceleration) was applied downward to the top edge of the top steel shoe. A density $\rho_b = 1.8\times10^3$ kg/m^3 and mass-proportional damping corresponding to a damping ratio ζ = 5% were used for the solid elements of the wall to model inertia and damping effects. Based on a mesh sensitivity analysis performed as described for the previous benchmark example, the mesh used for the SMMs of the CSEB masonry wallettes consisted of 12 interface elements employed for each bed joints (i.e., six interface elements for the bed joint of each half masonry unit), five interface elements for each head joint and for the potential vertical cracks, and 30 elements for each half of the expanded masonry units. Each half of the expanded masonry units was represented by a rigid element for the SMM-I.

The material properties of the different components used in the SMMs were obtained from existing experimental results on tension, shear, and compression tests available in [79,167,173]. An elastic modulus E_b = 2550 MPa and a Poisson ratio ν_b = 0.17 were used for the expanded masonry units in SMMs-II and SMM-III. The properties of the masonry joint and potential crack interface used in the different SMMs are given in **Table 5.6**, where $k_{\mathrm{n}}^{\mathrm{b}}$ and $k_{\mathrm{s}}^{\mathrm{b}}$ denote the normal and shear stiffness, respectively, of the masonry joint interfaces corresponding to the bed masonry joints; and $k_{\mathrm{n}}^{\mathrm{h}}$ and $k_{\mathrm{s}}^{\mathrm{h}}$ denote the normal and shear stiffness, respectively, of the masonry joint interfaces corresponding to the head masonry joints. For the potential crack interfaces, $k_{\mathrm{n}}^{\mathrm{b}} = k_{\mathrm{n}}$

denote the normal stiffness, and $k_s^b = k_s$ denote the shear stiffness of the interface. The input parameters given in the **Table 5.6** were used to describe the stress-strain curve for the expanded masonry units in SMM-III based on a hardening/softening constitutive law used for the compression cap failure criterion of the CTSIM, see chapter 4. The other CDPM parameters used in the SMM-III are: $\psi_c = 38°$, $e_c = 0.1$, $\beta_{bc} = 1.16$, $K_c = 0.67$, $\eta = 8.5\times10^{-5}$.

Table 5.6. Properties of masonry joint/potential crack interfaces (SMM-I, SMM-II, and SMM-III) and inelastic compressive properties for the expanded masonry units (SMM-III) of the CSEB masonry wallettes.

Properties		Masonry joint interface			Potential crack interface		
		SMM-I	SMM-II	SMM-III	SMM-I	SMM-II	SMM-III
k_n^b	(N/mm^3)	24.38	907.10	907.10	159.00	2555.00	2555.00
k_s^b	(N/mm^3)	10.44	429.67	429.67	69	1091.45	1091.45
k_n^h	(N/mm^3)	17.89	907.10	907.10	-	-	-
k_s^h	(N/mm^3)	7.66	429.67	429.67	-	-	-
f_t	(MPa)	0.146	0.146	0.146	0.510	0.510	0.510
C_0	(MPa)	0.290	0.290	0.290	0.714	0.714	0.714
C_{Q0}	(MPa)	29.000	29.000	29.000	0.714	0.714	0.714
$\tan\phi_0$	(-)	1.51	1.51	1.51	1.00	1.00	1.00
$\tan\phi_r$	(-)	1.51	1.51	1.51	1.00	1.00	1.00
$\tan\psi_0$	(-)	0.440	0.440	0.440	1.00	1.00	1.00
$\tan\psi_r$	(-)	0.044	0.044	0.044	1.00	1.00	1.00
G_f^I	(N/mm)	0.00212	0.00212	0.00212	0.0090	0.0090	0.0090
G_f^{II}	(N/mm)	0.02120	0.02120	0.02120	0.0495	0.0495	0.0495
$\bar{\sigma}_0$	(MPa)	1.29	1.29	$\underline{1.29}$	-	-	-
$\bar{\sigma}_p$	(MPa)	3.88	3.88	$\underline{3.88}$	-	-	-
$\bar{\sigma}_m$	(MPa)	1.94	1.94	$\underline{1.94}$	-	-	-
$\bar{\sigma}_r$	(MPa)	0.55	0.55	$\underline{0.55}$	-	-	-
κ_p	(-)	0.011	0.011	$\underline{0.011}$	-	-	-
κ_m	(-)	0.044	0.044	$\underline{0.044}$	-	-	-
C_{ss}	(-)	9.0	9.0	-	-	-	-

Note: underlined values are for expanded masonry units of SMM-III.

The steel shoes were modeled as linear elastic for all the SMMs, with a surface-based tie constraint [223] imposed between the masonry and the steel shoes. The steel shoes were modeled also using CPS4R elements [223], with elastic modulus E_{steel} = 21,000 MPa, Poisson ratio ν_{steel} = 0.30, density ρ_{steel} = 7.85 × 10^3 kg/m^3, and damping ratio ζ_{steel} = 5%. The mesh of the steel shoes was extruded from the masonry wallettes in order to obtain a continuous mesh. Two elements were used across the thickness of the steel shoes.

5.6.3. *FE Results*

Figure 5.10(a) compares the FE force-displacement responses obtained using the different SMMs considered in this investigation with the corresponding experimentally-measured response obtained from the diagonal compression test. Positive and negative displacements correspond to horizontal extension and vertical contraction, respectively, which were experimentally recorded using the displacement transducers A and B, as shown in the **Figure 5.10**(a). **Figure 5.10**(b) presents the CTRs corresponding to the different FE models, which shows that SMM-I is the least computationally demanding model, whereas SMM-III is the most computationally expensive one. The six error measures considered in this study and corresponding to the different SMMs are reported in **Table 5.7**. The crack patterns and distribution of in-plane minimum principal stress observed at 0.25mm displacement and at the displacement corresponding to the peak load for the SMMs of the CSEB masonry wallettes are presented in **Figure 5.11**(a) and (d) for SMM-I, **Figure 5.11**(b) and (e) for SMM-II, and **Figure 5.11**(c) and (f) for SMM-III. In order to make the cracks visible, the deformed shape in **Figure 5.11** is magnified by a factor 10. The FE crack patterns of the SMMs do not match the experimental crack patterns of the CSEB masonry wallettes shown in **Figure 5.9**. In fact, the cracks simulated in all SMMs are mostly concentrated at the bottom two masonry bed joints and at the head joints and potential crack interfaces of the bottom two courses of the masonry wallette. As expected, the SMMs are unable to simulate the diagonal cracks observed experimentally in the earthen blocks and, thus, cannot capture the experimental failure mode of the CSEB masonry wallettes.

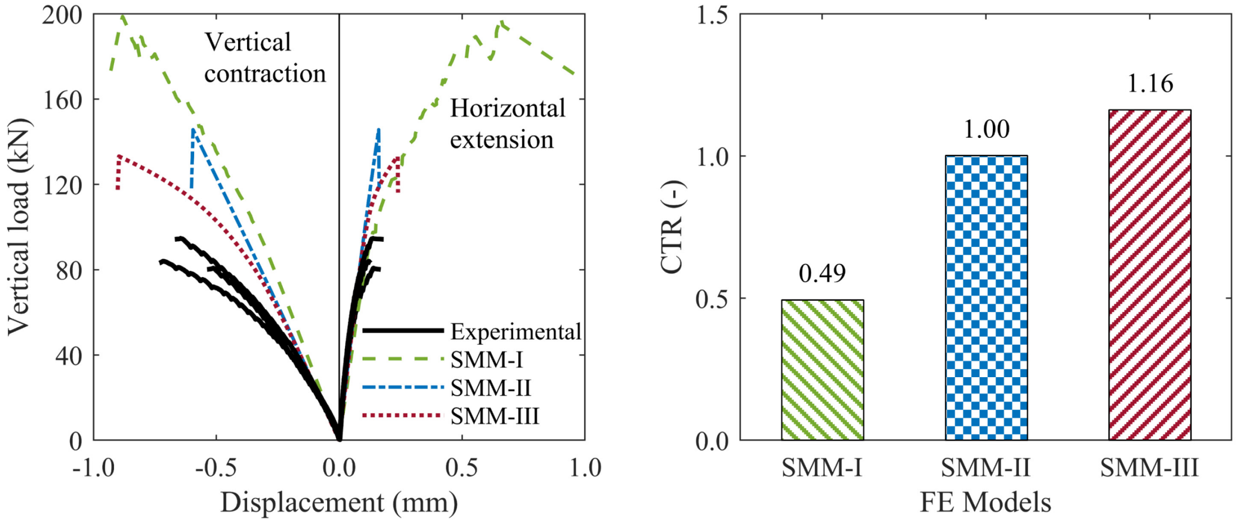

(a) (b)

Figure 5.10. FE results for the CSEB masonry wallettes: (a) comparison of the experimental and FE load-displacement responses, and (b) CTRs corresponding to different FE models.

Table 5.7. Comparison of the FE simulation results for the CSEB masonry wallettes in term of errors between experimental and FE load-displacement curves.

Displacements	FE Model (-)	$\varepsilon_{P_{\max}}$ (%)	ε_k (%)	ε_{Δ_f} (%)	$\varepsilon_{\text{mean}}$ (%)	ε_{RMS} (%)	ε_{abs} (%)
Horizontal extension	SMM-I	129.85	-44.18	507.53	-11.59	22.95	18.35
	SMM-II	68.44	-31.01	1.80	10.01	27.62	22.39
	SMM-III	53.96	-31.01	49.95	4.51	20.54	17.45
Vertical contraction	SMM-I	-	-10.55	44.50	53.09	59.24	54.45
	SMM-II	-	-25.67	-6.96	16.49	47.32	39.87
	SMM-III	-	-25.67	39.55	20.97	26.84	24.77

It is concluded that the SMMs are unable to simulate the behavior of the CSEB masonry wallettes subjected to a diagonal compression test. This result is due to the fact that CSEB masonry does not satisfy the hypothesis that mortar and unit-mortar interfaces are significantly weaker than the masonry units, which is at the basis of the SMMs. In fact, the assumption that the inelastic behavior is concentrated along the masonry joints and the middle plane of the masonry units is not valid for CSEB masonry, where the experimental evidence shows cracking patterns that are similarly distributed across joints and masonry units. It is also concluded that a modeling approach different than SMM is needed to properly describe the mechanical behavior of CSEB masonry walls with masonry units of similar strength and stiffness as the mortar and the unit-mortar interfaces. Such new modeling approach needs to be able to model the propagation of cracks with any inclination within the masonry units and the mortar.

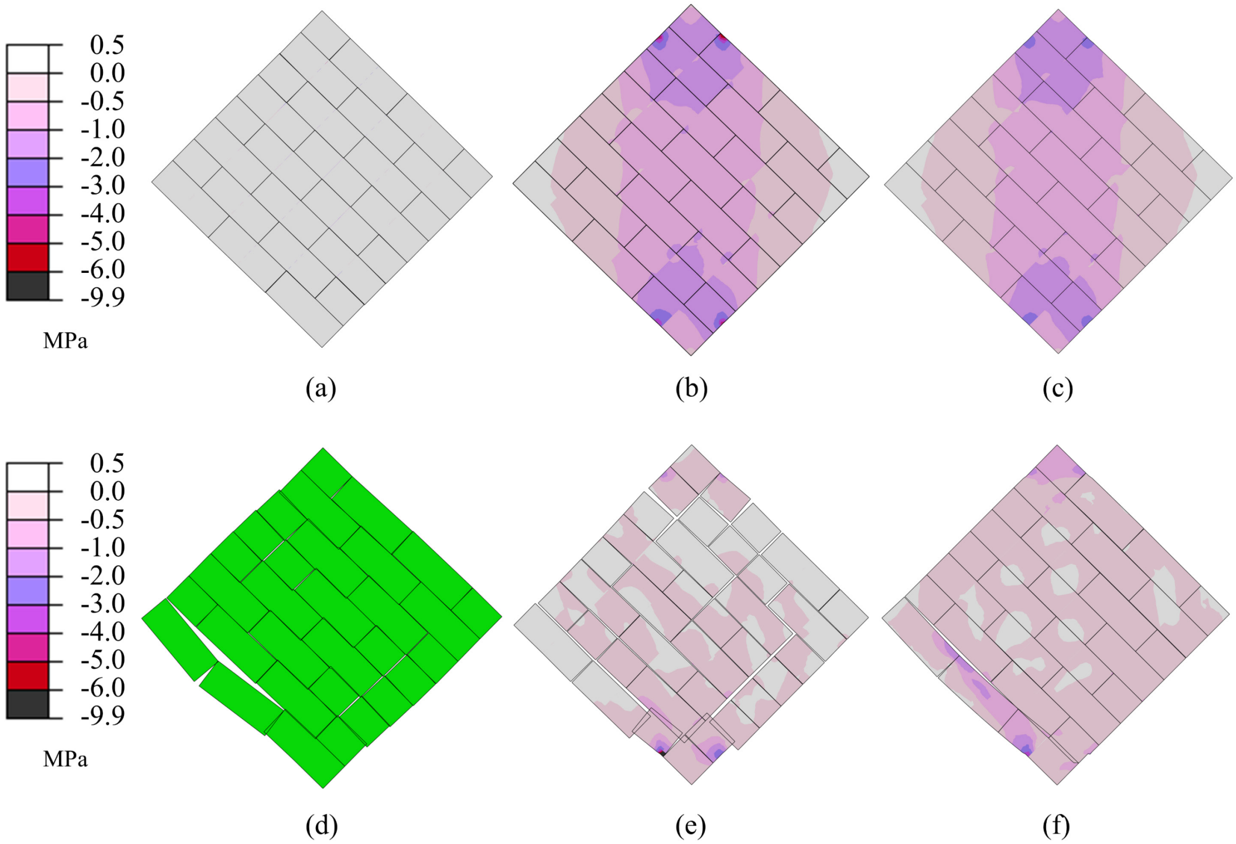

Figure 5.11. FE crack patterns and distribution of in-plane minimum principal stress for the SMMs of the CSEB masonry wallettes: (a-c) SMM-I, SMM-II and SMM-III, respectively, at 0.25 mm displacement; and (d-f) SMM-I, SMM-II and SMM-III, respectively, at displacement corresponding to peak load.

5.7. Conclusion

In this study, the capabilities and limitations of FE simplified micro-modeling techniques were investigated through a comparative analysis of their simulation capabilities with respect to two different types of masonry, i.e., fired-clay brick (FCB) and compressed and stabilized earth block (CSEB) masonry. In the simplified micro-modeling technique, mortar and adjacent unit-mortar interfaces in the masonry are represented by zero-thickness interface elements between expanded masonry units, with a vertical potential crack interface placed in the middle of the expanded masonry units. Different simplified micro-models (SMMs) can be developed based on the different material constitutive models used for the masonry units. This study considered rigid (SMM-I), elastic (SMM-II), and elasto-plastic (SMM-III) constitutive models. The comparative analysis was made between experimentally-measured and numerically-simulated responses of benchmark unreinforced masonry walls that are representative of the two masonry types and for which well-documented experimental data are available in the literature.

This chapter also provides recommendations on the use of different FE solvers and on the mesh and time step discretization for developing accurate and robust SMMs within the FE framework. In particular, it is shown that implicit static, implicit dynamic, and explicit dynamic solvers produce similar mechanical responses when used to simulate the nonlinear inelastic behavior of unreinforced masonry walls; however, the explicit dynamic solver is significantly more efficient than the other solvers from a computational point of view.

The FCB unreinforced masonry shear walls showed experimental inelastic behavior and cracks concentrated in the masonry joints (i.e., mortar and unit-mortar interfaces) and in potential crack zones corresponding to the vertical middle plane of the masonry units, whereas CSEB masonry had an experimental inelastic behavior and cracks spread across all masonry constituents. This different behavior is likely because, in the FCB masonry walls, the masonry units are significantly stronger and have higher stiffness than the mortar and the unit-mortar interfaces, whereas the different masonry components have similar strength and stiffness in the CSEB masonry walls.

The FE simulation results indicate that simplified micro-modeling techniques can properly simulate the FE behavior for the FCB masonry shear walls. In fact, all three SMM approaches (i.e., SMM-I, SMM-II, and SMM-III) appear to provide similarly accurate results in terms of global load-displacement responses, peak loads (with errors contained between -4.08 and 15.26%), and initial stiffnesses (with errors contained between -11.40 and 6.29%). The models are less accurate in estimating the displacements at failure (with errors contained between -13.22% and 27.71%); however, this result may also be due to the lack of knowledge on the specific criterion used to terminate the experimental tests. It is observed that: (1) the computational costs increase from SMM-I to SMM-II and from SMM-II to SMM-III, (2) the accuracy in predicting the mechanical response of FCB masonry walls is similar for SMM-II and SMM-III and slightly better than SMM-I, and (3) the accuracy slightly degrades for increasing axial compression applied on the walls.

By contrast, these SMMs are in general not suitable for modeling the mechanical response of CSEB masonry walls, because they are unable to reproduce the failure mechanisms produced by cracks propagating across all masonry components. Therefore, a different modeling approach is needed to describe the mechanical behavior of masonry walls and systems in which the different masonry components have similar strength and stiffness, as for CSEB masonry systems. A possible alternative that should be investigated in future studies is the use of a FE detailed micro-modeling approach, in which each component of a masonry system is modeled separately from the others through an appropriate nonlinear constitutive model.

CHAPTER 6. FINITE ELEMENT DETAILED MICRO-MODELING OF UNREINFORCED EARTH BLOCK MASONRY SYSTEM

6.1. Introduction

Earth block masonry is one of the oldest construction techniques [2,28], which has lost its prevalence in industrialized countries after the advent of modern materials such as concrete, steel, and engineered timber [62,63]. Only recently, earth block masonry is receiving renewed attention because of its low cost, low carbon footprint, high energy efficiency, use of indigenous materials, and inherent simplicity [1,2,94]. Most of the recent research studies focused on investigating the mechanical behavior of earth block masonry systems at the material, component, or structure level [21,85,88,90,167]. Numerical studies to model the behavior of earth block masonry focused mainly on the use of continuum finite element (FE) models based on homogenization [281] or FE simplified micro-models (SMMs) originally developed for ordinary masonry [91,282].

In particular, SMMs have been commonly employed to investigate the local and global mechanical response of masonry structures [180,183,184,198,236]. In an SMM, the mortar joint and the two adjacent unit-mortar interfaces (referred to as masonry joints hereinafter) are lumped into zero-thickness interfaces (referred to as masonry joint interfaces hereinafter), which connect expanded masonry units. The expanded masonry units are augmented with an additional zero-thickness interface (referred to as potential crack interface hereinafter), which is vertically placed in the middle of the expanded masonry units to model the potential crack that are often experimentally observed within the masonry units. Based on the different constitutive models adopted for the expanded masonry units, three SMMs are commonly found in the literature, i.e., SMMs with rigid (referred to SMM-I hereinafter), elastic (referred to SMM-II hereinafter), and inelastic (referred to SMM-III hereinafter) constitutive models for the expanded masonry units. SMMs assume that most of the inelastic behavior of a masonry wall is concentrated at known locations that can be modeled using interface elements, i.e., at the masonry joint and potential crack interfaces [180,236]. However, the chapter 5 demonstrated that, while SMMs can successfully model the mechanical behavior of ordinary masonry satisfying the above hypothesis, SMMs cannot accurately simulate the mechanical behavior of masonry systems in which cracks and/or plasticity develop in the masonry units, as commonly observed in earth block masonry [167].

The present study investigates the use of FE detailed micro-models (DMMs) to simulate the mechanical behavior of earth block masonry systems for which cracks and plastic behavior is spread across the different components, i.e., mortar, mortar-unit interfaces, and masonry units. In a DMM, masonry units and mortar are represented by continuum elements, and the unit-mortar interfaces are represented by zero-thickness interface elements with constitutive models describing the relation between the traction vector and the relative displacement vector. Unlike SMMs, in which all failure mechanisms are modeled through the masonry joint and potential crack interfaces [180], a DMM explicitly models the behavior of the individual masonry constituents and addresses the intrinsic discontinuity and heterogeneity of the masonry structure. In particular, crushing and tension cracking of masonry units are modeled via the constitutive model associated with the masonry units, crushing and tension cracking of mortar are modeled via the constitutive model associated with the mortar, and sliding and cracking failures of unit-mortar interfaces are modeled via the constitutive model associated with the zero-thickness interface. DMMs are computationally expensive and, thus, have been rarely employed to simulate the mechanical behaviour of masonry systems [180,236]. More recently, thanks to the advancement in computational capabilities, DMMs have been used to model multi-perforated clay brick masonry [283], partially-grouted reinforced masonry [238], and brick masonry [237,240]. To the best of the authors' knowledge, DMMs have not yet been used to simulate the mechanical behavior of earth block masonry.

This chapter first presents a DMM specifically tailored to model earth block masonry systems. Then, through a series of FE simulations of representative volume elements (RVEs) of masonry subjected to three-point bending and to shear loading, this study identifies the conditions (in terms of relative strength of masonry units and mortar, and of loading conditions) under which the structural response results obtained using different SMMs and the DMM are consistent. Finally, the new DMM is validated through a comparison of its FE response with existing experimental results for earth block masonry wallettes subject to diagonal compression, for which SMMs were previously demonstrated to provide inaccurate results.

6.2. Research Novelty and Significance

This investigation extends the use of FE DMMs to analyze the mechanical behavior of earth block masonry systems for the first time. It also identifies the range of validity for SMMs of masonry walls as a function of the relative strength and stiffness of mortar and masonry units, and of the type of loading conditions. The new knowledge presented in this chapter advances the FE modeling of unreinforced masonry (URM), particularly for systems characterized by masonry units that are very weak or very strong when compared to the associated mortar. These results and the FE DMM approach developed in this study are critical to promote the practical use of earth block masonry, as they provides the structural engineering community with an accurate tool for the numerical modeling of the structural behavior of URM.

6.3. Finite Element (FE) Detailed Micro-Modeling

DMMs explicitly model the different components of unreinforced masonry, generally providing a more realistic and detailed model than SMMs. Another advantage of DMMs over SMMs is that the parameters needed to define the FE constitutive models can be obtained from experimental testing of masonry components, which is easier and less expensive than the testing typically needed to define the constitutive model paramaters used in SMMs. However, these advantages come to the cost of additional computational effort. The description of a DMM of an unreinforced masonry wall is shown in **Figure 6.1**, which also defines the RVE in **Figure 6.1**(b) and shows a typical FE discretization in **Figure 6.1**(c).

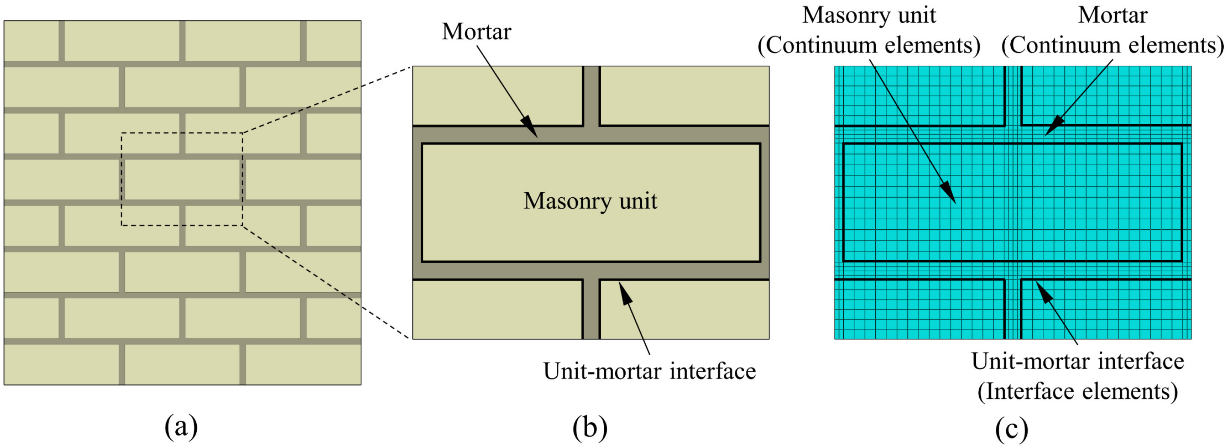

Figure 6.1. DMM of an URM wall: (a) masory wall, (b) RVE, and (c) FE discretization.

In this study, the nonlinear behavior of the zero-thickness interface elements is modeled using the recently developed coupled tension-shear interface model (CTSIM), presented in the chapter 4, whereas the masonry units and mortar are modeled using the concrete damaged plasticity model (CDPM) [267,268]. The CTSIM is based on a convex composite failure surface comprising a tension-shear and a compression cap failure criterion, and requires the following input parameters: tensile strength $\left(f_{\mathrm{t}}\right)$; initial cohesion $\left(C_0\right)$; apparent initial cohesion $\left(C_{\mathrm{Q0}}\right)$; initial friction angle

(ϕ_0); residual friction angle (ϕ_r); initial dilatancy angle (ψ_0); residual dilatancy angle (ψ_r); mode-I fracture energy $(G_\mathrm{f}^\mathrm{I})$; mode-II fracture energy $(G_\mathrm{f}^\mathrm{II})$; compressive stress at proportional limit $(\bar{\sigma}_0)$; peak compressive stress $(\bar{\sigma}_\mathrm{p})$; intermediate compressive stress corresponding to the inflection point in the softening branch $(\bar{\sigma}_\mathrm{m})$; residual compressive yield stresses $(\bar{\sigma}_\mathrm{r})$; plastic strain at peak compressive stress (κ_p); total plastic strain at intermediate compressive stress (κ_m) ; and the parameter that controls the width of the compression cap failure surface along the shear stress axis (C_ss). In DMMs, the compression cap failure criterion within the CTSIM can be deactivated, as compression failure mechanisms are described through the constitutive models associated with the mansonry units and the mortar, thus removing the need to evaluate the following constitutive parameters: $\bar{\sigma}_0$, $\bar{\sigma}_\mathrm{p}$, $\bar{\sigma}_\mathrm{m}$, $\bar{\sigma}_\mathrm{r}$, κ_p, κ_m, and C_ss. The remaining input parameters for the zero-thickness interface element are derived from the following experimental tests: (1) masonry couplet specimens under uniaxial tensile loading, which provide f_t and G_f^I; and (2) masonry triplet specimens subjected to direct shear test with different pre-compression loads, which provide C_0, C_Q0, ϕ_0, ϕ_r, ψ_0, ψ_r and G_f^II.

The CDPM is a continuum, plasticity-based, damage model for concrete and other quasi-brittle materials such as rocks, mortar, and ceramics [267,268]. This model requires a compressive stress-plastic strain curve and the following additional input parameters: tensile strength (f_t), mode-I fracture energy $(G_\mathrm{f}^\mathrm{I})$, dilation angle (ψ_c), eccentricity (e_c), ratio of bi-axial compressive strength and uniaxial compressive strength (β_bc), ratio of the second stress invariant on the tensile meridian and on the compressive meridian (K_c), and viscosity parameter (η). The input parameters for the masonry unit and mortar of the DMM are derived from the following experimental tests: (1) masonry unit and mortar specimens subjected to uniaxial tensile and compressive loading, which provide f_t, G_f^I and the compressive stress-plastic strain curve for each of the two components; (2) masonry unit and mortar specimens subjected to shear load, which provides ψ_c; and (3) masonry unit and mortar specimens subjected to biaxial loads, which provide β_bc and K_c. The parameters e_c and η are generally obtained from calibration of the constitutive model to the results obtained from the experimental tests listed above. In this study, the compressive stress-plastic strain curves for both masonry units and mortar are assumed to follow the same hardening/softening relation used for the compression cap failure criterion adopted in the CTSIM; therefore, they are fully defined by the following parameters: $\overline{\sigma}_0$, $\overline{\sigma}_\mathrm{p}$, $\overline{\sigma}_\mathrm{m}$, $\overline{\sigma}_\mathrm{r}$, κ_p, and κ_m (see chapter 4).

In addition to the plastic properties previously described, the FE models require also the definition of the elastic properties for the two material constitutive models. These properties are defined by the following parameters: (1) normal and shear stiffness, k_n and k_s, respectively, for the CTSIM; and (2) elastic modulus, E, and Poisson ratio, ν, for the CDPM. In this study, the materials are assumed isotropic and homogeneous, based on previous findings valid for CSEBs [80,81,173].

6.4. FE Analysis Assumptions

In this study, a two-dimensional plane stress condition is assumed for all FE models of masonry walls, which can provide accurate results for structures with single-wythe masonry walls and moderate levels of compressions [246,275]. In addition, the FE analyses are performed using an explicit dynamic integration algorithm with a maximum time step equal to the critical time step needed to ensure numerical stability [270,284]. In the chapter 5, the explicit dynamic integrator was found to provide the best compromise between accuracy and computational cost in simulating the behavior of masonry using SMMs. It was also found that the critical time step in SMMs, which generally depends on the mesh size and the material properties of the FE model, is always controlled by the properties and thickness of the interface elements. The FE discretization used in this investigation is obtained through a mesh sensitivity analysis performed as described in the chapter 5, by identifying the coarser mesh discretization with changes in the force-displacement response smaller than a target value assumed here equal to 1%. This mesh discretization is used to ensure a good compromise between accuracy and computational cost.

In the present study, all FE models of masonry are developed in ABAQUS 6.14 [284], a commercially available FE analysis software for multiphysics applications. The masonry units and mortar (for the DMMs) and the expanded masonry units (for the SMMs) are modeled using a 4-node bilinear plane stress quadrilateral element with reduced integration and hourglass control corresponding to the CPS4R element in ABAQUS, whereas the unit-mortar interfaces (for the DMMs and SMMs) and the joint and potential crack interfaces (for the SMMs) are modeled by using a 4-node two-dimensional cohesive element corresponding to the COH2D4 element in ABAQUS [284].

6.5. Comparison of DMM and SMM Results using RVE Test

This study compares the FE response results obtained using DMMs and SMMs of masonry RVEs subject to two different loading conditions, i.e., three-point bending and shear loading, as shown in **Figure 6.2**. Previous research in the chapter 5 suggested that the controlling parameter for determining the accuracy of SMMs in predicting the response of URM may be the ratio between the masonry unit and the masonry joint strength ratio. This hypothesis is investigated here by considering the following strength ratios $\left(\mathrm{r}_\sigma\right)$: 0.1, 0.2, 0.5, 1.0, 2.0, 5.0, and 10.0. This investigation compares the results obtained using the DMM proposed in this chapter with those obtained using SMM-I, SMM-II, and SMM-III, which were previously investigated in the chapter 5. The FE results obtained using the DMMs are considered as the reference solution and the FE results obtained from the different SMMs are compared in terms of crack patterns at failure and of relative differences in the peak load $\left(P_{\max}\right)$, and initial stiffness $\left(k\right)$, which are defined as:

$$\delta_X = \frac{X_m - X_{\mathrm{ref}}}{X_{\mathrm{ref}}} \tag{6.1}$$

where $X = P_{\max}$ or k; m = SMM-I, SMM-II, or SMM-III; and ref = DMM.

All FE models are analyzed using an explicit dynamic FE solver with a maximum time step equal to the critical time step = 1.0 × 10^{-6} s. The inertia and damping properties of the systems are modeled using a density $\rho_b = 1.8\times10^3$ kg/m^3 and mass-proportional damping corresponding to a damping ratio $\zeta = 5\%$ for the solid elements of each model.

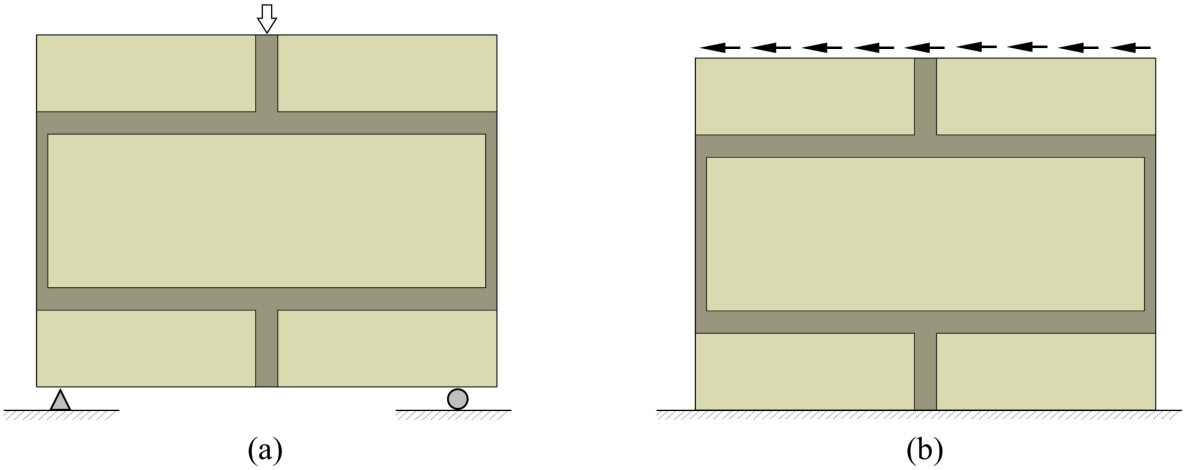
(a)
(b)

Figure 6.2. Loading conditions for the FE result comparison of RVEs: (a) three-point bending and (b) shear loading.

6.5.1. *Description of DMMs*

The mesh discretization used for the DMMs comprises 34 FE elements across the length and 11 elements across thickness of each earth block, for a total of 374 elements for a full earth block, with denser elements in correspondence of the vertical line in the middle of each earth block, as shown in **Figure 6.1**(c). Four elements are employed across the mortar thickness, with the other dimension chosen to match that of the mesh of the masonry units. The material constitutive properties of the masonry units, mortar, and unit-mortar interfaces corresponding to different r_σ considered in this study are reported in **Table 6.1**. To achieve the different r_σ, the properties of the mortar and of the unit-mortar interfaces are kept constant, whereas the properties of the masonry units are varied according to the r_σ of interest. The properties of the mortar used in this investigation are taken from Cuellar-Azcarate [167] and are representative of compressed and stabilized earth block (CSEB) mansonry. The properties of the unit-mortar interfaces are assumed equal to those of the mortar, whereas the constitutive model parameters for the masonry units (i.e., E_{unit}, $f_{\text{t, unit}}$, $G^{I}_{f,\text{ unit}}$, $\bar{\sigma}_{\text{0, unit}}$, $\bar{\sigma}_{\text{p, unit}}$, $\bar{\sigma}_{\text{m, unit}}$, $\bar{\sigma}_{\text{r, unit}}$, $\kappa_{\text{p, unit}}$, and $\kappa_{\text{m, unit}}$) are varied proportionally to the corresponding parameters of the mortar, accordin to r_σ. This assumption is supported by: (1) the linear correlation between the E_{unit} and $\bar{\sigma}_{\text{p, unit}}$ reported in the literature for adobe bricks [285] and clay brick [286]; and (2) the relationship describing the fracture energy for a quasi-brittle material as proportional to the square of its strength and inversely proportional to its elastic modulus [287]. The Poisson ratio, ν, is assumed constant and equal to 0.15 [288,289]. The values of the other parameters needed to fully define the CDPM for the masonry units and mortar in the DMM are taken from the literature and are assumed equal to ψ_{c} = 38°, e_{c} = 0.1, β_{bc} = 1.16, K_{c} = 0.67, and η = 8.5×10^{-5} [277–279].

Table 6.1. Properties of mortar, unit-mortar interface, and masonry units corresponding to different r_σ used for developing the DMMs of the RVEs.

Properties		Mortar	Unit-mortar interface	Masonry units (for different r_σ)						
				0.1	0.2	0.5	1.0	2.0	5.0	10.0
E	(MPa)	2100	-	210	420	1050	2100	4200	10500	21000
ν	(-)	0.15	-	0.15	0.15	0.15	0.15	0.15	0.15	0.15
k_n	(N/mm^3)	-	2100	-	-	-	-	-	-	-
k_s	(N/mm^3)	-	913	-	-	-	-	-	-	-
f_t	(MPa)	0.550	0.550	0.055	0.110	0.275	0.550	1.100	2.750	5.500
C_0	(MPa)	-	0.5772	-	-	-	-	-	-	-
C_{Q0}	(MPa)	-	2.8860	-	-	-	-	-	-	-
$\tan\phi_0$	(-)	-	0.5500	-	-	-	-	-	-	-
$\tan\phi_r$	(-)	-	0.0055	-	-	-	-	-	-	-
$\tan\psi_0$	(-)	-	0.3300	-	-	-	-	-	-	-
$\tan\psi_r$	(-)	-	0.0033	-	-	-	-	-	-	-
G_f^I	(N/mm)	0.0110	0.0549	0.0011	0.0022	0.0055	0.0110	0.0220	0.0550	0.1100
G_f^{II}	(N/mm)	-	0.5490	-	-	-	-	-	-	-
$\bar{\sigma}_0$	(MPa)	0.703	-	0.070	0.141	0.352	0.703	1.406	3.515	7.030
$\bar{\sigma}_\mathrm{p}$	(MPa)	2.110	-	0.211	0.422	1.055	2.110	4.220	10.550	21.100
$\bar{\sigma}_\mathrm{m}$	(MPa)	1.055	-	0.106	0.211	0.528	1.055	2.110	5.275	10.550
$\bar{\sigma}_\mathrm{r}$	(MPa)	0.301	-	0.030	0.060	0.151	0.301	0.602	1.505	3.010
κ_p	(-)	0.0090	-	0.0009	0.0018	0.0045	0.0090	0.0180	0.0450	0.0900
κ_m	(-)	0.0330	-	0.0033	0.0066	0.0165	0.0330	0.0660	0.1650	0.3300

6.5.2. *Description of SMMs*

The mesh discretization used for the zero-thickness interfaces of all SMMs consists of 16 interface elements for each bed joint (i.e., eight interface elements for the bed joint of each half masonry unit), and six interface elements for each head joint and for the potential vertical cracks. In total, 96 elements are used for each expanded masonry unit in SMM-II and SMM-III, whereas each half of the expanded masonry units are modeled with a single rigid element for SMM-I. The material properties used for developing the different SMMs are obtained from the properties corresponding to the masonry units, mortar, and unit-mortar interfaces of the DMMs. The elastic properties of the masonry joint interface corresponding to the different r_σ were determined based on different relations available in the literature for the SMM-I [183], which provide different values for the properties of the bed and head joints, and for the SMM-II and SMM-III [212], which provide equal values for the properties of bed and head joints. These elastic properties are tabulated in **Table 6.2**. For the expanded masonry units in SMM-II and SMM-III, the value of elastic modulus and Poisson ratio were equal to the value of E_{unit} and v_{unit} of the DMMs and are reported in **Table 6.1**. The inelastic properties of the masonry joint interfaces in the SMMs include: (1) the inelastic properties for tension-shear failure criterion of the CTSIM, which are equal to the corresponding inelastic properties for the unit-mortar interfaces in the DMMs, and are reported in **Table 6.1**; and (2) the inelastic properties for the compression cap failure criterion of the CTSIM (SMM-I and SMM-II), which are obtained from the computational homogenization [290] of the RVE subjected to compressive load using the DMM corresponding to the same value of r_{σ}, and are tabulated in **Table 6.3**. For SMM-III, the inelastic compressive properties (i.e., $\bar{\sigma}_0$, $\bar{\sigma}_{\mathrm{p}}$, $\bar{\sigma}_{\mathrm{m}}$, $\bar{\sigma}_{\mathrm{r}}$, κ_{p}, and κ_{m}) are used to define the CDPM for the expanded masonry units. The properties of the potential crack interface corresponding to different r_{σ} for the different SMMs of the RVE are given in **Table 6.4**. It is noted here that the CSTIM for the potential crack interface requires only the properties associated with the shear-tension failure criterion. Therefore, the only required paramaters are: f_{t}, C_0, C_{Q0}, ϕ_0, ϕ_{r}, ψ_0, ψ_{r}, $G_{\mathrm{f}}^{\mathrm{I}}$, and $G_{\mathrm{f}}^{\mathrm{II}}$; where f_{t} and $G_{\mathrm{f}}^{\mathrm{I}}$ are obtained from the properties of the masonry units for the DMM; ϕ_0, ϕ_{r}, ψ_0, and ψ_{r} are assumed equal to 1; and C_0, C_{Q0}, and $G_{\mathrm{f}}^{\mathrm{II}}$ are defined as functions of f_{t} or $G_{\mathrm{f}}^{\mathrm{I}}$ [184].

Table 6.2. Elastic properties of the masonry joint interface in the RVEs for SMMs corresponding to different r_σ.

Joint	Properties (N/mm^3)	SMM-I							SMM-II and SMM-III						
		0.1	0.2	0.5	1.0	2.0	5.0	10.0	0.1	0.2	0.5	1.0	2.0	5.0	10.0
Bed	k_n	2.33	4.59	10.99	20.59	36.52	68.18	95.89	17.9	40.4	161.5	2100.0	323.1	201.9	179.5
	k_s	1.01	1.99	4.78	8.95	15.88	29.64	41.69	7.8	17.6	70.2	913.0	140.5	87.8	78.0
Head	k_n	1.64	3.24	7.87	15.00	27.45	54.69	81.71	17.9	40.4	161.5	2100.0	323.1	201.9	179.5
	k_s	0.71	1.41	3.42	6.52	11.94	23.78	35.53	7.8	17.6	70.2	913.0	140.5	87.8	78.0

Table 6.3. Inelastic compressive properties of the masonry joint interface (SMM-I and SMM-II) or expanded masonry unit (SMM-III) in the RVEs for SMMs corresponding to different r_σ.

Properties		0.1	0.2	0.5	1.0	2.0	5.0	10.0
$\bar{\sigma}_0$	(MPa)	0.0741	0.1638	0.4437	0.9038	0.9155	0.9178	0.9179
$\bar{\sigma}_p$	(MPa)	0.2223	0.4915	1.3311	2.7114	2.7465	2.7535	2.7536
$\bar{\sigma}_m$	(MPa)	0.1111	0.2457	0.6655	1.3557	1.3732	1.3767	1.3768
$\bar{\sigma}_r$	(MPa)	0.0318	0.0702	0.1902	0.3873	0.3924	0.3934	0.3934
κ_p	(-)	0.0002	0.0006	0.0025	0.0087	0.0018	0.0012	0.0011
κ_m	(-)	0.0007	0.0015	0.0037	0.0101	0.0026	0.0017	0.0016
C_{ss}	(-)	9.0	9.0	9.0	9.0	9.0	9.0	9.0

Table 6.4. Properties of the potential crack interface in the RVEs for SMMs corresponding to different r_σ.

Properties		0.1	0.2	0.5	1.0	2.0	5.0	10.0
k_n	(N/mm^3)	210	420	1050	2100	4200	10500	21000
k_s	(N/mm^3)	91	183	457	913	1826	4565	9130
f_t	(MPa)	0.055	0.110	0.275	0.550	1.100	2.750	5.500
C_0	(MPa)	0.077	0.154	0.385	0.770	1.540	3.850	7.700
C_{Q0}	(MPa)	0.077	0.154	0.385	0.770	1.540	3.850	7.700
$\tan\phi_0$	(-)	1.000	1.000	1.000	1.000	1.000	1.000	1.000
$\tan\phi_r$	(-)	1.000	1.000	1.000	1.000	1.000	1.000	1.000
$\tan\psi_0$	(-)	1.000	1.000	1.000	1.000	1.000	1.000	1.000
$\tan\psi_r$	(-)	1.000	1.000	1.000	1.000	1.000	1.000	1.000
G_f^{I}	(N/mm)	0.0011	0.0022	0.0055	0.0110	0.0220	0.0550	0.1100
G_f^{II}	(N/mm)	0.0110	0.0220	0.0550	0.1100	0.2200	0.5500	1.1000

6.5.3. *Three-point bending test results*

The FE models of the RVE for different r_σ were subjected to a three-point bending loading by imposing a monotonically increasing midspan deflection up to 1.0 mm. The relative difference in the peak flexural load, $\delta_{P_{\max}}$, and initial stiffness, δ_k, for the SMMs of the RVE with respect to the corresponding FE response of the DMMs are presented in **Table 6.5**. The results corresponding to $P_{\max}$ show that: (1) all the SMMs overpredict $P_{\max}$ with the exception of the SMM-I for r_σ = 2.0; (2) $\delta_{P_{\max}}$ for $\mathrm{r}_\sigma \leq 1.0$ are greater than 119.50%, 80.54%, and 22.70%, for SMM-I, SMM-II, and SMM-III, respectively, and $\delta_{P_{\max}}$ corresponding to the SMM-I and SMM-II increases for decreasing r_σ, whereas $\delta_{P_{\max}}$ corresponding to the SMM-III decreases for decreasing r_σ; (3) $\delta_{P_{\max}}$ for $2.0 \leq \mathrm{r}_\sigma \leq 5.0$ vary between -1.46% and 10.89%, indicating that all SMMs predict $P_{\max}$ values that are consistent with those obtained using the DMM within this range of r_σ; and (4) $\delta_{P_{\max}}$ for r_σ = 10.0 are equal to 133.27%, 85.04%, and 41.41%, for SMM-I, SMM-II, and SMM-III, respectively. In addition, the SMMs provide k values that are consistent with those obtained using the DMM for $\mathrm{r}_\sigma \geq 1.0$, for which δ_k varies between -6.44% to 11.49%. By contrast, all SMMs underpredict the k obtained from the DMM for $\mathrm{r}_\sigma \leq 0.5$, and δ_k increases in absolute value for decreasing r_σ.

Table 6.5. Comparison of FE results using DMM and SMMs for the RVE of masonry subjected to three-point bending for varying r_σ.

r_σ	$\delta_{P_{\max}}$ (%)			δ_k (%)			Match crack pattern with DMM		
	SMM-I	SMM-II	SMM-III	SMM-I	SMM-II	SMM-III	SMM-I	SMM-II	SMM-III
0.1	745.54	520.42	22.70	-36.56	-37.29	-36.80	No	No	Yes
0.2	291.42	280.65	36.70	-33.06	-32.38	-31.21	No	No	Yes
0.5	226.83	233.63	75.80	-15.58	-19.28	-18.95	No	No	No
1.0	119.50	80.54	93.47	0.54	-6.04	-6.44	No	No	No
2.0	-1.46	5.99	6.58	-2.95	1.09	0.07	Yes	Yes	Yes
5.0	9.09	6.79	10.89	7.85	2.07	5.62	Yes	Yes	Yes
10.0	133.27	85.04	41.41	11.49	1.76	8.17	No	No	No

Figure 6.3 depicts the FE crack patterns and distribution of in-plane maximum principal plastic strains observed at 1.0 mm midspan deflection for SMMs and DMM of RVEs subjected to three-point bending. **Table 6.5** also indicates (with a Yes/No) if the FE crack patterns obtained using the SMMs match with those obtained using the DMM. The cracks in the masonry units and mortar in the DMMs are identified by large values of the plastic strain. The FE crack patterns and the distribution of in-plane maximum plastic strains for the DMMs of the RVEs subjected to three-point bending show that: (1) for $r_\sigma \leq 0.2$, the RVEs fail in compression-shear at the pinned supports in the bottom masonry units and in compression at the point of load application in the top masonry units; (2) for $0.5 \leq r_\sigma \leq 1.0$, the RVEs fail in compression at the point of load application in the top masonry units; (3) for $2.0 \leq r_\sigma \leq 5.0$, the RVEs fail due to the opening of a crack in the middle of RVEs; and (4) for $r_\sigma = 10.0$, the RVE fails in tension/shear, with the formation of a mechanism in which the masonry unit near the roller support detaches from the rest of the RVE. By comparing the crack patterns of the SMMs with those of the corresponding DMMs, it is observed that these crack patterns are consistent across all models for $2.0 \leq r_\sigma \leq 5.0$; however, SMM-I and SMM-II provide very different failure modes from those obtained using the DMM for any other value of r_σ; whereas SMM-III provide failure modes consistent with those obtaining using the DMMs for $r_\sigma \leq 0.2$, but not for other values of r_σ. As expected, SMM-I and SMM-II cannot capture failure modes involving failure of the masonry units that are not concentrated at the potential crack interfaces located in the middle of the expanded masonry units. SMM-III perform slightly better for very weak masonry units ($r_\sigma \leq 0.2$), by capturing the failure of the expanded masonry at the hinged support, but they are unable to capture the compression failure at the load application point because they do not explicitly model the compressive behavior of the masonry units, but only the homogenized compressive behavior of masonry (i.e., a combination of masonry unit and mortar behavior). For r_σ = 10, all SMMs fail to produce a realistic failure mechanism as the tensile strength of the masonry units (which coincides with the tensile strength of the potential crack interface), which is f_t = 5.50 MPa, is larger than the homogeneized compressive strength of masonry used to describe the masonry joint interfaces (SMM-I and SMM-II) or the expanded masonry units (SMM-III), which is $\bar{\sigma}_p$ = 2.754 MPa.

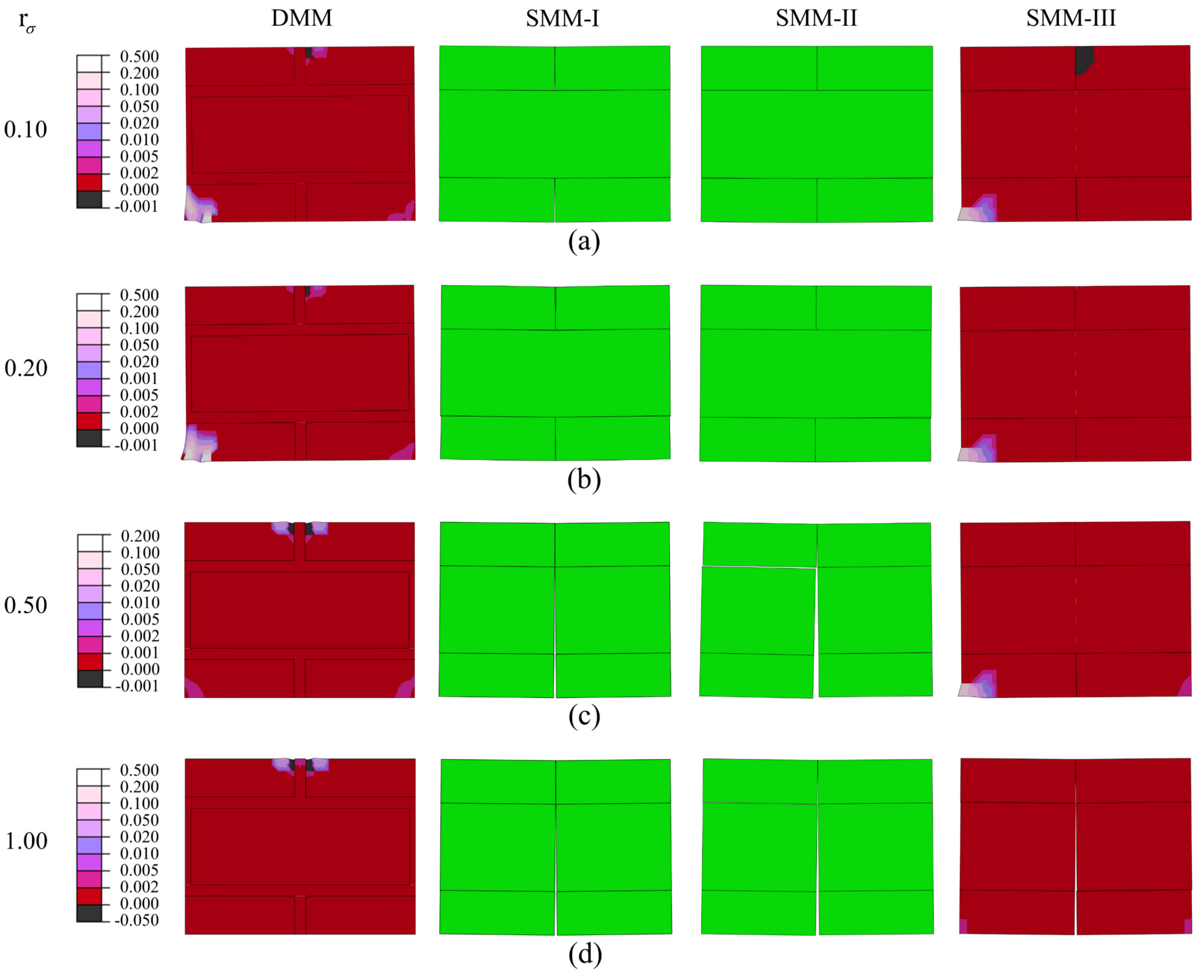

(a)

(b)

(c)

(d)

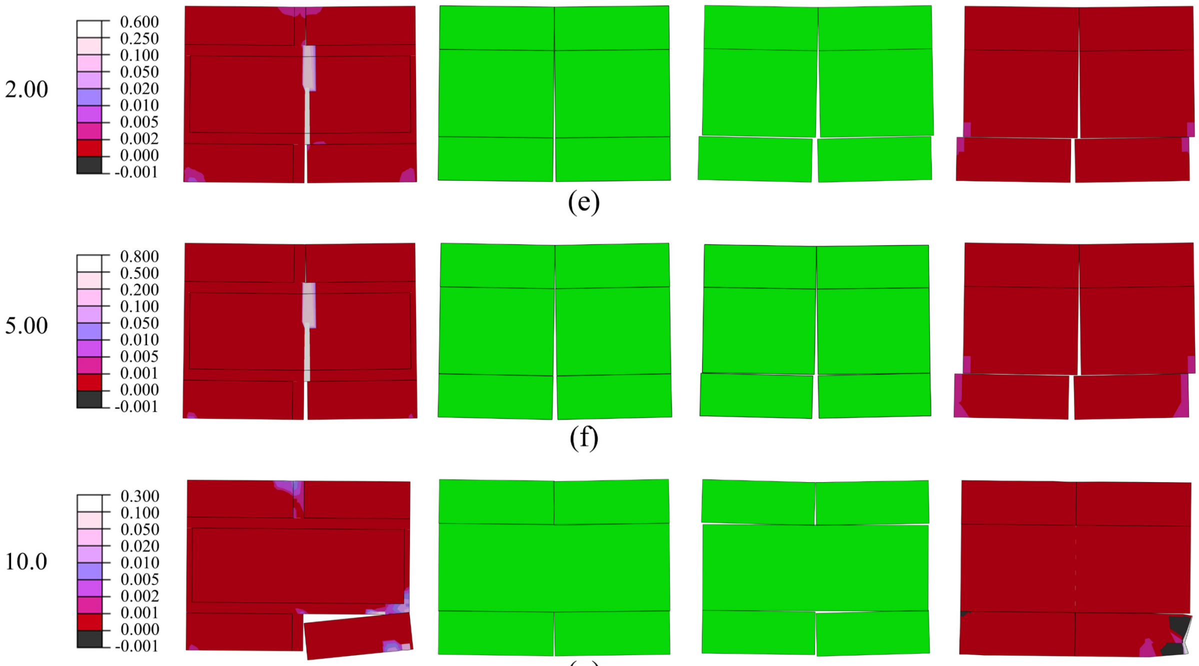

(e)

(f)

(g)

Figure 6.3. FE crack patterns and distribution of in-plane maximum principal plastic strain of the SMMs and DMM for the RVE of masonry subjected to three-point bending for varying r_σ : (a) 0.1, (b) 0.2, (c) 0.5, (d) 1.0, (e) 2.0, (f) 5.0, and (g) 10.0.

6.5.4. *Shear test results*

The FE models of the RVE for different r_σ were subjected to shear loading by imposing a monotonically increasing horizontal displacement of the top boundary of the model up to 1.0 mm. The relative difference in the peak shear load, $\delta_{P_{\max}}$, and initial stiffness, δ_k , for SMMs of the RVE with respect to the corresponding FE response of the DMMs are presented in **Table 6.6**. The results corresponding to $P_{\max}$ show that: (1) all SMMs overpredict the $P_{\max}$; (2) the $\delta_{P_{\max}}$ for $r_\sigma \leq 1.0$ are greater than 30.83%, 29.52%, and 23.09% for SMM-I, SMM-II, and SMM-III, respectively, and $\delta_{P_{\max}}$ corresponding to SMM-I and SMM-II increase for decreasing r_σ ; and (3) $\delta_{P_{\max}}$ for $r_\sigma \geq 2.0$ varies between 2.43% and 14.77%, which suggests that all SMMs can predict $P_{\max}$ values that are consistent with those obtained using the DMM when the masory units are significantly stronger than the mortar and the unit-mortar interface. SMM-II and SMM-III provide k values that are consistent with those obtained using the DMM for $\mathrm{r}_\sigma \geq 1.0$, for which δ_k varies between 0.80% and 2.21%. However, the δ_k values for the SMM-I are higher and vary between 13.41% and 20.08% when $\mathrm{r}_\sigma \geq 1.0$. Furthermore, all SMMs underpredict k for $\mathrm{r}_\sigma \leq 0.5$, as δ_k assume negative values larger in absolute value than 5.56%, 12.69%, and 11.74% for SMM-I, SMM-II and SMM-III. These negative values of δ_k increase in absolute value with decreasing r_σ.

Table 6.6. Comparison of FE results using DMM and SMMs for the RVE of masonry subjected to shear loading for varying r_σ.

r_σ	$\delta_{P_{\max}}$ (%)			δ_k (%)			Match crack pattern with DMM		
	SMM-I	SMM-II	SMM-III	SMM-I	SMM-II	SMM-III	SMM-I	SMM-II	SMM-III
0.1	486.14	126.56	48.51	-9.98	-23.28	-18.71	No	No	No
0.2	115.61	88.49	43.23	-8.49	-19.19	-17.08	No	No	No
0.5	64.22	57.10	63.28	-5.56	-12.69	-11.74	No	No	No
1.0	30.83	29.52	23.09	19.15	0.80	0.80	No	No	No
2.0	8.88	13.81	8.06	20.08	1.78	1.78	Yes	Yes	Yes
5.0	11.84	14.77	13.67	13.47	2.21	2.07	Yes	Yes	Yes
10.0	6.56	2.43	7.08	13.47	1.91	2.28	Yes	Yes	Yes

Figure 6.4 presents the FE crack patterns and the distribution of the in-plane maximum principal plastic strains observed at 1.0 mm shear displacement for the SMMs and DMM of the RVEs subjected to shear loading. The deformed shapes in the **Figure 6.4** are magnified by a factor 3 ito better show the crack patterns. **Table 6.6** also indicates (with a Yes/No) if the FE crack patterns obtained using the SMMs match with those obtained using the DMM. For the DMM, the cracks in the masonry units and the mortar are identified by large values of the plastic strain. The FE crack patterns and distribution of in-plane maximum plastic strains for the DMM of the RVE subjected to the shear loading show that: (1) for $\mathrm{r}_\sigma \leq 0.2$, the RVE fails in compression-shear where the loading is applied (top left masonry unit) and at the support (bottom right masonry unit);

(2) for $0.5 \le r_\sigma \le 1.0$, the RVE fails due to a diagonal crack in the middle masonry unit; and (3) for $r_\sigma \ge 2.0$, the RVE fails in shear at the unit-mortar interface and mortar of the DMM. By comparing the crack patterns of the SMMs with those of the corresponding DMMs, it is observed that these crack patterns are consistent across all models for $r_\sigma \ge 2.0$. However, SMMs provide very different failure modes from those obtained using the DMM for $r_\sigma \le 1.0$. As expected, the SMMs are unable to reproduce the failure modes of the DMM when the cracking takes place in the masonry units.

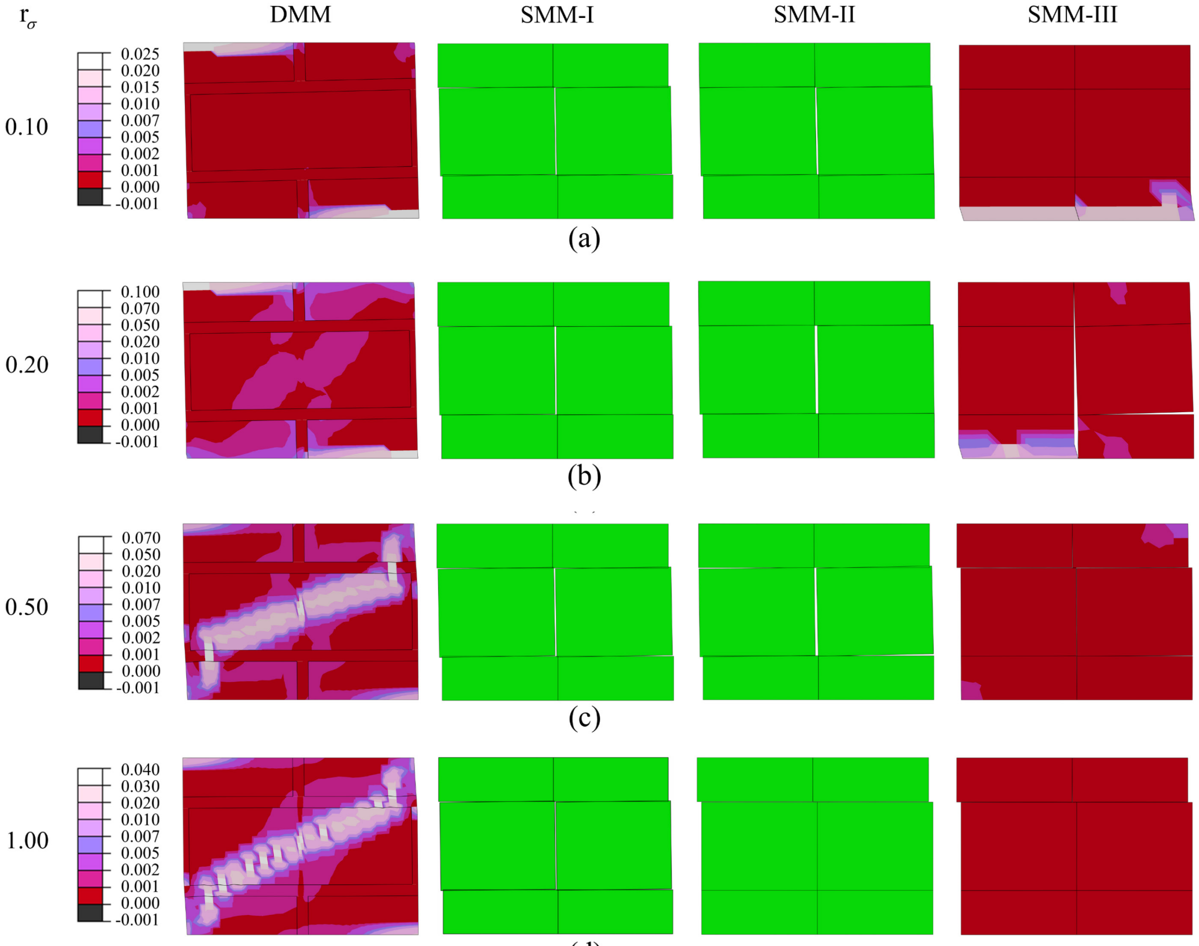

(a)

(b)

(c)

(d)

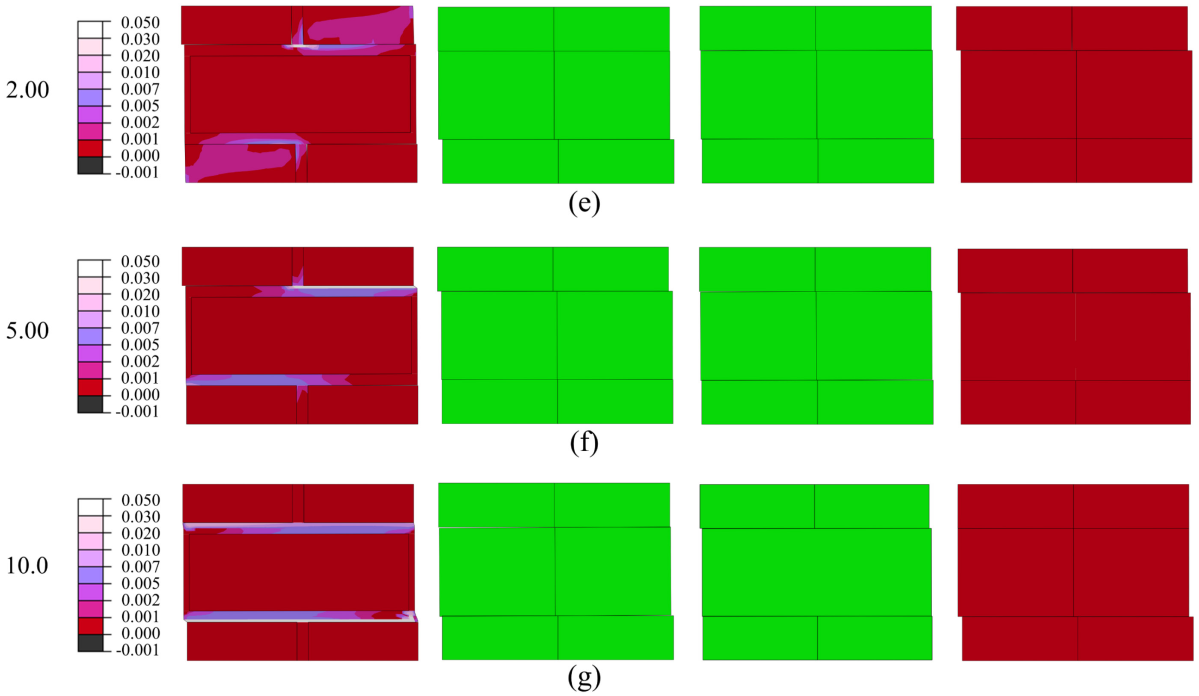

(e)

(f)

(g)

Figure 6.4. FE crack patterns and distribution of in-plane maximum principal plastic strain of the SMMs and DMM for the RVE of masonry subjected to shear load for varying r_σ: (a) 0.1, (b) 0.2, (c) 0.5, (d) 1.0, (e) 2.0, (f) 5.0, and (g) 10.0.

6.6. Validation of DMM Results for CSEB Masonry

The FE response obtained using the DMM proposed in this study was compared for validation purposes with the experimentally-measured response of CSEB wallettes subjected to diagonal compression, which is documented in the literature [167]. This comparison also includes the FE responses obtained using different SMMs, which were found to provide inaccurate predictions of the experimental response in the chapter 5. The comparison between numerical and experimental responses is quantified in terms of the point-wise relative errors in the peak load $\left(P_{\max}\right)$, initial stiffness $\left(k\right)$, and displacement at peak load $\left(\Delta_{\mathrm{p}}\right)$, which are defined as follows:

$$\varepsilon_X = \frac{X_{\mathrm{FE}} - X_{\exp}}{X_{\exp}} \tag{6.2}$$

where $X = P_{\max}$, k, or Δ_{p}; and the subscript FE denotes DMM, SMM-I, SMM-II, or SMM-III. Since the experiment included three nominally-identical of the CSEB wallettes, $X_{\exp}$ is taken as the average of the corresponding experimentally-measured values. In addition, the accuracy of the different FE models in estimating the force-displacement response curve is evaluated using three different global relative errors, i.e., the mean error $(\varepsilon_{\mathrm{mean}})$, root mean squared error $(\varepsilon_{\mathrm{RMS}})$, and mean absolute error $(\varepsilon_{\mathrm{abs}})$, which are defined as:

$$\varepsilon_{\mathrm{mean}} = \frac{1}{n_s}\sum_{j=1}^{n_s}\left[\frac{1}{n_j}\sum_{i=1}^{n_j}\frac{\left(P_{\mathrm{FE}}^{(i)} - P_{\exp,j}^{(i)}\right)}{P_{\exp,j}^{(i)}}\right] \tag{6.3}$$

$$\varepsilon_{\mathrm{RMS}} = \frac{1}{n_s}\sum_{j=1}^{n_s}\left[\sqrt{\frac{1}{n_j}\sum_{i=1}^{n_j}\left[\frac{P_{\mathrm{FE}}^{(i)} - P_{\exp,j}^{(i)}}{P_{\exp,j}^{(i)}}\right]^2}\right] \tag{6.4}$$

$$\varepsilon_{\mathrm{abs}} = \frac{1}{n_s}\sum_{j=1}^{n_s}\left[\frac{1}{n_j}\sum_{i=1}^{n_j}\frac{\left|P_{\mathrm{FE}}^{(i)} - P_{\exp,j}^{(i)}\right|}{P_{\exp,j}^{(i)}}\right] \tag{6.5}$$

in which $P_{\exp,j}^{(i)}$ and $P_{\mathrm{FE}}^{(i)}$ denote the experimentally-measured and numerically simulated values, respectively, of the reaction force for a given masonry wall measured at a given level of displacement, $\Delta^{(i)}$; n_j denotes the number of recorded displacement levels for the *j*-th experimental sample and corresponds to the maximum displacement level corresponding to the experimental displacement at failure; and n_s denotes the number of experimental specimens. In this investigation, the global relative errors were calculated using displacement increments equal to 0.01 mm.

6.6.1. *Description of experimental tests*

This study uses as benchmark the experimental results from a diagonal compression test performed on unreinforced CSEB masonry wallettes and available in the literature [167]. Three nominally identical single-leaf CSEB masonry wallettes were tested. They had dimensions of 864 mm × 787 mm × 178 mm and were constituted by 8 courses, as shown in **Figure 6.5**(a). The wallettes were built using CSEBs with dimensions equal to 254 mm × 178 mm × 89 mm and fabricated using silty loam soil and 6% cement. The earthen mortar layers had thickness equal to 13 mm, and the mortar was fabricated using a cement:soil:sand proportion by weight equal to 1:1:6 and a water-to-cement ratio equal to 2.4. The CSEB masonry wallettes were tested in a diagonal compression test, as shown in **Figure 6.6**, with the help of steel shoes that were attached to the top and bottom corner of the wall. The experimental test involved a monotonically increasing downward vertical displacement applied on the steel shoe at the top of the masonry wallettes, whereas the steel shoe at bottom of the masonry wallette was kept fixed. The horizontal extension and vertical contraction were recorded using two displacement transducers, indicated as transducers A and B, respectively, in **Figure 6.5**(a).

Figure 6.6 shows the experimental crack patterns of the three CSEB masonry wallettes (identified as Wall-1, Wall-2, and Wall-3, respectively) at the end of the diagonal compression test. The three specimens exhibited consistent failure modes with diagonal cracks parallel to the direction of the load and inclined by approximately 45° with respect to the bed joints. The cracks at failure were observed mainly through the CSEBs and to a lesser extent along the head and bed joints, whereas they affected only in a minor manner the mortar or the unit-mortar interfaces.

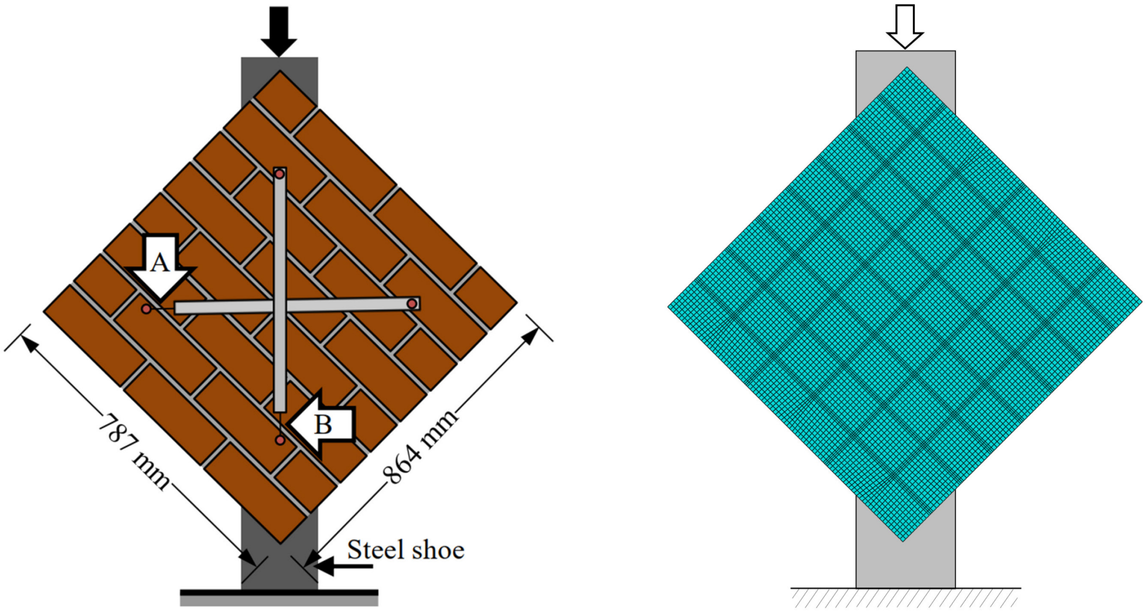

(a) (b)

Figure 6.5. Unreinforced CSEB masonry wallettes: (a) diagonal compression test setup, and (b) FE discretization of the DMM.

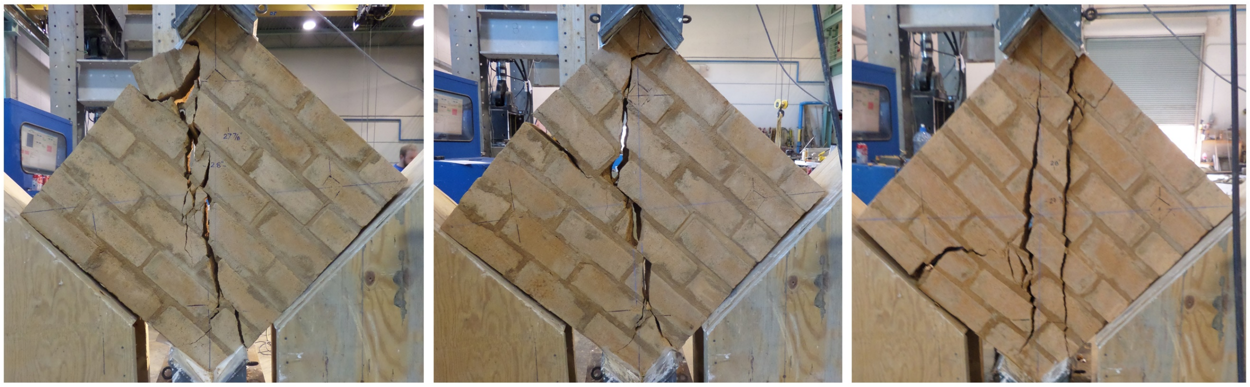

(a) (b) (c)

Figure 6.6. Experimental crack patterns of the unreinforced CSEB masonry wallettes: (a) Wall-1, (b) Wall-2, and (c) Wall-3.

6.6.2. *Description of the DMM developed for the CSEB masonry*

Figure 6.5(b) shows the FE discretization for the DMM of the CSEB masonry wallettes used in this study. The mesh discretization comprised 27 and nine elements employed across the length and thickness, respectively, of each earth block, for a total of 243 elements. Three elements were employed for the mortar thickness. The size of the elements in the blocks was kept constant, except for the regions corresponding to the middle of the earth blocks, where the element size was reduced to match the dimension of the elements in the head joints. The unit-mortar interfaces where discretized using zero-length elements with the same length of the adjacent continuum elements. In addition, the steel shoes were modeled as linear elastic, and a surface-based tie constraint [284] was imposed between the masonry wallettes and the steel shoes. The DMM was analyzed using the explicit dynamic FE solver with time step equal to the critical time step of 1.0×10^{-6} s. All degrees of freedoms at the bottom edge of the bottom steel shoe were fixed, and a constant vertical velocity of $V = 0.1$ mm/s (i.e., with zero acceleration) was applied downward to the top edge of the top steel shoe. A density $\rho_b = 1.8 \times 10^3$ kg/m^3 and a mass-proportional damping corresponding to a damping ratio $\zeta = 5\%$ were used for the solid elements of the wallette to model inertia and damping effects. The steel shoes were modeled as linear elastic with elastic modulus $E_s = 21000$ MPa, Poisson ratio $\nu_s = 0.30$, density $\rho_s = 7.85 \times 10^3$ kg/m^3, and damping ratio $\zeta_s = 5\%$. The mesh of the steel shoes was extruded from that of the masonry wallettes in order to produce a continuous mesh. Two elements were used across the thickness of the steel shoes. The material properties of different constituents used in the DMM were obtained from existing experimental results from tension, shear, and compression tests of the components, which are available in the literature [167,173]. The properties of the masonry units, mortar, and unit-mortar interface used for developing the DMM are tabulated in unreinforced **Table 6.7**. The remaining CDPM parameters used to fully describe the masonry units and mortar are: $\psi_c = 38°$, $e_c = 0.1$, $\beta_{bc} = 1.16$, $K_c = 0.67$, $\eta = 8.5 \times 10^{-5}$.

Table 6.7. Material properties of different components used in the DMM of unreinforced CSEB masonry wallettes.

Properties		Masonry units	Unit-mortar interface	Mortar
E	(MPa)	2550	-	2100
ν	(-)	0.17	-	0.150
k_n	(N/mm^3)	-	2100	-
k_s	(N/mm^3)	-	913	-
f_t	(MPa)	0.51	0.146	0.550
C_0	(MPa)	-	0.29	-
C_{Q0}	(MPa)	-	29.0	-
$\tan\phi_0$	(-)	-	1.51	-
$\tan\phi_r$	(-)	-	1.51	-
$\tan\psi_0$	(-)	-	0.440	-
$\tan\psi_r$	(-)	-	0.044	-
G_f^I	(N/mm)	0.009	0.0031	0.011
G_f^{II}	(N/mm)	-	0.0310	-
$\bar{\sigma}_0$	(MPa)	1.03	-	0.70
$\bar{\sigma}_p$	(MPa)	3.10	-	2.11
$\bar{\sigma}_m$	(MPa)	1.55	-	1.06
$\bar{\sigma}_r$	(MPa)	0.12	-	0.30
κ_p	(-)	0.0042	-	0.0009
κ_m	(-)	0.0082	-	0.0033

6.6.3. *FE response of unreinforced CSEB masonry*

Figure 6.7 shows the force-displacement responses obtained from the experimental diagonal compression test with the FE responses corresponding to the DMM and the three SMMs. Positive and negative displacements correspond to the horizontal extension and vertical contraction, respectively, as shown in **Figure 6.5**(a). The error measures for the different FE models are reported in **Table 6.8**, together with the CPU time ratios (CTRs) for the different models with respect to the CPU time corresponding to the SMM-II, which is assumed as reference (i.e., CTR = 1.00 for SMM-II).

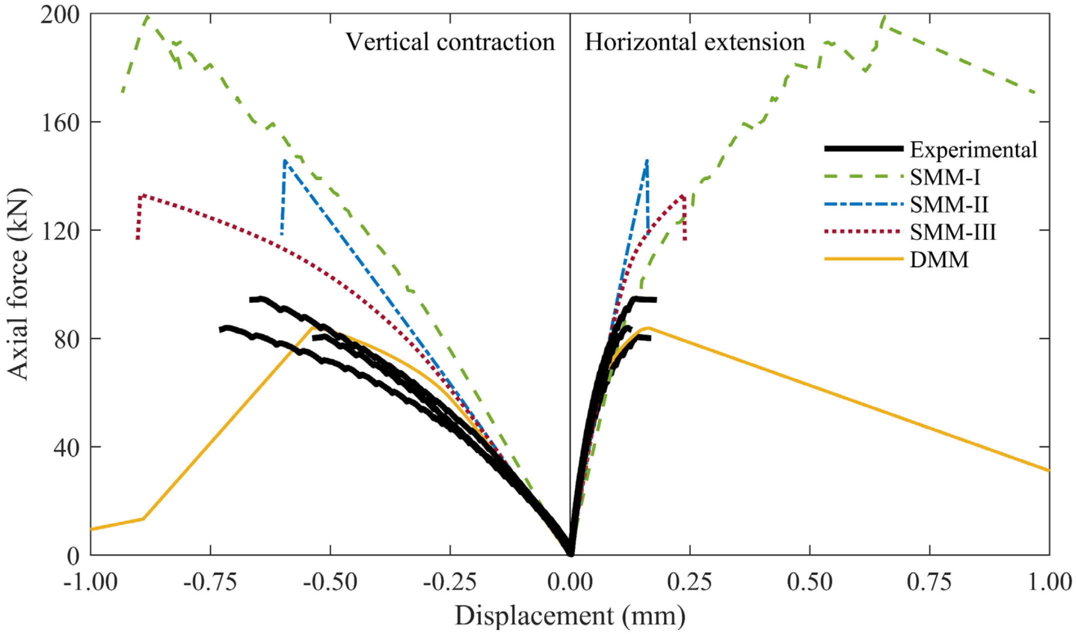

Figure 6.7. Comparison between experimental and FE responses for CSEB wallettes

It is observed that the DMM accurately estimates the peak strength of the CSEB wallette (i.e., $\varepsilon_{P_{\max}}$ = -3.10%), whereas the SMMs significantly over-estimate $P_{\max}$, with errors $\varepsilon_{P_{\max}}$ = 129.85%, 68.44%, and 53.96% for SMM-I, SMM-II, and SMM-III, respectively. All the FE models under-estimate the initial stiffness, in particular, DMM provides the lowest absolute value of ε_k for the horizontal extension (i.e., ε_k = -26.51%), but the highest for the vertical contraction (i.e., ε_k = -28.44%); whereas SMM-I present the highest absolute value of ε_k for the horizontal extension (i.e., ε_k = -44.18%), but the lowest for the vertical contraction (i.e., ε_k = -10.55%). In terms of displacement at the peak load, the SMM-II produces the most accurate estimates, with ε_{Δ_p} = 21.31% and -11.72% for the horizontal extension and the vertical contraction, respectively. The DMM provides results that are very close to those of the SMM-II, with ε_{Δ_p} = 24.96% and -13.81% for the horizontal extension and the vertical contraction, respectively. When considering the global relative errors, the DMM provides the most accurate prediction of the force-displacement response of the CSEB masonry wallette in both the horizontal extension and the vertical contraction, with $\varepsilon_{\text{mean}}$ = -4.13%, ε_{RMS} = 10.88%, and ε_{abs} = 8.71% for the horizontal extension, and $\varepsilon_{\text{mean}}$ = 2.22%, ε_{RMS} = 16.04%, and ε_{abs} = 13.27% for the vertical contraction. In terms of CTRs, as expected, the SMM-I is the least computationally demanding model, with CTR = 0.49, followed by the SMM-II (CTR = 1.0), SMM-III (CTR = 1.16), and DMM (CTR = 5.07), which is significantly more computationally expensive than the other models.

Table 6.8. Comparison between experimental and FE responses for CSEB wallettes in terms of proposed error measures.

Displacement transducers	FE Model	$\varepsilon_{P_{\max}}$ (%)	ε_k (%)	ε_{Δ_p} (%)	$\varepsilon_{\text{mean}}$ (%)	ε_{RMS} (%)	ε_{abs} (%)	CTR (-)
Horizontal extension	SMM-I	129.85	-44.18	384.98	-11.59	22.95	18.35	0.49
	SMM-II	68.44	-31.01	21.31	10.01	27.62	22.39	1.00
	SMM-III	53.96	-31.01	79.68	4.51	20.54	17.45	1.16
	DMM	-3.10	-26.51	24.96	-4.13	10.88	8.71	5.07
Vertical contraction	SMM-I	-	-10.55	37.33	53.09	59.24	54.45	-
	SMM-II	-	-25.67	-11.72	16.49	47.32	39.87	-
	SMM-III	-	-25.67	43.54	20.97	26.84	24.77	-
	DMM	-	-28.44	-13.81	2.22	16.04	13.27	-

The FE crack patterns and in-plane maximum principal plastic strains observed at 0.25 mm, 0.50 mm, and 1.0 mm vertical contraction for the DMM of CSEB masonry wallettes are presented in **Figure 6.8**. The deformed shapes in **Figure 6.8** are magnified by a factor 10 in order to make the cracks in the unit-mortar interface more visible, whereas the cracks in the masonry units and mortar are identified by large values of the plastic strain. In **Figure 6.8**(a), i.e., vertical contraction equal to 0.25 mm, small zones of concentrated plastic strain are observed at the top and bottom corners of the CSEB masonry wallettes. For increasing values of vertical contraction, these small zones of concentrated plastic strain evolve into a wide diagonal band of increasing plastic strain. This diagonal band is parallel to the loading direction and goes across the masonry wallettes affecting both masonry units and mortar. **Figure 6.8**(b) shows this diagonal band of plastic strain at 0.50 mm vertical contraction (which corresponds to the vertical contraction immediately before the peak vertical load is reached). After the peak load is achieved, the plastic strain rapidly increases in the middle of the masonry wallettes and concentrates into a narrow diagonal band passing through both masonry units and mortar. and leads to the failure of the CSEB masonry wallettes. This narrow diagonal band, which represents the cracks forming across the masonry wallettes, is almost parallel to the loading direction and has plastic strains varying between 0.05 mm/mm and 0.10 mm/mm at 1.00 mm vertical contraction, as shown in **Figure 6.8**(c). It is observed that this narrow band of concentrated plastic strain in the DMM is very similar to the cracks observed during the experiments, as reported in **Figure 6.6**. It is concluded that the DMM can match the experimental crack patterns of the CSEB masonry wallettes. This result is in contrast with the FE crack patterns predicted by the SMMs, which do not match the experimental crack patterns of the CSEB masonry wallettes, as reported in the chapter 5. The numerically simulated cracks in the SMMs are mostly concentrated along the bottom two masonry bed joints, and at the head joints and potential crack interfaces of the bottom two courses of the masonry wallette.

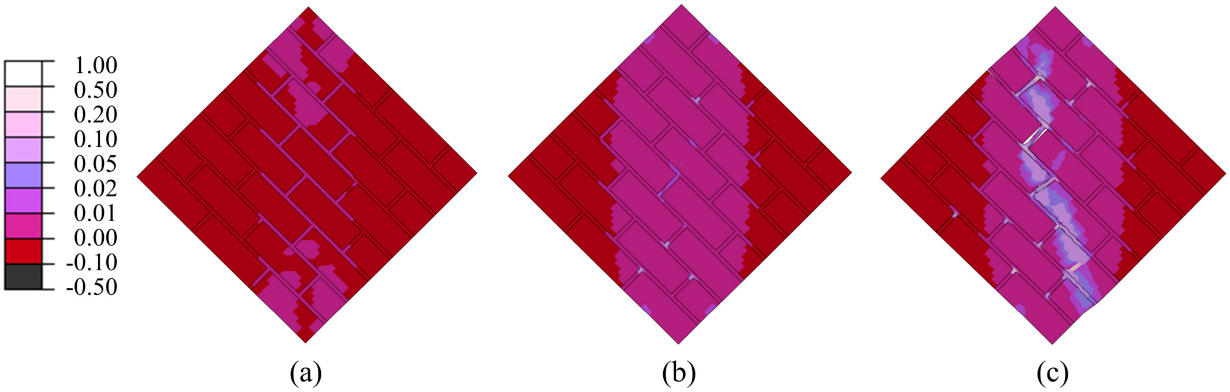

Figure 6.8. FE crack patterns and distribution of in-plane maximum principal plastic strain for DMMs of the CSEB masonry wallettes at different vertical contraction: (a) 0.25 mm, (b) 0.50 mm and (c) 1.0 mm.

Figure 6.9 presents the distribution of the in-plane minimum principal stress observed at 0.25 mm, 0.50 mm, and 1.0 mm of vertical contraction for the DMM of the CSEB masonry wallettes. When a vertical load is applied in the DMM, a diagonal compressive strut forms in the middle of the masonry wallettes and parallel to the loading direction. **Figure 6.9**(a) and (b) show that the width of this diagonal compressive strut increases for increasing vertical load. However, this diagonal compressive strut quickly disappears after the peak load is reached because of the significant increase of plastic strain corresponding to the cracks in the middle of the masonry wallettes, which ultimately lead to the failure of the CSEB wallettes, as shown in **Figure 6.9**(c). The in-plane minimum principal stress in the compressive strut varies between 0.5 and 1.0 MPa at the peak vertical load, which is significantly lower than the compressive strength of the When compared to the $\bar{\sigma}_p$ of masonry units ($\bar{\sigma}_p$ = 3.10 MPa) and mortar ($\bar{\sigma}_p$ = 2.11 MPa). In addition, the negative maximum principal plastic strain (which corresponds to the plastic behavior in compression) is negligible, as observed in **Figure 6.8**. These results confirm that the assumed two-dimensional plane stress condition is valid for the considered problem [246,275].

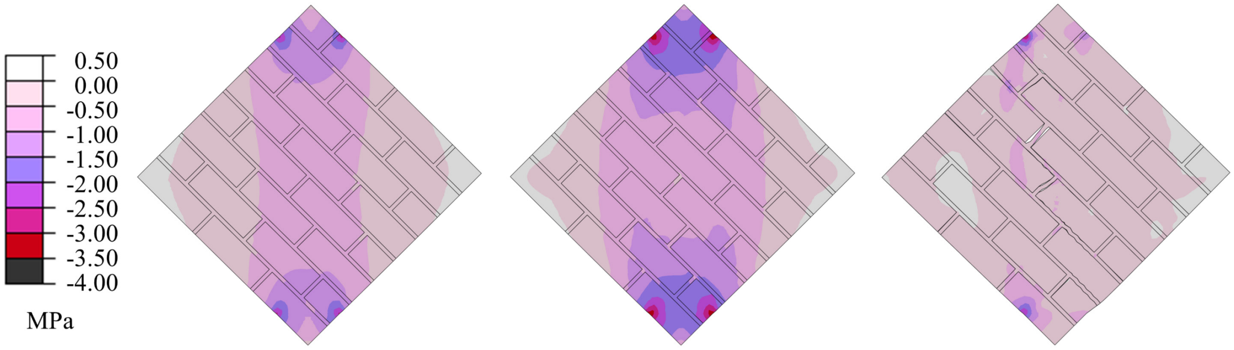

(a) (b) (c)

Figure 6.9. Distribution of in-plane minimum principal stress for the DMM of the CSEB masonry wallettes at different vertical contraction: (a) 0.25 mm, (b) 0.50 mm, and (c) 1.0 mm.

It is concluded that: (1) the proposed DMM can successfully simulate the mechanical behavior of CSEB masonry wallettes subjected to a diagonal compression test; and (2) although more computationally expensive than the SMMs, the use of the DMM is necessary to capture the crack propagation through the masonry units and the mortar that is typically observed in earth block masonry, for which the strength and stiffness properties of the masonry units and the mortar are similar.

6.7. Conclusion

This study presents a finite element (FE) detailed micro-model (DMM) approach for simulating the structural response of unreinforced masonry (URM). This DMM is specifically tailored to predict the mechanical behavior of compressed and stabilized earth block (CSEB) masonry, whose failure modes are often characterized by plasticity and cracking that are spread across the different masonry components, namely units, mortar, and unit-mortar interfaces. Through the FE response simulation of masonry's representative volume elements (RVEs) subject to different loading conditions, this study also identifies the specific conditions, in terms of the ratio r_σ between the strength of masonry units and mortar, under which the proposed DMM and commonly-used simplified micro-models (SMMs) provide consistent or inconsistent simulations of URM structural response. It is found that the FE results obtained using the proposed DMM and the existing SMMs are consistent only in the range $2.0 \leq r_\sigma \leq 5.0$ for a loading condition corresponding to a three-point bending test, and for $r_\sigma \leq 2.0$ for a loading condition corresponding to a shear loading test. In fact, for $r_\sigma \leq 1.0$ and both loading conditions considered in this study, the SMMs cannot describe the spread of the inelastic behavior across the different masonry components, which by contrast is captured by the DMM.

In addition, the proposed DMM was also validated by comparing its FE response results with experimental data available in the literature for CSEB wallette subjected to a diagonal compression test. For this specific test, the SMMs were previously shown to provide FE results that are in poor agreement with the experimentally-measured response. This study shows that the proposed DMM can successfully simulate the mechanical behavior of CSEB masonry by providing accurate estimates of the strength, initial stiffness, deflection at peak load, force-displacement response, and failure mechanism. It is concluded that the proposed DMM represents a useful tool for simulation and prediction of the mechanical response of URM systems with units of equal or lower strength than the mortar, and in particular of CSEB masonry systems.

CHAPTER 7. CONCLUSIONS AND RECOMMENDATIONS FOR FUTURE WORK

In this chapter, the main conclusions drawn from the studies in Chapter 2 through Chapter 6 are summarized, and recommendations for future work are offered.

7.1. Conclusions

Chapter 2 presents the structural, architectural, and economic feasibility study for compressed and stabilized earth block (CSEB) construction in the U.S. Gulf Coast. The main conclusions from the feasibility study are summarized as follows:

1. The CSEBs fabricated with at least 9% in weight (wt.%) of cement content satisfy the minimum strength requirements for building single-story dwellings in high wind regions.
2. Soil-sand-cement mortars with 15 wt.% cement and at least 30 wt.% sand can be used with CSEBs.
3. Exterior CSEB walls need a protection from the weather conditions in a humid climate, and a dual layer plaster consisting of a soil-cement stucco with a coat of cement paste seems to provide a sufficient protection.
4. Hurricane-resistant earthen dwellings can be built using single- or double-wythe CSEB masonry walls.
5. CSEB masonry systems can be used to build houses based on local vernacular architecture, which could promote their acceptance from the local population.
6. Mortarless Interlocking CSEB walls can be built at a lower cost than other traditional wall systems, i.e. (in order of increasing average cost), light-frame wood, concrete block, and fired clay brick wall systems. By contrast, traditional mortared CSEB walls are generally expensive

because of the high labor required for their construction, resulting less expensive than only fired-clay brick walls.

In chapter 3, the effect of sugarcane bagasse fibers (SCBF) on the mechanical strength and durability properties of CSEBs was examined and compared with recommendations available in design standards and the literature. The conclusions drawn from these investigations are as follows:

1. The scanning electron microscopy results show that increasing the cement content in the CSEBs led to a denser and more homogeneous soil-cement matrix. The X-ray crystallography results suggest that the formation of Ca-bearing minerals (e.g., anorthite, rankinite, ettringite, and portlandite) makes the soil-cement matrix denser and stronger.
2. The modulus of rupture (MOR) and the flexural modulus of elasticity (MOE_f) of CSEBs improved with increasing cement content and given SCBF content; however, the flexural toughness index ($FT\text{-}I_5$) decreased. The effect of the SCBF content for a given cement content was dependent on the amount of cement, with positive effects on both MOR and $FT\text{-}I_5$ up to a critical fiber content due to fiber-bridging of the cracks. The critical fiber content was identified as 0.5 wt.% for CSEBs without cement. It is hypothesized that the value of the critical fiber content increases with the cement content until the failure mechanism is controlled by fiber fracture. Increasing SCBF content always corresponded to a decrease in MOE_f for any constant cement content.
3. For a constant SCBF content, the dry compressive strength (f_{bd}) and modulus of elasticity (MOE_d) increased, whereas the dry compressive toughness index ($DCT\text{-}I_5$) showed only a small decrease for increasing cement content. For any given cement content, the f_{bd} reached their maximum values at 0.5 wt.% SCBF content, the MOE_d decreased, and the $DCT\text{-}I_5$

behavior was dependent on the cement amount. In particular, the DCT-I5 reached a peak value for 0.5 wt.% SCBF content at 0.0 wt.% cement, whereas it monotonically increased for increasing SCBF content at both 6 wt.% and 12 wt.% cement contents. Similar to the flexural properties, it is hypothesized that a critical fiber content exists for different cement contents; however, the compressive behavior is controlled by a confinement effect produced by the fibers on the soil-cement matrix.

4. The earth blocks fabricated without stabilization (i.e., without cement addition) did not survive the wet compression test nor the wetting and drying cycles of the durability test. Therefore, stabilization is necessary to produce earth blocks that can endure severe wetting and drying cycles.
5. The mechanical properties of CSEBs under wet conditions followed trends similar to those of the corresponding dry mechanical properties. The wet compressive strength and wet modulus of elasticity were 41-59% and 29-43% lower, respectively, than their dry counterparts, whereas the wet compressive toughness index values are very similar to their dry counterparts.
6. Higher amounts of cement corresponded to better durability for any given SCBF amount. The CSEBs that survived the durability test showed an increase in loss in mass and water absorption with increasing SCBF content and constant cement content; however, variations of SCBF amount did not affect the dry density of CSEBs.
7. The CSEBs stabilized with 6 wt.% cement showed a reduction in wet compressive strength (between 29% and 61%) and modulus of elasticity (between 23% and 62%); whereas the wet compressive toughness index showed changes between 17% increase and 7% decrease. By contrast, the CSEBs stabilized with 12 wt.% cement had an 11-26% increase in wet

compressive strength, an 11-17% increase in wet modulus of elasticity, and a 3-23% reduction in wet compressive toughness index.

8. The CSEBs with 0.5 wt.% or 1.0 wt.% SCBF and 12 wt.% cement contents provided the best compromise between strength and durability among the compositions considered in this study.

Chapter 4 introduced a new interface element's constitutive model, referred to as coupled tension-shear interface model (CTSIM), for FE analysis of masonry structures using the simplified micro-modeling approach. This new model can simulate tension cracking, shear slipping, and compression failure and is defined by a convex composite failure surface consisting of a tension-shear failure criterion and a compression cap failure criterion. The performance of the CTSIM in terms of robustness, computational cost, and accuracy was compared to other similar models available in the literature through a series of one-element tests and through the comparison of FE response simulation and experimental results for an unreinforced masonry shear wall. It was found that:

1. The CTSIM is at least as efficient as and more robust than the other constitutive models for varying load step sizes and load paths in one-element tests.
2. The use of a single failure surface for mode-I and mode-II failure can improve the computational efficiency and robustness of the constitutive model when compared to constitutive models that use two separate failure surfaces.
3. The use of a single failure surface for all failure mechanisms has negative effects on the computational efficiency and robustness of the constitutive model when compared to constitutive models that use multi-surface criteria.
4. Constitutive models based on the hypothesis of strain hardening seem to be more efficient and robust than those based on the hypothesis of work hardening.

In Chapter 5, the capabilities and limitations of different FE simplified micro-modeling techniques were investigated through a comparative analysis of their simulation capabilities for two different types of masonry, i.e., FCB and CSEB masonry. Three different simplified micro-model (SMM) were developed for each benchmark examples, based on the different material constitutive models used for the masonry units, i.e., rigid (SMM-I), elastic (SMM-II), and elasto-plastic (SMM-III) constitutive models. Based on the FE simulation results, the following conclusions are made:

1. The inelastic behavior of FCB walls with masonry units significantly stronger than mortar and unit-mortar interfaces is concentrated along the masonry joints and potential crack surfaces of known locations. This behavior is consistent with the assumptions made to build SMMs.
2. The inelastic behavior of CSEB walls with masonry units of strength similar to that of mortar and unit-mortar interfaces is spread across all masonry components. This behavior is not consistent with the assumptions made to build SMMs.
3. All versions of the simplified micro-modeling techniques can accurately simulate the FE response behavior of the FCB masonry walls; however, this technique is not suitable for the CSEB masonry, because the simplified micro-modeling approach does not allow crack propagation through the expanded masonry units. Therefore, a FE detailed micro-modeling approach must be developed and used to simulate the behavior of masonry with inelastic behavior spread among all masonry components, such as in the case of CSEB masonry systems.
4. The comparison of FE and experimental peak strength shows that SMMs tend to overestimate the shear strength of the wall, and this overestimation increases for increasing levels of initial vertical pressure. This overestimation of the shear strength by SMMs is probably because of

the constraint imposed on the crack path by the single vertical potential crack interface, which is deterministically located in the middle of the masonry units.

This Chapter also provides recommendations on the use of different FE solvers and on the mesh and time step discretization for developing accurate and robust SMMs within the FE framework. In particular, it is shown that implicit static, implicit dynamic, and explicit dynamic solvers produce similar mechanical responses when used to simulate the nonlinear inelastic behavior of unreinforced masonry walls; however, the explicit dynamic solver is significantly more efficient than the other solvers from a computational point of view.

Chapter 6 presents a FE detailed micro-model (DMM) approach for simulating the structural response of unreinforced masonry. This DMM is specifically tailored to predict the mechanical behavior of CSEB masonry, whose failure modes are often characterized by plasticity and cracking that are spread across the different masonry components, namely units, mortar, and unit-mortar interfaces. Through the FE response simulation of masonry's representative volume elements (RVEs) subject to different loading conditions, this study also identifies the specific conditions, in terms of the ratio r_σ between the strength of masonry units and mortar (i.e., $r_\sigma = 0.1, 0.2, 0.5, 1.0, 2.0, 5.0$, and 10.0), under which the proposed DMM and commonly-used SMMs provide consistent or inconsistent simulations of unreinforced masonry structural response. Based on the FE simulation results, the following conclusions are made:

1. The SMMs are consistent only in the range $2.0 \leq r_\sigma \leq 5.0$ for a loading condition corresponding to a three-point bending test, and for $r_\sigma \leq 2.0$ for a loading condition corresponding to a shear loading test.

2. For $r_\sigma \leq 1.0$ and both loading conditions considered in this study, the SMMs cannot describe the spread of the inelastic behavior across the different masonry components, which by contrast is captured by the DMM.

In addition, the proposed DMM was also validated by comparing its FE response results with experimental data available in the literature for CSEB wallette subjected to a diagonal compression test, and the DMM can successfully simulate the mechanical behavior of CSEB masonry by providing accurate estimates of the strength, initial stiffness, deflection at peak load, force-displacement response, and failure mechanism.

7.2. Future research work

The research presented in this dissertation advanced the engineering knowledge needed to pave the way for a broader usage of earthen buildings. It also highlighted research questions that are still open and should be addressed in future work. This section summarizes the major issues that could be object of future studies by organizing them by chapter of the dissertation.

7.2.1. *Recommendations for future research work based on chapter 2*

1. In the present study, Portland cement was used as the stabilizer material and as an ingredient of the weather protection plaster for CSEB houses. Other more sustainable solutions should also be considered in future studies, e.g.: using lime as stabilizer; modifying foundations, roofing, and building geometry to minimize the weather effects in rainy environments; and evaluating other rendering solutions to protect the building envelope (e.g., earthen plasters stabilized with lime, acrylic emulsions, polymers, asphalt emulsions, and agave juice).
2. Further detailed investigations are required to fully understand the performance of earthen dwellings and to provide guidance for the development of modern design codes and standards

for this type of structures. In particular, both experimental and numerical investigations are needed to determine the structural resistance and reliability of CSEB systems against extreme loads because of natural hazards (e.g., high winds and earthquakes), the appropriate dimensioning and performance of different type of reinforcements, the effects of different stabilizers and fabrication procedures on the performance of CSEBs and CSEB masonry, and the proper configurations of architectural and structural details (e.g., taller foundation walls to separate the wall from the wet soil, alternative wall coating and/or rendering surfaces, shading/shielding elements, specific roofing and grading details, connections between walls and foundation and/or between walls and roof, details of window and door openings).

3. To promote acceptance of CSEB houses by the local population, there is a need to develop more CSEBs based single- or multi-family house prototype designs that are representative of the local cultural heritage and environmental context, with the same appearance of houses built using other more common and widely used construction techniques.

7.2.2. *Recommendations for future research work based on chapter 3*

1. In the present investigation, the CSEBs achieved the maximum dry density and resistance to water absorption when the blocks were reinforced with 0.5 wt.% SCBFs. This result is in disagreement with the results reported by Danso et al. [83] on reinforced CEBs. Several hypotheses were proposed in the study. However, further investigation is needed to identify the actual reason(s) for this difference.
2. The present study observed an increase in the coefficient of variation (COV) of (a) the dry density with increasing SCBF content, and (b) of the water absorption for increasing SCBF content. It was hypothesized that these results may be caused by the fabrication method and by

the random distribution and orientation of the fibers near the surface of the specimens. However, these hypotheses need further testing in future investigations.

3. Further studies are needed to better understand and quantify the interaction between soil properties, fiber properties, cement amount, and SCBF amount under different conditions and, ideally, to develop a mechanistic model that can be used to select the optimal amounts of cement and SCBF for a given soil and predict the mechanical properties of the corresponding CSEBs.
4. The present study observed increase in strength due to the progression of the cement hydration during the wet cycles of the durability test. It was hypothesized that the high content of clay and silt combined with the relatively high cement content may have prevented full hydration of the cement during the 28-day curing period after which the specimens not subjected to the durability test were originally tested. However, further investigation is needed to fully test this hypothesis.
5. A further detailed scanning electron microscope (SEM) analysis is needed to understand the fiber-bridging properties of the cracks during the flexure test and confinement effect produced by the fibers on the soil-cement matrix during the compression test through detailed and specifically tailored SEM images. In addition, an SEM analysis of the specimens after the durability tests should also be performed to observe potential modifications in the microstructure of the specimens.
6. A detailed investigation is needed for rigorous comparison of the mechanical and physical properties obtained from flexurally-tested and pristine specimens and to fully confirm the observation that the flexure test had only negligible effects on the compressive strength and durability of the CSEB specimens.

7. More research is needed to optimize the dimensions of the SCBFs, and further investigate the influence of fiber slenderness and surface finish on the mechanical behavior of CSEB reinforced with SCBF.

7.2.3. *Recommendations for future research work based on chapter 4 through chapter 6*

1. The newly proposed interface element's constitutive model, i.e., CTSIM, can be further extent to include the cyclic/hysteretic behavior.
2. Further investigation is needed to assess the limitation and capability of SMMs based on integrated approaches employing complementary experimental and numerical campaigns having various loading conditions.
3. The DMM presented in this dissertation can be further extended to simulate the cyclic behavior of the CSEB masonry systems.
4. The DMM of earth block masonry presented in this dissertation can be used for developing the macro-model and micro-element model for CSEB masonry systems, which will increase the scope of the numerical modeling of CSEBs masonry system and decrease the computational demand.

APPENDIX A. DETAILED DRAWINGS OF THE DOGTROT AND SHOTGUN PROTOTYPE HOUSES

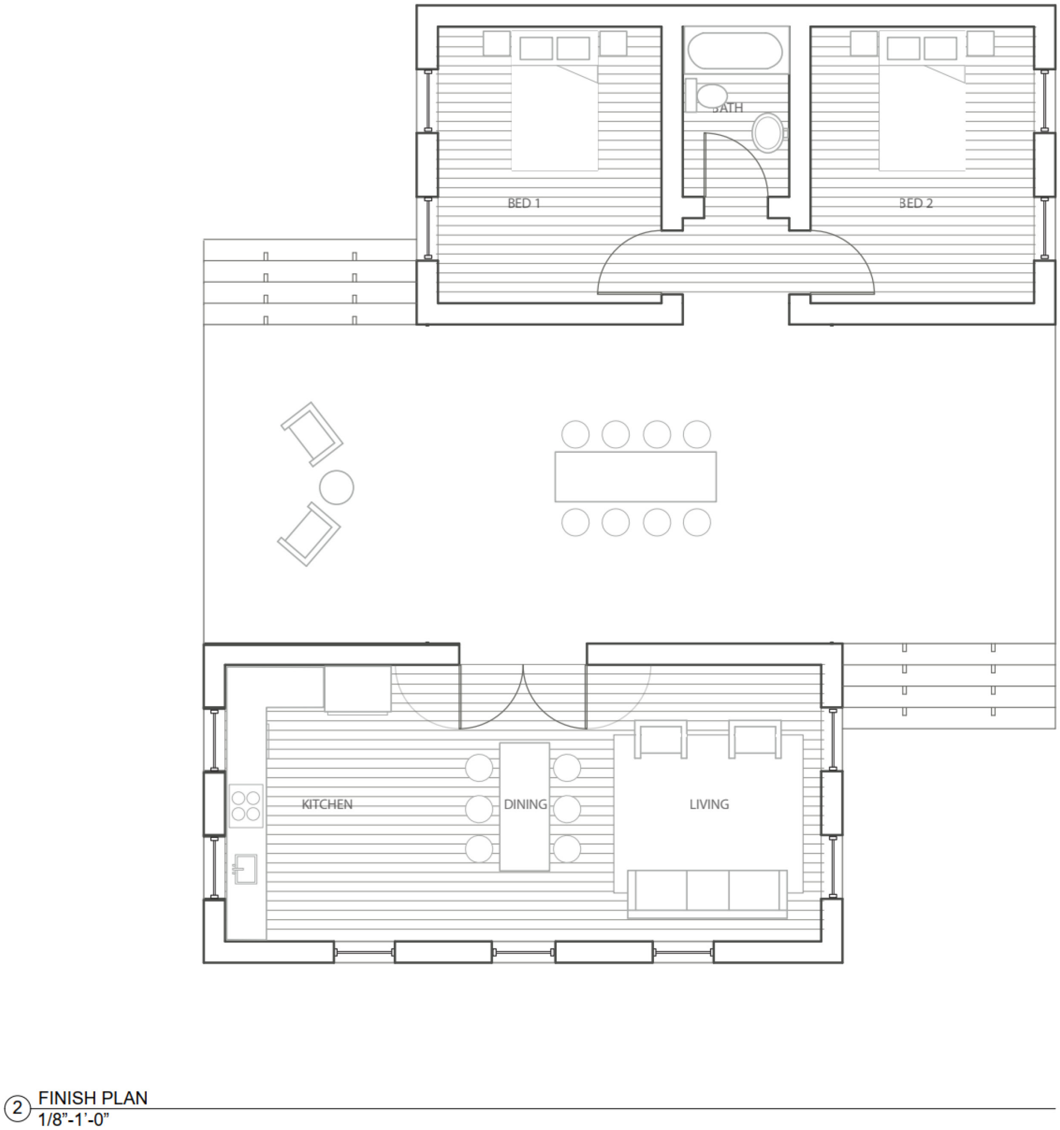

Figure A.1. Finish plan of the dogtrot prototype houses

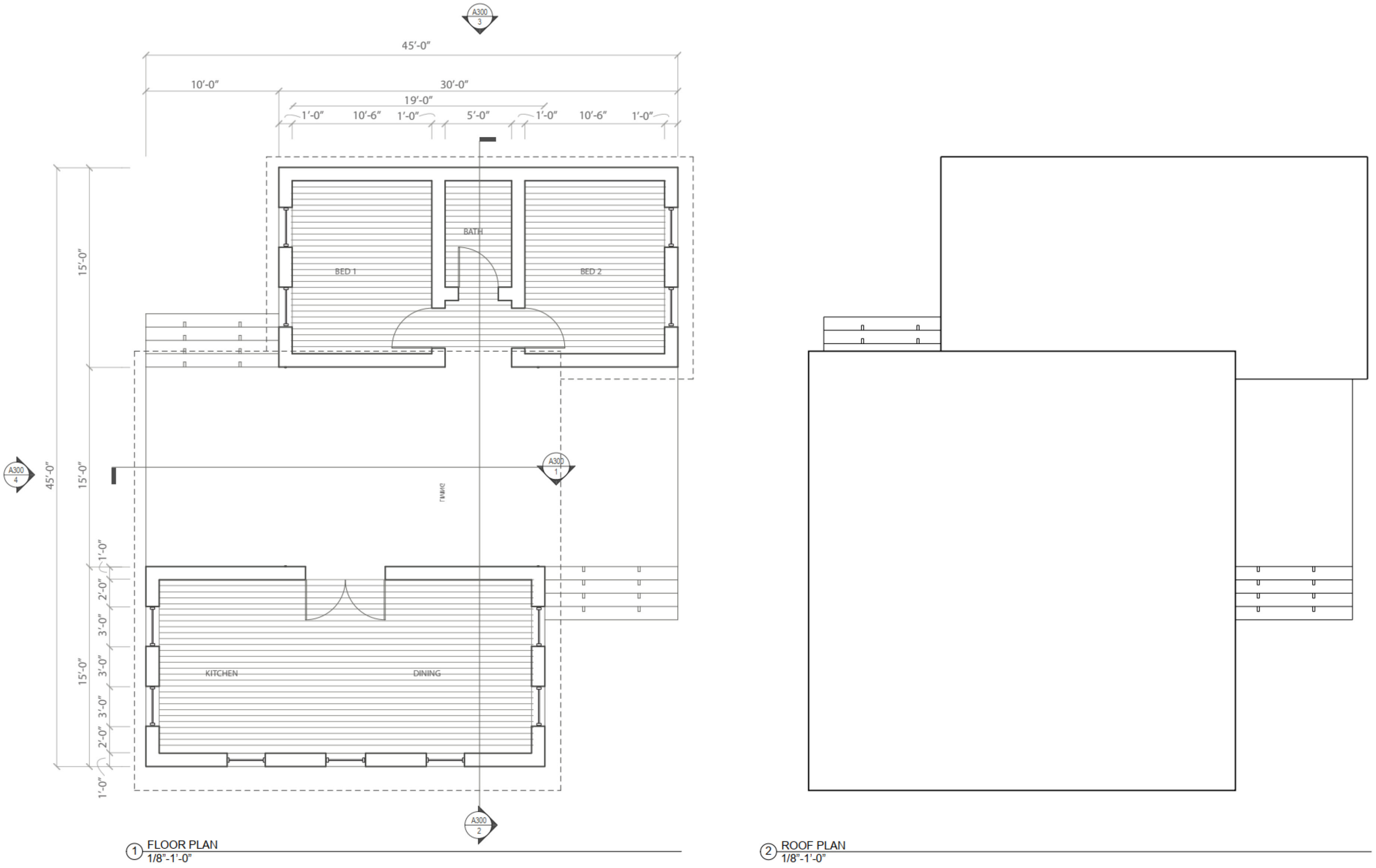

Figure A.2. Floor and roof plan of the dogtrot prototype houses

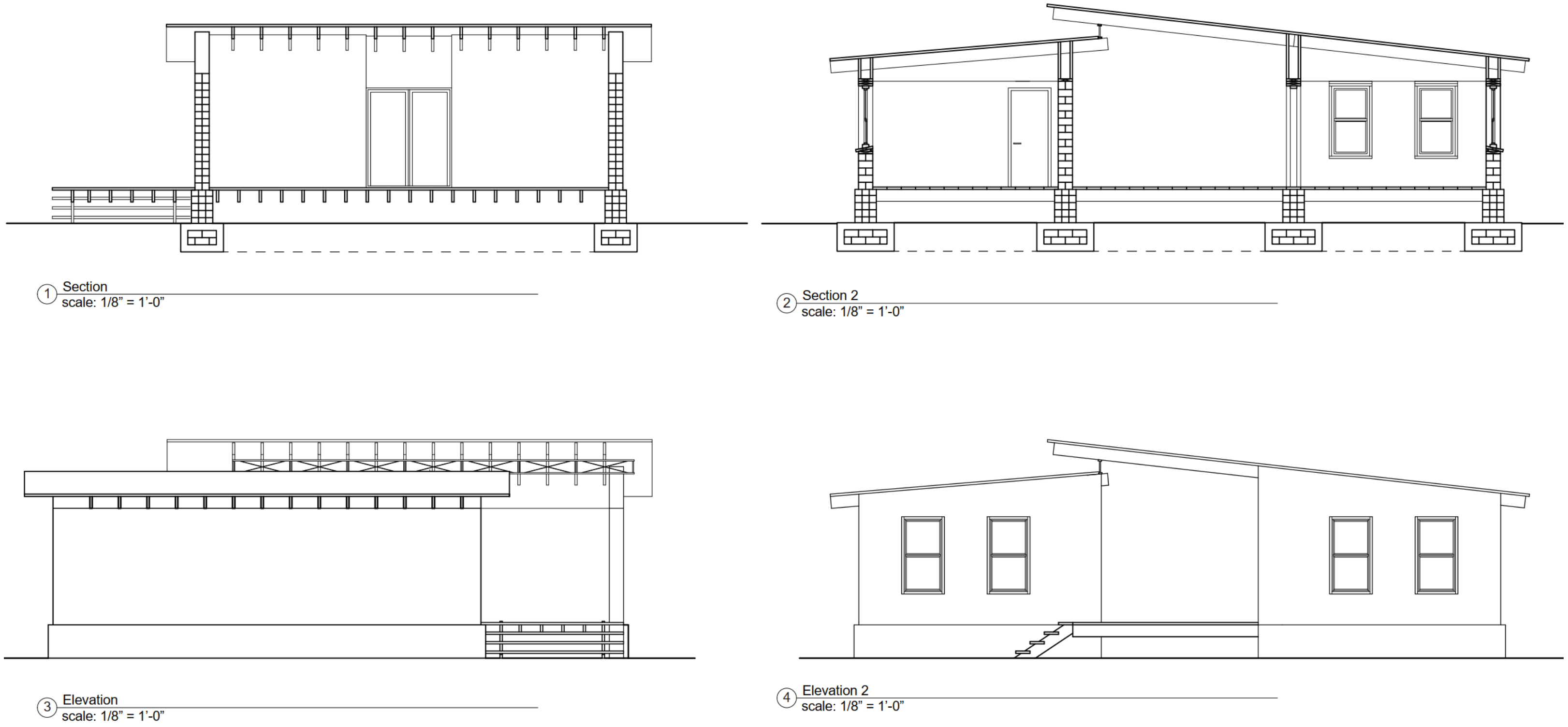

① Section
scale: 1/8" = 1'-0"

② Section 2
scale: 1/8" = 1'-0"

③ Elevation
scale: 1/8" = 1'-0"

④ Elevation 2
scale: 1/8" = 1'-0"

Figure A.3. Section and elevation plan of the dogtrot prototype houses

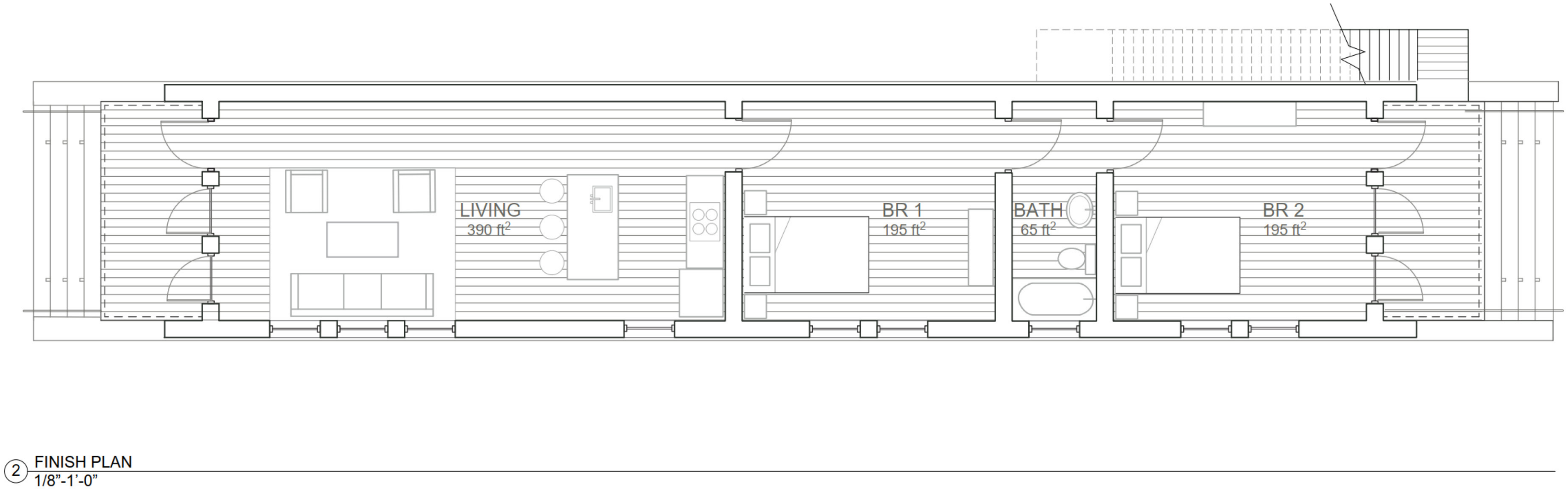

Figure A.4. Finish plan of the shotgun prototype houses

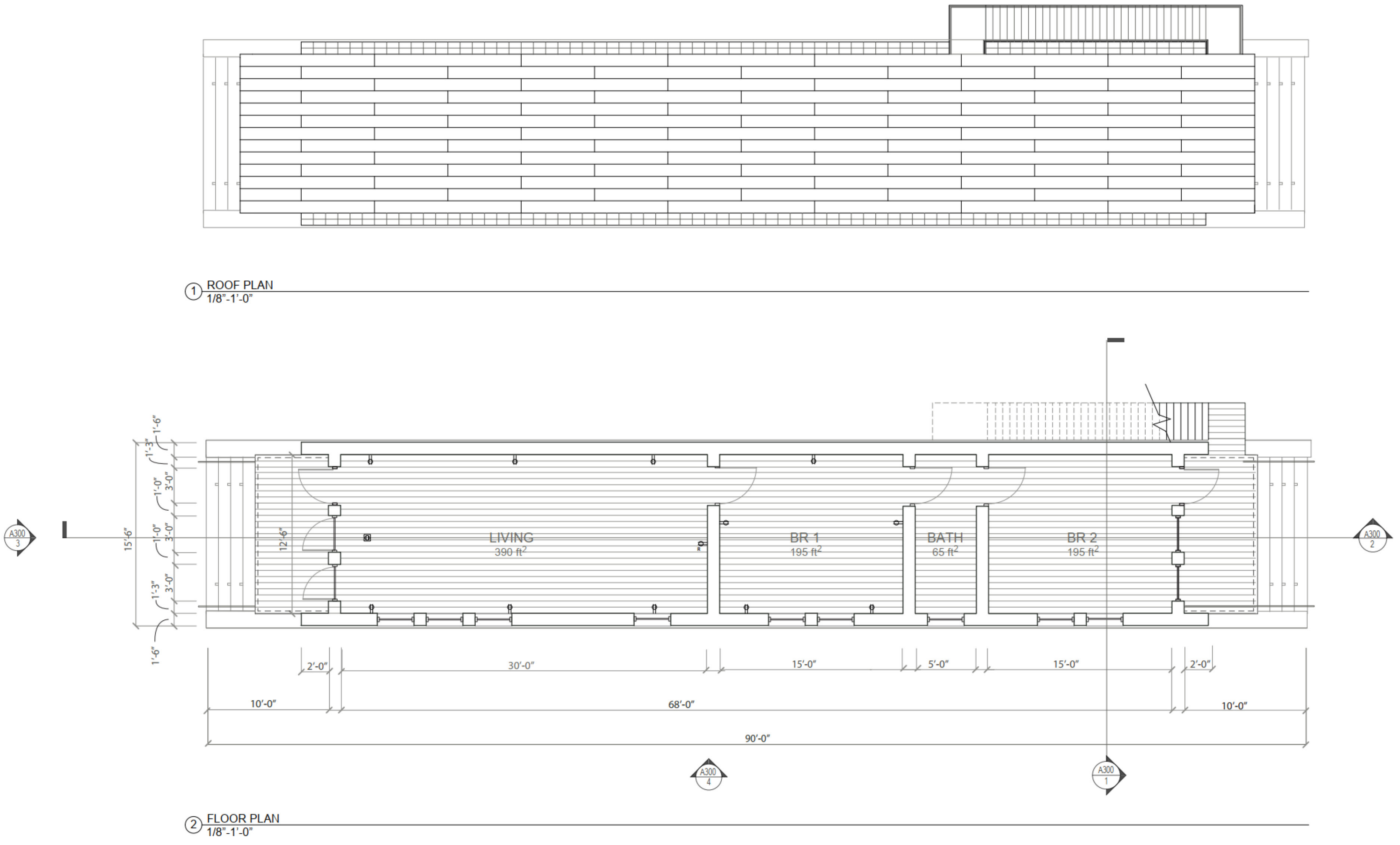

Figure A.5. Floor and roof plan of the shotgun prototype houses

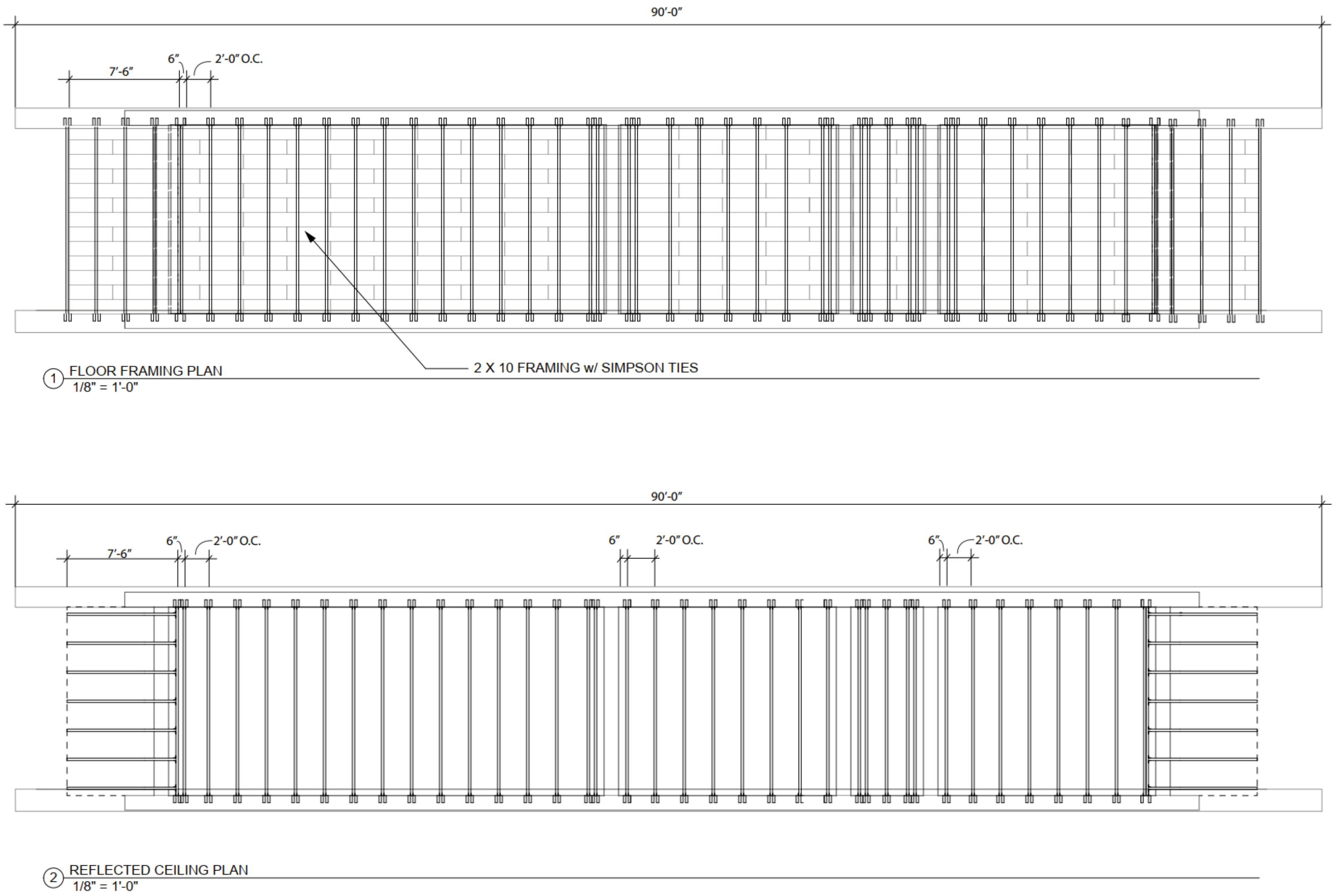

Figure A.6. Floor framing and reflected ceiling of the shotgun prototype houses

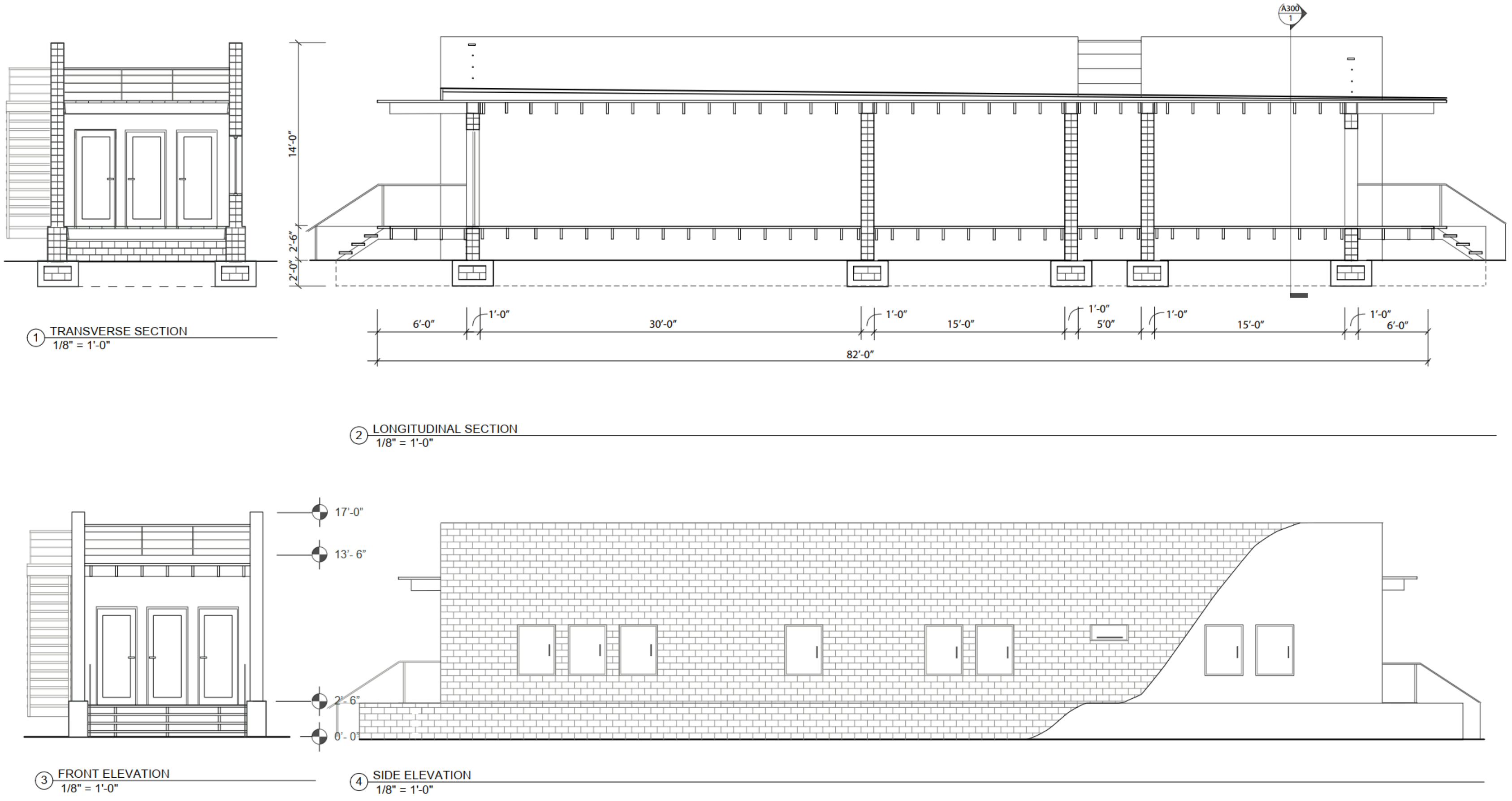

Figure A.7. Section and elevation plan of the shotgun prototype houses

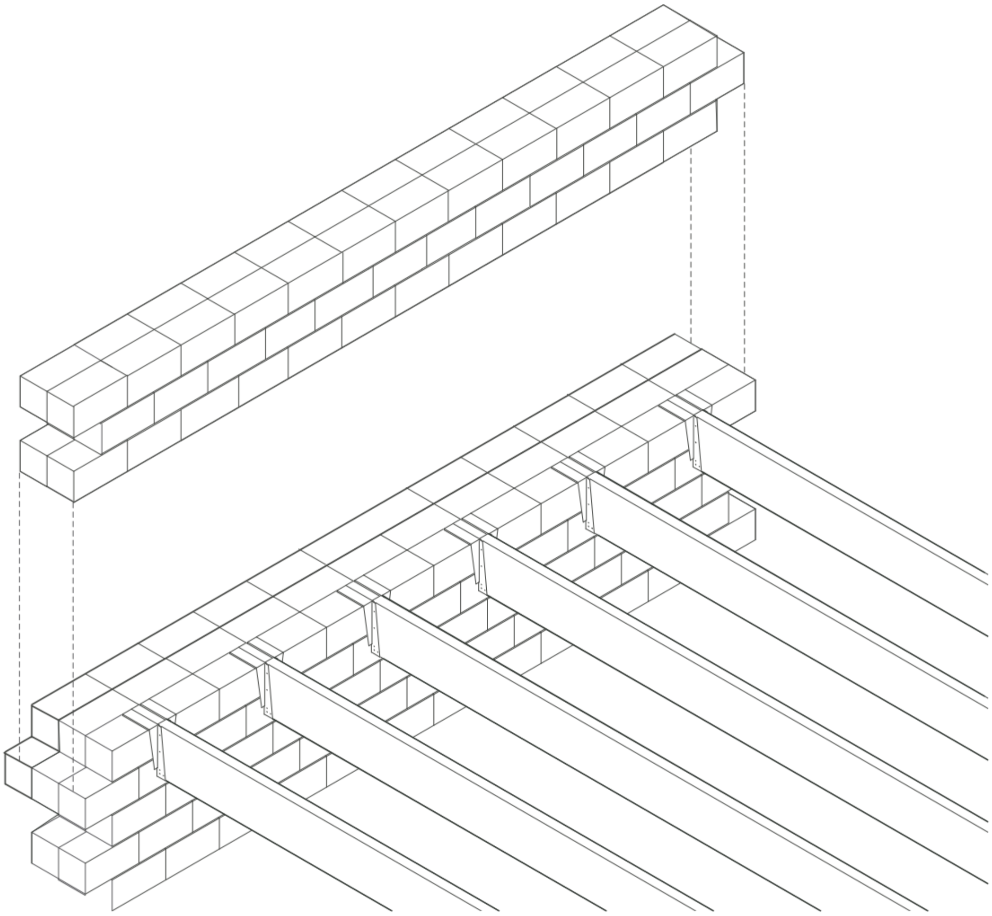

Figure A.8. Floor joist to wall connection details of the prototype houses

APPENDIX B. DETAILED COST ESTIMATES OF DIFFERENT REFERENCE PROTOTYPE HOUSE

Table B.1 Detailed cost estimates of light wooden walls for reference prototype house

				Per unit				Total Cost ($)		
Item	Qty.	Qty./Unit		Mat.	Labor Hr.	Labor Cost	Installation	Mat.	Labor cost	Total
Walls										
Framing system (ext. & partition)										
exterior, long wall	1922	1	ft^2	0.68	0.023	1.15	1.29	1307	2479	3786
2"x4" studs, 16" O.C.		1	ft^2	0.46	0.015	0.750	0.80			
Plates, 2"x4", double top, single bottom		0.375	ft.	0.17	0.005	0.250	0.30			
corner bracing, let-in, 1"x6"		0.063	ft.	0.05	0.003	0.150	0.19			
Exterior sheathing, plywood sheets	2355	1	ft^2	0.72	0.011	0.55	0.63	1696	1484	3179
Exterior wood siding system	2355	1	ft^2	2.60	0.057	2.85	3.06	6123	7206	13329
white cedar shingles, 16"		1	ft^2	2.11	0.033	1.650	1.84			
building warp, polypropylene		1.1	ft^2	0.17	0.002	0.100	0.12			
trim, cedar		0.125	ft^2	0.16	0.005	0.250	0.28			
paint, primer & 2 coats		1	ft^2	0.16	0.017	0.850	0.82			
Insulation, exterior wall	2355	1	ft^2	0.62	0.01	0.50	0.55	1460	1295	2755
Interior, short wall	610	1	ft^2	0.68	0.023	1.15	1.29	415	787	1202
2"x4" studs, 16" O.C.		1	ft^2	0.46	0.015	0.750	0.80			
Plates, 2"x4", double top, single bottom		0.375	ft.	0.17	0.005	0.250	0.30			
corner bracing, let-in, 1"x6"		0.063	ft.	0.05	0.003	0.150	0.19			
Interior finish system	3222			1.14	0.035	1.75	1.77	3673	5703	9376
gypsum wallboard, 5/8", standard		1	ft^2	0.36	0.008	0.400	0.44			
Finish, taped & finish joints		1	ft^2	0.05	0.008	0.400	0.44			
corners, taped & finished,		0.08	ft.	0.01	0.002	0.100	0.08			
painting, prime & 2 coats		1	ft^2	0.21	0.011	0.550	0.50			
Moldings, 9/12"x4-1/2, red oak		0.125	ft.	0.49	0.005	0.250	0.25			
paints trim, to 6", primer + 1 coat enamel		0.125	ft.	0.02	0.001	0.050	0.06			
Window & door openings										
window 3'x4'	9	1	no.	4.38	0.267	13.350	14.70	39	132	172
door 3'x7.5'	8	1	no.	4.38	0.267	13.350	14.70	35	118	153
Vent 34"x22"	1	1	no.	4.38	0.267	13.350	14.70	4	15	19
Stem walls	450	1	ft^2	2.32	0.051	2.55	2.81	1044	1265	2309
2"x4" studs, 16" O.C., treated		1	ft^2	0.56	0.015	0.750	0.80			
Plates, 2"x4", double top, single bottom		0.750	ft.	0.42	0.011	0.550	0.60			
sheathing., 1/2", exterior grade, CDX		1.000	ft.	0.90	0.014	0.700	0.78			
Asphalt paper, 15# roll		1.000	ft.	0.07	0.002	0.100	0.13			
Vapor barrier, 4 mil polyethylene		1.000	ft.	0.04	0.002	0.100	0.12			
fiberglass insulation, 3-1/2" thick		0.063	ft.	0.33	0.007	0.350	0.38			
USA Average Total ($)								*15796*	*20484*	36280
Weighted Location factor (Baton Rouge)								*0.991*	*0.637*	
Baton Rouge Total ($)								*15638*	*13069*	28707
Total cost for General Contractor including overhead ($)									**40,970**	

Table B.2 Detailed cost estimates of fired brick masonry walls for reference prototype house

Item	Quantity	Unit	Per Unit Material	Per Unit Inst.	Cost ($) Material	Cost ($) Labor cost	Cost ($) Total
Walls							
stem walls	450	ft^2	10.90	23.50	4905	10575	15480
long walls	1922	ft^2	5.65	14.20	10859	27292	38152
short walls	610	ft^2	5.65	14.20	3447	8662	12109
Masonry Paint							
Interior	2898	ft^2	0.23	0.760	667	2202	2869
Exterior	3066	ft^2	0.23	0.760	705	2330	3035
USA Average Total ($)					20583	51062	71645
Weighted Location factor (Baton Rouge)					0.95	0.541	
Baton Rouge Total ($)					19533	27625	47157
Total cost for General Contractor including overhead ($)						66,997	

Table B.3 Detailed cost estimates of concrete blocks walls for reference prototype house

Item	Quantity	Unit	Per Unit Material	Per Unit Inst.	Cost ($) Material	Cost ($) Labor cost	Cost ($) Total
Walls							
stem walls [8" thick]	450	ft^2	4.63	9.40	2084	4230	6314
long walls [6" thick]	1922	ft^2	3.69	7.10	7092	13646	20738
short walls [6" thick]	610	ft^2	3.69	7.10	2251	4331	6582
Stucco							
Interior	2898	ft^2	0	0.00	0	0	0
Exterior	3066	ft^2	0.24	3.49	736	10700	11436
Masonry Paint							
Interior	2898	ft^2	0.23	0.76	667	2202	2869
Exterior	3066	ft^2	0.23	0.76	705	2330	3035
USA Average Total ($)					**13534**	**37440**	**50974**
Weighted Location factor (Baton Rouge)					0.95	0.541	
Baton Rouge Total ($)					12844	20255	**33099**
Total cost for General Contractor including overhead ($)						46,981	

Table B.4 Detailed cost estimates associated with other components of reference prototype house

				Per unit				Total Cost ($)		
Item	Qty.	Qty./Unit		Mat.	Labor Hr.	Labor Cost	Installation	Mat.	Labor	Total
Foundation										
Footing excavation										
Building, 24'x38', 4' Deep	1	1	Ea.	0.00	13.76	688.00	1404.22	0	1404	1404
cut & chip light trees to 6 "		0.19	Acre	0.00	9.120	456.00	750.500			
Excavate, hydraulic, crawler		174.00	C.Y.	0.00	3.480	174.00	368.88			
backfill, dozer, 4" lift, no compaction		87.00	C.Y.	0.00	0.580	29.00	142.42			
Rouge grade, dozer, 30' from building		87.00	C.Y.	0.00	0.580	29.00	142.42			
Footing System										
8" thick by 18" wide footing	319	1	L.F.	6.68	0.15	7.55	7.45	2131	2377	4507
concrete, 3000 psi		0.400	C.Y.	4.48	0.000	0.00	0.00			
plain concrete, direct chute		0.400	C.Y.	0.00	0.016	0.80	0.71			
forms, footing, 4 uses		1.330	SFCA	1.09	0.103	5.15	4.95			
reinforcing, 1/2" diameter bars, 2 each		1.380	lb.	0.73	0.011	0.55	0.63			
keyways, 2"x4", beveled, 4 uses		1.000	ft.	0.25	0.015	0.75	0.83			
Dowels, 1/2" bars, 2' long, 6' O.C.		0.166	Ea.	0.13	0.006	0.30	0.33			
Floor										
framing system	1057	1	ft^2	3.07	0.073	3.65	4.04	3245	4270	7515
wood joists 2"x8", 16 O.C.		1.0	ft^2	1.01	0.015	0.75	0.80			
bridging, 1"x3", 6 O.C.		0.08	Pr.	0.06	0.005	0.250	0.27			
box sills, 2"x8"		0.15	ft.	0.15	0.002	0.10	0.12			
concrete filled steel column, 4"		0.125	ft.	0.27	0.002	0.10	0.13			
Grinder, build up from three 2"x8"		0.125	ft.	0.38	0.013	0.65	0.73			
Sheathing, plywood, subfloor (1/2")		1	ft^2	0.72	0.011	0.55	0.63			
furring, 1"x3", 16 O.C.		1	ft.	0.42	0.023	1.15	1.26			
joist hangers		0.036	Ea.	0.06	0.002	0.10	0.10			
Carpet system										
carpet, nylon, level loop 26 oz.	1057	1	ft^2	3.04	0.018	2.75	0.87	3213	920	4133
Roof										
framing system	1057	1	ft^2	1.53	0.036	1.80	1.97	1617	2082	3700
wood joists 2"x6", 24 O.C., 4/12 pitch		0.94	ft.	0.69	0.015	0.75	0.83			
bridging, 1"x3", 6 O.C.		0.06	pr.	0.04	0.004	0.20	0.31			
Fascia, 2"x6"		0.10	ft.	0.08	0.006	0.30	0.20			
Sheathing, exterior grade plywood		1.23	ft^2	0.72	0.011	0.55	0.63			
Asphalts, roof shingles, Class A	1057	1	ft^2	1.90	0.043	2.15	2.21	2008	2336	4344
shingles		1.23	ft^2	1.14	0.019	0.95	0.97			
drip edge, aluminum, 5"		0.10	ft.	0.06	0.002	0.10	0.11			
building paper, #15 asphalt felt		1.3	ft^2	0.08	0.002	0.10	0.09			
aluminum, vented, 1' overhang		0.08	ft.	0.39	0.012	0.60	0.64			
rake trim, 1"x6"		0.043	ft.	0.05	0.002	0.10	0.10			
rake trim, primer & paint		0.043	ft.	0.01	0.002	0.10	0.09			
gutter, seamless, aluminum, paint		0.040	ft.	0.12	0.003	0.15	0.16			
downspouts, painted aluminum		0.020	ft.	0.05	0.001	0.05	0.05			

Interior ceiling system	1057	1	ft^2	0.73	0.033	1.69	1.46	772	1543	2315
Gypsum wallboard, 1/2", water rest.		1	ft^2	0.43	0.008	0.44	0.44			
Finish, taped & finish joints		1	ft^2	0.05	0.008	0.44	0.44			
corners, taped & finished, 12'x12' room		0.33	ft.	0.04	0.006	0.31	0.08			
painting, prime & 2 coats		1	ft^2	0.21	0.011	0.50	0.50			
Door and windows										
Exterior Doors	2	1		498.20	6.250	312.50	330.53	996	661	1657
door, solid core, 3' x 6'8"		1.0	Ea.	130	1.067	53.35	59			
frame, 4-9/16", exterior casing		17.0	ft.	147.05	0.725	36.25	39.95			
interior casing, 1-1/2"		18.0	ft.	27.9	0.576	28.80	31.68			
sill, 8/4 x 8" deep		3.0	ft.	67.5	0.48	24.00	26.4			
butt hinges, brass, 4-1/2' x 4-1/2"		1.5	pr.	32.25	0	0.00	0			
Average quality		1.0	Ea.	55	0.571	28.55	31.5			
Weather stripping, spring type, bronze		1.0	set	25.5	1.053	52.65	58			
paint door and frame, oil, 2 coats		2.0	face	13	1.778	88.90	84			
Interior Doors System	3	1	no.	297.33	7.389	369.45	378.29	892	1135	2027
door, flush, birch, hallow core, 2'8" x 6'8"		1.0	Ea.	55.5	0.889	44.45	49			
frame, pine 4-5/8" jamb		17.0	ft.	91.8	0.725	36.25	39.95			
casing, ogee, 11/16"x2-1/2", pine		34.0	ft.	52.7	1.008	50.40	59.84			
butt hinges, chrome, 3-1/2' x 3-1/2"		1.5	pr.	45.75	0	0.00	0			
lockset, passage		1.0	Ea.	33	0.5	25.00	27.5			
prime door & frame, oil, Bruch work		2.0	Face	7.58	1.6	80.00	76			
paint door and frame, oil, 2 coats		2.0	Face	11	2.667	133.35	126			
Standard Windows System	8	1	No.	519.56	2.98	149.00	156.80	4156	1254	5411
window, plastic, 3'x4', single glass		1	Ea.	435	0.889	44.45	49.0			
trim, interior casing		15	ft.	23.25	0.480	24.00	26.4			
paint, interior, primer & 2 coat		1	Face	1.31	0.889	44.45	42.0			
caulking		14	ft.	3.50	0.389	19.45	21.0			
snap-in grille		1	set	56.50	0.333	16.65	18.4			
Vent Window	1	1	no.	340.71	2.45	122.50	126.98	341	127	468
window, plastic, 34"x22", single glass		1	Ea.	290	0.800	40.00	44			
trim, interior casing		10.5	ft.	16.30	0.350	17.50	18.50			
paint, interior, primer & 2 coat		1	face	1.03	0.73	36.35	35.53			
caulking		9.5	ft.	2.38	0.306	15.30	14.25			
snap-in grille		1	Ea.	31	0.267	13.35	14.70			
Kitchen System										
kitchen, economic grade	10	1	ft.	194.21	0.86	42.85	47.34	1942	473	2416
top cabinets		1	ft.	61.76	0.171	8.55	9.44			
bottom cabinets		1	ft.	92.64	0.256	12.80	14.16			
square edge, plastic face countertop		1	ft.	36.50	0.267	13.35	14.70			
blocking, wood, 2"x4"		1	ft.	0.47	0.032	1.60	1.76			
soffit, framing, wood, 2"x4"		4	ft.	1.88	0.071	3.55	3.92			
soffit, drywall		2	ft^2	0.84	0.047	2.35	2.62			
drywall painting		2	ft^2	0.12	0.013	0.65	0.74			
Three fix bathroom systems										
bathroom with wall hung lavatory	1	1	Set	2583.62	21.517	1075.85	1271.40	2584	1271	3855

water closet, floor mounted, 2 pieces		1	Ea.	261.00	3.019	150.95	174.00			
rough-in, vent, 2" dia. DWV piping		1	Ea.	49.60	0.955	47.75	55.00			
waste, 4" dia. DWV piping		1	Ea.	63.00	0.828	41.40	47.70			
1/2" dia. type "L" copper supply piping		1	Ea.	24.42	0.593	29.65	37.80			
Lavatory, 20"x18" P.E. cast iron		1	Ea.	305.00	2.000	100.00	115.00			
rough-in, waste, 1'-1/2" dia. DWV		1	Ea.	97.20	1.803	90.15	103.60			
1/2" dia. type "L" copper piping		1	Ea.	40.70	0.988	49.40	63.00			
bathtub, P.E. cast iron, 5' with accessories		1	Ea.	1250	3.636	181.80	209.00			
rough-in, waste, 4" dia. DWV piping		1	Ea.	63.00	0.828	41.40	47.70			
1/2" dia. type "L" copper piping		1	Ea.	40.70	0.988	49.40	63.00			
vent, 1'-1/2" dia. DWV piping		1	Ea.	49.20	0.593	29.65	37.80			
piping, 1/2" dia. type "L" copper		10	ft.	40.70	0.988	49.40	63.00			
waste, 4" dia. DWV piping		6	ft.	126.00	1.655	82.75	95.40			
vent, 2" dia. DWV piping		6	ft.	68.10	1.500	75.00	86.40			
carrier, steel, for studs, no arms		1	Ea.	105.00	1.143	57.15	73.00			
Electric service system										
100 Amp service	1	1	set	400.10	12.30	615.05	738.30	400	738	1138
weather cap		1	Ea.	9.65	0.667	33.40	40.00			
service entrance cable		10	ft.	40.90	0.762	38.10	45.80			
meter socket		1	Ea.	47.50	2.500	125.00	150.00			
ground rod with clamp		1	Ea.	22.00	1.455	72.80	87.50			
ground cable		5	ft.	7.05	0.250	12.50	15.00			
panel board 12 circuit		1	Ea.	273.00	6.667	333.40	400.00			
Appliances Systems										
kitchen, economy	1	1	set	4965	41	2050	2419	4965	2419	7384
range, countertop, 4 burners		1	Ea.	410.0	3.3	167	200.0			
compactor		1	Ea.	730	2.215	111	125			
dishwasher		1	Ea.	475	6.735	337	425			
garbage disposer		1	Ea.	192	2.81	141	179			
microwave oven		1	Ea.	154	2.615	131	157			
range hood		1	Ea.	114	4.658	233	267			
refrigerator, 16 cu. ft.		1	Ea.	580	2	100	82			
Sink, stainless steel, 16''x20''		1	Ea.	935	10.334	517	595			
water heater, electric, 30 gallons		1	Ea.	525	3.636	182	233			
Wall, terminal heater/air conditioner 6000 BTUH cool, 8800 BTU heat		1	Ea.	850	2.667	133	156			
Bath accessories	1	1	set	332	2	94	104	332	104	436
Certain rod, stainless, 1'' dia. x 5'		1	Ea.	31	0.615	31	34			
grab bar, 1"dia x 12'		1	Ea.	27	0.283	14	15.65			
medicine chest, mirror, 18"x24"		1	Ea.	213	0.4	20	22			
toilet tissue dispenser		1	Ea.	19.6	0.267	13	14.7			
tower bar, 24"		1	Ea.	41.5	0.313	16	17.3			
Electric										
Wiring device system, non-metallic	1			293	9	458	550			1374
air conditioning system		1	Ea.	22	0.8	40	48	22	48	
disposal wiring		1	Ea.	19.7	0.889	44	53.5	19.7	53.5	
Dryer circuit		1	Ea.	39.5	1.455	73	87.5	39.5	87.5	
duplex receptacles		10	Ea.	22	0.615	31	37	220	370	
Exhaust fan		1	Ea.	24	0.8	40	48	24	48	

lighting wiring		1	Ea.	24.5	0.5	25	30	24.5	30	
rang wiring		1	Ea.	85	2	100	120	85	120	
switch, single pole		1	Ea.	24	0.5	25	30	24	30	
water heater		1	Ea.	32	1.6	80	96	32	96	
Lighting fixture, non-metallic	1			105	2	86	104			417
incandescent, surface mount 60W		2	Ea.	48	0.8	40	49	96	98	
fluorescent strip, surface		2	Ea.	56.5	0.914	46	55	113	110	
USA Average Total ($)								30295	24206	54501
Weighted Location factor (Baton Rouge)								0.991	0.637	
Baton Rouge Total ($)								30022	15419	45441
Total cost for General Contractor including overhead ($)									**65,110**	

APPENDIX C. Experimental Test Results of SCBF-reinforced CSEBs

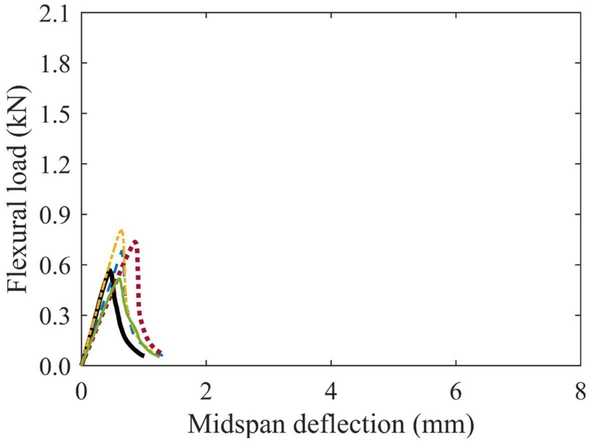

(a)

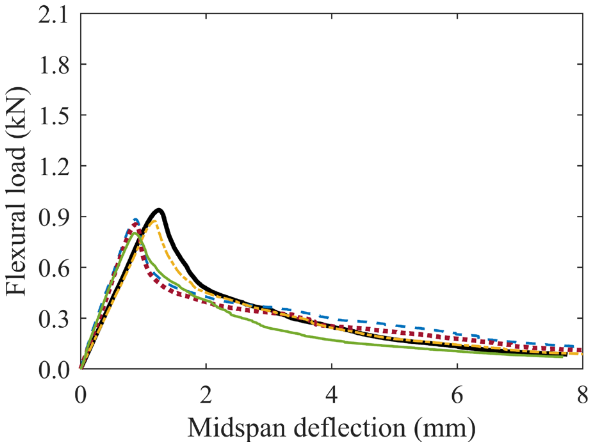

(b)

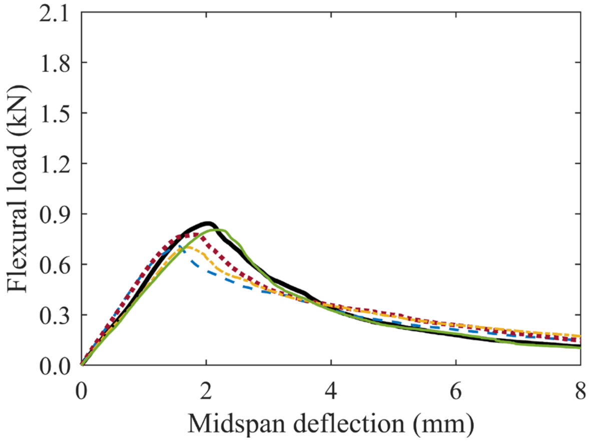

(c)

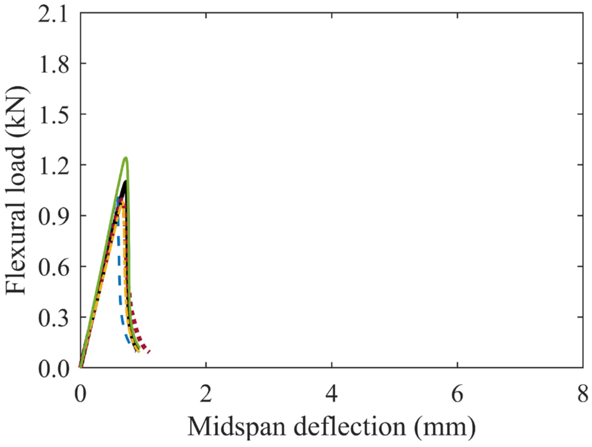

(d)

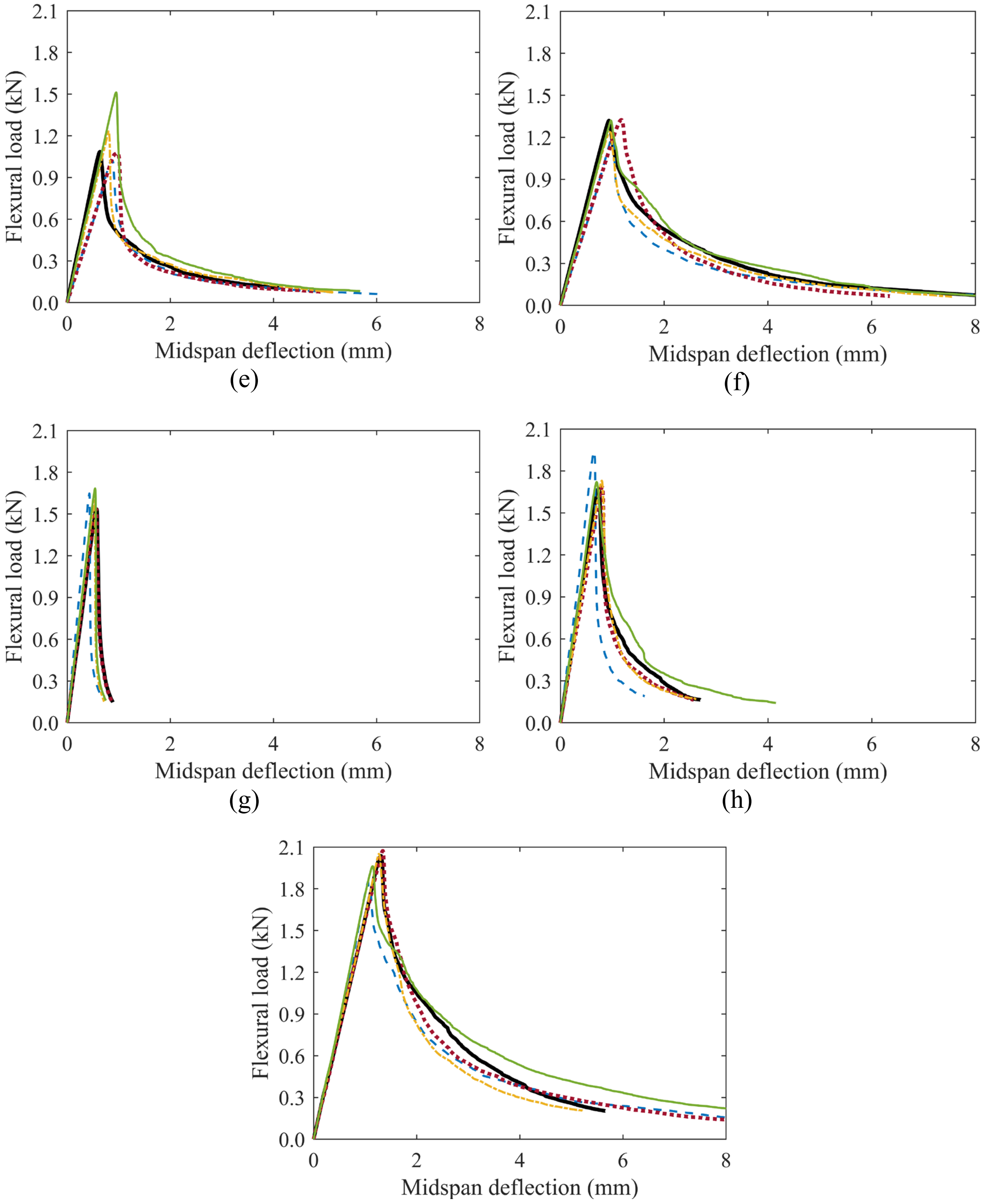

(e) (f) (g) (h) (i)

Figure C.1. Load-displacement curve from flexure test of: (a) EB-00-00, (b) EB-00-05, (c) EB-00-10, (d) EB-06-00, (e) EB-06-05, (f) EB-06-10, (g) EB-12-00, (h) EB-12-05, and (i) EB-12-10.

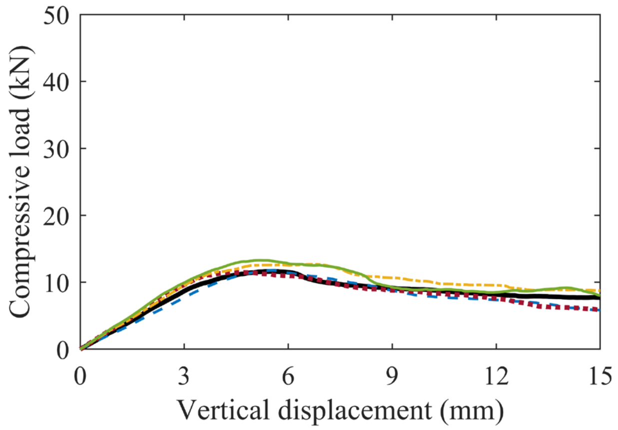
Compressive load (kN)
0
10
20
30
40
50
0
3
6
9
12
15
Vertical displacement (mm)

(a)

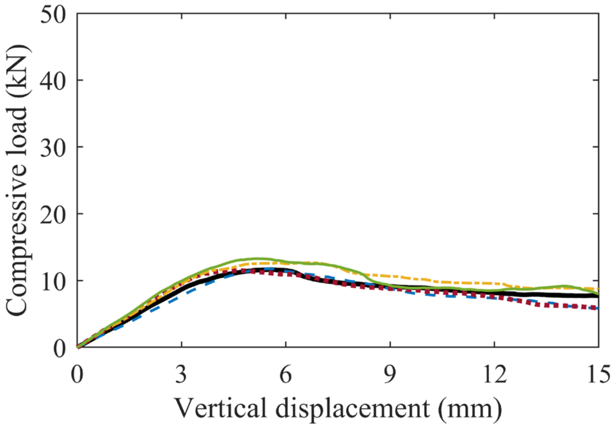
Compressive load (kN)
0
10
20
30
40
50
0
3
6
9
12
15
Vertical displacement (mm)

(b)

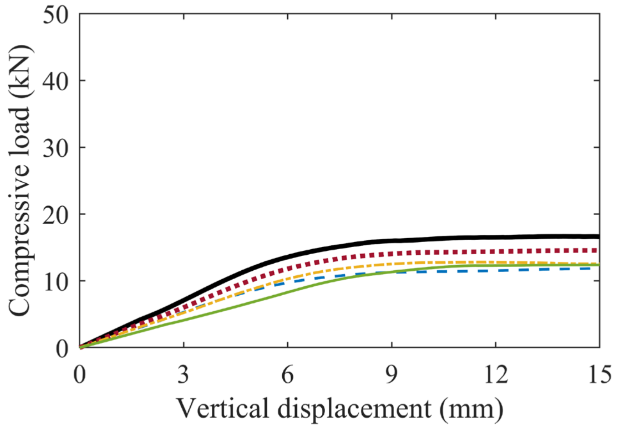
Compressive load (kN)
0
10
20
30
40
50
0
3
6
9
12
15
Vertical displacement (mm)

(c)

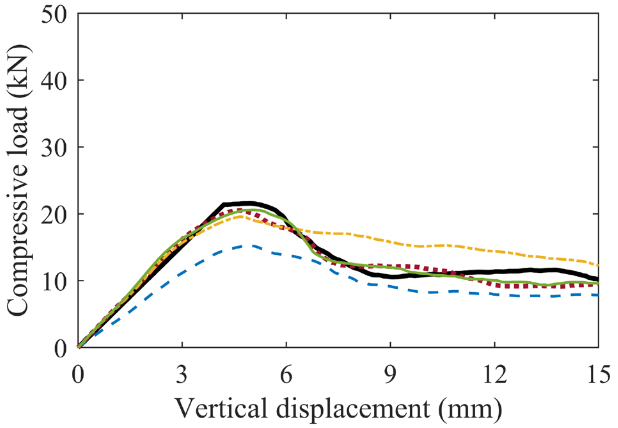
Compressive load (kN)
0
10
20
30
40
50
0
3
6
9
12
15
Vertical displacement (mm)

(d)

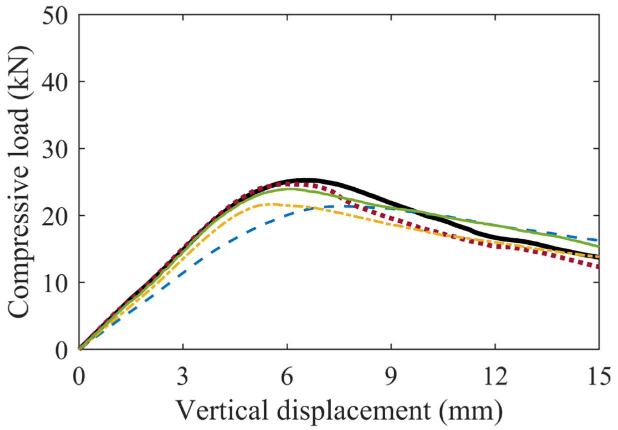
Compressive load (kN)
0
10
20
30
40
50
0
3
6
9
12
15
Vertical displacement (mm)

(e)

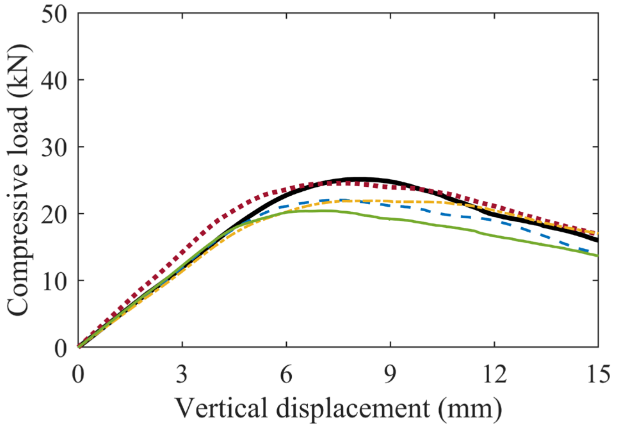
Compressive load (kN)
0
10
20
30
40
50
0
3
6
9
12
15
Vertical displacement (mm)

(f)

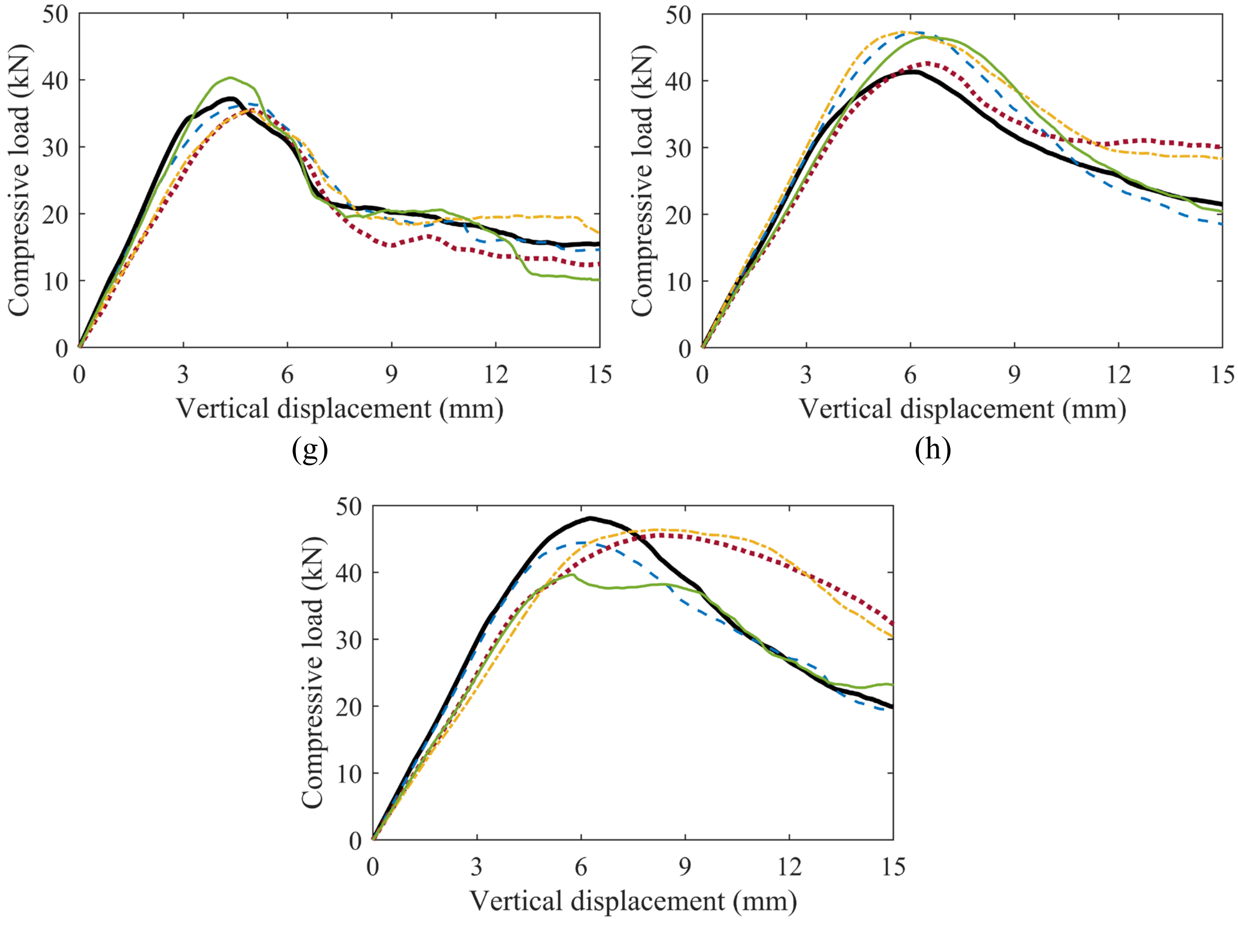

(g)

(h)

(i)

Figure C.2. Load-displacement curve from dry compression test of: (a) EB-00-00, (b) EB-00-05, (c) EB-00-10, (d) EB-06-00, (e) EB-06-05, (f) EB-06-10, (g) EB-12-00, (h) EB-12-05, and (i) EB-12-10.

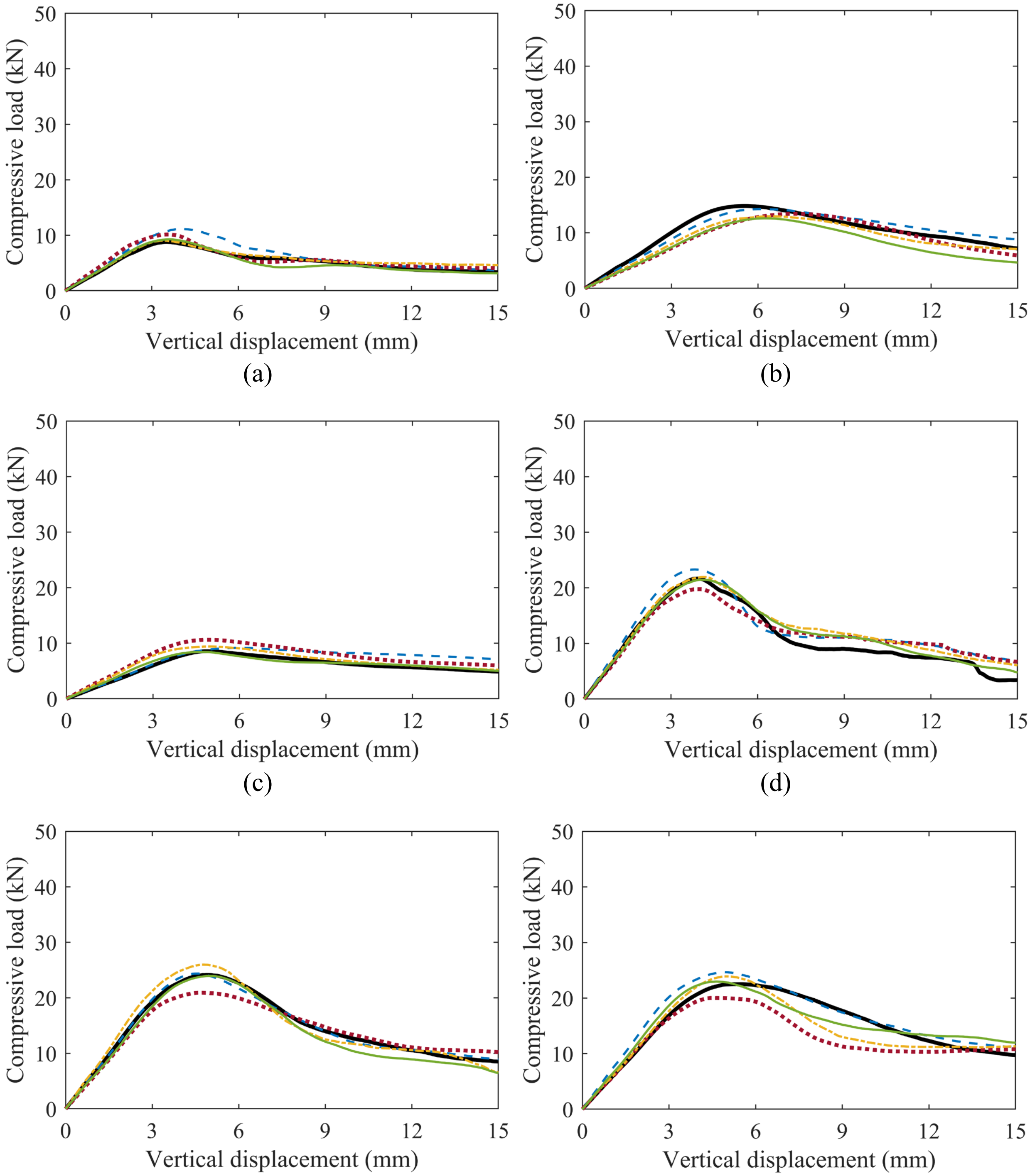

(a) (b) (c) (d) (e) (f)

Figure C.3. Load-displacement curve from wet compression test of: (a) EB-06-00, (b) EB-06-05, (c) EB-06-10, (d) EB-12-00, (e) EB-12-05, and (f) EB-12-10.

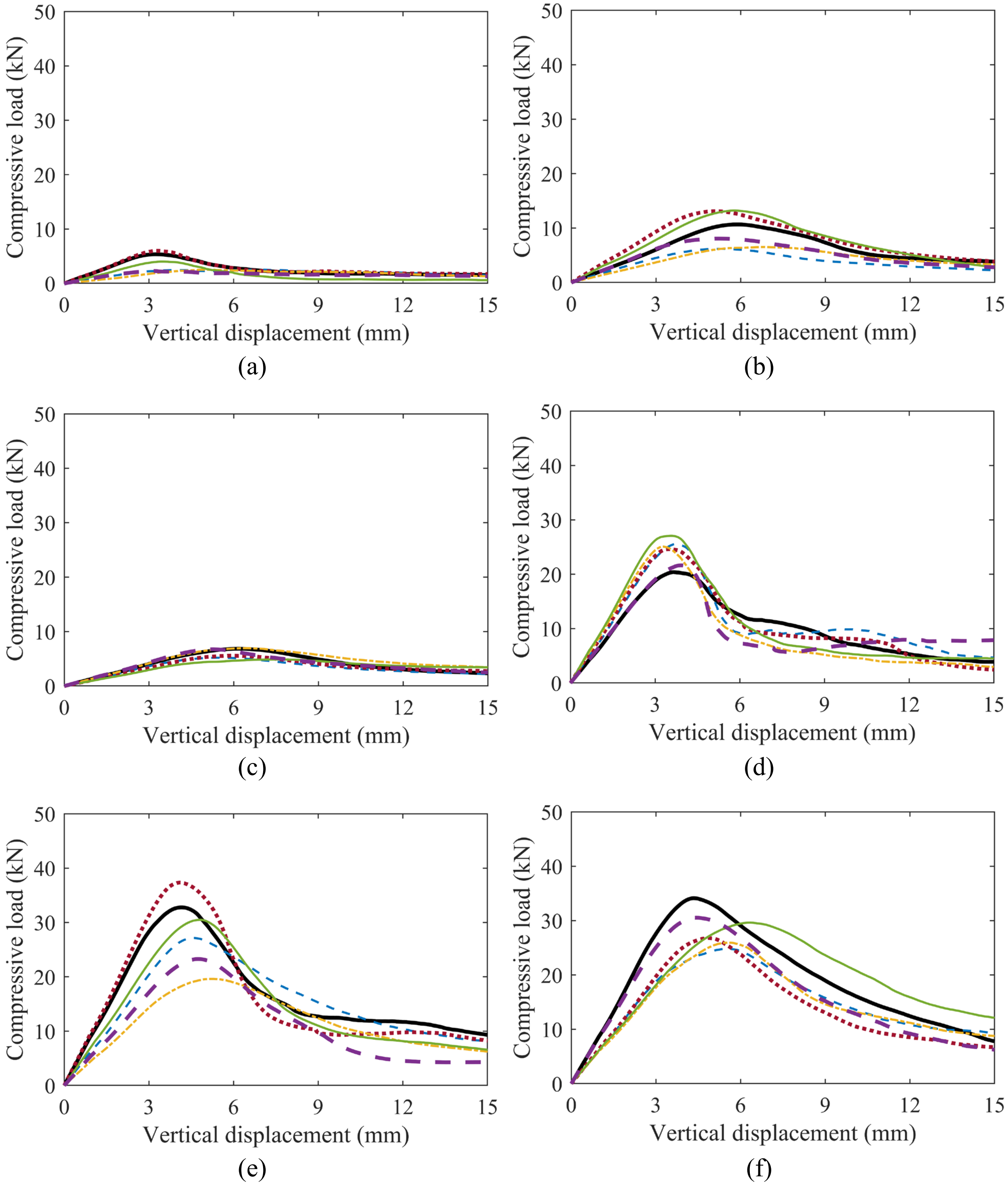

(a)

(b)

(c)

(d)

(e)

(f)

Figure C.4. Load-displacement curve from wet compression test after durability test: (a) EB-06-00, (b) EB-06-05, (c) EB-06-10, (d) EB-12-00, (e) EB-12-05, and (f) EB-12-10.

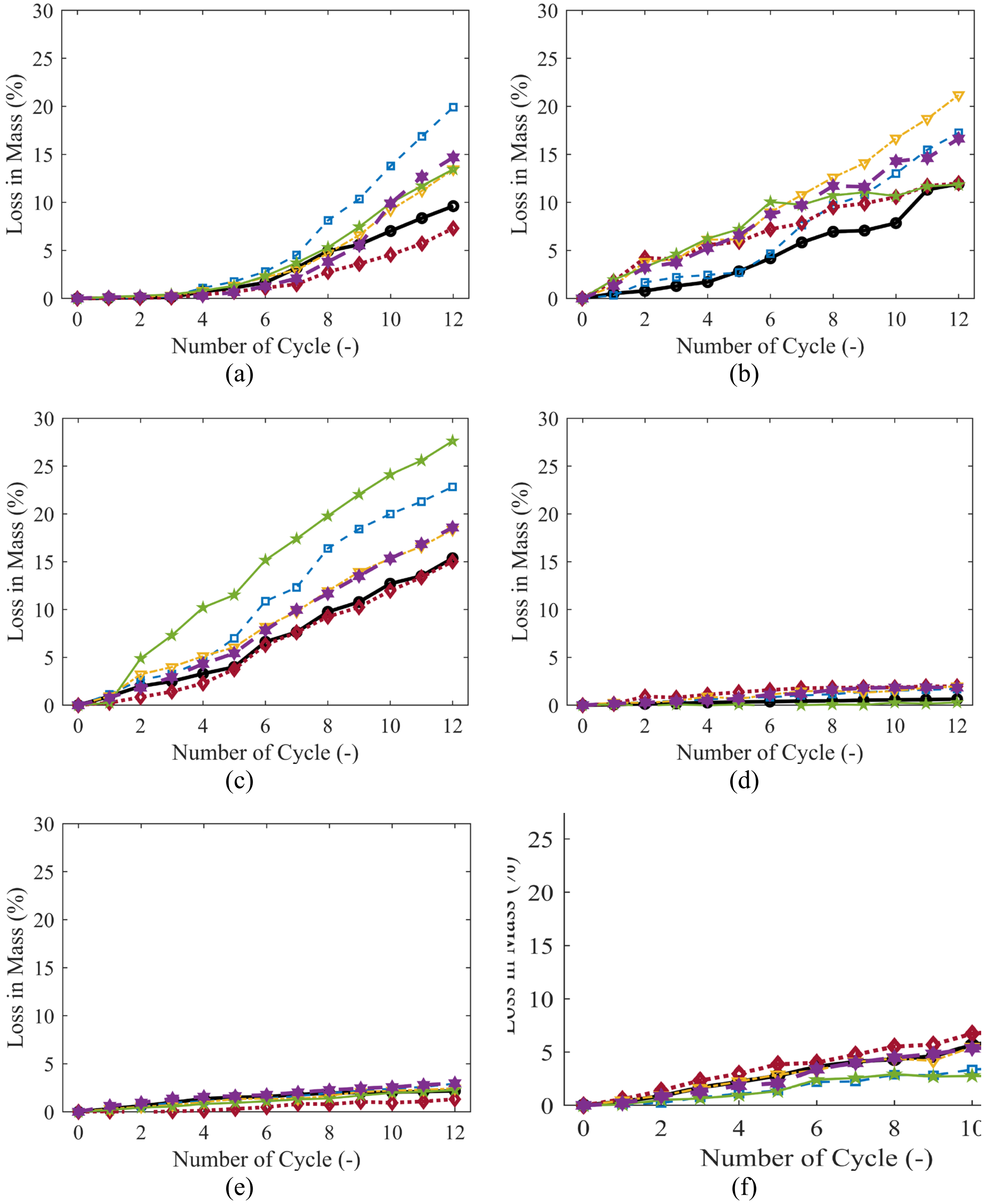

(a)

(b)

(c)

(d)

(e)

(f)

Figure C.5. Loss in mass during wetting and drying durability test: (a) EB-06-00, (b) EB-06-05, (c) EB-06-10, (d) EB-12-00, (e) EB-12-05, and (f) EB-12-10.

APPENDIX D. COMPARISON OF FLEXURALLY TESTED AND PRISTINE SPECIMENS

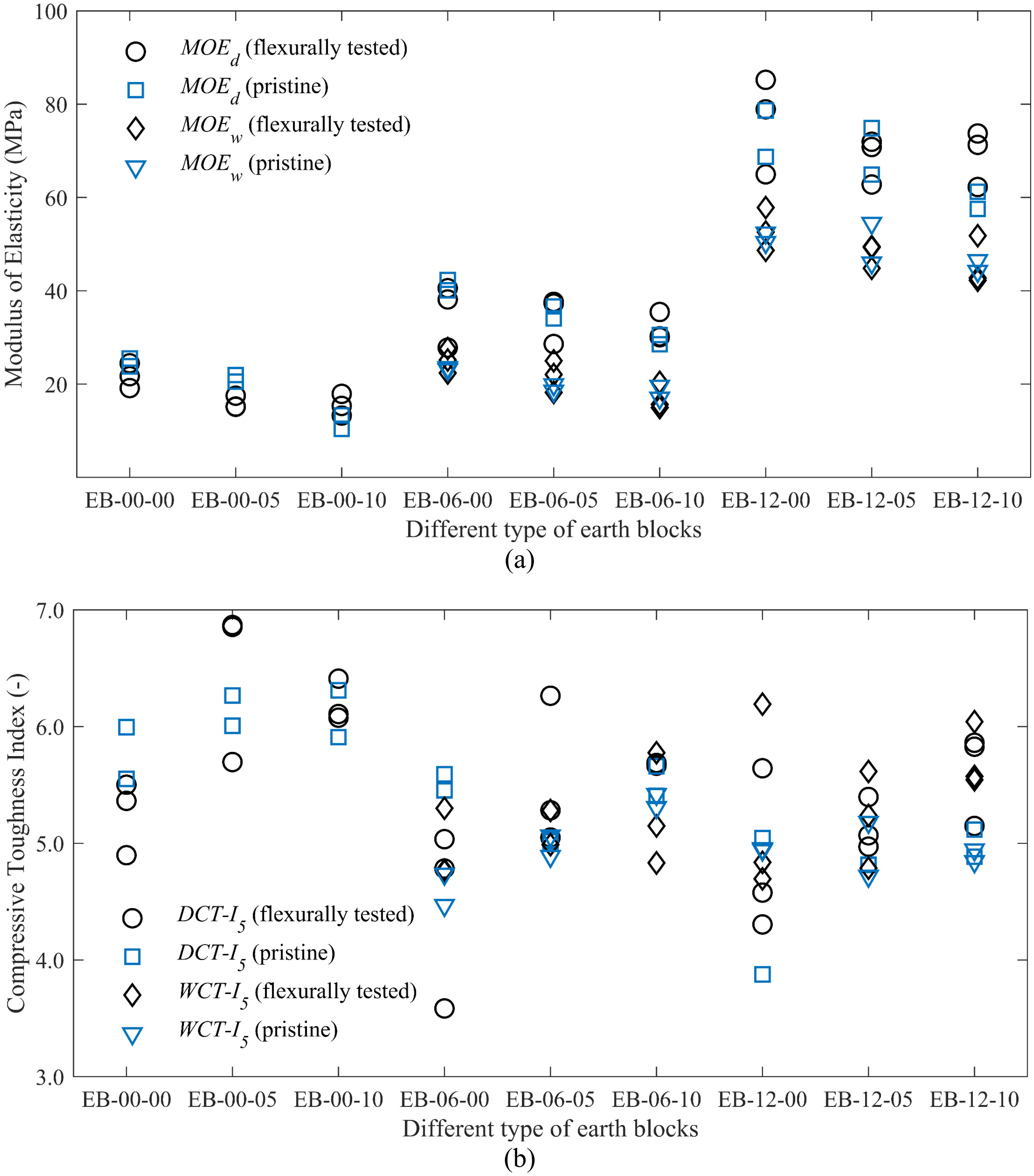

(a)

(b)

Figure D.1. Comparison of flexurally tested and pristine specimens (a) dry and wet modulus of elasticity, and (d) dry and wet compressive toughness index.

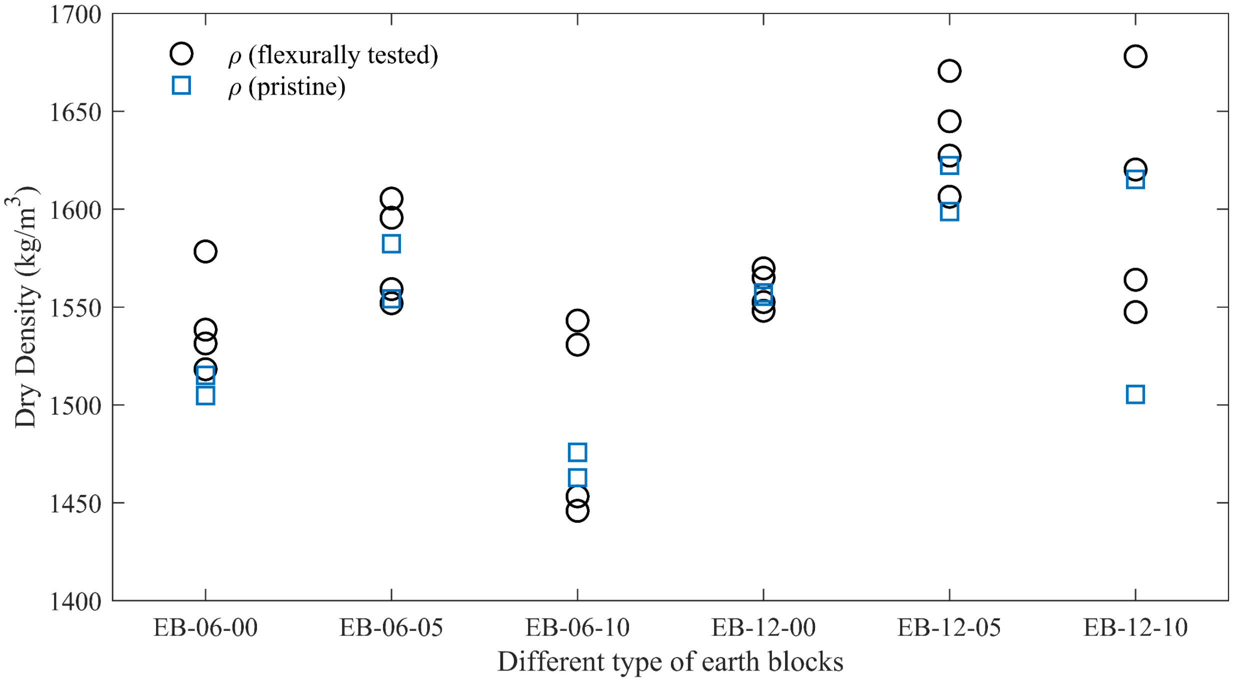

(a)

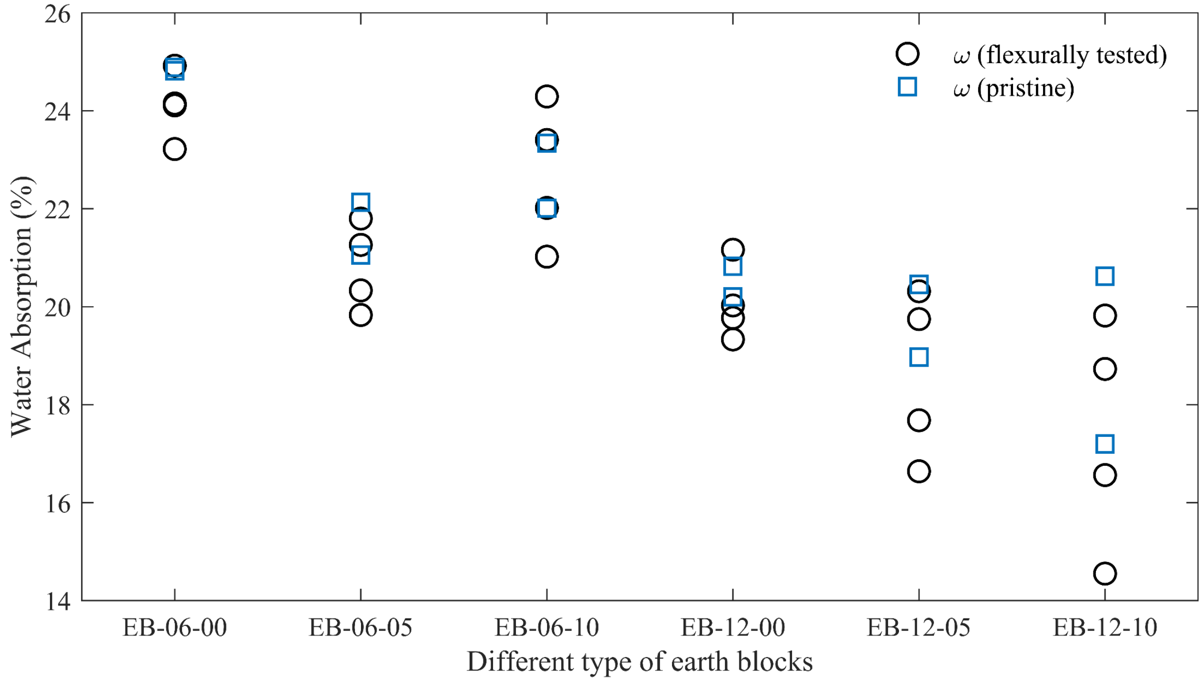

(b)

Figure D.2. Comparison of flexurally tested and pristine specimens: (a) dry density, and (b) water absorption.

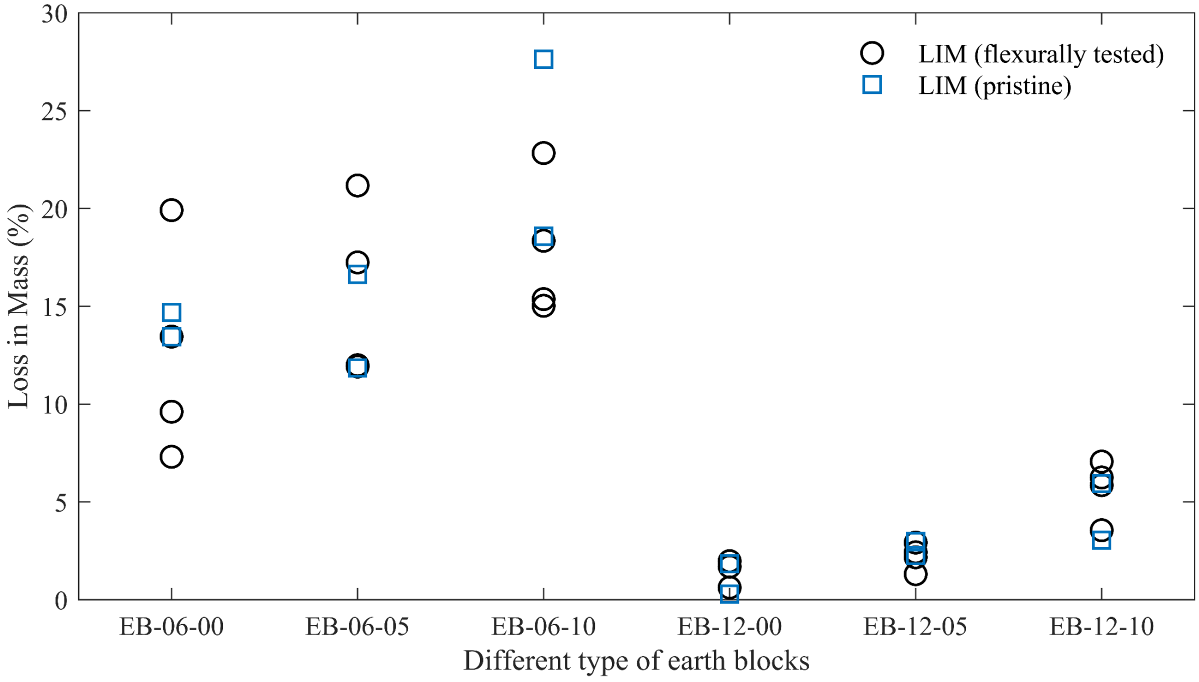
30
25
20
15
10
5
0
Loss in Mass (%)
LIM (flexurally tested)
LIM (pristine)
EB-06-00
EB-06-05
EB-06-10
EB-12-00
EB-12-05
EB-12-10
Different type of earth blocks

(a)

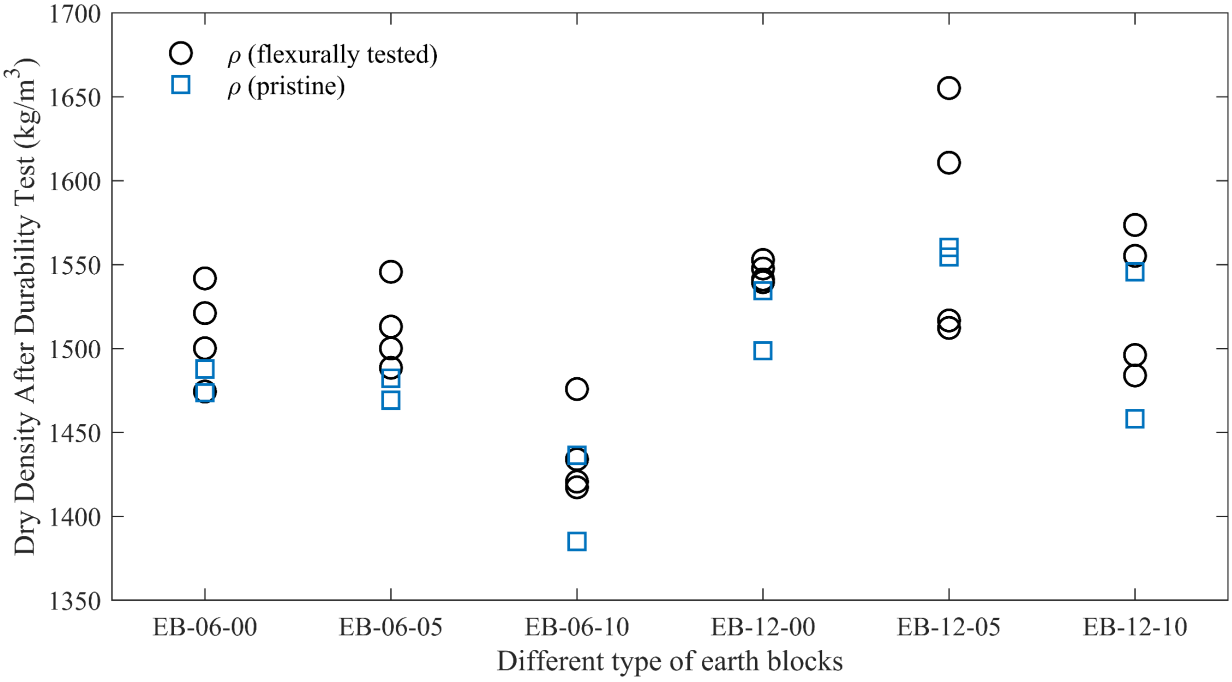
1700
1650
1600
1550
1500
1450
1400
1350
Dry Density After Durability Test (kg/m^3)
ρ (flexurally tested)
ρ (pristine)
EB-06-00
EB-06-05
EB-06-10
EB-12-00
EB-12-05
EB-12-10
Different type of earth blocks

(b)

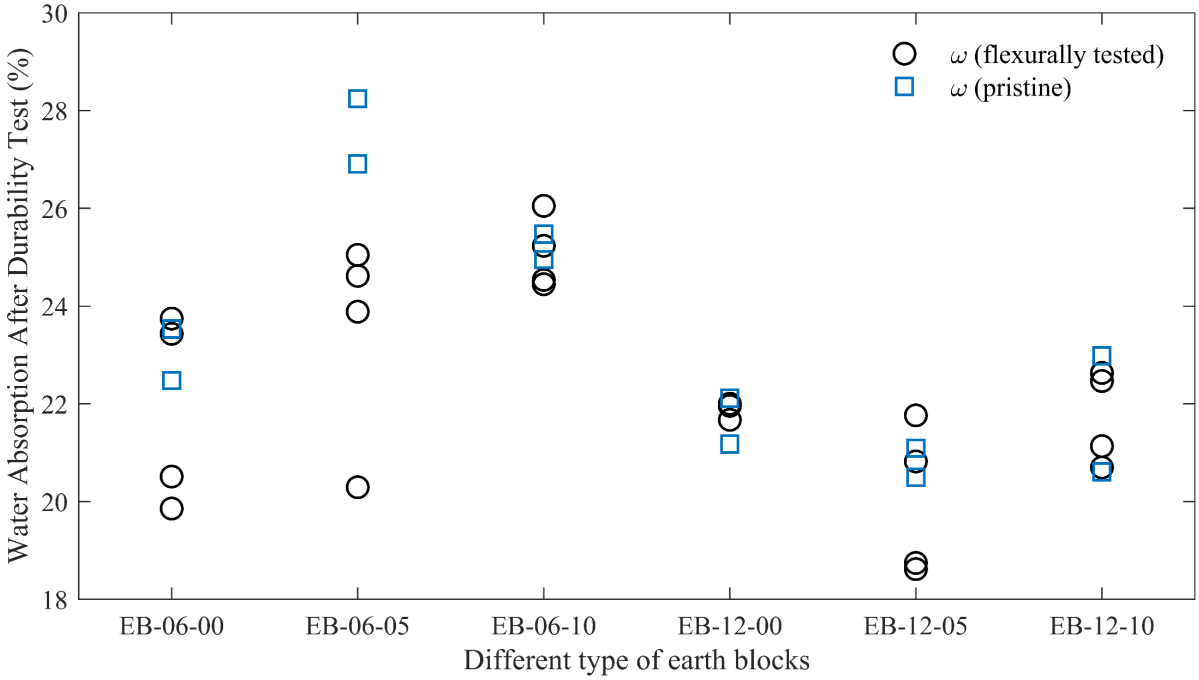

(c)

Figure D.3. Comparison of flexurally tested and pristine specimens (after durability test): (a) loss in mass, (b) dry density, and (c) water absorption.

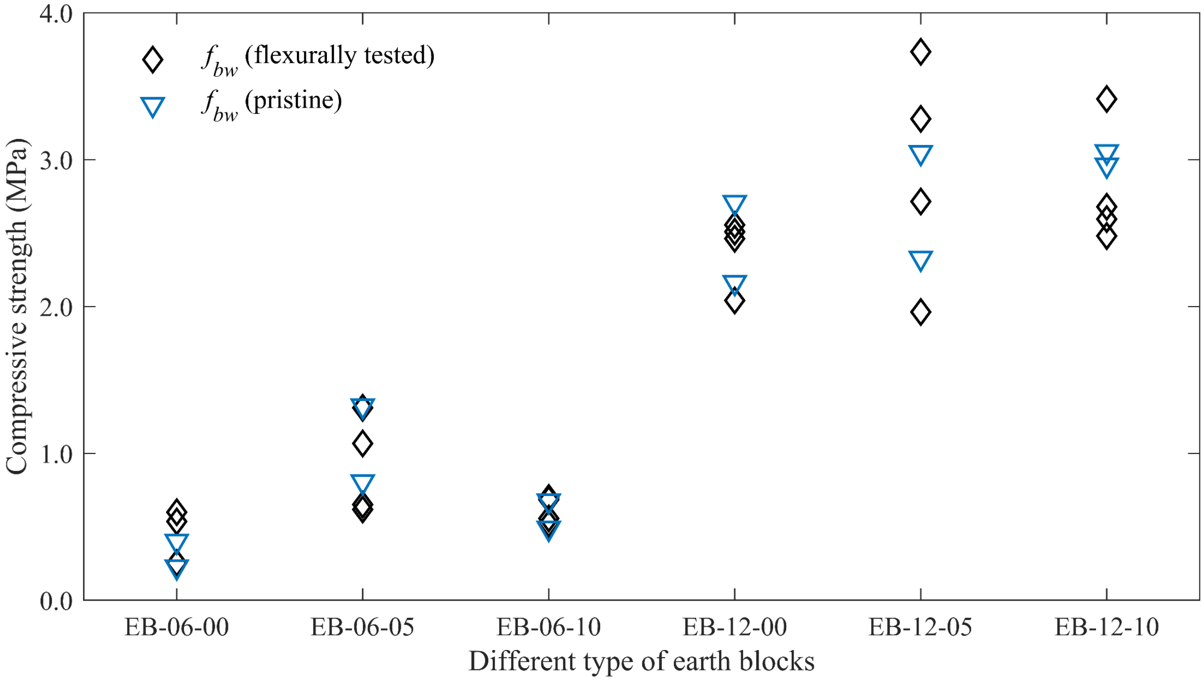

(a)

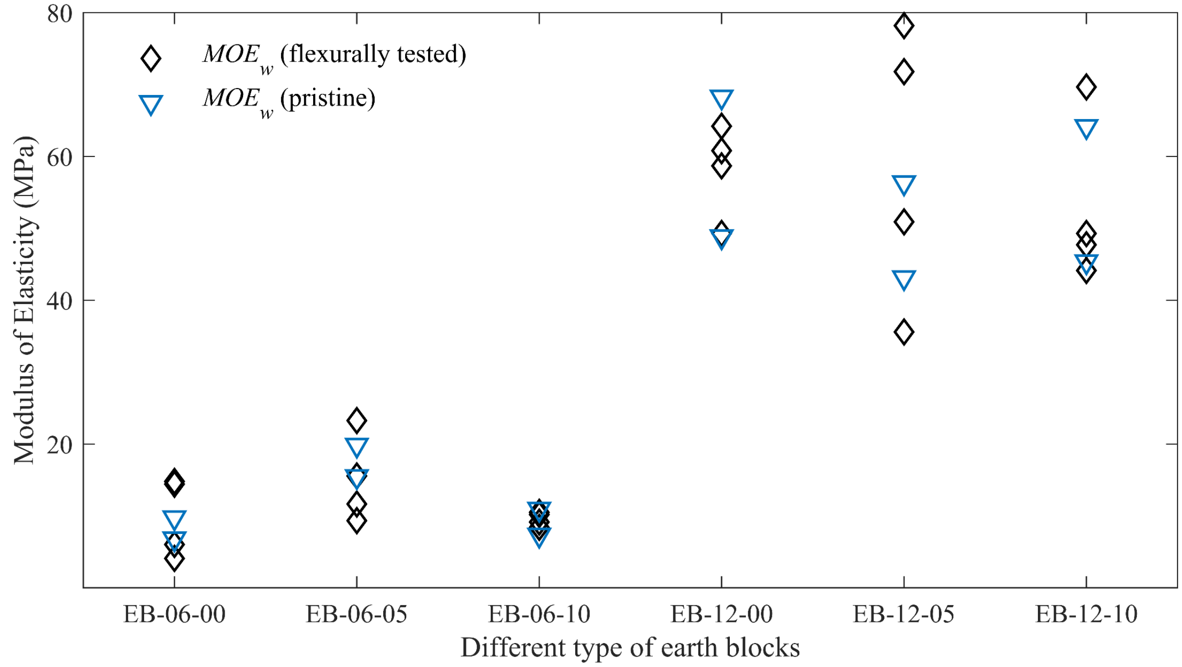

(b)

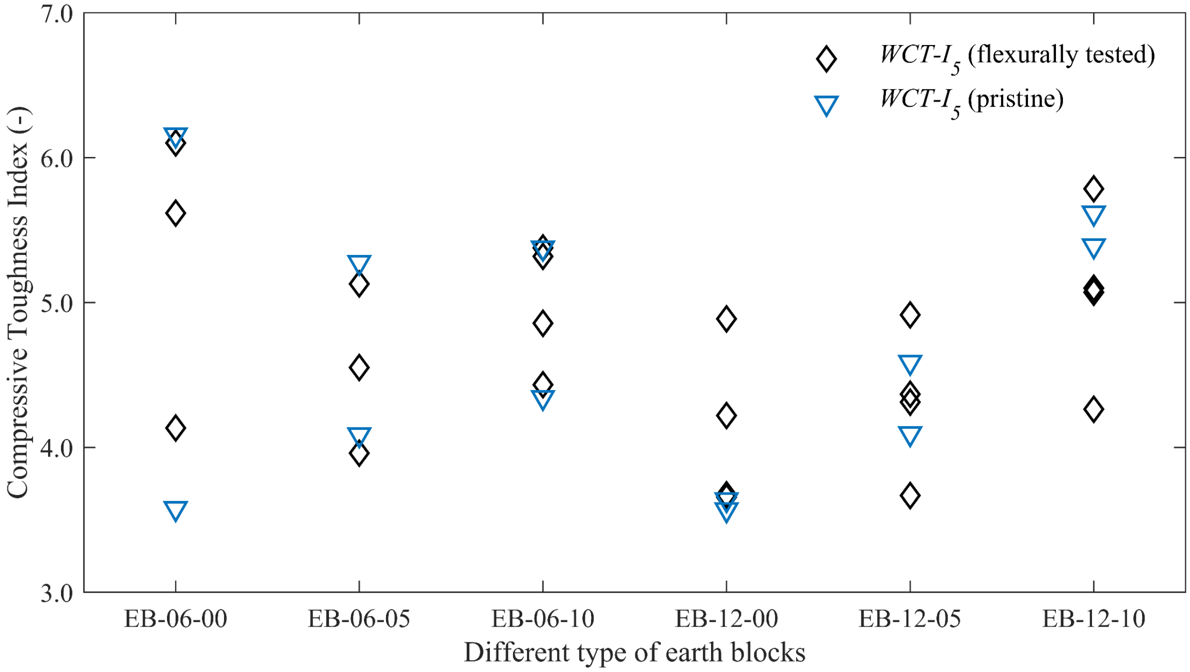

(c)

Figure D.4. Comparison of flexurally tested and pristine specimens (after durability test): (a) wet compressive strength, (b) wet modulus of elasticity, and (c) wet compressive toughness index.

APPENDIX E. DETAILED INTEGRATION SCHEME, SUB-STEPPING STRATEGY, AND EXPRESSION OF FIRST AND SECOND DERIVATIVES OF CTSIM AND OTHER CONSTITUTIVE MODELS

E.1. Jacobian of the Residuals

The local/global Newton-Raphson strategy [184,216,226] is used to solve the nonlinear system of algebraic equations obtained from the implicit backward Euler integration [220] of the CTSIM. This integration procedure leads to a set of algebraic-incremental equations that are solved using an elastic predictor-plastic corrector approach. The plastic correction step is performed when the trial stress violates at least one failure criteria (failure surfaces) and consists in an iteration process that requires: (1) evaluating the residuals of the non-linear constitutive equations, (2) evaluating the Jacobian of the residuals, (3) solving the set of algebraic equations to obtain the increments of the independent variables, (4) evaluating the updated residuals and repeating the iteration until these residuals become smaller than a specified tolerance. Three different cases can occur in the plastic correction step with their Jacobian of the residuals are:

1. Violation of the tension-shear failure criterion, with independent variables $\boldsymbol{\sigma}$, κ_1, κ_2, and $\Delta\lambda_1$:

$$\boldsymbol{J}\left(\boldsymbol{\sigma},\kappa_1,\kappa_2,\Delta\lambda_1\right)=\begin{bmatrix} \boldsymbol{I}_3+\boldsymbol{k}\cdot\Delta\lambda_1\cdot\dfrac{\partial^2 Q_1}{\partial\boldsymbol{\sigma}^2} & \boldsymbol{k}\cdot\Delta\lambda_1\cdot\dfrac{\partial^2 Q_1}{\partial\kappa_1\partial\boldsymbol{\sigma}} & \boldsymbol{k}\cdot\Delta\lambda_1\cdot\dfrac{\partial^2 Q_1}{\partial\kappa_2\partial\boldsymbol{\sigma}} & \boldsymbol{k}\cdot\dfrac{\partial Q_1}{\partial\boldsymbol{\sigma}} \\ -\dfrac{\partial\Delta\kappa_1}{\partial\boldsymbol{\sigma}} & 1-\dfrac{\partial\Delta\kappa_1}{\partial\kappa_1} & -\dfrac{\partial\Delta\kappa_1}{\partial\kappa_2} & -\dfrac{\partial\Delta\kappa_1}{\partial\lambda_1} \\ -\dfrac{\partial\Delta\kappa_2}{\partial\boldsymbol{\sigma}} & -\dfrac{\partial\Delta\kappa_2}{\partial\kappa_1} & 1-\dfrac{\partial\Delta\kappa_2}{\partial\kappa_2} & -\dfrac{\partial\Delta\kappa_2}{\partial\lambda_1} \\ -\dfrac{\partial F_1}{\partial\boldsymbol{\sigma}} & \dfrac{\partial F_1}{\partial\kappa_1} & \dfrac{\partial F_1}{\partial\kappa_2} & 0 \end{bmatrix}_{6\times 6} \qquad \text{(E.1)}$$

where $\boldsymbol{I}_3$ represents the 3×3 identity matrix and $\Delta\lambda_1$ denotes the increment of the plastic multiplier for the tension-shear failure surface $F_1(\boldsymbol{\sigma}, \kappa_1, \kappa_2)$.

2. Violation of the compression cap failure criterion, with independent variables $\boldsymbol{\sigma}$, κ_3, and $\Delta\lambda_2$:

$$\boldsymbol{J}\left(\boldsymbol{\sigma}, \kappa_3, \Delta\lambda_2\right) = \begin{bmatrix} \boldsymbol{I}_3 + \boldsymbol{k} \cdot \Delta\lambda_2 \cdot \dfrac{\partial^2 F_2}{\partial \boldsymbol{\sigma}^2} & \boldsymbol{k} \cdot \Delta\lambda_2 \cdot \dfrac{\partial^2 F_2}{\partial \kappa_3 \partial \boldsymbol{\sigma}} & \boldsymbol{k} \cdot \dfrac{\partial F_2}{\partial \boldsymbol{\sigma}} \\ -\dfrac{\partial \Delta\kappa_3}{\partial \boldsymbol{\sigma}} & 1 - \dfrac{\partial \Delta\kappa_3}{\partial \kappa_3} & -\dfrac{\partial \Delta\kappa_3}{\partial \lambda_2} \\ -\dfrac{\partial F_2}{\partial \boldsymbol{\sigma}} & \dfrac{\partial F_2}{\partial \kappa_3} & 0 \end{bmatrix}_{5\times5} \tag{E.2}$$

where $\Delta\lambda_2$ denotes the increment of the plastic multiplier for the compression cap failure surface $F_2(\boldsymbol{\sigma}, \kappa_3)$.

3. Violation of both tension-shear and compression cap failure criteria (S-C corner), with independent variables $\boldsymbol{\sigma}$, κ_1, κ_2, κ_3, $\Delta\lambda_1$ and $\Delta\lambda_2$:

$$\boldsymbol{J}\left(\boldsymbol{\sigma}, \boldsymbol{\kappa}, \Delta\lambda_1, \Delta\lambda_2\right) = \begin{bmatrix} \boldsymbol{I}_3 + \boldsymbol{k} \cdot \Delta\lambda_1 \cdot \dfrac{\partial^2 Q_1}{\partial \boldsymbol{\sigma}^2} + \boldsymbol{k} \cdot \Delta\lambda_2 \cdot \dfrac{\partial^2 F_2}{\partial \boldsymbol{\sigma}^2} & \boldsymbol{k} \cdot \Delta\lambda_1 \cdot \dfrac{\partial^2 Q_1}{\partial \boldsymbol{\kappa}\, \partial \boldsymbol{\sigma}} + \boldsymbol{k} \cdot \Delta\lambda_2 \cdot \dfrac{\partial^2 F_2}{\partial \boldsymbol{\kappa}\, \partial \boldsymbol{\sigma}} & \boldsymbol{k} \cdot \dfrac{\partial Q_1}{\partial \boldsymbol{\sigma}} & \boldsymbol{k} \dfrac{\partial F_2}{\partial \boldsymbol{\sigma}} \\ -\dfrac{\partial \Delta\boldsymbol{\kappa}}{\partial \boldsymbol{\sigma}} & \boldsymbol{I}_3 - \dfrac{\partial \Delta\boldsymbol{\kappa}}{\partial \boldsymbol{\kappa}} & -\dfrac{\partial \Delta\boldsymbol{\kappa}}{\partial \lambda_1} & -\dfrac{\partial \Delta\boldsymbol{\kappa}}{\partial \lambda_2} \\ -\dfrac{\partial F_1}{\partial \boldsymbol{\sigma}} & \dfrac{\partial F_1}{\partial \boldsymbol{\kappa}} & 0 & 0 \\ -\dfrac{\partial F_2}{\partial \boldsymbol{\sigma}} & \dfrac{\partial F_2}{\partial \boldsymbol{\kappa}} & 0 & 0 \end{bmatrix}_{8\times8}$$

(E.3)

where $\boldsymbol{\kappa} = \{\kappa_1, \kappa_2, \kappa_3\}^T$. Note that some of the terms in Eqs. (E.1), (E.2), and (E.3) are matrices or vectors.

E.2. Numerical Integration Scheme

The CSTIM is consist of two failure criteria ($F_1(\boldsymbol{\sigma}, \kappa_1, \kappa_2)$ and $F_2(\boldsymbol{\sigma}, \kappa_3)$), which interact non-smoothly at singularity point. Thus, the stress ($\boldsymbol{\sigma}$), consistent tangent operator $(\partial\boldsymbol{\sigma} / \partial\boldsymbol{u})$ and internal parameters were determined with the help of multi-surface plasticity solutions. The implicit backward Euler integration method is used to integrate the differential constitutive equations. The integration procedure leads to a set of algebraic-incremental equations, which can be split into elastic predictor, followed by plastic corrector if and only if the trial stress-state violates the current yield condition. Time discretization of interval of interest can be done as $[0,T] = U_{n=1}^{N}[t_n, t_{n+1}]$ and the relevant problem can be seen with in time interval $[t_n, t_{n+1}]$, it is assumed that the stress at current time $t = t_{n+1}$ should satisfy the equilibrium condition and remain of yield surfaces. For prescribed increment in relative displacements $\Delta\mathbf{u}$ at the time step $t_{n+1} = t_n + \Delta t$, the relative displacement is given by $\mathbf{u}_{n+1} = \mathbf{u}_n + \Delta\mathbf{u}$. According to the elastic predictor-plastic correct strategy, the stress and internal parameters can be written in their incremental form as following

$$\begin{aligned}
&\boldsymbol{\sigma}_{n+1} = \boldsymbol{\sigma}_n + \boldsymbol{k}\Delta\boldsymbol{u}^e = \boldsymbol{\sigma}_n + \boldsymbol{k}\left(\Delta\boldsymbol{u} - \Delta\boldsymbol{u}^p\right) = \boldsymbol{\sigma}_{n+1}^{trial} + \Delta\lambda_{n+1}\boldsymbol{km}_{n+1} \\
&\boldsymbol{\kappa}_{n+1} = \boldsymbol{\kappa}_n + \Delta\boldsymbol{\kappa} \\
&\boldsymbol{\kappa}_{3,n+1} = \boldsymbol{\kappa}_{3,n} + \Delta\boldsymbol{\kappa}_3 \\
&F_1\left(\boldsymbol{\sigma}_{n+1}, \boldsymbol{\kappa}_{n+1}\right) = 0 \\
&F_2\left(\boldsymbol{\sigma}_{n+1}, \kappa_{3,n+1}\right) = 0
\end{aligned} \tag{E.4}$$

Increment in elastic relative displacements $\Delta\boldsymbol{u}^e$ and plastic relative displacements $\Delta\boldsymbol{u}^p$ reads

$$\begin{aligned}
\Delta\boldsymbol{u}^e &= \sqrt{\left(\Delta u_n^e\right)^2 + \left(\Delta u_s^e\right)^2 + \left(\Delta u_t^e\right)^2} \\
\Delta\boldsymbol{u}^p &= \sqrt{\left(\Delta u_n^p\right)^2 + \left(\Delta u_s^p\right)^2 + \left(\Delta u_t^p\right)^2}
\end{aligned} \tag{E.5}$$

where u_n^e, u_s^e, and u_t^e denote the elastic relative displacements and u_n^p, u_s^p, and u_t^p denote the plastic relative displacements in the *n*, *s*, and *t* directions, respectively. Three different cases can occur for the elastic predictor-plastic correct strategy: (1) violation of the $F_1(\boldsymbol{\sigma},\boldsymbol{\kappa})$ surface; (2) violation of the $F_2(\boldsymbol{\sigma},\kappa_3)$ surface; and (3) violation of both yield surface, i.e., $F_1(\boldsymbol{\sigma},\boldsymbol{\kappa})$ and $F_2(\boldsymbol{\sigma},\kappa_3)$ surface. In the following, the procedure employed for the third case (multi-surface plasticity) is described in detailed, which is the most general case for the integration of non-linear system of equations. Newton–Raphson strategy is used for the solution of non-linear equation in monolithic format, as illustrated in the Ottosen and Ristinmaa [226], Caballero et al. [216], and Macorini and Izzuddin [184].

The solution of multi-surface plasticity is obtained by assuming the Kuhn–Tucker complementarity conditions and Koiter's flow rules [220]. The increment of total relative displacements can be divided into two components, the elastic $(\Delta\mathbf{u}^e)$ and the plastic $(\Delta\mathbf{u}^p)$ parts. In addition, plastic part consists of the two parts attributed from the tension-shear $\left(\Delta\mathbf{u}_{F_1}^p\right)$ and compression cap $\left(\Delta\mathbf{u}_{F_2}^p\right)$ potential surfaces:

$$\Delta\mathbf{u} = \Delta\mathbf{u}^e + \Delta\mathbf{u}_{F_1}^p + \Delta\mathbf{u}_{F_2}^p \tag{E.6}$$

With

$$\Delta\mathbf{u}_{F_1}^p = \Delta\lambda_1 \frac{\partial Q_1}{\partial\boldsymbol{\sigma}} \tag{E.7}$$

$$\Delta\mathbf{u}_{F_2}^p = \Delta\lambda_2 \frac{\partial F_2}{\partial\boldsymbol{\sigma}} \tag{E.8}$$

Where $\Delta\lambda_1$ and $\Delta\lambda_2$ are the increments of the plastic multipliers for $F_1(\boldsymbol{\sigma},\kappa)$ and $F_2(\boldsymbol{\sigma},\kappa_3)$ surfaces, respectively. The solution is obtained by considering the loading/unloading conditions:

$$\begin{array}{lll} \Delta\lambda_1 \geq 0, & F_1(\boldsymbol{\sigma},\boldsymbol{\kappa}) \leq 0, & \Delta\lambda_1 F_1(\boldsymbol{\sigma},\boldsymbol{\kappa}) = 0 \\ \Delta\lambda_2 \geq 0, & F_2(\boldsymbol{\sigma},\kappa_3) \leq 0, & \Delta\lambda_2 F_2(\boldsymbol{\sigma},\kappa_3) = 0 \end{array} \tag{E.9}$$

Where, $\boldsymbol{\kappa} = \{\kappa_1, \kappa_2\}^T$, and the determination of residual for the Eq. (E.4) and can be written as

$$\boldsymbol{r}(\boldsymbol{\sigma}_{n+1},\boldsymbol{\kappa}_{n+1},\kappa_{3,n+1},\Delta\lambda_{1,n+1},\Delta\lambda_{2,n+1}) = \begin{cases} \boldsymbol{\sigma}_{n+I} - \boldsymbol{\sigma}_{n+1}^{trial} + \Delta\lambda_{n+1}\boldsymbol{km}_{n+1} \\ \boldsymbol{\kappa}_{n+1} - \boldsymbol{\kappa}_n + \Delta\boldsymbol{\kappa}_n \\ \kappa_{3,n+1} - \kappa_{3,n} + \Delta\kappa_{3,n} \\ F_1(\boldsymbol{\sigma}_{\mathrm{n+1}},\boldsymbol{\kappa}_{n+1}) = 0 \\ F_2(\boldsymbol{\sigma}_{\mathrm{n+1}},\kappa_{3,n+1}) = 0 \end{cases} \tag{E.10}$$

Linearization of the residual and expanding the residual. We can write

$$\begin{aligned} &= \boldsymbol{r}(\boldsymbol{\sigma}+\delta\boldsymbol{\sigma},\boldsymbol{\kappa}+\delta\boldsymbol{\kappa},\kappa_3+\delta\kappa_3,\Delta\lambda_1+\delta\Delta\lambda_1,\Delta\lambda_2+\delta\Delta\lambda_2) \\ &= \boldsymbol{r}(\boldsymbol{\sigma},\boldsymbol{\kappa},\kappa_3,\Delta\lambda_1,\Delta\lambda_2) + \frac{\boldsymbol{r}(\boldsymbol{\sigma},\boldsymbol{\kappa},\kappa_3,\Delta\lambda_1,\Delta\lambda_2)}{\partial(\boldsymbol{\sigma},\boldsymbol{\kappa},\kappa_3,\Delta\lambda_1,\Delta\lambda_2)} \begin{bmatrix} \delta\boldsymbol{\sigma} \\ \delta\boldsymbol{\kappa} \\ \delta\kappa_3 \\ \delta\Delta\lambda_1 \\ \delta\Delta\lambda_2 \end{bmatrix} + O(\delta^2) \end{aligned} \tag{E.11}$$

where the truncation after first order term is zero (i.e., $O(\delta^2) \cong 0$), and $\dfrac{\boldsymbol{r}(\boldsymbol{\sigma},\boldsymbol{\kappa},\kappa_3,\Delta\lambda_1,\Delta\lambda_2)}{\partial(\boldsymbol{\sigma},\boldsymbol{\kappa},\kappa_3,\Delta\lambda_1,\Delta\lambda_2)}$ is the gradient of residual with respect to its dependent variable (i.e., $\boldsymbol{\sigma},\boldsymbol{\kappa},\Delta\lambda_1,\Delta\lambda_2$) commonly known as Jacobian $\boldsymbol{J}(\boldsymbol{\sigma},\boldsymbol{\kappa},\kappa_3,\Delta\lambda_1,\Delta\lambda_2)$. The Jacobian ($\boldsymbol{J}(\boldsymbol{\sigma},\boldsymbol{\kappa},\kappa_3,\Delta\lambda_1,\Delta\lambda_2)$) at time step $n+1$ can be express as

$$J=\begin{bmatrix} \boldsymbol{I}_3+\boldsymbol{k}\Delta\lambda_1\dfrac{\partial^2 Q_1}{\partial\boldsymbol{\sigma}^2}+\boldsymbol{k}\Delta\lambda_2\dfrac{\partial^2 F_2}{\partial\boldsymbol{\sigma}^2} & \boldsymbol{k}\Delta\lambda_1\dfrac{\partial^2 Q_1}{\partial\boldsymbol{\sigma}\,\partial\boldsymbol{\kappa}} & \boldsymbol{k}\Delta\lambda_2\dfrac{\partial^2 F_2}{\partial\boldsymbol{\sigma}\,\partial\kappa_3} & \boldsymbol{k}\dfrac{\partial Q_1}{\partial\boldsymbol{\sigma}} & \boldsymbol{k}\dfrac{\partial F_2}{\partial\boldsymbol{\sigma}} \\ -\dfrac{\partial\Delta\boldsymbol{\kappa}}{\partial\boldsymbol{\sigma}} & \boldsymbol{I}_2-\dfrac{\partial\Delta\boldsymbol{\kappa}}{\partial\boldsymbol{\kappa}} & 0 & -\dfrac{\partial\Delta\boldsymbol{\kappa}_1}{\partial\lambda_1} & 0 \\ -\dfrac{\partial\Delta\kappa_3}{\partial\boldsymbol{\sigma}} & 0 & 1-\dfrac{\partial\Delta\kappa_3}{\partial\kappa_3} & 0 & -\dfrac{\partial\Delta\kappa_3}{\partial\lambda_2} \\ -\dfrac{\partial F_1}{\partial\boldsymbol{\sigma}} & \dfrac{\partial F_1}{\partial\boldsymbol{\kappa}} & 0 & 0 & 0 \\ -\dfrac{\partial F_2}{\partial\boldsymbol{\sigma}} & 0 & \dfrac{\partial F_2}{\partial\kappa_3} & 0 & 0 \end{bmatrix}$$

(E.12)

where $\boldsymbol{I}_3$ represents the 3×3 identity matrix, and $\boldsymbol{I}_2$ represents the 2×2 identity matrix. The actual solution is achieved by letting the residual go to zero for that current time step during plastic loading. This can be achieved by performing iterations cycles. The iteration will end when residual becomes smaller then prescribed tolerance value. The residual reads

$$0=\boldsymbol{r}(\boldsymbol{\sigma}_{n+1}^{k},\boldsymbol{\kappa}_{n+1}^{k},\kappa_{3,n+1}^{k},\Delta\lambda_{1,n+1}^{k},\Delta\lambda_{2,n+1}^{k})+\boldsymbol{J}(\boldsymbol{\sigma}_{n+1}^{k},\boldsymbol{\kappa}_{n+1}^{k},\kappa_{3,n+1}^{k},\Delta\lambda_{1,n+1}^{k},\Delta\lambda_{2,n+1}^{k})\begin{bmatrix}\delta\boldsymbol{\sigma}_{n+1}^{k+1}\\ \delta\boldsymbol{\kappa}_{n+1}^{k+1}\\ \delta\kappa_{3,n+1}^{k+1}\\ \delta\Delta\lambda_{1,n+1}^{k+1}\\ \delta\Delta\lambda_{2,n+1}^{k+1}\end{bmatrix} \tag{E.13}$$

Finally, we get

$$\begin{bmatrix}\delta\boldsymbol{\sigma}_{n+1}^{k+1}\\ \delta\boldsymbol{\kappa}_{n+1}^{k+1}\\ \delta\kappa_{3,n+1}^{k+1}\\ \delta\Delta\lambda_{1,n+1}^{k+1}\\ \delta\Delta\lambda_{2,n+1}^{k+1}\end{bmatrix}=-\boldsymbol{J}^{-1}(\boldsymbol{\sigma}_{n+1}^{k},\boldsymbol{\kappa}_{n+1}^{k},\kappa_{3,n+1}^{k},\Delta\lambda_{1,n+1}^{k},\Delta\lambda_{2,n+1}^{k})\,\boldsymbol{r}(\boldsymbol{\sigma}_{n+1}^{k},\boldsymbol{\kappa}_{n+1}^{k},\kappa_{3,n+1}^{k},\Delta\lambda_{1,n+1}^{k},\Delta\lambda_{2,n+1}^{k}) \tag{E.14}$$

and

$$\begin{bmatrix} \boldsymbol{\sigma}_{n+1}^{k+1} \\ \boldsymbol{\kappa}_{n+1}^{k+1} \\ \kappa_{3,n+1}^{k+1} \\ \Delta\lambda_{1,n+1}^{k+1} \\ \Delta\lambda_{2,n+1}^{k+1} \end{bmatrix} = \begin{bmatrix} \boldsymbol{\sigma}_{n}^{k} \\ \boldsymbol{\kappa}_{n+1}^{k} \\ \kappa_{3,n+1}^{k} \\ \Delta\lambda_{1,n+1}^{k} \\ \Delta\lambda_{2,n+1}^{k} \end{bmatrix} + \begin{bmatrix} \delta\boldsymbol{\sigma}_{n+1}^{k+1} \\ \delta\boldsymbol{\kappa}_{n+1}^{k+1} \\ \delta\kappa_{3,n+1}^{k+1} \\ \delta\Delta\lambda_{1,n+1}^{k+1} \\ \delta\Delta\lambda_{2,n+1}^{k+1} \end{bmatrix} \tag{E.15}$$

To solve the local problem, an initial approximation for the unknown is also needed. The standard choice is the elastic trial state, which is

$$\begin{bmatrix} \boldsymbol{\sigma}_{n+1}^{0} \\ \boldsymbol{\kappa}_{n+1}^{0} \\ \kappa_{3,n+1}^{0} \\ \Delta\lambda_{1,n+1}^{0} \\ \Delta\lambda_{2,n+1}^{0} \end{bmatrix} = \begin{bmatrix} \boldsymbol{\sigma}_{n} \\ \boldsymbol{\kappa}_{n} \\ \kappa_{3,n} \\ 0 \\ 0 \end{bmatrix} \tag{E.16}$$

At the end of the iterative process, the local tangent operator $(\partial\boldsymbol{\sigma} / \partial u)$ is obtained as the first derivative of the stresses with respect to the relative displacements. It can be determined by linearizing the non-linear equations from Eq. (E.4) [ref], and we get

$$\frac{\partial\boldsymbol{\sigma}}{\partial\boldsymbol{u}} = \boldsymbol{P}^T\boldsymbol{J}^{-1}(\boldsymbol{\sigma},\boldsymbol{\kappa},\kappa_3,\Delta\lambda_1,\Delta\lambda_2)\boldsymbol{Pk} \tag{E.17}$$

where $\boldsymbol{P}$ the projection matrix on the stress is space, $\boldsymbol{P} = \left[I_3\ 0_{3X5}\right]^T$ and 0_{3X5} is a 3×5 null matrix.

E.3. Sub-stepping Strategy

An adaptive multi-level sub-stepping strategy is employed when: (1) prescribed relative displacement $\Delta\mathbf{u}$ is greater than predefined maximum relative displacement, (2) solution of local procedure does not reach convergence within a prescribed number of iterations. In the first case, the prescribed relative displacement $\Delta\mathbf{u}$ is divided into equal parts such that increment in relative displacement become smaller the predefined maximum relative displacement. In latter cases, the increment in relative displacement is halved each time until the solution is achieved or the increment in relative displacement becomes smaller than predefined minimum relative displacement, in this case, global iteration is recalled. Therefore, any increment could be subdivided into n sub-increments, which could be of different sizes, but they always fulfill that the total displacement at the end of the increment is equal to the sum of all sub-increments:

$$\Delta\mathbf{u}_{n+1} = \sum_{I=1}^{n} \Delta\mathbf{u}_{n+1}^{I} = \Delta\mathbf{u}_{n+1}\left(\sum_{I=1}^{n}\alpha^{I}\right); \quad 0 < \alpha^{I} < 1, \quad \sum_{I=1}^{n}\alpha^{I} = 1 \tag{E.18}$$

At each sub-step, first, the elastic trial stress is obtained. Then, the violation of either or both yield surfaces is subsequently checked as in the case of without sub-stepping. For each sub-step, I the stress vector, the softening/hardening parameters, and plastic multipliers are computed by solving Eq.(E.4), where $\Delta\mathbf{u}_{n+1}$ is substituted by $\Delta\mathbf{u}_{n+1}^{I}$, and then transferred the converged solution to the next step, until a solution is obtained for the last sub-step. Finally, the consistent tangent operator $(\partial\boldsymbol{\sigma}/\partial\boldsymbol{u})$ is determined by adding the different contributions from each sub-step, using the method proposed in [ref] by using the following equation, which provides quadratic convergence at the global level:

$$\left[\frac{\partial\boldsymbol{\sigma}^{I}}{\partial\boldsymbol{u}}\right] = \boldsymbol{P}^{T}\,\boldsymbol{J}^{-1}(\boldsymbol{\sigma}^{I},\boldsymbol{\kappa}^{I},\kappa_3^{I},\Delta\lambda_1^{I},\Delta\lambda_2^{I})\begin{bmatrix}\dfrac{\partial\boldsymbol{\sigma}^{I-1}}{\partial\boldsymbol{u}}+\alpha^{I}\boldsymbol{k}\\ \dfrac{\partial\boldsymbol{\kappa}^{I-1}}{\partial\boldsymbol{u}}\\ \dfrac{\partial\kappa_3^{I-1}}{\partial\boldsymbol{u}}\\ 0\\ 0\end{bmatrix} \tag{E.19}$$

For the first sub-increment $\partial \boldsymbol{\sigma}^0 / \partial \boldsymbol{u} = \boldsymbol{0}$, $\partial \boldsymbol{\kappa}^0 / \partial \boldsymbol{u} = \boldsymbol{0}$ and $\partial \kappa_1^0 / \partial \boldsymbol{u} = \boldsymbol{0}$.

E.4. Expression of First and Second Derivatives of CTSIM

Tension-shear Failure Criterion

$$\frac{\partial F_1}{\partial \boldsymbol{\sigma}} = n = \begin{bmatrix} \tan\phi & \dfrac{\tau_s}{\sqrt{\tau_s^2 + \tau_t^2 + (C - \bar{\sigma}_{f_t} \tan\phi)^2}} & \dfrac{\tau_t}{\sqrt{\tau_s^2 + \tau_t^2 + (C - \bar{\sigma}_{f_t} \tan\phi)^2}} \end{bmatrix} \tag{E.20}$$

$$\frac{\partial Q_1}{\partial \boldsymbol{\sigma}} = m = \begin{bmatrix} 2\tan\psi(C_Q - \sigma\tan\psi) & 2\tau_s & 2\tau_t \end{bmatrix} \tag{E.21}$$

$$\frac{\partial^2 Q_1}{\partial \boldsymbol{\sigma}^2} = \begin{bmatrix} -2(\tan\psi)^2 & 0 & 0 \\ 0 & 2 & 0 \\ 0 & 0 & 2 \end{bmatrix} \tag{E.22}$$

$$A = \sqrt{\left(\frac{f_t}{G_f^I}\kappa_1\right)^2 + \left(\frac{C_0}{G_f^{II}}\kappa_2\right)^2} \tag{E.23}$$

$$\frac{\partial C}{\partial \boldsymbol{\kappa}} = \begin{bmatrix} \dfrac{\partial C}{\partial \kappa_1} & \dfrac{\partial C}{\partial \kappa_2} \end{bmatrix} = \begin{bmatrix} \dfrac{-C_0\kappa_1\left(\dfrac{f_t}{G_f^I}\right)^2 e^{-A}}{A} & \dfrac{-C_0\kappa_2\left(\dfrac{C_0}{G_f^{II}}\right)^2 e^{-A}}{A} \end{bmatrix} \tag{E.24}$$

$$\frac{\partial C_Q}{\partial \boldsymbol{\kappa}} = \begin{bmatrix} \dfrac{\partial C_Q}{\partial \kappa_1} & \dfrac{\partial C_Q}{\partial \kappa_2} \end{bmatrix} = \begin{bmatrix} \dfrac{-C_{Q,0}\kappa_1\left(\dfrac{f_t}{G_f^I}\right)^2 e^{-A}}{A} & \dfrac{-C_{Q,0}\kappa_2\left(\dfrac{C_0}{G_f^{II}}\right)^2 e^{-A}}{A} \end{bmatrix} \tag{E.25}$$

$$\frac{\partial \bar{\sigma}_{f_t}}{\partial \boldsymbol{\kappa}} = \begin{bmatrix} \dfrac{\partial \bar{\sigma}_{f_t}}{\partial \kappa_1} & \dfrac{\partial \bar{\sigma}_{f_t}}{\partial \kappa_2} \end{bmatrix} = \begin{bmatrix} \dfrac{-f_t\kappa_1\left(\dfrac{f_t}{G_f^I}\right)^2 e^{-A}}{A} & \dfrac{-f_t\kappa_2\left(\dfrac{C_0}{G_f^{II}}\right)^2 e^{-A}}{A} \end{bmatrix} \tag{E.26}$$

$$\frac{\partial \tan\phi}{\partial \boldsymbol{\kappa}} = \begin{bmatrix} \dfrac{\partial \tan\phi}{\partial \kappa_1} & \dfrac{\partial \tan\phi}{\partial \kappa_2} \end{bmatrix} = \begin{bmatrix} (\tan\phi_r - \tan\phi_0)\dfrac{\partial C}{\partial \kappa_1}\dfrac{1}{C_0} & (\tan\phi_r - \tan\phi_0)\dfrac{\partial C}{\partial \kappa_2}\dfrac{1}{C_0} \end{bmatrix} \tag{E.27}$$

$$\frac{\partial \tan\psi}{\partial \boldsymbol{\kappa}} = \begin{bmatrix} \dfrac{\partial \tan\psi}{\partial \kappa_1} & \dfrac{\partial \tan\psi}{\partial \kappa_2} \end{bmatrix} = \begin{bmatrix} (\tan\psi_r - \tan\psi_0)\dfrac{\partial C}{\partial \kappa_1}\dfrac{1}{C_0} & (\tan\psi_r - \tan\psi_0)\dfrac{\partial C}{\partial \kappa_2}\dfrac{1}{C_0} \end{bmatrix}$$

(E.28)

$$\frac{\partial^2 Q_1}{\partial \boldsymbol{\sigma}\,\partial \boldsymbol{\kappa}} = \begin{bmatrix} \dfrac{\partial m_1}{\partial \kappa_1} & \dfrac{\partial m_1}{\partial \kappa_2} \\ \dfrac{\partial m_2}{\partial \kappa_1} & \dfrac{\partial m_2}{\partial \kappa_2} \\ \dfrac{\partial m_3}{\partial \kappa_1} & \dfrac{\partial m_3}{\partial \kappa_2} \end{bmatrix} = \begin{bmatrix} 2\left(C_Q - \sigma\tan\psi\right)\dfrac{\partial \tan\psi}{\partial \kappa_1} + 2\tan\psi\left(\dfrac{\partial C_Q}{\partial \kappa_1} - \sigma\dfrac{\partial \tan\psi}{\partial \kappa_1}\right) & 0 & 0 \\ 2\left(C_Q - \sigma\tan\psi\right)\dfrac{\partial \tan\psi}{\partial \kappa_2} + 2\tan\psi\left(\dfrac{\partial C_Q}{\partial \kappa_2} - \sigma\dfrac{\partial \tan\psi}{\partial \kappa_2}\right) & 0 & 0 \end{bmatrix}^T$$

(E.29)

$$\frac{\partial \Delta\kappa_I}{\partial \boldsymbol{\sigma}} = \Delta\lambda_1 \frac{\partial Q_1}{\partial \boldsymbol{\sigma}} \tag{E.30}$$

$$\frac{\partial \Delta\kappa_2}{\partial \boldsymbol{\sigma}} = \frac{\Delta\lambda_1}{\sqrt{n_2^2 + n_3^2}} \frac{\partial Q_1}{\partial \boldsymbol{\sigma}} \begin{bmatrix} 1 & 0 \\ 0 & 1 \end{bmatrix} \frac{\partial^2 Q_1}{\partial \boldsymbol{\sigma}^2} \tag{E.31}$$

$$\frac{\partial \Delta\boldsymbol{\kappa}}{\partial \boldsymbol{\kappa}} = \Delta\lambda_1 \begin{bmatrix} \dfrac{1}{\partial m_1 / \partial \kappa_1} & \dfrac{1}{\partial m_1 / \partial \kappa_2} \\ \dfrac{m_2\left(\partial m_2 / \partial \kappa_1\right) + m_3\left(\partial m_3 / \partial \kappa_1\right)}{\sqrt{m_2^2 + m_3^2}} & \dfrac{m_2\left(\partial m_2 / \partial \kappa_2\right) + m_3\left(\partial m_3 / \partial \kappa_2\right)}{\sqrt{m_2^2 + m_3^2}} \end{bmatrix} \tag{E.32}$$

$$\frac{\partial \Delta\boldsymbol{\kappa}}{\partial \lambda_1} = \begin{bmatrix} m_1 \\ \sqrt{m_2^2 + m_3^2} \end{bmatrix} \tag{E.33}$$

$$\frac{\partial F_1}{\partial \boldsymbol{\kappa}} = \begin{bmatrix} \left(\sigma \frac{\partial \tan\phi}{\partial \kappa_1} - \frac{\partial C}{\partial \kappa_1} \right) + \frac{(C - \bar{\sigma}_{f_t} \tan\phi)}{\sqrt{\tau_s^2 + \tau_t^2 + (C - \bar{\sigma}_{f_t} \tan\phi)^2}} \left(\frac{\partial C}{\partial \kappa_1} - \tan\phi \frac{\partial \bar{\sigma}_{f_t}}{\partial \kappa_1} - \bar{\sigma}_{f_t} \frac{\partial \tan\phi}{\partial \kappa_1} \right) \\ \left(\sigma \frac{\partial \tan\phi}{\partial \kappa_2} - \frac{\partial C}{\partial \kappa_2} \right) + \frac{(C - \bar{\sigma}_{f_t} \tan\phi)}{\sqrt{\tau_s^2 + \tau_t^2 + (C - \bar{\sigma}_{f_t} \tan\phi)^2}} \left(\frac{\partial C}{\partial \kappa_2} - \tan\phi \frac{\partial \bar{\sigma}_{f_t}}{\partial \kappa_2} - \bar{\sigma}_{f_t} \frac{\partial \tan\phi}{\partial \kappa_2} \right) \end{bmatrix}^T \tag{E.34}$$

Compressive Cap Failure Criterion

$$\frac{\partial F_2}{\partial \boldsymbol{\sigma}} = n = \begin{bmatrix} 2\sigma & 2C_{ss}\tau_s & 2C_{ss}\tau_t \end{bmatrix} \tag{E.35}$$

$$\frac{\partial^2 F_2}{\partial \boldsymbol{\sigma}^2} = \begin{bmatrix} 2 & 0 & 0 \\ 0 & 2C_{ss} & 0 \\ 0 & 0 & 2C_{ss} \end{bmatrix} \tag{E.36}$$

$$\frac{\partial^2 F_2}{\partial \boldsymbol{\sigma}\, \partial \kappa_3} = \begin{bmatrix} 0 & 0 & 0 \end{bmatrix} \tag{E.37}$$

$$\frac{\partial \Delta\kappa_3}{\partial \boldsymbol{\sigma}} = \frac{\Delta\lambda_2}{\sqrt{n_1^2 + n_2^2 + n_3^2}} \frac{\partial F_2}{\partial \boldsymbol{\sigma}} \frac{\partial^2 F_2}{\partial \boldsymbol{\sigma}^2} \tag{E.38}$$

$$\frac{\partial \Delta\kappa_3}{\partial \kappa_3} = \frac{\Delta\lambda_2}{\sqrt{n_1^2 + n_2^2 + n_3^2}} \frac{\partial F_2}{\partial \boldsymbol{\sigma}} \frac{\partial^2 F_2}{\partial \boldsymbol{\sigma}\, \partial \kappa_3} \tag{E.39}$$

$$\frac{\partial \Delta\kappa_3}{\partial \lambda_2} = \frac{1}{\sqrt{n_1^2 + n_2^2 + n_3^2}} \tag{E.40}$$

$$\frac{\partial \bar{\sigma}_{comp}}{\partial \kappa_3} = \begin{cases} 2\left(\bar{\sigma}_p - \bar{\sigma}_0\right)\left(\dfrac{2}{\kappa_p} - \dfrac{2\kappa_3}{\kappa_p^2}\right), & if\, \kappa_3 \le \kappa_p \\ 2\left(\bar{\sigma}_m - \bar{\sigma}_p\right)\left[\dfrac{\kappa_3 - \kappa_p}{\left(\kappa_m - \kappa_p\right)^2}\right], & if\, \kappa_p < \kappa_3 \le \kappa_m \\ m \exp^{m\left(\frac{\kappa_3 - \kappa_m}{\bar{\sigma}_m - \bar{\sigma}_r}\right)}, m = 2\dfrac{\bar{\sigma}_m - \bar{\sigma}_p}{\kappa_m - \kappa_p}, & if\, \kappa_3 > \kappa_m \end{cases} \tag{E.41}$$

$$\frac{\partial F_2}{\partial \kappa_3} = -2\bar{\sigma}_{comp} \frac{\partial \bar{\sigma}_{comp}}{\partial \kappa_3} \tag{E.42}$$

E.5. Prominent Equations of Lourenco's Model

Yield Function

$$F_1(\boldsymbol{\sigma}, \kappa_1, \kappa_2) = \sigma - \bar{\sigma}_1(\kappa_1, \kappa_2) \tag{E.43}$$

$$F_2(\boldsymbol{\sigma}, \kappa_1, \kappa_2) = |\tau| - \sigma \tan\phi(\kappa_1, \kappa_2) - C(\kappa_1, \kappa_2) \tag{E.44}$$

$$F_3(\boldsymbol{\sigma}, \kappa_3) = C_{nn}\sigma^2 + C_{nn}\tau^2 + C_n\sigma - \bar{\sigma}_{comp}^2(\kappa_3) \tag{E.45}$$

Potential Function

$$Q_1(\boldsymbol{\sigma}, \kappa_1, \kappa_2) = F_1(\boldsymbol{\sigma}, \kappa_1, \kappa_2) \tag{E.46}$$

$$Q_2(\boldsymbol{\sigma}, \kappa_1, \kappa_2) = |\tau| - \sigma \tan\psi(\kappa_1, \kappa_2) - C_Q(\kappa_1, \kappa_2) \tag{E.47}$$

$$Q_3(\boldsymbol{\sigma}, \kappa_3) = F_3(\boldsymbol{\sigma}, \kappa_3) \tag{E.48}$$

Evolution Law

$$\dot{\kappa}_1 = \left\langle \dot{u}_n^p \right\rangle + \left(\frac{G_f^I}{G_f^{II}} \frac{C_0}{f_t} \sqrt{\left|\dot{u}_s^p\right|^2 + \left|\dot{u}_t^p\right|^2} \right) \tag{E.49}$$

$$\dot{\kappa}_2 = \sqrt{\left|\dot{u}_s^p\right|^2 + \left|\dot{u}_t^p\right|^2} + \left(\frac{G_f^{II}}{G_f^I}\frac{f_t}{C_0}\left\langle \dot{u}_n^p \right\rangle\right) \tag{E.50}$$

$$\dot{\kappa}_3 = \sqrt{\left(\dot{u}_n^p\right)^2 + \left(\dot{u}_s^p\right)^2 + \left(\dot{u}_t^p\right)^2} \tag{E.51}$$

Important Internal Variables

$$A(\kappa_1, \kappa_2) = A_0 \exp\left(-\sqrt{\left(\frac{f_t}{G_f^I}\kappa_1\right)^2 - \left(\frac{C_0}{G_f^{II}}\kappa_2\right)^2}\right), A = C, C_Q, \bar{\sigma}_{f_t} \tag{E.52}$$

$$B(\kappa_1, \kappa_2) = B_r + \left(B_0 - B_r\right)\frac{C}{C_0}, \qquad\qquad B = \tan\phi, \tan\psi \tag{E.53}$$

$$\bar{\sigma}_{comp}(\kappa_3) = \begin{cases} \bar{\sigma}_0 + \left(\bar{\sigma}_p - \bar{\sigma}_0\right)\sqrt{\dfrac{2\kappa_3}{\kappa_p} - \dfrac{\kappa_3^2}{\kappa_p^2}} & if\, \kappa_3 \le \kappa_p \\ \bar{\sigma}_p + \left(\bar{\sigma}_m - \bar{\sigma}_p\right)\left(\dfrac{\kappa_3 - \kappa_p}{\kappa_m - \kappa_p}\right)^2 & if\, \kappa_p < \kappa_3 \le \kappa_m \\ \bar{\sigma}_r + \left(\bar{\sigma}_m - \bar{\sigma}_r\right)\exp\left(m\dfrac{\kappa_3 - \kappa_m}{\bar{\sigma}_m - \bar{\sigma}_r}\right) & if\, \kappa_3 > \kappa_m \end{cases} \tag{E.54}$$

E.6. Prominent Equations of Macorini's Model

Yield Function

$$F_1(\boldsymbol{\sigma}, w_1) = \tau_s^2 + \tau_t^2 - [C(w_1) - \sigma\tan\phi(w_1)]^2 + [C(w_1) - \bar{\sigma}_{f_t}(w_1)\tan\phi(w_1)]^2 \tag{E.55}$$

$$F_2(\boldsymbol{\sigma}, w_2) = \tau_s^2 + \tau_t^2 - [D(w_2) + \sigma\tan\theta(w_2)]^2 + [D(w_2) - \bar{\sigma}_{comp}(w_2)\tan\theta(w_2)]^2 \tag{E.56}$$

Potential Function

$$Q_1(\boldsymbol{\sigma}, w_1) = \tau_s^2 + \tau_t^2 - [C_Q(w_1) - \sigma\tan\psi(w_1)]^2 + [C_Q(w_1) - \bar{\sigma}_{f_t}(w_1)\tan\psi(w_1)]^2 \tag{E.57}$$

$$Q_2(\boldsymbol{\sigma}, w_2) = F_2(\boldsymbol{\sigma}, w_2) \tag{E.58}$$

Evolution Law

$$\dot{w}_1 = \begin{cases} \boldsymbol{\sigma}\,\dot{\mathbf{u}}^p, & \sigma \geq 0 \\ \left(\sqrt{\tau_s^2 + \tau_t^2} + \sigma \tan\phi\right)\sqrt{\left(\dot{u}_s^p\right)^2 + \left(\dot{u}_t^p\right)^2}, & \sigma < 0 \end{cases} \tag{E.59}$$

$$\dot{w}_2 = \boldsymbol{\sigma}\,\dot{\mathbf{u}}^p \tag{E.60}$$

Important Internal Variables

$$\zeta_1^i = \begin{cases} \dfrac{1}{2}\left[1 - \cos\left(\dfrac{\pi w_1}{G_f^i}\right)\right], & 0 \leq w_1 \leq G_f^i \\ 1, & w_1 \leq G_f^i \end{cases}, i = I, II \tag{E.61}$$

$$\zeta_2 = \begin{cases} \dfrac{1}{2}\left[1 - \cos\left(\dfrac{\pi w_2}{G_c}\right)\right], & 0 \leq w_1 \leq G_c \\ 1, & w_1 \leq G_f^{comp} \end{cases} \tag{E.62}$$

$$A(w_1) = A_0(1 - \zeta_1^{II}), \qquad A = C, C_Q \tag{E.63}$$

$$B(w_1) = B_0 - (B_0 - B_r)\zeta_1^{II}, \quad \mathrm{B} = \tan\phi, \tan\psi \tag{E.64}$$

$$A(w_1) = A_0(1 - \zeta_1^{I}), \qquad A = \bar{\sigma}_{f_t} \tag{E.65}$$

$$A(w_2) = A_0(1 - \zeta_2), \qquad A = D \tag{E.66}$$

$$B(w_2) = B_0 - (B_0 - B_r)\zeta_2, \quad \mathrm{B} = \tan\theta, \bar{\sigma}_{comp} \tag{E.67}$$

E.7. Prominent Equations of Citto's Model

Yield Function

$$F(\boldsymbol{\sigma},\boldsymbol{q}) = -[C(\boldsymbol{\sigma},\boldsymbol{q}) - \sigma \tan\phi(\boldsymbol{\sigma},\boldsymbol{q})]^2 F_c(\boldsymbol{\sigma},\boldsymbol{q}) \\ + [C(\boldsymbol{\sigma},\boldsymbol{q}) - \bar{\sigma}_{f_t}(\boldsymbol{\sigma},\boldsymbol{q}) \tan\phi(\boldsymbol{\sigma},\boldsymbol{q})]^2 F_c(\boldsymbol{\sigma},\boldsymbol{q}) + \tau_s^2 + \tau_t^2 \tag{E.68}$$

Potential Function

$$Q(\boldsymbol{\sigma},\boldsymbol{q}) = -[C_Q(\boldsymbol{\sigma},\boldsymbol{q}) - \sigma \tan\psi(\boldsymbol{\sigma},\boldsymbol{q})]^2 F_c(\boldsymbol{\sigma},\boldsymbol{q}) \\ + [C_Q(\boldsymbol{\sigma},\boldsymbol{q}) - \bar{\sigma}_{f_t}(\boldsymbol{\sigma},\boldsymbol{q}) \tan\psi(\boldsymbol{\sigma},\boldsymbol{q})]^2 F_c(\boldsymbol{\sigma},\boldsymbol{q}) + \tau_s^2 + \tau_t^2 \tag{E.69}$$

$$F_c(\boldsymbol{\sigma},\boldsymbol{q}) = 2\arctan\left((\sigma - \bar{\sigma}_{comp}) / \beta\right) / \pi \tag{E.70}$$

$$\boldsymbol{q} = \boldsymbol{q}(C, C, \phi, \psi, \bar{\sigma}_{f_t}, \bar{\sigma}_{comp}) \tag{E.71}$$

Evolution Law

$$\dot{w}_1 = \langle \sigma \rangle \, \dot{u}_n^p \tag{E.72}$$

$$\dot{w}_2 = \left(\sqrt{\tau_s^2 + \tau_t^2} - \tau_{r1} sign(\tau)\right) \sqrt{\left(\dot{u}_s^p\right)^2 + \left(\dot{u}_t^p\right)^2} \tag{E.73}$$

$$\dot{w}_3 = \left(\tau_{r1} - \tau_{r2}\right) sign(\tau) \sqrt{\left(\dot{u}_s^p\right)^2 + \left(\dot{u}_t^p\right)^2} \tag{E.74}$$

$$\dot{w}_4 = \left\langle\left\langle \sigma - \bar{\sigma}_{comp} \right\rangle\right\rangle \dot{u}_n^p \tag{E.75}$$

Important Internal Variables

$$\bar{\sigma}_{f_t}(\boldsymbol{\sigma},\boldsymbol{q}) = f_t \exp\left(-\alpha_{f_t}\left(\frac{w_1}{G_f^I} + \frac{w_2}{G_f^{II}}\right)\right) \tag{E.76}$$

$$A(\boldsymbol{\sigma},\boldsymbol{q}) = A_r + (A_0 - A_r)\exp\left(-\alpha_A\left(\frac{w_1}{G_f^I} + \frac{w_2}{G_f^{II}}\right)\right), A = C, C_Q \tag{E.77}$$

$$A(\boldsymbol{\sigma},\boldsymbol{q}) = A_r + (A_0 - A_r)\exp\left(-\alpha_A w_3\right), A = \phi, \psi \tag{E.78}$$

$$\bar{\sigma}_{comp}(w_4) = \begin{cases} \bar{\sigma}_p + \left(\bar{\sigma}_0 - \bar{\sigma}_p\right)\exp\left(-\alpha_{\bar{\sigma}_{comp1}} w_4\right) & if\ \ w_4 \le \kappa_p \\ \bar{\sigma}_r + \left(\bar{\sigma}_p - \bar{\sigma}_r\right)\exp\left(-\alpha_{\bar{\sigma}_{comp1}}(w_4 - \kappa_p)\right) & if\ \ w_4 \le \kappa_p \end{cases} \tag{E.79}$$

APPENDIX F. NUMERICAL CHARACTERIZATION OF COMPRESSIVE BEHAVIOR OF COMPRESSED AND STABILIZED EARTH BLOCKS

Based on the experimental results presented in the previous study [173], it was hypothesized that the stress-strain responses obtained from the middle-third portion of the specimens with aspect ratio equal to 2 could be used to define a constitutive model for the CSEB material. In order to test this hypothesis, numerical analyses of the direct unit test of CSEB specimens (performed in previous study [173]) were performed based on the FE method. The FE analyses were performed using the commercial FE software ABAQUS [223]. CSEB cylindrical specimens with aspect ratio equal to 2, 1, and 0.5 were modeled using 4-node bilinear plane stress quadrilateral elements with reduced integration (CPS4R).

Figure F.1 shows the adopted FE model domain for the direct unit test of CSEB specimens. The symmetry of the problem was exploited; therefore, only one-half of the cylindrical CSEB specimens was modeled. In addition to the CSEB, the FE models also included the steel plates and the layer of polytet-rafluoroethylene (PTFE), which were used during the experimental tests. Both steel plates and PTFE sheets were considered elastic. The modulus of elasticity and Poisson's ratio of the steel plate were defined as 210 GPa and 0.29 respectively. The modulus of elasticity and Poisson's ratio of the PTFE sheets were defined as 500 GPa and 0.42 respectively, as specified by the manufacturer. In addition, frictional contact was defined between the CSEB specimen and PTFE sheet through a penalty formula-tion. The steel plates and the PTFE sheets were considered perfectly bonded since they were glued to-gether during the experimental tests. The coefficient of friction between the steel and PTFE sheets was determined as 0.48 per ASTM G115 [291] and ASTM D1894 [292].

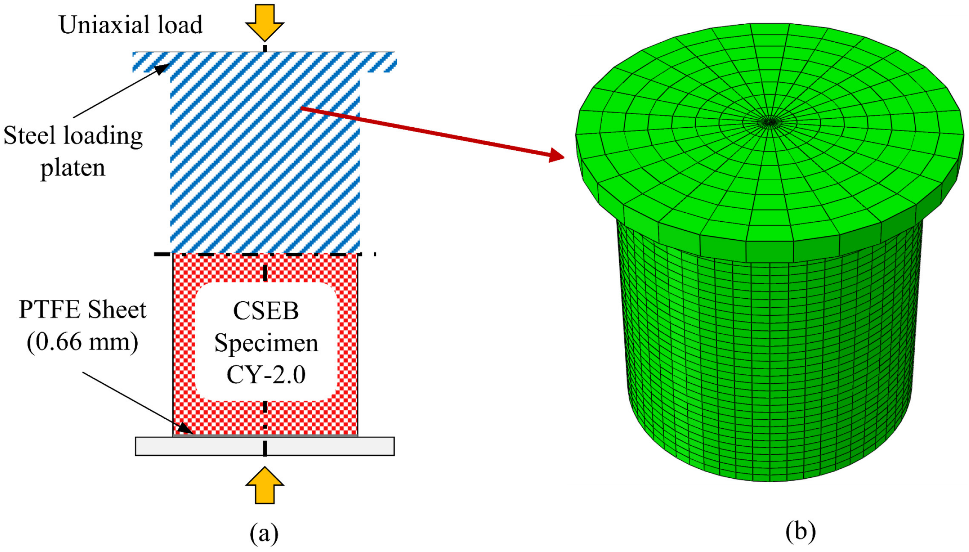

Figure F.1. Schematics and FE discretization CSEB cylindrical specimens

A concrete damaged plasticity model (CDPM) was adopted to simulate the elastoplastic behavior of the CSEB material. The uniaxial compressive behavior of CSEBs was calibrated using the experimental results obtained from the middle one-third portion of the cylindrical specimens with aspect ratio equal to 2. **Figure F.2** shows the experimental uniaxial compressive stress-strain curves as well as the numerical model obtained by estimating the mean values of the model parameters based on the experimental results.

Here, it is noted that the experimental data after peak strength were deemed not sufficiently reliable and that the post-peak curve was defined by estimating the necessary model parameters from the measured peak strength. Therefore, the present study focuses on the CSEB stress-strain response up to peak stress to gain some preliminary insight into the unconfined uniaxial compressive behavior of CSEB materials. In addition, the uniaxial tensile behavior was calibrated using the three-point flexural test results available in [167] for CSEBs specimens similar to the specimens used in the present study.

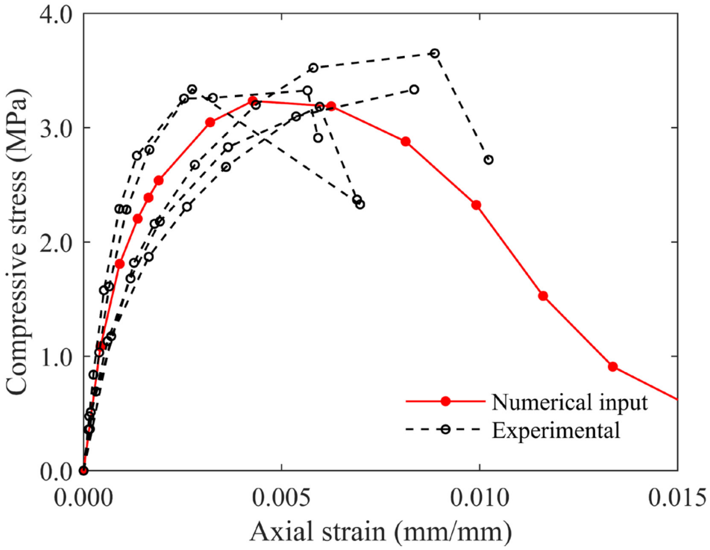

Figure F.2. Stress-strain curves from middle-third of CSEB specimens with aspect ratio equal to 2

Table 3 summarizes the model parameters used to describe the CSEB specimens constitutive behavior. In the CDPM, β_{bc} is ratio of bi-axial compressive strength and uniaxial compressive strength, K_c is ratio of the second stress invariant on the tensile meridian and on the compressive meridian, and η is viscosity parameter. The values of E, ν, f_t and G_f^I are the mean values obtained from the experimental data. The CDPM parameter values used in this study are those recommended in the literature for concrete [267,268,277,278], which are expected to provide at least qualitatively reasonable results for the CSEB quasi-brittle material considered here. Whereas this selection is acceptable for the preliminary investigation presented in this appendix of the dissertation, it is recommended that future studies are based on CDPM parameter values obtained for CSEBs through an appropriate experimental campaign enlisting, e.g., bi-axial compressive strength tests.

Table F.1 Material properties for FE modeling of CSEB specimens.

Elastic parameters	Modulus of elasticity E (MPa)	2546
	Poisson's ratio ν (-)	0.17
Tensile behavior parameters	Modulus of rupture f_t (MPa)	0.510
	Mode-I fracture energy G_f^I (N/mm)	0.009
CDPM parameters	Dilation angle ψ_c	38°
	Eccentricity e_c	0.10
	β_{bc}	1.16
	K_c	0.67
	η	8.5×10^{-5}

Figure F.3(a) and (b) present a comparison between the experimental and numerical load-displacement curves for cylindrical specimens with aspect ratio 2 and 1, respectively. It is noted that the markers along the experimental curves in **Figure F.3** indicate the loads selected for the acquisition of images for 3D-DIC analysis. The simulation results are in fair-to-good agreement with those from the physical tests. In particular, the experimental and numerical load-displacement values are in good agreement up to the peak load, which indicates that the numerical input curve, which was obtained from the experimental data, is representative of the unconfined uniaxial compression behavior of the CSEB. **Table F.2** reports the experimental and numerical estimates of the peak strength and initial stiffness of the three sets of specimens, together with their percentage differences. It is observed that the developed FE models are able to predict the stiffness of the cylindrical CSEBs specimens with good accuracy where percentage difference in the numerical and experimental value of stiffness are 9%, 5% and 14% for the cylinder with aspect ratio 2, 1, and 0.5, respectively. The percentage difference in peak strength for the cylindrical specimens with aspect ratio 2 is 3%; however, this differences substantially increases for decreasing aspect ratio, with values of 21% and 47% for cylindrical specimens with aspect ratio 1 and 0.5, respectively. These results suggest that the stress-strain curves obtained from the middle-third portion of cylindrical specimens with aspect ratio equal to 2 may be used to define a material constitutive model for the unconfined uniaxial compression behavior of CSEBs, but also that the FE model used in this investigation does not fully capture the effects of confinement in axial compression tests.

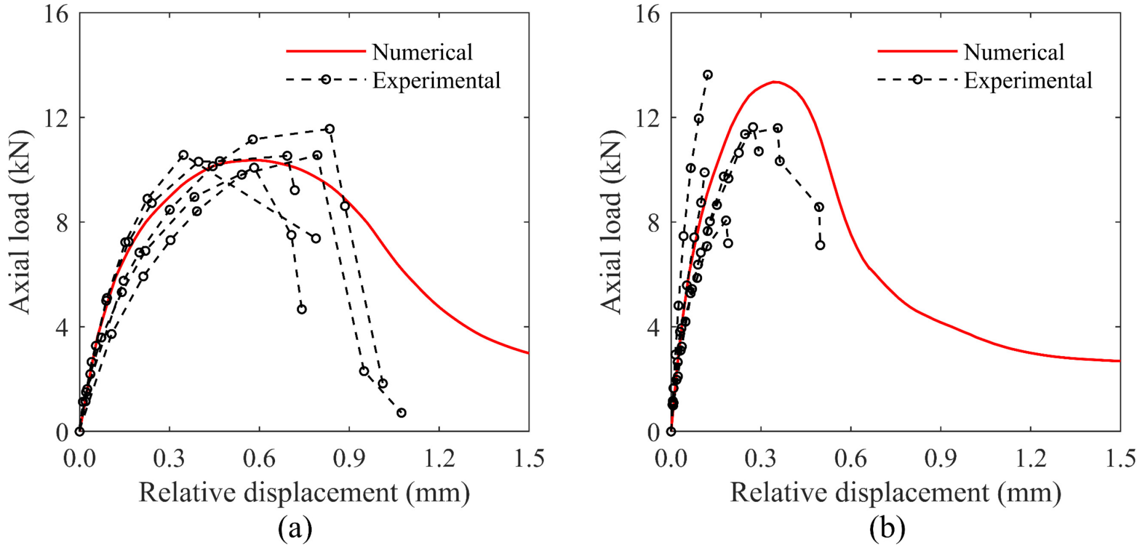

(a) (b)

Figure F.3. Compressive load-displacement curves of CSEB specimens with aspect ratio of: (a) 2, and (b) 1

The numerical analysis results indicate that the stress-strain curves obtained from the middle-third portion of cylindrical specimens with an aspect ratio of 2 may be suitable to define a constitutive model for the unconfined uniaxial compression behavior of CSEB materials. More research is ongoing to more effectively simulate the effects of confinement in uniaxial compression tests.

Table F.2 Comparison of experimental and numerical maximum load and stiffness.

	Maximum Compressive Load (kN)			Stiffness (kN-mm)		
	Experimental	Numerical	Difference	Experimental	Numerical	Difference
CY-2.0	10.7	10.4	3%	57.4	62.4	9%
CY-1.0	11.1	13.4	21%	128.9	122.9	5%
CY-0.5	16.3	23.9	47%	223.4	192.8	14%

APPENDIX G. PARAMETRIC STUDY FOR DMM OF CSEB MASONRY WALLETTE SUBJECTED TO DIAGONAL COMPRESSION LOAD

G.1. Parameters Corresponding to CDPM

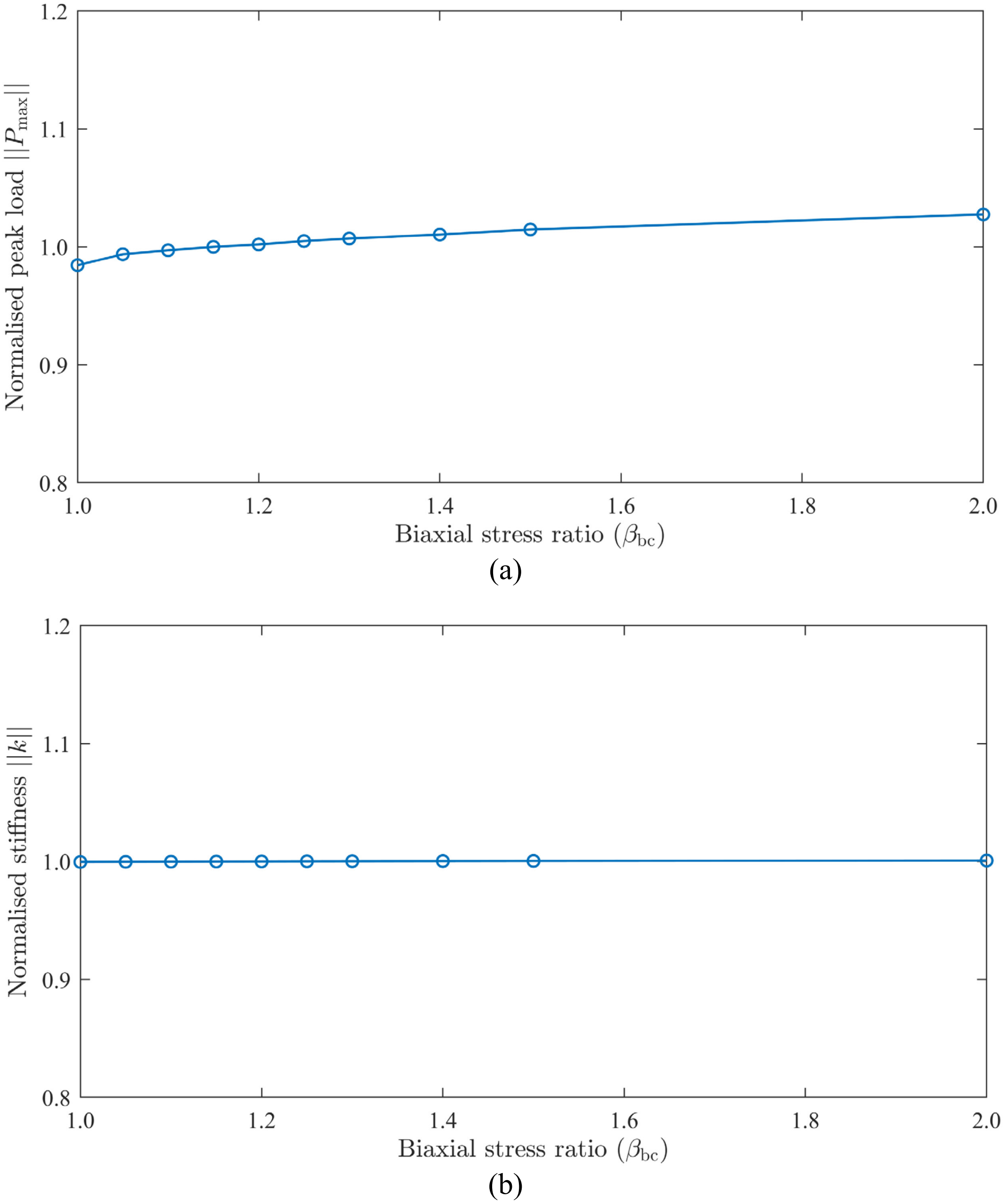

(a)

(b)

Figure G.1. Parametric study of biaxial stress ratio for DMM of the CSEB masonry wallette subjected to diagonal compression load: (a) peak load, and (b) initial stiffness.

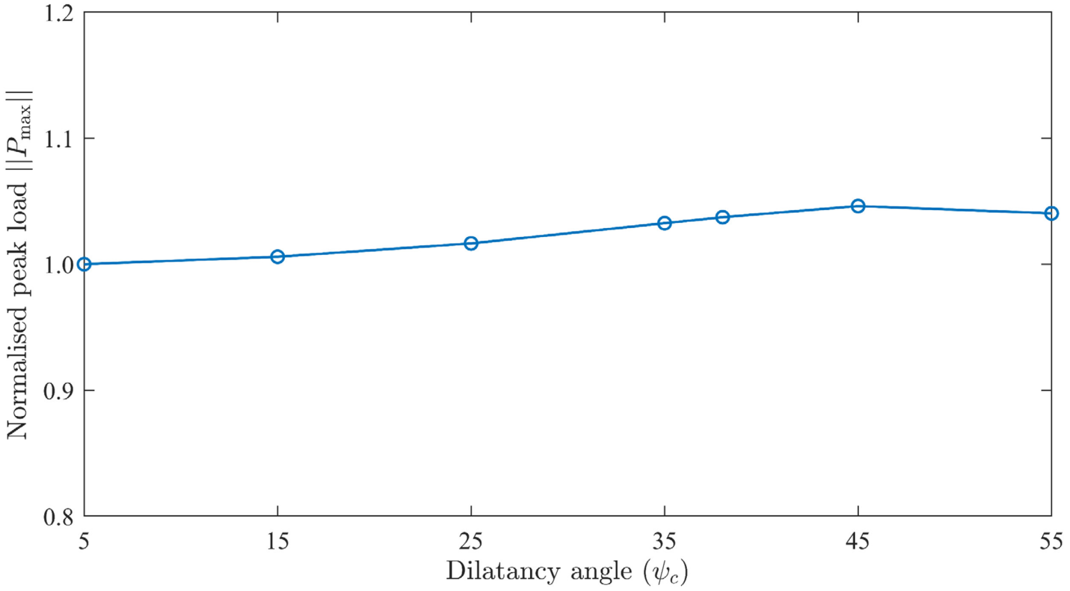

(a)

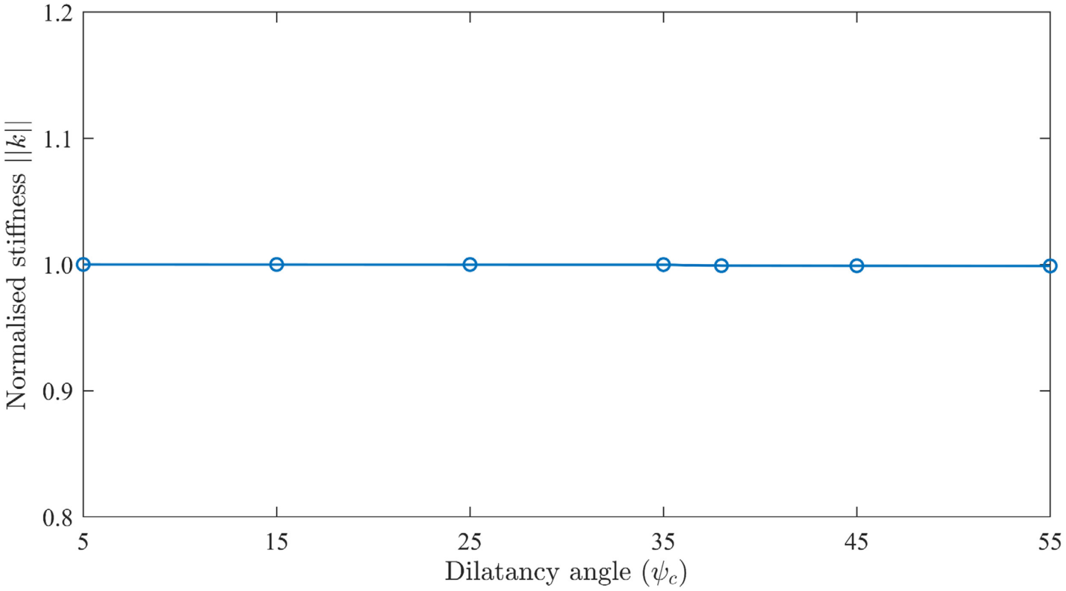

(b)

Figure G.2. Parametric study of dilatancy angle (CDPM) for DMM of the CSEB masonry wallette subjected to diagonal compression load: (a) peak load, and (b) initial stiffness.

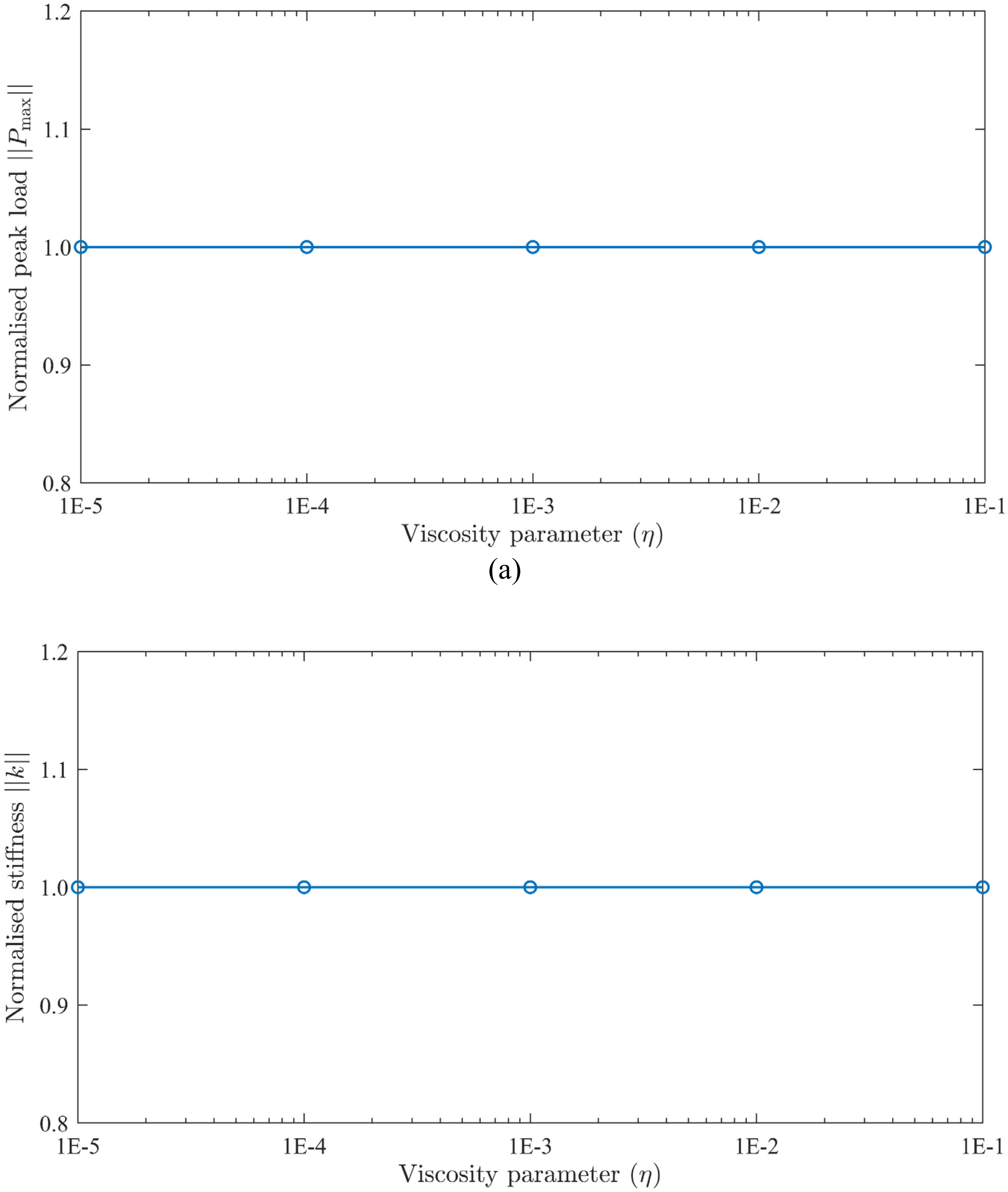

(a)

(b)

Figure G.3. Parametric study of viscosity parameter (CDPM) for DMM of the CSEB masonry wallette subjected to diagonal compression load: (a) peak load, and (b) initial stiffness.

G.2. Tensile Strength

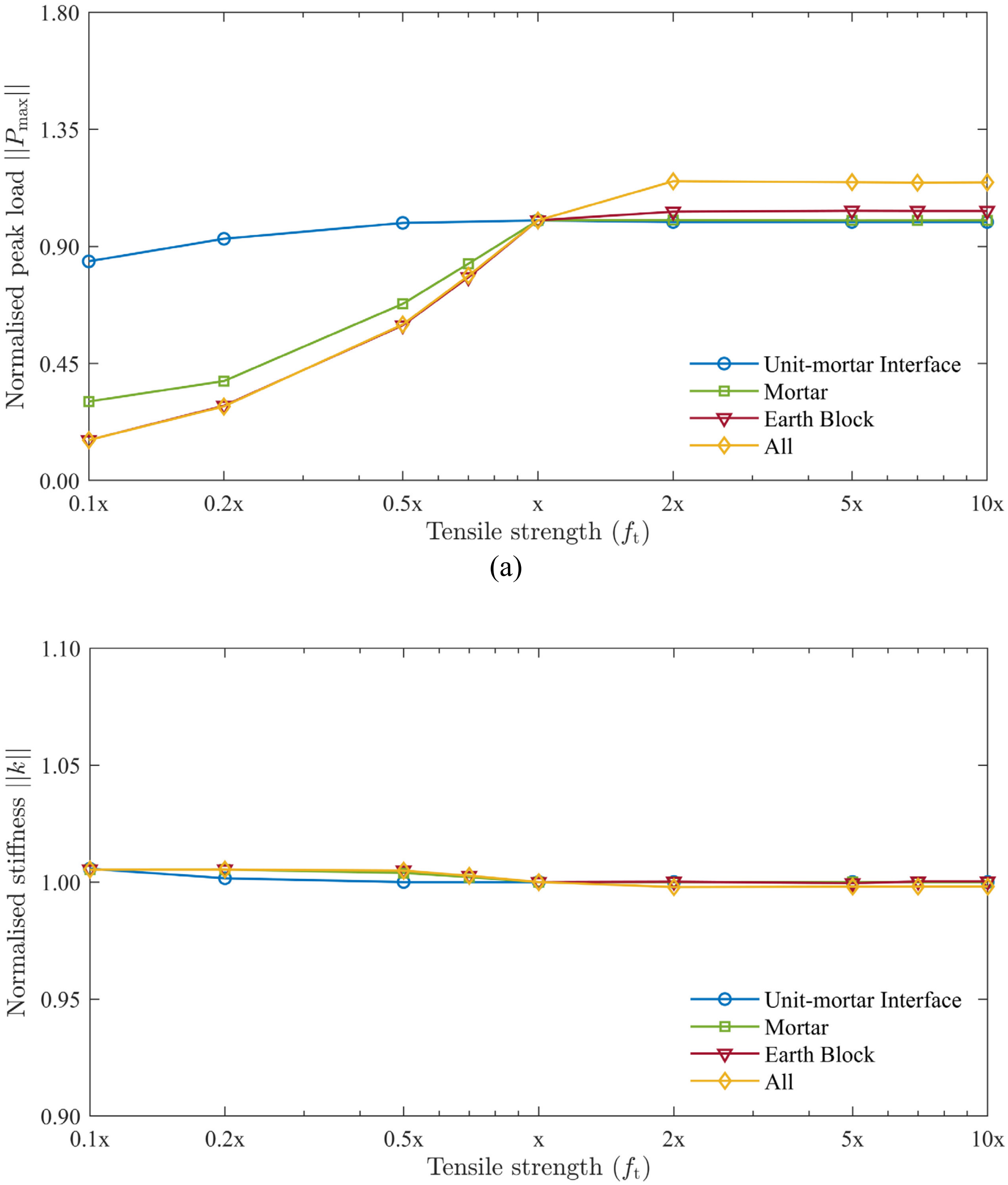

(a)

(b)

Figure G.4. Parametric study of tensile strength for DMM of the CSEB masonry wallette subjected to diagonal compression load: (a) peak load, and (b) initial stiffness.

G.3. Mode-I Fracture Energy

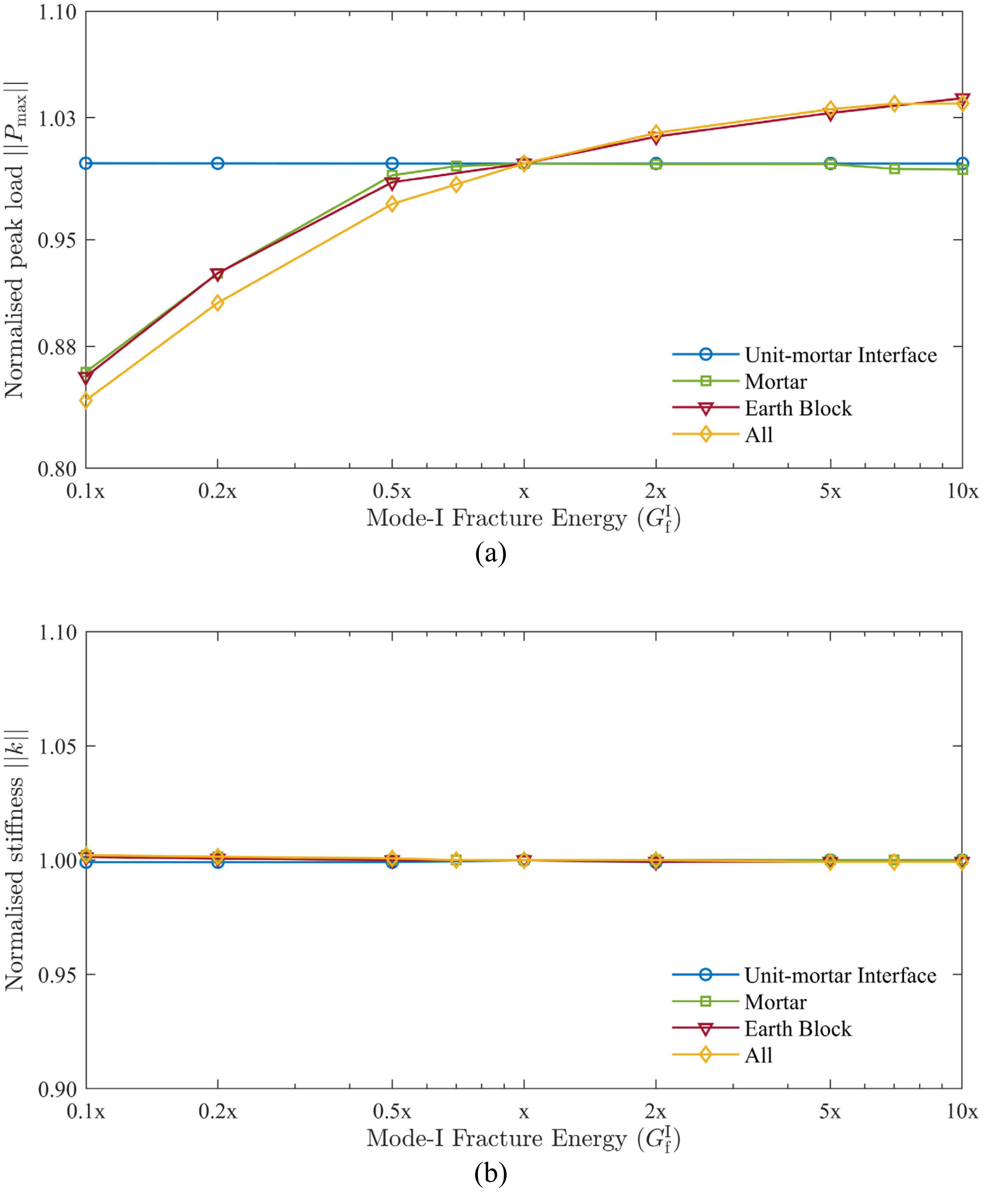

Figure G.5. Parametric study of Mode-I fracture energy for DMM of the CSEB masonry wallette subjected to diagonal compression load: (a) peak load, and (b) initial stiffness.

G.4. Compressive Strength

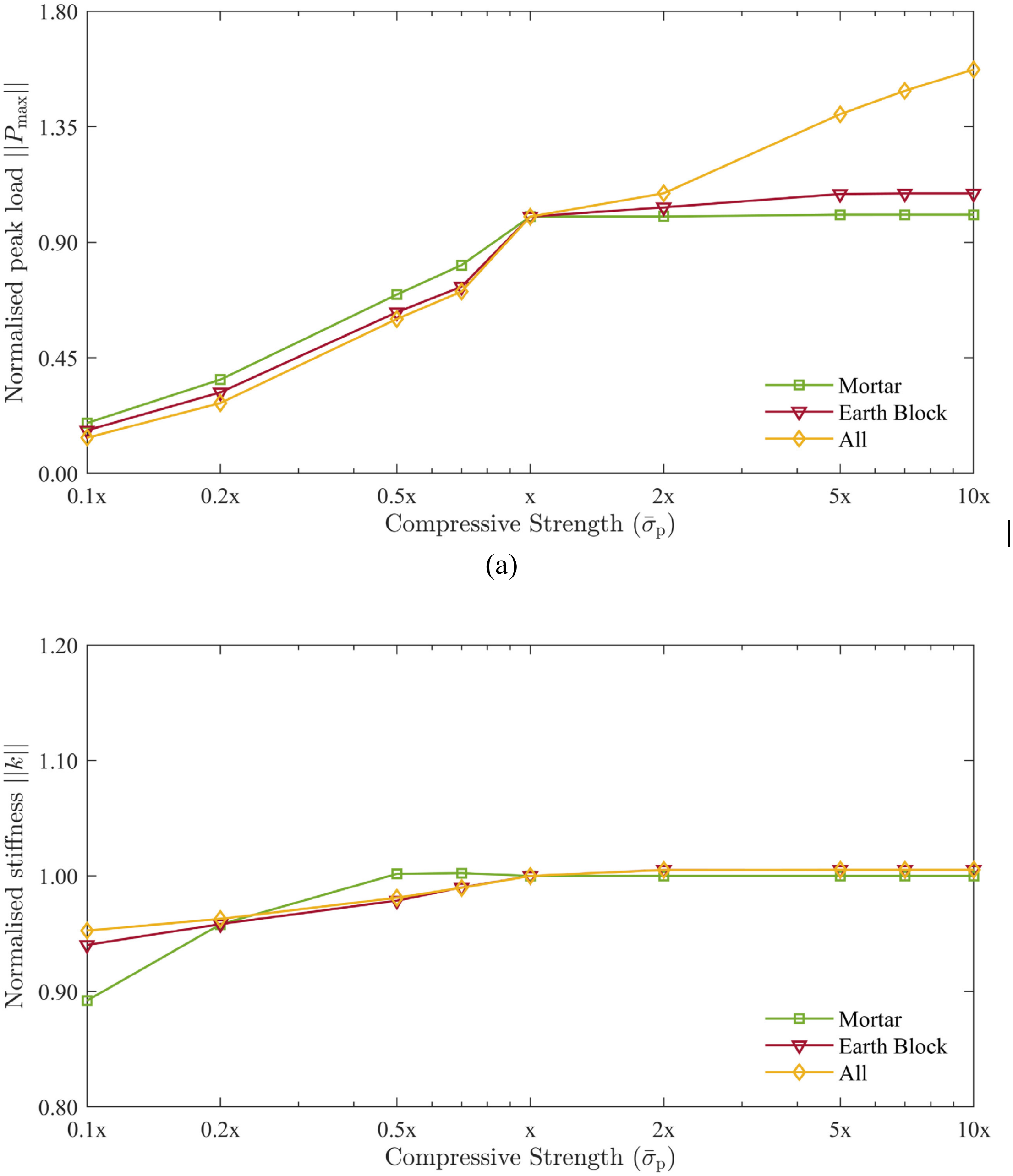

(a)

(b)

Figure G.6. Parametric study of compressive strength for DMM of the CSEB masonry wallette subjected to diagonal compression load: (a) peak load, and (b) initial stiffness.

G.5. Compressive Plastic Strain

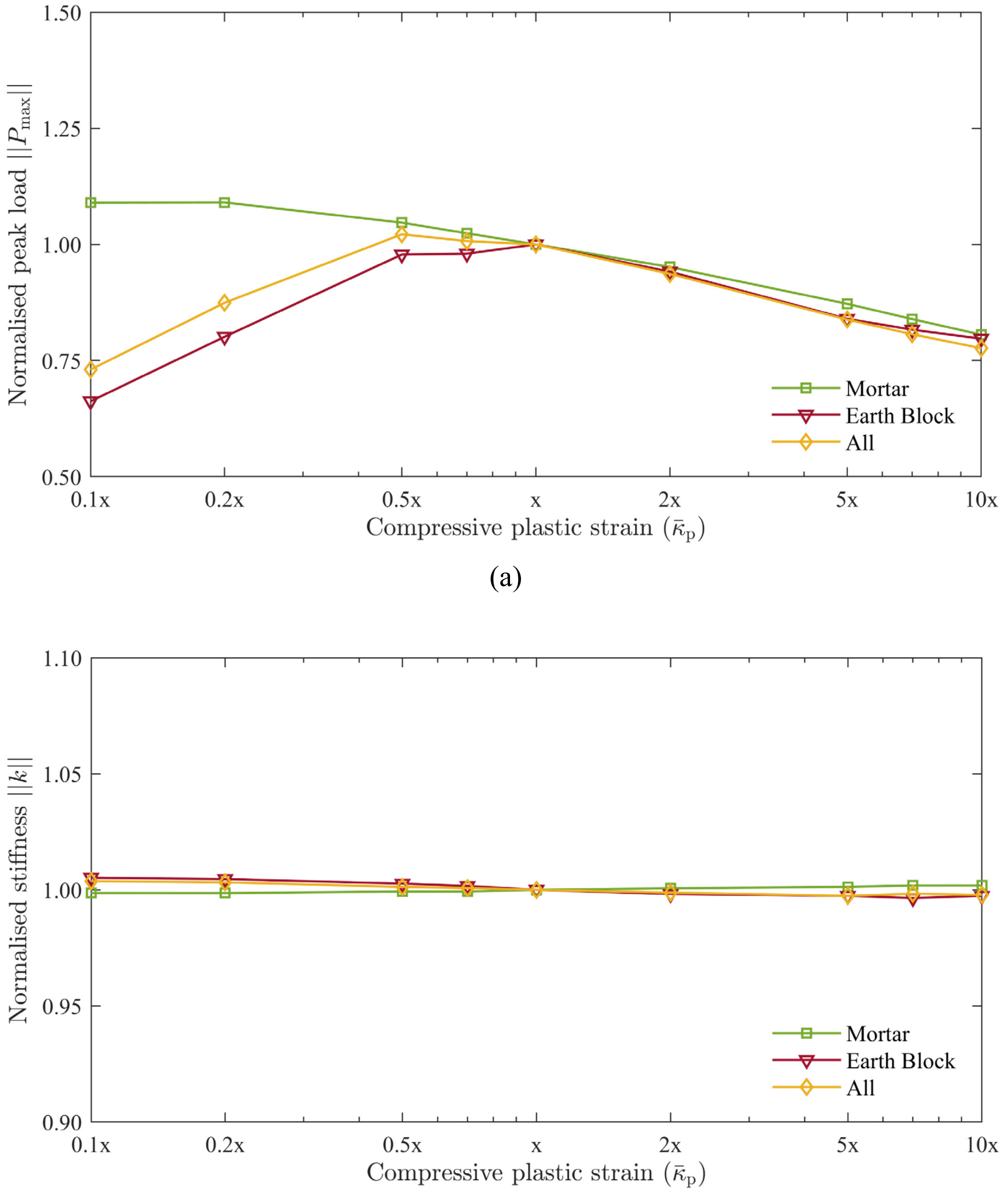

(a)

(b)

Figure G.7. Parametric study of compressive plastic strains for DMM of the CSEB masonry wallette subjected to diagonal compression load: (a) peak load, and (b) initial stiffness.

G.6. Other Parameters Corresponding to Unit-mortar Interface

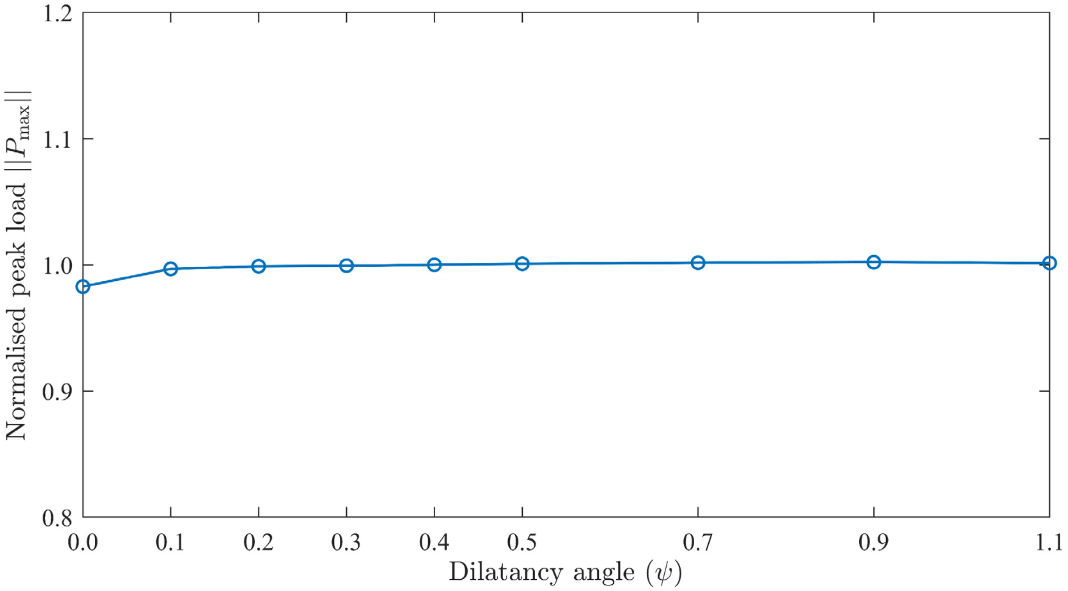

(a)

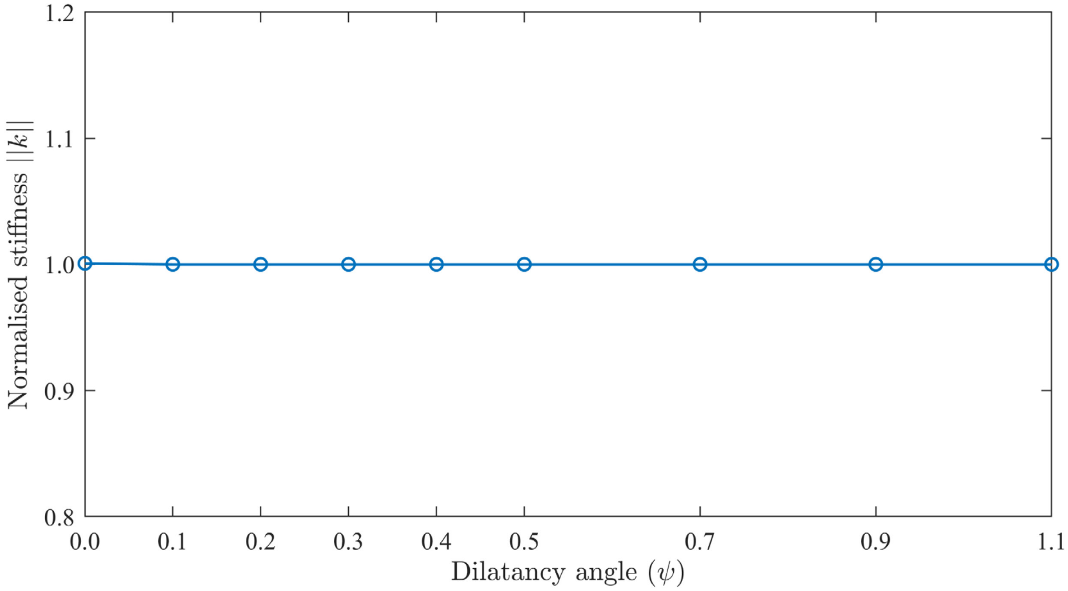

(b)

Figure G.8. Parametric study of dilatancy angle for DMM of the CSEB masonry wallette subjected to diagonal compression load: (a) peak load, and (b) initial stiffness.

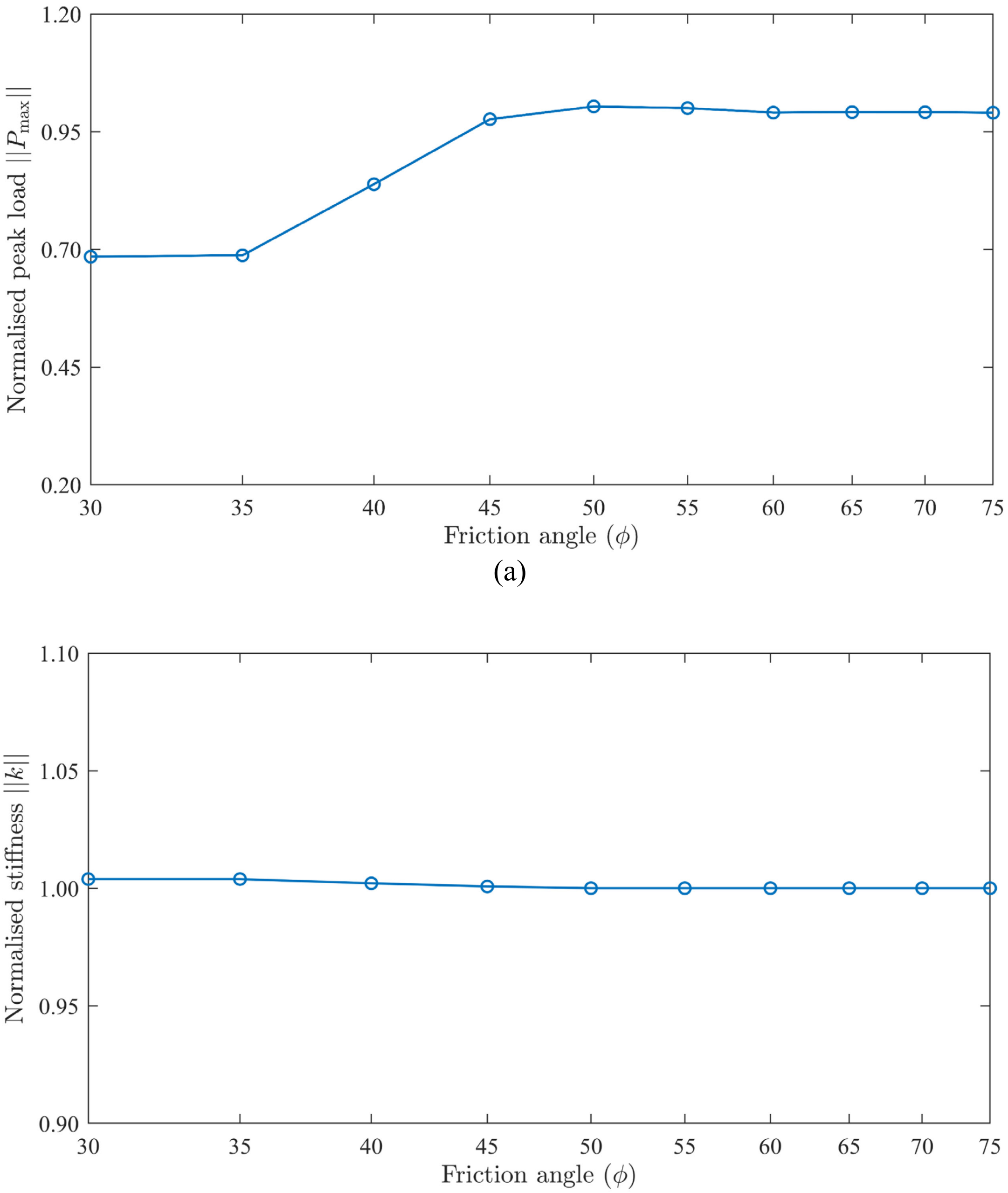

(a)

(b)

Figure G.9. Parametric study of friction angle for DMM of the CSEB masonry wallette subjected to diagonal compression load: (a) peak load, and (b) initial stiffness.

REFERENCES

[1] F. Pacheco-Torgal, S. Jalali, "Earth Construction: Lessons from the Past for Future Eco-Efficient Construction." *Construction and Building Materials*. 29 (2012) 512–519. https://doi.org/10.1016/j.conbuildmat.2011.10.054.

[2] G. Minke, *Building with Earth: Design and Technology of a Sustainable Architecture*, 2nd ed., Birkhaeuser Publishers for Architecture, Basel, Berlin, 2012. ISBN: 000-3764389923.

[3] G. Minke, *Construction Manual for Earthquake-Resistant Houses Built of Earth*, Gesellschaft für Technische Zusammenarbeit, Eschborn, Germany, 2001.

[4] S. Dhengare, S. Amrodiya, M. Shelote, A. Asati, N. Bandwal, A. Khangan, R. Jichkar, "Utilization of Sugarcane Bagasse Ash As a Supplementary Cementitious Material in Concrete and Mortar-a Review." *International Journal of Civil Engineering and Technology (IJCIET)*. 0976 (2015) 94–106.

[5] K. Ramamurthy, E.K. Kunhanandan Nambiar, "Accelerated Masonry Construction Review and Future Prospects." *Progress in Structural Engineering and Materials*. 6 (2004) 1–9. https://doi.org/10.1002/pse.162.

[6] K.B.B. Anand, K. Ramamurthy, "Development and Performance Evaluation of Interlocking-Block Masonry." *Journal of Architectural Engineering*. 6 (2000) 45–51. https://doi.org/10.1061/(ASCE)1076-0431(2000)6:2(45).

[7] T. Morton, *Earth Masonry: Design and Construction Guidelines*, IHS BRE Press, Bracknell, UK, 2008. ISBN: 978-1-86081-978-0.

[8] C. Thormark, "The Effect of Material Choice on the Total Energy Need and Recycling Potential of a Building." *Building and Environment*. 41 (2006) 1019–1026. https://doi.org/10.1016/j.buildenv.2005.04.026.

[9] M.J. González, J. García Navarro, "Assessment of the Decrease of CO2 Emissions in the Construction Field through the Selection of Materials: Practical Case Study of Three Houses of Low Environmental Impact." *Building and Environment*. 41 (2006) 902–909. https://doi.org/10.1016/j.buildenv.2005.04.006.

[10] A. Shukla, G.N. Tiwari, M.S. Sodha, "Embodied Energy Analysis of Adobe House." *Renewable Energy*. 34 (2009) 755–761. https://doi.org/10.1016/j.renene.2008.04.002.

[11] B. V. Venkatarama Reddy, P. Prasanna Kumar, "Embodied Energy in Cement Stabilised Rammed Earth Walls." *Energy and Buildings*. 42 (2010) 380–385. https://doi.org/10.1016/j.enbuild.2009.10.005.

[12] F. Pacheco-Torgal, S. Jalali, *Eco-Efficient Construction and Building Materials*, Springer Science & Business Media, London, UK, 2011. https://doi.org/https://doi.org/10.1007/978-0-85729-892-8.

[13] L. Sanchez, A. Sanchez, *Adobe Houses for Today: Flexible Plans for Your Adobe Home*, Sunstone Press, Santa Fe, NM, 2008.

[14] R. Rael, *Earth Architecture*, Princeton Architectural Press, New York, USA, 2009. https://doi.org/10.5860/choice.46-3659.

[15] B. Windstorm, *A Report of Contemporary Rammed Earth Construction*, in: International Workshop on Rammed Earth Materials and Sustainable Structures & Hakka Tulou Forum 2011: Structures of Sustainability at International Symposium on Innovation & Sustainability of Structures in Civil Engineering, Xiamen University, 2011: p. 10. https://web.statler.wvu.edu/~rliang/ihta/papers/21 FINAL Bly Windstorm_paper_workshop.pdf.

[16] L. Holliday, C. Ramseyer, M. Reyes, D. Butko, "Building with Compressed Earth Block within the Building Code." *Journal of Architectural Engineering*. 22 (2016) 04016007. https://doi.org/10.1061/(asce)ae.1943-5568.0000198.

[17] A.J. Anselm, *Earth Shelters; A Review of Energy Conservation Properties in Earth Sheltered Housing*, in: Energy Conservation, InTech, 2012. https://doi.org/10.5772/51873.

[18] L. Ben-Alon, V. Loftness, K.A. Harries, E.C. Hameen, M. Bridges, "Integrating Earthen Building Materials and Methods into Mainstream Construction." *Journal of Green Building*. 15 (2020) 87–106. https://doi.org/10.3992/1943-4618.15.1.87.

[19] D. Allinson, M. Hall, "Hygrothermal Analysis of a Stabilised Rammed Earth Test Building in the UK." *Energy and Buildings*. 42 (2010) 845–852. https://doi.org/10.1016/j.enbuild.2009.12.005.

[20] G.F. Middleton, L.M. Schneider, *CSIRO Experimental Building Station Bulletin 5: Earth-Wall Construction*, 4th ed, CSIRO Department of Housing and Construction, Collingwood, Australia, 1987. ISBN: 0 643 0544 9.

[21] F. Matta, M.C. Cuellar-Azcarate, E. Garbin, M.C. Cuéllar-Azcárate, E. Garbin, "Earthen Masonry Dwelling Structures for Extreme Wind Loads." *Engineering Structures*. 83 (2015) 163–175. https://doi.org/10.1016/j.engstruct.2014.10.043.

[22] E. da C. Nepomuceno, Use of Municipal Waste to Build Ecological Blocks, *MS Thesis*, School of Technology and Management of Bragança, Bragança, Portugal, 2019.

[23] G.L. Gontijo, Thermal Behaviour of Compressed Earth Blocks with Municipal Organic

Waste Incorporation, *MS Thesis*, School of Technology and Management of Bragança, Bragança, Portugal, 2020.

[24] M. Buson, N. Lopes, H. Varum, R.M. Sposto, P.V. Real, "Fire Resistance of Walls Made of Soil-Cement and Kraftterra Compressed Earth Blocks." *Fire and Materials*. 37 (2013) 547–562. https://doi.org/10.1002/fam.2148.

[25] N. Kumar, M. Barbato, *Properties of Compressed and Stabilized Earth Blocks Produced with Recycled Soil Mixes*, in: Proceedings for the Tenth International Earthbuilding Conference (Earth USA 2019), Adobe in Action, La Madera, New Mexico, 2019: pp. 254–260.

[26] H. Danso, Use of Agricultural Waste Fibres as Enhancement of Soil Blocks for Low-Cost Housing in Ghana, *PhD Thesis*, University of Portsmouth, Portsmouth, UK, 2016.

[27] J. Fleming, H. Honour, N. Pevsner, *The Penguin Dictionary of Architecture*, Penguin Books, London, UK, 1991. ISBN: 0140512411.

[28] P.G. McHenry, *Adobe and Rammed Earth Buildings: Design and Construction*, University of Arizona Press, Tucson, Arizona, 1989. ISBN: 0816511241.

[29] L. Keefe, *Earth Building: Methods and Materials, Repair and Conservation*, Routledge, London, UK, 2012. https://doi.org/10.4324/9780203342336.

[30] A. Weismann, K. Bryce, *Building with Cob: A Step-by-Step Guide*, Green Books Ltd, London, UK, 2006. ISBN: 1903998727.

[31] C. Snell, T. Callahan, *Building Green: A Complete How-to Guide to Alternative Building Methods: Earth Plaster, Straw Bale, Cordwood, Cob, Living Roofs*, Sterling Publishing Company, Inc., New York, USA, 2009. ISBN: 1600595340.

[32] R.E. Klingner, "Behavior of Masonry in the Northridge (US) and Tecomán–Colima (Mexico) Earthquakes: Lessons Learned, and Changes in US Design Provisions." *Construction and Building Materials*. 20 (2006) 209–219. https://doi.org/10.1016/j.conbuildmat.2005.08.024.

[33] M. Blondet, J. Vargas, N. Tarque, *Observed Behaviour of Earthen Structures during the Pisco (Peru) Earthquake of August 15, 2007*, in: 14th World Conference on Earthquake Engineering, International Association for Earthquake Engineering, 2008: pp. 12–17. https://www.iitk.ac.in/nicee/wcee/article/14_01-1031.PDF.

[34] H.H. Korkmaz, S.Z. Korkmaz, M.S. Donduren, "Earthquake Hazard and Damage on Traditional Rural Structures in Turkey." *Natural Hazards and Earth System Sciences*. 10 (2010) 605–622. https://doi.org/10.5194/nhess-10-605-2010.

[35] E. Sayın, B. Yön, Y. Calayır, M. Karaton, "Failures of Masonry and Adobe Buildings during the June 23, 2011 Maden-(Elazığ) Earthquake in Turkey." *Engineering Failure Analysis*. 34 (2013) 779–791. https://doi.org/10.1016/j.engfailanal.2012.10.016.

[36] M.I. Gomes, M. Lopes, J. De Brito, "Seismic Resistance of Earth Construction in Portugal." *Engineering Structures*. 33 (2011) 932–941. https://doi.org/10.1016/j.engstruct.2010.12.014.

[37] H. Houben, H. Guillaud, *Earth Construction: A Comprehensive Guide*, Intermediate Technology Publications, London, UK, 1994. ISBN: 9781853391934; 185339193X.

[38] D.E.M. Gooding, Improved Processes for the Production of Soil-Cement Building Blocks, *PhD Dissertation*, University of Warwick, Coventry, UK, 1994.

[39] D. Webb, Stabilised Soil Building Blocks, *PhD Dissertation*, Newcastle University, Newcastle upon Tyne, UK, 1988.

[40] G. Enteiche, D. Augusta, *Soil Cement: Its Use in Building*, United Nations Department of Economic and Social Affairs, New York, USA, 1964.

[41] S. Deboucha, R. Hashim, "A Review on Bricks and Stabilized Compressed Earth Blocks." *Scientific Research and Essays*. 6 (2011) 499–506. https://doi.org/10.5897/SRE09.356.

[42] V. Rigassi, *Compressed Earth Blocks: Volume I. Manual of Production*, Deutsche Gesellschaft fur Technische Zusammenarbeit (GTZ) GmbH, Eschborn, Germany, 1995. ISBN: 3528020792.

[43] A.G. Kerali, Durability of Compressed and Cement-Stabilised Building Blocks, *PhD Dissertation*, University of Warwick, Coventry, UK, 2001.

[44] M.C. Jiménez Delgado, I.C. Guerrero, "The Selection of Soils for Unstabilised Earth Building: A Normative Review." *Construction and Building Materials*. 21 (2007) 237–251. https://doi.org/10.1016/j.conbuildmat.2005.08.006.

[45] J. Brown, M. Evans, C. Morrow, *Model Block Press*, California Polytechnic State University, San Luis Obispo, USA, 2014. https://digitalcommons.calpoly.edu/cgi/viewcontent.cgi?referer=&httpsredir=1&article=1260&context=mesp.

[46] A. Guettala, A. Abibsi, H. Houari, "Durability Study of Stabilized Earth Concrete under Both Laboratory and Climatic Conditions Exposure." *Construction and Building Materials*. 20 (2006) 119–127. https://doi.org/10.1016/j.conbuildmat.2005.02.001.

[47] F.V. Riza, I.A. Rahman, A.M.A. Zaidi, "Preliminary Study of Compressed Stabilized Earth Brick (CSEB)." *Australian Journal of Basic and Applied Sciences*. 5 (2011) 6–12.

[48] M.R. Hall, R. Lindsay, M. Krayenhoff, *Modern Earth Buildings: Materials, Engineering, Constructions and Applications*, Elsevier, 2012. ISBN: 978-0-85709-026-3.

[49] V. Maniatidis, P. Walker, *A Review of Rammed Earth Construction*, University of Bath, Somerset, UK, 2003. https://people.bath.ac.uk/abspw/rammedearth/review.pdf.

[50] Standards New Zealand, *NZS 4298:1998 Materials and Workmanship for Earth Buildings*, Standards New Zealand, Wellington, New Zealand, 1998.

[51] Standards New Zealand, *NZS 4297: Engineering Design of Earth Buildings*, Standards New Zealand, Wellington, New Zealand, 1998.

[52] Standards New Zealand, *NZS 4299: Earth Buildings Not Requiring Specific Design*, Standards New Zealand, Wellington, New Zealand, 1998.

[53] H. Guillaud, T. Joffroy, P. Odul, *Compressed Earth Blocks: Volume II. Manual of Design and Construction*, Deutsche Gesellschaft fur Technische Zusammenarbeit (GTZ) GmbH, Eschborn, Germany, 1995. ISBN: 3528020806.

[54] P. Walker, Standards Australia, *Australian Earth Building Handbook*, Standards Australia International Ltd, Sydney, Australia, 2001. ISBN: 0733740006.

[55] ASTM International, *E2392/E2392M Standard Guide for Design of Earthen Wall Building Systems*, in: ASTM International, 2016: pp. 1–6. https://doi.org/10.1520/E2392.

[56] State of New Mexico, Construction Industries Division of the Regulation and Licensing Department, *NMAC Title 14, Chapter 7, Part 4: 2015 New Mexico Earthen Building Materials Code*, The Commission of Public Records Administrative Law Division, Santa Fe, NM, 2015. https://doi.org/10.5151/cidi2017-060.

[57] International Code Council (ICC), *2021 International Residential Code (IRC) - Appendix AU: Cob Construction (Monolithic Adobe)*, 2021.

[58] California Building Standars Commission, *2021 California Building Code - Section 2109: Empirical Design of Adobe Masonry*, Sacramento, CA, 2021. ISBN: 9781580019743.

[59] International Code Council, *2019 International Building Code - Section 2109: Empirical Design of Adobe Masonry*, 2019. ISBN: 9781609830403.

[60] Standards New Zealand, *NZS 4298:1998 Materials and Workmanship for Earth Buildings*, Standards New Zealand, Wellington, New Zealand, 1998.

[61] Indian Standard, *Improving Earthquake Resistance of Earthen Buildings-Guidelines*, Bureau of Indian Standards, New Delhi, India, 1993.

[62] B. King, *Review of Earthen Building Codes and Standards from Around the World*,

Sausalito, California, 2006. https://buildwellsource.org/materials/natural-materials-rural/earth/40-review-of-earthen-building-codes-and-standards-from-around-the-world-bruce-king-pe-2006.

[63] A. Fabbri, J.-C. Morel, J.-E. Aubert, Q.-B. Bui, D. Gallipoli, B.V.V. Reddy, *Testing and Characterisation of Earth-Based Building Materials and Elements*, Springer, Cham, 2022. https://doi.org/https://doi.org/10.1007/978-3-030-83297-1.

[64] P. Walker, "Bond Characteristics of Earth Block Masonry." *Journal of Materials in Civil Engineering*. 11 (1999) 249–256. https://doi.org/10.1061/(ASCE)0899-1561(1999)11:3(249).

[65] J.C. Morel, A. Pkla, P. Walker, "Compressive Strength Testing of Compressed Earth Blocks." *Construction and Building Materials*. 21 (2007) 303–309. https://doi.org/10.1016/j.conbuildmat.2005.08.021.

[66] P. Walker, T. Stace, "Properties of Some Cement Stabilised Compressed Earth Blocks and Mortars." *Materials and Structures*. 30 (1997) 545–551. https://doi.org/10.1007/BF02486398.

[67] B.V.V. Reddy, R. Lal, K.S.N. Rao, "Enhancing Bond Strength and Characteristics of Soil-Cement Block Masonry." *Journal of Materials in Civil Engineering*. 19 (2007) 164–172. https://doi.org/10.1061/(ASCE)0899-1561(2007)19:2(164).

[68] P. Walker, "Strength and Erosion Characteristics of Earth Blocks and Earth Block Masonry." *Journal of Materials in Civil Engineering*. 16 (2004) 497–506. https://doi.org/10.1061/(asce)0899-1561(2004)16:5(497).

[69] A.S. Muntohar, "Engineering Characteristics of the Compressed-Stabilized Earth Brick." *Construction and Building Materials*. 25 (2011) 4215–4220. https://doi.org/10.1016/j.conbuildmat.2011.04.061.

[70] B.V. Venkatarama Reddy, A. Gupta, "Influence of Sand Grading on the Characteristics of Mortars and Soil–Cement Block Masonry." *Construction and Building Materials*. 22 (2008) 1614–1623. https://doi.org/10.1016/j.conbuildmat.2007.06.014.

[71] B. V Venkatarama Reddy, R. Lal, K.S. Nanjunda Rao, "Optimum Soil Grading for the Soil-Cement Blocks." *Journal of Materials in Civil Engineering*. 19 (2007) 139–148. https://doi.org/10.1061/(ASCE)0899-1561(2007)19:2(139).

[72] B. V Venkatarama Reddy, A. Gupta, "Strength and Elastic Properties of Stabilized Mud Block Masonry Using Cement-Soil Mortars." *Journal of Materials in Civil Engineering*. 18 (2006) 472–476. https://doi.org/10.1061/(ASCE)0899-1561(2006)18:3(472).

[73] E. Obonyo, J. Exelbirt, M. Baskaran, “Durability of Compressed Earth Bricks: Assessing Erosion Resistance Using the Modified Spray Testing.” *Sustainability*. 2 (2010) 3639–3649. https://doi.org/10.3390/su2123639.

[74] Q. Piattoni, E. Quagliarini, S. Lenci, “Experimental Analysis and Modelling of the Mechanical Behaviour of Earthen Bricks.” *Construction and Building Materials*. 25 (2011) 2067–2075. https://doi.org/10.1016/j.conbuildmat.2010.11.039.

[75] A. Mesbah, J.C. Morel, P. Walker, K. Ghavami, “Development of a Direct Tensile Test for Compacted Earth Blocks Reinforced with Natural Fibers.” *Journal of Materials in Civil Engineering*. 16 (2004) 95–98. https://doi.org/10.1061/(ASCE)0899-1561(2004)16:1(95).

[76] J.C. Morel, A. Pkla, “A Model to Measure Compressive Strength of Compressed Earth Blocks with the ‘3 Points Bending Test.’” *Construction and Building Materials*. 16 (2002) 303–310. https://doi.org/10.1016/S0950-0618(02)00023-5.

[77] B.V.V. Reddy, R. Lal, K.S.N. Rao, “Influence of Joint Thickness and Mortar-Block Elastic Properties on the Strength and Stresses Developed in Soil-Cement Block Masonry.” *Journal of Materials in Civil Engineering*. 21 (2009) 535–542. https://doi.org/10.1061/(ASCE)0899-1561(2009)21:10(535).

[78] A. Brencich, S. Lagomarsino, *A Macroelement Dynamic Model for Masonry Shear Walls*, in: G.N. Pande, J. Middleton, B. Kra (Eds.), Computer Methods in Structural Masonry - 4, E & FN SPON, London, UK, 1998: pp. 67–75. ISBN: 0 419 23540 X.

[79] E.L. Rengifo-López, N. Kumar, F. Matta, M. Barbato, *Experimental Characterization and Numerical Simulation of Compressive Behavior of Compressed and Stabilized Earth Block Specimens*, in: Proceedings for the Tenth International Earthbuilding Conference (Earth USA 2019), Adobe in Action, La Madera, New Mexico, 2019: pp. 314–320.

[80] E.L. Rengifo-López, N. Kumar, F. Matta, M. Barbato, *Can Compressed and Stabilized Earth Block Materials Be Regarded as Homogeneous and Isotropic?*, in: G. Garrity, A. Milani, S. Taliercio (Eds.), 10th International Masonry Conference (10th IMC), International Masonry Society, Surrey, UK, 2018: pp. 618–627. ISSN: 2523532X.

[81] E.L. Rengifo-López, N. Kumar, F. Matta, M. Barbato, *Variability of Compressive Strength and Stiffness of Compressed and Stabilized Earth Blocks*, in: Proceedings for the Ninth International Earthbuilding Conference (Earth USA 2017), Adobe in Action, La Madera, New Mexico, 2017.

[82] H. Danso, D.B. Martinson, M. Ali, J.B. Williams, “Mechanisms by Which the Inclusion of Natural Fibres Enhance the Properties of Soil Blocks for Construction.” *Journal of Composite Materials*. 51 (2017) 3835–3845. https://doi.org/10.1177/0021998317693293.

[83] H. Danso, D.B. Martinson, M. Ali, J.B. Williams, "Physical, Mechanical and Durability Properties of Soil Building Blocks Reinforced with Natural Fibres." *Construction and Building Materials*. 101 (2015) 797–809. https://doi.org/10.1016/j.conbuildmat.2015.10.069.

[84] J. Herrera, S. Moreira, R. Aguilar, L. Ramos, T. Sturm, P. Lourenço, A. Campos, *Nonlinear Static and Dynamic Analysis of a Dry-Stack ICEB Masonry House Tested on a Shaking Table*, in: 16th European Conference on Earthquake Engineering, European association for earthquake Engineering (EAEE), Thessaloniki, Greece, 2018.

[85] T. Sturm, L.F. Ramos, P.B. Lourenço, "Characterization of Dry-Stack Interlocking Compressed Earth Blocks." *Materials and Structures*. 48 (2015) 3059–3074. https://doi.org/10.1617/s11527-014-0379-3.

[86] N.A. Herskedal, Investigation of Out-of-Plane Properties of Interlocking Compressed Earth Block Walls, *PhD Dissertation*, California Polytechnic State University, San Luis Obispo, California, 2012. https://doi.org/10.15368/theses.2012.235.

[87] B.J. Stirling, Flexural Behavior of Interlocking Compressed Earth Block Shear Walls Subjected to In-Plane Loading, California Polytechnic State University, San Luis Obispo, California, 2011. https://doi.org/10.15368/theses.2011.152.

[88] A.G. Tennant, C.D. Foster, B.V.V. Reddy, "Verification of Masonry Building Code to Flexural Behavior of Cement-Stabilized Soil Block." *Journal of Materials in Civil Engineering*. 25 (2013) 303–307. https://doi.org/10.1061/(ASCE)MT.1943-5533.0000566.

[89] M.C. Cuéllar-Azcárate, F. Matta, *Structural Design of Affordable and Energy-Efficient Earth Masonry Dwellings for Tornado Wind Loads*, in: Structures Congress 2014, American Society of Civil Engineers, Reston, VA, 2014: pp. 1336–1347. https://doi.org/10.1061/9780784413357.118.

[90] P.T. Laursen, N.A. Herskedal, D.C. Jansen, B. Qu, "Out-of-Plane Structural Response of Interlocking Compressed Earth Block Walls." *Materials and Structures/Materiaux et Constructions*. 48 (2015) 321–336. https://doi.org/10.1617/s11527-013-0186-2.

[91] L. Miccoli, A. Garofano, P. Fontana, U. Müller, "Experimental Testing and Finite Element Modelling of Earth Block Masonry." *Engineering Structures*. 104 (2015) 80–94. https://doi.org/10.1016/j.engstruct.2015.09.020.

[92] L. Miccoli, R.A. Silva, A. Garofano, D. V Oliveira, *In-Plane Behaviors of Earthen Materials: A Numerical Comparison Between Adobe Masonry, Rammed Earth and Cob*, in: Proceedings of the 6th International Conference on Computational Methods in Structural Dynamics and Earthquake Engineering (COMPDYN 2015), Institute of Structural Analysis

and Antiseismic Research School of Civil Engineering National Technical University of Athens (NTUA) Greece, Athens, 2017: pp. 2478–2504. https://doi.org/10.7712/120117.5583.17606.

[93] W.I. De Villiers, J. Fourie, W.P. Boshoff, *Numerical Modelling of Alternative Masonry Units*, in: Proceedings in International RILEM Symposium on Concrete Modelling (CONMOD18), Delft, The Netherlands, 2018.

[94] J.C. Morel, A. Mesbah, M. Oggero, P. Walker, "Building Houses with Local Materials: Means to Drastically Reduce the Environmental Impact of Construction." *Building and Environment*. 36 (2001) 1119–1126. https://doi.org/10.1016/S0360-1323(00)00054-8.

[95] FreddieMac Economic & Housing Research group, *2020 Insight Report - The Housing Supply Shortage: State of the States*, 2020.

[96] S. Smith, "The World Needs to Build More than Two Billion New Homes over the next 80 Years." *World Economic Forum*. (2018). https://theconversation.com/the-world-needs-to-build-more-than-two-billion-new-homes-over-the-next-80-years-91794 (accessed August 5, 2020).

[97] W. Lutz, S. Kc, "Global Human Capital: Integrating Education and Population." *Science*. 333 (2011) 587–592. https://doi.org/10.1126/science.1206964.

[98] United Nations, *World Population Prospects The 2015 Revision - Key Findings and Advance Tables*, United Nations, Department of Economic and Social Affairs, Population Division, New York, USA, 2015.

[99] M. Bradbury, M.N. Peterson, J. Liu, "Long-Term Dynamics of Household Size and Their Environmental Implications." *Population and Environment*. 36 (2014) 73–84. https://doi.org/10.1007/s11111-014-0203-6.

[100] E. Avrami, H. Guillaud, M. Hardy, *An Overview of Research in Earthen Architecture Conservation*, in: Terra Literature Review: An Overview of Earthen Architecture Conservation, The Getty Conservation Institute, Los Angeles, USA, 2008: pp. 45–55.

[101] T. Morton, F. Stevenson, B. Taylor, N.C. Smith, "Low Cost Earth Brick Construction." *Arc Chartered Architects, Fife*. (2005).

[102] D. Gandreau, L. Delboy, *World Heritage: Inventory of Earthen Architecture*, United Nations Educational Scientific and Cultural Organization, Grenoble, France, 2012. ISBN: 9782906901704.

[103] O. Geiger, "Impact Testing Earthco Megablocks with Blackpowder Cannon." *Natural Building Blog*. (2011). http://www.naturalbuildingblog.com/impact-testing-earthco-

megablocks-with-blackpowder-cannon/ (accessed September 12, 2021).

[104] Louisiana Housing Finance Agency, *Louisiana Housing Needs Assessment 2010 Executive Summary*, New Orleans, LA, USA, 2010.

[105] P. Emrath, *Impact of Home Building and Remodeling on the US Economy*, Washington, DC, 2014.

[106] C. Davenport, C. Robertson, "Resettling the First American 'Climate Refugees.'" *The New York Times*. (2016).

[107] M.R. Taylor, "The Fort Selden Adobe Test Wall Project." *APT Bulletin: The Journal of Preservation Technology*. 22 (1990) 35–41. https://www.jstor.org/stable/1504326.

[108] M.R. Taylor, *An Evaluation of the New Mexico State Monuments Adobe Test Walls at Fort Selden*, in: 6th International Conference on the Conservation of Earthen Architecture, Getty Conservation Institute, Las Cruces, New Mexico, USA, 1990: pp. 383–389. ISBN: 0892361816.

[109] ASTM International, *D2487-11 Standard Practice for Classification of Soils for Engineering Purposes (Unified Soil Classification System)*, in: ASTM Standards, ASTM International, West Conshohocken, PA, 2011. www.astm.org.

[110] USDA, United States Department of Agriculture, USDA, *Soil Taxonomy: A Basic System of Soil Classification for Making and Interpreting Soil Surveys*, US Department of Agriculture, Soil Conservation Service, Washington, DC, USA, 1999. https://doi.org/10.1097/00010694-197704000-00011.

[111] ASTM International, *ASTM D4318-17e1 Standard Test Methods for Liquid Limit, Plastic Limit, and Plasticity Index of Soils*, in: ASTM Standards, ASTM International, West Conshohocken, PA, 2017. https://doi.org/https://doi.org/10.1520/D4318-17E01.

[112] ASTM International, *ASTM D6913/D6913M-17 Standard Test Methods for Particle-Size Distribution (Gradation) of Soils Using Sieve Analysis*, in: ASTM Standards, ASTM International, West Conshohocken, PA, 2017. https://doi.org/https://doi.org/10.1520/D6913_D6913M-17.

[113] ASTM International, *ASTM D7928-17 Standard Test Method for Particle-Size Distribution (Gradation) of Fine-Grained Soils Using the Sedimentation (Hydrometer) Analysis*, in: ASTM Standards, ASTM International, West Conshohocken, PA, 2017. https://doi.org/https://doi.org/10.1520/D7928-17.

[114] M.G. Lunt, *Stabilised Soil Blocks for Building*, in: Building in Hot Climates. A Selection of Overseas Building Notes, Her Majesty's stationery office, London, UK, 1980: pp. 127–144.

[115] P. Maillard, J.-E. Aubert, "Effects of the Anisotropy of Extruded Earth Bricks on Their Hygrothermal Properties." *Construction and Building Materials*. 63 (2014) 56–61. https://doi.org/10.1016/j.conbuildmat.2014.04.001.

[116] S. Meriani, *Available Technologies for Local Building Materials*, International Centre for Science and High Technology, Trieste, Italy, 2008.

[117] P. Walker, "Specifications for Stabilised Pressed Earth Blocks." *Masonry International*. 10 (1996) 1–6.

[118] G. Middleton, L. Schneider, *Earth-Wall Construction*, 4th ed., CSIRO Division of Building. Construction and Engineering, North Ryde, NSW, Australia, 1992.

[119] B. V Venkatarama Reddy, A. Gupta, "Characteristics of Cement-Soil Mortars." *Materials and Structures*. 38 (2005) 639–650. https://doi.org/10.1007/BF02481595.

[120] B. V. Venkatarama Reddy, A. Gupta, "Tensile Bond Strength of Soil-Cement Block Masonry Couplets Using Cement-Soil Mortars." *Journal of Materials in Civil Engineering*. 18 (2006) 36–45. https://doi.org/10.1061/(ASCE)0899-1561(2006)18:1(36).

[121] ASTM International, *C109/C109M-16a Standard Test Method for Compressive Strength of Hydraulic Cement Mortars (Using 2-in. or 50-Mm Cube Specimens)*, in: ASTM Standards, West Conshohocken, PA, USA, 2016. https://doi.org/10.1520/C0109_C0109M-21.

[122] Standards New Zealand, *NZS 4297:1998 Engineering Design of Earth Buildings [Building Code Compliance Documents B1 (VM1), B2 (AS1)]*, Standards New Zealand, Wellington, New Zealand, 1998. www.standards.co.nz.

[123] ASCE, *Minimum Design Loads for Buildings and Other Structures*, American Society of Civil Engineers, Reston, VA, 2013. https://doi.org/10.1061/9780784412916.

[124] European Committee for Standardization, *Eurocode 6: Design of Masonry Structures - Part 1-1: General Rules for Reinforced and Unreinforced Masonry Structures*, Brussels, Belgium, 2005.

[125] Masonry Standards Joint Committee, *TMS 402/602-16 Building Code Requirements and Specification for Masonry Structures*, The Masonry Society, Boulder, Colorado, 2016. ISBN: 978-1-929081-52-3.

[126] A.J. Francis, C.B. Horman, L.E. Jerrems, *The Effect of Joint Thickness and Other Factors on the Compressive Strength of Brickwork*, in: Proceedings of 2nd International Brick Masonry Conference, Stoke-on-trent, UK, 1971: pp. 31–37.

[127] C.-L. Khoo, A. Hendry, *A Failure Criterion for Brickwork in Axial Compression*, in: 3rd International Brick and Block Masonry Conference, University of Edinburgh, Edinburgh,

Scotland, 1973: pp. 139–145.

[128] A.W. Hendry, *Structural Masonry*, 2nd ed., Scholium International, London, UK, 1998. ISBN: 134914827X.

[129] A. Zucchini, P.B. Lourenço, "Mechanics of Masonry in Compression: Results from a Homogenisation Approach." *Computers & Structures*. 85 (2007) 193–204. https://doi.org/10.1016/j.compstruc.2006.08.054.

[130] Auroville Earth Institute, "Auroville Earth Institute." (2021). http://www.earth-auroville.com.

[131] J. Edwards, *A Creole Lexicon: Architecture, Landscape, People*, Louisiana State University Press, Baton Rouge, LA, USA, 2004. ISBN: 0807138320.

[132] G. Wheeler, *Interlocking Compressed Earth Blocks Volume II. Manual of Construction*, Center for Vocational Building Technology, Udon Thani, Thailand, 2005.

[133] RSMeans, *RSMeans Concrete and Masonry Cost Data 2016*, Gordian RSMeans Data, Rockland, MA, USA, 2015. ISBN: 1943215030.

[134] Dwell Earth, "No Title." (2016). http://dwellearth.com (accessed December 4, 2017).

[135] H.G. Harris, K. Oh, A.A. Hamid, *Development of New Interlocking and Mortarless Block Masonry Units for Efficient Building Systems*, in: Proceedings of the 6th Canadian Masonry Symposium, University of Saskatchewan, Saskatoon, Canada, 1992.

[136] T. Hines, *Benefits of Drystack Interlocking Concrete Masonry as a Component of Cost Effective Construction*, in: Proceedings 6th North American Masonry Conference, The Masonry Society, Boulder, Colorado, 1993: pp. 849–861.

[137] RSMeans, *RSMeans Residential Cost Data 2015*, Gordian RSMeans Data, Rockland, MA, USA, 2014. ISBN: 194023865X.

[138] J.W. van de Lindt, T.N. Dao, "Performance-Based Wind Engineering for Wood-Frame Buildings." *Journal of Structural Engineering*. 135 (2009) 169–177. https://doi.org/10.1061/(ASCE)0733-9445(2009)135:2(169).

[139] J. Norton, *Building with Earth: A Handbook*, Intermediate Technology Publications, London, UK, 1997. ISBN: 1853393371.

[140] E. Avrami, H. Guillaud, M. Hardy, eds., *Terra Literature Review: An Overview of Research in Earthen Architecture Conservation*, The Getty Conservation Institute, Los Angeles, USA, 2008.

[141] R. Fitzmaurice, *Manual on Stabilized Soil Construction for Housing*, Technical Assistance

Programme, New York, USA, 1958. https://www.bcin.ca/bcin/detail.app?id=236323 (accessed July 22, 2019).

[142] R.P.C. Gowda, Experimental Study of Cement Stabilized Fiber Reinforced Compressed Earth Blocks as an Alternative Building Material, *MS thesis*, Arizona State University, Tempe, USA, 2016.

[143] C. Bock-hyeng, A.N. Ofori-boadu, E. Yamb-bell, M.A. Shofoluwe, “Mechanical Properties of Sustainable Adobe Bricks Stabilized with Recycled Sugarcane Fiber Waste.” *International Journal of Engineering Research and Application*. 6 (2016) 50–59.

[144] P. Lertwattanaruk, J. Choksiriwanna, “The Physical and Thermal Properties of Adobe Brick Containing Bagasse for Earth Construction.” *Built*. 1 (2011) 53–62. https://doi.org/10.14456/built.2011.5.

[145] R.M. Eko, G.L. Riskowski, “A Procedure for Processing Mixtures of Soil, Cement, and Sugar Cane Bagasse.” *Agricultural Engineering International: The CIGR Journal of Scientific Research and Development*. 3 (2001). https://hdl.handle.net/1813/10249.

[146] Freddie Mac, *The Major Challenge of Inadequate U.S. Housing Supply*, McLean, VA, 2018. http://www.freddiemac.com/fmac-resources/research/pdf/201811-Insight-06.pdf.

[147] S.C. Lee, M. Mariatti, “The Effect of Bagasse Fibers Obtained (from Rind and Pith Component) on the Properties of Unsaturated Polyester Composites.” *Materials Letters*. 62 (2008) 2253–2256. https://doi.org/10.1016/j.matlet.2007.11.097.

[148] Indian Council of Agricultural Research, “World Statistics: World Sugarcane Scenario.” (2020). https://sugarcane.icar.gov.in/images/sbi/charts/world_sugarcane_scenario.pdf?phpMyAdmin=11c501a2a5dt8788ed6 (accessed August 5, 2020).

[149] United States Department of Agriculture, “2017 Census of Agriculture: Louisiana.” *United States Department of Agriculture*. (2019).

[150] B.. Lavarack, G.. Griffin, D. Rodman, “Measured Kinetics of the Acid-Catalysed Hydrolysis of Sugar Cane Bagasse to Produce Xylose.” *Catalysis Today*. 63 (2000) 257–265. https://doi.org/10.1016/S0920-5861(00)00467-3.

[151] ASTM International, *ASTM D698-12e2 Standard Test Methods for Laboratory Compaction Characteristics of Soil Using Standard Effort (12 400 Ft-Lbf/Ft3 (600 KN-m/M3))*, in: ASTM Standards, ASTM International, West Conshohocken, PA, 2012. https://doi.org/https://doi.org/10.1520/D0698-12E02.

[152] ASTM International, *ASTM C150/C150M-19a Standard Specification for Portland Cement*,

in: ASTM Standards, ASTM International, West Conshohocken, PA, 2019. https://doi.org/https://doi.org/10.1520/C0150_C0150M-19A.

[153] V. Rigassi, *Compressed Earth Blocks: Manual of Production*, Deutsche Gesellschaft fur Technische Zusammenarbeit (GTZ) GmbH, Eschborn, Germany, 1995. ISBN: 3528020792.

[154] B.H. Toby, R.B. Von Dreele, "GSAS-II : The Genesis of a Modern Open-Source All Purpose Crystallography Software Package." *Journal of Applied Crystallography*. 46 (2013) 544–549. https://doi.org/10.1107/S0021889813003531.

[155] A.X.S. Bruker, "DIFFRAC. EVA, Version 4.1." (2015). www.bruker.com.

[156] ASTM International, *ASTM C1018-97 Standard Test Method for Flexural Toughness and First-Crack Strength of Fiber Reinforced Concrete (Using Beam with Third-Point Loading)*, in: ASTM Standards, ASTM International, West Conshohocken, PA, 1997. https://doi.org/10.1520/C1018-97.

[157] B.J. Winer, *Statistical Principles in Experimental Design*, 2d ed., McGraw-Hill, New York, USA, 2012. ISBN: 1258260581.

[158] ASTM International, *ASTM C67/C67M-18 Standard Test Methods for Sampling and Testing Brick and Structural Clay Tile*, in: ASTM Standards, ASTM International, West Conshohocken, PA, 2018. https://doi.org/https://doi.org/10.1520/C0067_C0067M-18.

[159] ASTM International, *ASTM D559/D559M-15 Standard Test Methods for Wetting and Drying Compacted Soil-Cement Mixtures*, in: ASTM Standards, ASTM International, West Conshohocken, PA, 2015. https://doi.org/https://doi.org/10.1520/D0559_D0559M-15.

[160] A. Rutherford, *Anova and Ancova*, Second Edi, John Wiley & Sons, Inc., Hoboken, New Jersey, 2011. https://doi.org/10.1002/9781118491683.

[161] MATLAB, "Statistics and Machine Learning Toolbox^{TM}: User's Guide." (2019). https://www.mathworks.com/help/releases/R2019b/pdf_doc/stats/index.html.

[162] L.M. Lix, J.C. Keselman, H.J. Keselman, "Consequences of Assumption Violations Revisited: A Quantitative Review of Alternatives to the One-Way Analysis of Variance F Test." *Review of Educational Research*. 66 (1996) 579–619. https://doi.org/https://doi.org/10.3102/00346543066004579.

[163] H. Levene, "Robust Tests for Equality of Variances." *Contributions to Probability and Statistics. Essays in Honor of Harold Hotelling*. (1961) 279–292.

[164] B.L. Welch, "On the Comparison of Several Mean Values: An Alternative Approach." *Biometrika*. 38 (1951) 330–336. https://doi.org/10.2307/2332579.

[165] P.A. Games, J.F. Howell, "Pairwise Multiple Comparison Procedures with Unequal N's and/or Variances: A Monte Carlo Study." *Journal of Educational Statistics*. 1 (1976) 113–125. https://doi.org/10.3102/10769986001002113.

[166] C. Rezende, M. de Lima, P. Maziero, E. DeAzevedo, W. Garcia, I. Polikarpov, "Chemical and Morphological Characterization of Sugarcane Bagasse Submitted to a Delignification Process for Enhanced Enzymatic Digestibility." *Biotechnology for Biofuels*. 4 (2011) 54. https://doi.org/10.1186/1754-6834-4-54.

[167] M.C. Cuellar-Azcarate, Engineered Earthen Masonry Structures for Extreme Wind Loads, *PhD Dissertation*, University of South Carolina, Columbia, South Carolina, 2016.

[168] B. V. Venkatarama Reddy, A. Gupta, "Characteristics of Soil-Cement Blocks Using Highly Sandy Soils." *Materials and Structures*. 38 (2005) 651–658. https://doi.org/10.1007/BF02481596.

[169] European Standards, *BS EN 772-11 Methods of Test for Masonry Units - Determination of Water Absorption of Aggregate Concrete, Autoclaved Aerated Concrete, Manufactured Stone and Natural Stone Masonry Units Due to Capillary Action and the Initial Rate of Water Absorption*, in: European Standards Adopted by British Standards Institution, 2011. ISBN: 9780580702587.

[170] M. Bouhicha, F. Aouissi, S. Kenai, "Performance of Composite Soil Reinforced with Barley Straw." *Cement and Concrete Composites*. 27 (2005) 617–621. https://doi.org/10.1016/j.cemconcomp.2004.09.013.

[171] M. Mostafa, N. Uddin, "Experimental Analysis of Compressed Earth Block (CEB) with Banana Fibers Resisting Flexural and Compression Forces." *Case Studies in Construction Materials*. 5 (2016) 53–63. https://doi.org/10.1016/j.cscm.2016.07.001.

[172] Y. Millogo, J.-C. Morel, J.-E. Aubert, K. Ghavami, "Experimental Analysis of Pressed Adobe Blocks Reinforced with Hibiscus Cannabinus Fibers." *Construction and Building Materials*. 52 (2014) 71–78. https://doi.org/10.1016/j.conbuildmat.2013.10.094.

[173] E.L. Rengifo-López, N. Kumar, F. Matta, M. Barbato, *Experimental and Numerical Study of Uniaxial Compression Behavior of Compressed and Stabilized Earth Blocks*, in: Proceedings of the 13th North American Masonry Conference, The Masonry Society, Longmont, Colorado, 2019: pp. 925–936. ISBN: 1053-2366.

[174] Fetra Venny Riza, Ismail Abdul Rahman, Ahmad Mujahid Ahmad Zaidi, *A Brief Review of Compressed Stabilized Earth Brick (CSEB)*, in: 2010 International Conference on Science and Social Research (CSSR 2010), IEEE, 2010: pp. 999–1004. https://doi.org/10.1109/CSSR.2010.5773936.

[175] M. Ben Mansour, A. Jelidi, A.S. Cherif, S. Ben Jabrallah, "Optimizing Thermal and Mechanical Performance of Compressed Earth Blocks (CEB)." *Construction and Building Materials*. 104 (2016) 44–51. https://doi.org/10.1016/j.conbuildmat.2015.12.024.

[176] S. Ismail, Z. Yaacob, "Properties of Laterite Brick Reinforced with Oil Palm Empty Fruit Bunch Fibres." *Pertanika Journal of Science and Technology*. 19 (2011) 33–43. ISSN: 01287680.

[177] R. Medjo Eko, E.D. Offa, T. Yatchoupou Ngatcha, L. Seba Minsili, "Potential of Salvaged Steel Fibers for Reinforcement of Unfired Earth Blocks." *Construction and Building Materials*. 35 (2012) 340–346. https://doi.org/10.1016/j.conbuildmat.2011.11.050.

[178] European Committee for Stranded, *BS EN 12390-3: 2019 Testing Hardened Concrete. Compressive Strength of Test Specimens*, British Standards Institution, London, UK, 2019. ISBN: 978 0 580 98442 6.

[179] Soil Engineering and Rock Mechanics Sectional Committee, *IS 1725 (1982): Soil Based Blocks Used in General Building Construction [CED 30: Clay and Stabilized Soil Products for Construction]*, Bureau of Indian Standards, New Delhi, India, 1982.

[180] P.B. Lourenço, Computational Strategies for Masonry Structures, *PhD Dissertation*, Technische Universiteit Delft, Delft, Netherlands, 1996.

[181] L. Pelà, Continuum Damage Model for Nonlinear Analysis of Masonry Structures, *PhD Dissertation*, Università degli studi di Ferrara, Catalonia, Spain, 2009.

[182] A.W.A.W. Page, "Finite Element Model for Masonry." *Journal of the Structural Division*. 104 (1978) 1267–1285. https://doi.org/10.1061/JSDEAG.0004969.

[183] K.M. Dolatshahi, A.J. Aref, "Two-Dimensional Computational Framework of Meso-Scale Rigid and Line Interface Elements for Masonry Structures." *Engineering Structures*. 33 (2011) 3657–3667. https://doi.org/10.1016/j.engstruct.2011.07.030.

[184] L. Macorini, B.A. Izzuddin, "A Non-Linear Interface Element for 3D Mesoscale Analysis of Brick-Masonry Structures." *International Journal for Numerical Methods in Engineering*. 85 (2011) 1584–1608. https://doi.org/10.1002/nme.3046.

[185] A.J. Aref, K.M. Dolatshahi, "A Three-Dimensional Cyclic Meso-Scale Numerical Procedure for Simulation of Unreinforced Masonry Structures." *Computers & Structures*. 120 (2013) 9–23. https://doi.org/10.1016/j.compstruc.2013.01.012.

[186] N. Kumar, R. Amirtham, M. Pandey, "Plasticity Based Approach for Failure Modelling of Unreinforced Masonry." *Engineering Structures*. 80 (2014). https://doi.org/10.1016/j.engstruct.2014.08.021.

[187] G. Giambanco, S. Rizzo, R. Spallino, "Numerical Analysis of Masonry Structures via Interface Models." *Computer Methods in Applied Mechanics and Engineering*. 190 (2001) 6493–6511. https://doi.org/10.1016/S0045-7825(01)00225-0.

[188] A. Spada, G. Giambanco, P. Rizzo, "Damage and Plasticity at the Interfaces in Composite Materials and Structures." *Computer Methods in Applied Mechanics and Engineering*. 198 (2009) 3884–3901. https://doi.org/10.1016/j.cma.2009.08.024.

[189] K. Chaimoon, M.M. Attard, "Modeling of Unreinforced Masonry Walls under Shear and Compression." *Engineering Structures*. 29 (2007) 2056–2068. https://doi.org/10.1016/j.engstruct.2006.10.019.

[190] H.R. Lotfi, P.B. Shing, "Interface Model Applied to Fracture of Masonry Structures." *Journal of Structural Engineering*. 120 (1994) 63–80. https://doi.org/10.1061/(ASCE)0733-9445(1994)120:1(63).

[191] U. Andreaus, "Failure Criteria for Masonry Panels under In-Plane Loading." *Journal of Structural Engineering*. 122 (1996) 37–46. https://doi.org/10.1061/(ASCE)0733-9445(1996)122:1(37).

[192] A.W. Page, "The Strength of Brick Masonry under Biaxial Tension-Compression." *International Journal of Masonry Construction*. 3 (1983) 26–31.

[193] M. Dhanasekar, P.W. Kleeman, A.W. Page, "Biaxial Stress-strain Relations for Brick Masonry." *Journal of Structural Engineering*. 111 (1985) 1085–1100. https://doi.org/10.1061/(ASCE)0733-9445(1985)111:5(1085).

[194] R.E. Goodman, R.L. Taylor, T.L. Brekke, "A Model for the Mechanics of Jointed Rock." *Journal of Soil Mechanics & Foundations Div*. 94 (1968) 637–659.

[195] G. Giambanco, L. Di Gati, "A Cohesive Interface Model for the Structural Mechanics of Block Masonry." *Mechanics Research Communications*. 24 (1997) 503–512. https://doi.org/10.1016/S0093-6413(97)00055-4.

[196] S.C. Anand, K.K. Yalamanchili, "Three-Dimensional Failure Analysis of Composite Masonry Walls." *Journal of Structural Engineering*. 122 (1996) 1031–1039. https://doi.org/10.1061/(ASCE)0733-9445(1996)122:9(1031).

[197] P.B. Lourenço, J.G. Rots, "Multisurface Interface Model for Analysis of Masonry Structures." *Journal of Engineering Mechanics*. 123 (1997) 660–668. https://doi.org/10.1061/(ASCE)0733-9399(1997)123:7(660).

[198] D.V. Oliveira, P.B. Lourenço, "Implementation and Validation of a Constitutive Model for the Cyclic Behaviour of Interface Elements." *Computers & Structures*. 82 (2004) 1451–

1461. https://doi.org/10.1016/j.compstruc.2004.03.041.

[199] N. Tarque, Numerical Modelling of the Seismic Behaviour of Adobe Buildings, *PhD Dissertation*, Università degli Studi di Pavia, and Istituto Universitario di Studi Superiori, 2011.

[200] A. Furukawa, R. Spence, Y. Ohta, E. So, "Analytical Study on Vulnerability Functions for Casualty Estimation in the Collapse of Adobe Buildings Induced by Earthquake." *Bulletin of Earthquake Engineering*. 8 (2010) 451–479. https://doi.org/10.1007/s10518-009-9156-z.

[201] E. Minga, L. Macorini, B.A. Izzuddin, "A 3D Mesoscale Damage-Plasticity Approach for Masonry Structures under Cyclic Loading." *Meccanica*. 53 (2018) 1591–1611. https://doi.org/10.1007/s11012-017-0793-z.

[202] A.J. Abbo, S.W. Sloan, "A Smooth Hyperbolic Approximation to the Mohr-Coulomb Yield Criterion." *Computers & Structures*. 54 (1995) 427–441. https://doi.org/10.1016/0045-7949(94)00339-5.

[203] P.B. Lourenço, J. Rots, *Analysis of Masonry Structures with Interface Elements: Theory and Applications*, Delft University of Technology, Delft, Netherlands, 1994. https://doi.org/TU-DELFT report no. 03-21-22-0-01 and TNO-BOUW report no. 94-NM-R0762.

[204] C. Citto, Two-Dimensional Interface Model Applied to Masonry Structures, *MS thesis*, University of Colorado, Denver, Colorado, 2008.

[205] T.T. Bakeer, Collapse Analysis of Masonry Structures under Earthquake Actions, *PhD Dissertation*, Technischen Universität Dresden, Dresden, Germany, 2009. ISBN: 978-3-86780-130-0.

[206] L. Gambarotta, S. Lagomarsino, "Damage Models for the Seismic Response of Brick Masonry Shear Walls. Part I: The Mortar Joint Model and Its Applications." *Earthquake Engineering & Structural Dynamics*. 26 (1997) 423–439. https://doi.org/https://doi.org/10.1002/(SICI)1096-9845(199704)26:4%3C423::AID-EQE650%3E3.0.CO;2-%23.

[207] L. Gambarotta, S. Lagomarsino, "Damage Models for the Seismic Response of Brick Masonry Shear Walls. Part II: The Continuum Model and Its Applications." *Earthquake Engineering & Structural Dynamics*. 26 (1997) 441–462. https://doi.org/10.1002/(SICI)1096-9845(199704)26:4<441::AID-EQE651>3.0.CO;2-0.

[208] I. Khisamitov, G. Meschke, "Variational Approach to Interface Element Modeling of Brittle Fracture Propagation." *Computer Methods in Applied Mechanics and Engineering*. 328 (2018) 452–476. https://doi.org/10.1016/j.cma.2017.08.031.

[209] F. Greco, L. Leonetti, R. Luciano, P. Trovalusci, “Multiscale Failure Analysis of Periodic Masonry Structures with Traditional and Fiber-Reinforced Mortar Joints.” *Composites Part B: Engineering*. 118 (2017) 75–95. https://doi.org/10.1016/j.compositesb.2017.03.004.

[210] P.B. Shing, T. Manzouri, *Analysis of Unreinforced Masonry Structures Using Elastic/Viscoplastic Models*, in: Sísmica 2004–6° Congresso Nacional de Sismologia e Engenharia Sísmica Livro de Actas, Universidade do Minho, Guimaraes, Portugal, 2004: pp. 137–150.

[211] H. TANG, F. BARTHELAT, H. ESPINOSA, “An Elasto-Viscoplastic Interface Model for Investigating the Constitutive Behavior of Nacre.” *Journal of the Mechanics and Physics of Solids*. 55 (2007) 1410–1438. https://doi.org/10.1016/j.jmps.2006.12.009.

[212] J.G. Rots, *Structural Masonry*, CRC Press, London, UK, 2021. https://doi.org/10.1201/9781003077961.

[213] C. Chisari, L. Macorini, C. Amadio, B.A. Izzuddin, “Identification of Mesoscale Model Parameters for Brick-Masonry.” *International Journal of Solids and Structures*. 146 (2018) 224–240. https://doi.org/10.1016/j.ijsolstr.2018.04.003.

[214] F. da Porto, G. Guidi, E. Garbin, C. Modena, “In-Plane Behavior of Clay Masonry Walls: Experimental Testing and Finite-Element Modeling.” *Journal of Structural Engineering*. 136 (2010) 1379–1392. https://doi.org/10.1061/(ASCE)ST.1943-541X.0000236.

[215] C. Chisari, L. Macorini, C. Amadio, B.A. Izzuddin, “An Inverse Analysis Procedure for Material Parameter Identification of Mortar Joints in Unreinforced Masonry.” *Computers & Structures*. 155 (2015) 97–105. https://doi.org/10.1016/j.compstruc.2015.02.008.

[216] A. Caballero, K.J. Willam, I. Carol, “Consistent Tangent Formulation for 3D Interface Modeling of Cracking/Fracture in Quasi-Brittle Materials.” *Computer Methods in Applied Mechanics and Engineering*. 197 (2008) 2804–2822. https://doi.org/10.1016/j.cma.2008.01.011.

[217] A. Caballero, 3D Meso-Mechanical Numerical Analysis of Concrete Fracture Using Interface Elements, *PhD Dissertation*, Polytechnic University of Catalonia, Barcelona, Spain, 2005.

[218] R.H. Atkinson, B.P. Amadei, S. Saeb, S. Sture, “Response of Masonry Bed Joints in Direct Shear.” *Journal of Structural Engineering*. 115 (1989) 2276–2296. https://doi.org/10.1061/(ASCE)0733-9445(1989)115:9(2276).

[219] R. Van der Pluijm, *Shear Behaviour of Bed Joints*, in: Proceedings of 6th North American Masonry Conference, The Masonry Society, Boulder, Colorado, 1993: pp. 125–136.

[220] J.C. Simo, T.J.R. Hughes, *Computational Inelasticity*, Springer-Verlag, New York, USA, 1998. https://doi.org/10.1007/b98904.

[221] J.C.J. Schellekens, Computational Strategies for Composite Structures, *PhD Dissertation*, Delft University of Technology, Delft, The Netherlands, 1992.

[222] H.R. Lotfi, P.B. Shing, "An Appraisal of Smeared Crack Models for Masonry Shear Wall Analysis." *Computers & Structures*. 41 (1991) 413–425. https://doi.org/10.1016/0045-7949(91)90134-8.

[223] Dassault Systèmes, *Abaqus 6.13 Documentation*, Dassault Systèmes, Providence, RI, 2013.

[224] M. Metcalf, J. Reid, M. Cohen, *Modern Fortran Explained (Numerical Mathematics and Scientific Computation)*, Oxford University Press, New York, USA, 2011. ISBN: 0199601410.

[225] K.-J. Bathe, *Finite Element Procedures*, Klaus-Jurgen Bathe, Watertown, MA, USA, 2006. ISBN: 097900490X.

[226] N.S. Ottosen, M. Ristinmaa, *The Mechanics of Constitutive Modeling*, Elsevier, Amsterdam, Netherland, 2005. ISBN: 0080525695.

[227] A. Pérez-Foguet, A. Rodríguez-Ferran, A. Huerta, "Consistent Tangent Matrices for Substepping Schemes." *Computer Methods in Applied Mechanics and Engineering*. 190 (2001) 4627–4647. https://doi.org/10.1016/S0045-7825(00)00336-4.

[228] A.T. Vermeltfoort, T.M.J. Raijmakers, *Deformation Controlled Tests in Masonry Shear Walls, Part 2 (in Dutch)*, Technische Universiteit Delft, Eindhoven, The Netherlands, 1993.

[229] T.M.J. Raijmakers, A.T. Vermeltfoort, *Deformation Controlled Tests in Masonry Shear Walls (in Dutch)*, Technische Universiteit Delft, Eindhoven, The Netherlands, 1992.

[230] J.C. Simo, R.L. Taylor, "A Return Mapping Algorithm for Plane Stress Elastoplasticity." *International Journal for Numerical Methods in Engineering*. 22 (1986) 649–670. https://doi.org/10.1002/nme.1620220310.

[231] R. De Borst, P.H. Feenstra, "Studies in Anisotropic Plasticity with Reference to the Hill Criterion." *International Journal for Numerical Methods in Engineering*. 29 (1990) 315–336. https://doi.org/10.1002/nme.1620290208.

[232] P. Fuschi, D. Perić, D.R.J. Owen, "Studies on Generalized Midpoint Integration in Rate-Independent Plasticity with Reference to Plane Stress J2-Flow Theory." *Computers & Structures*. 43 (1992) 1117–1133. https://doi.org/10.1016/0045-7949(92)90012-O.

[233] K.F. Abdulla, L.S. Cunningham, M. Gillie, "Simulating Masonry Wall Behaviour Using a

Simplified Micro-Model Approach." *Engineering Structures*. 151 (2017) 349–365. https://doi.org/10.1016/j.engstruct.2017.08.021.

[234] B. Pulatsu, E. Erdogmus, P.B. Lourenço, J. V Lemos, J. Hazzard, "Discontinuum Analysis of the Fracture Mechanism in Masonry Prisms and Wallettes via Discrete Element Method." *Meccanica*. 55 (2020) 505–523. https://doi.org/10.1007/s11012-020-01133-1.

[235] D. Baraldi, A. Cecchi, "A Full 3D Rigid Block Model for the Collapse Behaviour of Masonry Walls." *European Journal of Mechanics - A/Solids*. 64 (2017) 11–28. https://doi.org/10.1016/j.euromechsol.2017.01.012.

[236] A.M. D'Altri, V. Sarhosis, G. Milani, J. Rots, S. Cattari, S. Lagomarsino, E. Sacco, A. Tralli, G. Castellazzi, S. de Miranda, "Modeling Strategies for the Computational Analysis of Unreinforced Masonry Structures: Review and Classification." *Archives of Computational Methods in Engineering*. (2019) 1–33. https://doi.org/10.1007/s11831-019-09351-x.

[237] A. Drougkas, P. Roca, C. Molins, "Experimental Analysis and Detailed Micro-Modeling of Masonry Walls Subjected to in-Plane Shear." *Engineering Failure Analysis*. 95 (2019) 82–95. https://doi.org/10.1016/j.engfailanal.2018.08.030.

[238] S. Calderón, C. Sandoval, O. Arnau, "Shear Response of Partially-Grouted Reinforced Masonry Walls with a Central Opening: Testing and Detailed Micro-Modelling." *Materials & Design*. 118 (2017) 122–137. https://doi.org/10.1016/j.matdes.2017.01.019.

[239] S. Pourfalah, D.M. Cotsovos, B. Suryanto, "Modelling the Out-of-Plane Behaviour of Masonry Walls Retrofitted with Engineered Cementitious Composites." *Computers & Structures*. 201 (2018) 58–79. https://doi.org/10.1016/j.compstruc.2018.02.004.

[240] G. Andreotti, F. Graziotti, G. Magenes, "Detailed Micro-Modelling of the Direct Shear Tests of Brick Masonry Specimens: The Role of Dilatancy." *Engineering Structures*. 168 (2018) 929–949. https://doi.org/10.1016/j.engstruct.2018.05.019.

[241] E. Sacco, J. Toti, "Interface Elements for the Analysis of Masonry Structures." *International Journal for Computational Methods in Engineering Science and Mechanics*. 11 (2010) 354–373. https://doi.org/10.1080/15502287.2010.516793.

[242] O. Arnau, C. Sandoval, D. Murià-Vila, *Determination and Validation of Input Parameters for Detailed Micro-Modelling of Partially Grouted Reinforced Masonry Walls*, in: 10th Pacific Conference on Earthquake Engineering, 2015.

[243] S.K. Arya, G.A. Hegemier, *On Nonlinear Response Prediction of Concrete Masonry Assemblies*, in: Proceedings of the North American Masonry Conference, The Masonry Society, Boulder, Colorado, 1978: pp. 11–19.

[244] J.G. Rots, “Numerical Simulation of Cracking in Structural Masonry.” *Heron*. 36 (1991) 49–63.

[245] R. Senthivel, P.B. Lourenço, “Finite Element Modelling of Deformation Characteristics of Historical Stone Masonry Shear Walls.” *Engineering Structures*. 31 (2009) 1930–1943. https://doi.org/10.1016/j.engstruct.2009.02.046.

[246] M. Petracca, L. Pelà, R. Rossi, S. Zaghi, G. Camata, E. Spacone, “Micro-Scale Continuous and Discrete Numerical Models for Nonlinear Analysis of Masonry Shear Walls.” *Construction and Building Materials*. 149 (2017) 296–314. https://doi.org/10.1016/j.conbuildmat.2017.05.130.

[247] J. Vemuri, S. Ehteshamuddin, S. Kolluru, “Numerical Simulation of Soft Brick Unreinforced Masonry Walls Subjected to Lateral Loads.” *Cogent Engineering*. 5 (2018) 1–21. https://doi.org/https://doi.org/10.1080/23311916.2018.1551503.

[248] G.P.A.G. van Zijl, “Modeling Masonry Shear-Compression: Role of Dilatancy Highlighted.” *Journal of Engineering Mechanics*. 130 (2004) 1289–1296. https://doi.org/10.1061/(ASCE)0733-9399(2004)130:11(1289).

[249] Y. Zhang, L. Macorini, B.A. Izzuddin, “Mesoscale Partitioned Analysis of Brick-Masonry Arches.” *Engineering Structures*. 124 (2016) 142–166. https://doi.org/10.1016/j.engstruct.2016.05.046.

[250] G. Alfano, E. Sacco, “Combining Interface Damage and Friction in a Cohesive-Zone Model.” *International Journal for Numerical Methods in Engineering*. 68 (2006) 542–582. https://doi.org/10.1002/nme.1728.

[251] F. Parrinello, B. Failla, G. Borino, “Cohesive–Frictional Interface Constitutive Model.” *International Journal of Solids and Structures*. 46 (2009) 2680–2692. https://doi.org/10.1016/j.ijsolstr.2009.02.016.

[252] G. Formica, V. Sansalone, R. Casciaro, “A Mixed Solution Strategy for the Nonlinear Analysis of Brick Masonry Walls.” *Computer Methods in Applied Mechanics and Engineering*. 191 (2002) 5847–5876. https://doi.org/10.1016/S0045-7825(02)00501-7.

[253] K.M. Dolatshahi, M.T. Nikoukalam, K. Beyer, “Numerical Study on Factors That Influence the In-Plane Drift Capacity of Unreinforced Masonry Walls.” *Earthquake Engineering & Structural Dynamics*. 47 (2018) 1440–1459. https://doi.org/10.1002/eqe.3024.

[254] K.M. Dolatshahi, M. Yekrangnia, “Out-of-Plane Strength Reduction of Unreinforced Masonry Walls Because of in-Plane Damages.” *Earthquake Engineering & Structural Dynamics*. 44 (2015) 2157–2176. https://doi.org/10.1002/eqe.2574.

[255] K.M. Dolatshahi, A.J. Aref, “Multi-Directional Response of Unreinforced Masonry Walls: Experimental and Computational Investigations.” *Earthquake Engineering & Structural Dynamics*. 45 (2016) 1427–1449. https://doi.org/10.1002/eqe.2714.

[256] M. Bolhassani, A.A. Hamid, A.C.W. Lau, F. Moon, “Simplified Micro Modeling of Partially Grouted Masonry Assemblages.” *Construction and Building Materials*. 83 (2015) 159–173. https://doi.org/10.1016/j.conbuildmat.2015.03.021.

[257] C. Tang, B. Shi, W. Gao, F. Chen, Y. Cai, “Strength and Mechanical Behavior of Short Polypropylene Fiber Reinforced and Cement Stabilized Clayey Soil.” *Geotextiles and Geomembranes*. 25 (2007) 194–202. https://doi.org/10.1016/j.geotexmem.2006.11.002.

[258] A. Aghababaie Mobarake, M. Khanmohammadi, S.R. Mirghaderi, “A New Discrete Macro-Element in an Analytical Platform for Seismic Assessment of Unreinforced Masonry Buildings.” *Engineering Structures*. 152 (2017) 381–396. https://doi.org/10.1016/j.engstruct.2017.09.013.

[259] I. Caliò, M. Marletta, B. Pantò, “A New Discrete Element Model for the Evaluation of the Seismic Behaviour of Unreinforced Masonry Buildings.” *Engineering Structures*. 40 (2012) 327–338. https://doi.org/10.1016/j.engstruct.2012.02.039.

[260] D. Baraldi, A. Cecchi, “Discrete Approaches for the Nonlinear Analysis of in Plane Loaded Masonry Walls: Molecular Dynamic and Static Algorithm Solutions.” *European Journal of Mechanics - A/Solids*. 57 (2016) 165–177. https://doi.org/10.1016/j.euromechsol.2015.12.008.

[261] T.-T. Bui, A. Limam, V. Sarhosis, “Failure Analysis of Masonry Wall Panels Subjected to In-Plane and out-of-Plane Loading Using the Discrete Element Method.” *European Journal of Environmental and Civil Engineering*. (2019) 1–17. https://doi.org/10.1080/19648189.2018.1552897.

[262] P. Jaquin, *History of Earth Building Techniques*, in: Modern Earth Buildings: Materials, Engineering, Constructions and Applications, 2012: pp. 307–323. https://doi.org/10.1533/9780857096166.3.307.

[263] P. Hofmann, S. Stockl, “Tests on the Shear-Bond Behaviour in the Bed-Joints of Masonry.” *Masonry Int.* (1986) 1–15.

[264] R. Van der Pluijm, *Overview of Deformation Controlled Combined Tensile and Shear Tests*, Eindhoven University of Technology, Eindhoven, The Netherlands, 1998.

[265] A.W. Page, “The Biaxial Compressive Strength of Brick Masonry.” *Proceedings of the Institution of Civil Engineers*. 71 (1981) 893–906. https://doi.org/10.1680/iicep.1981.1825.

[266] J.J. Roberts, G.J. Edgel, A.J. Rathbone, *BS 5628:1985: British Standard Code of Practice for Use of Masonry Part 2: Structural Use of Reinforced and Prestressed Masonry*, Palladian Publications Limited, London, UK, 2018. https://doi.org/10.1201/9781482275636.

[267] J. Lubliner, J. Oliver, S. Oller, E. Oñate, "A Plastic-Damage Model for Concrete." *International Journal of Solids and Structures*. 25 (1989) 299–326. https://doi.org/10.1016/0020-7683(89)90050-4.

[268] J. Lee, G.L. Fenves, "Plastic-Damage Model for Cyclic Loading of Concrete Structures." *Journal of Engineering Mechanics*. 124 (1998) 892–900. https://doi.org/10.1061/(ASCE)0733-9399(1998)124:8(892).

[269] T.J.R. Hughes, *The Finite Element Method: Linear Static and Dynamic Finite Element Analysis*, Courier Corporation, 2012. ISBN: 0486135020.

[270] S.R. Wu, L. Gu, *Introduction to the Explicit Finite Element Method for Nonlinear Transient Dynamics*, Wiley, 2012. https://doi.org/10.1002/9781118382011.

[271] A. Ferrante, F. Clementi, G. Milani, "Dynamic Behavior of an Inclined Existing Masonry Tower in Italy." *Frontiers in Built Environment*. 5 (2019) 33. https://doi.org/10.3389/fbuil.2019.00033.

[272] L.C. Silva, P.B. Lourenço, G. Milani, "Numerical Homogenization-based Seismic Assessment of an English-bond Masonry Prototype: Structural Level Application." *Earthquake Engineering & Structural Dynamics*. 49 (2020) 841–862. https://doi.org/10.1002/eqe.3267.

[273] N.M. Newmark, "A Method of Computation for Structural Dynamics." *Journal of the Engineering Mechanics Division*. 85 (1959) 67–94. https://doi.org/10.1061/JMCEA3.0000098.

[274] A.K.C.A. Chopra, *Dynamics of Structures : Theory and Applications to Earthquake Engineering*, 4th ed, Pearson, Boston, Massachusetts, USA, 2014. ISBN: 0273774247.

[275] A. Anthoine, "Homogenization of Periodic Masonry: Plane Stress, Generalized Plane Strain or 3d Modelling?" *Communications in Numerical Methods in Engineering*. 13 (1997) 319–326. https://doi.org/10.1002/(SICI)1099-0887(199705)13:5<319::AID-CNM55>3.0.CO;2-S.

[276] D. Addessi, E. Sacco, "Nonlinear Analysis of Masonry Panels Using a Kinematic Enriched Plane State Formulation." *International Journal of Solids and Structures*. 90 (2016) 194–214. https://doi.org/10.1016/j.ijsolstr.2016.03.002.

[277] T. Jankowiak, T. Lodygowski, "Identification of Parameters of Concrete Damage Plasticity Constitutive Model." *Foundations of Civil and Environmental Engineering*. 6 (2005) 53–69. http://yadda.icm.edu.pl/yadda/element/bwmeta1.element.baztech-article-BPP1-0059-0053.

[278] H.B. Kupfer, K.H. Gerstle, "Behavior of Concrete under Biaxial Stresses." *Journal of the Engineering Mechanics Division*. 99 (1973) 853–866. https://doi.org/10.1061/JMCEA3.0001789.

[279] S. Michał, W. Andrzej, *Calibration of the CDP Model Parameters in Abaqus*, in: The 2015 World Congress on Advances in Structural Engineering and Mechanics (ASEM15), 2015.

[280] A.M. D'Altri, V. Sarhosis, G. Milani, J. Rots, S. Cattari, S. Lagomarsino, E. Sacco, A. Tralli, G. Castellazzi, S. de Miranda, *A Review of Numerical Models for Masonry Structures*, in: Numerical Modeling of Masonry and Historical Structures, Elsevier, 2019: pp. 3–53. https://doi.org/10.1016/B978-0-08-102439-3.00001-4.

[281] N. Tarque, G. Camata, E. Spacone, H. Varum, M. Blondet, "Nonlinear Dynamic Analysis of a Full-Scale Unreinforced Adobe Model." *Earthquake Spectra*. 30 (2014) 1643–1661. https://doi.org/10.1193/022512EQS053M.

[282] W.I. De Villiers, G.P. Van Zijl, W.P. Boshoff, "Finite Element Analysis of Single-Storey Unreinforced Alternative Masonry Walls." *Advances in Structural Engineering*. 24 (2021) 2011–2026. https://doi.org/10.1177/1369433221992483.

[283] C. Sandoval, O. Arnau, "Experimental Characterization and Detailed Micro-Modeling of Multi-Perforated Clay Brick Masonry Structural Response." *Materials and Structures*. 50 (2017) 34. https://doi.org/10.1617/s11527-016-0888-3.

[284] Dassault Systèmes, *Abaqus v6.14 User's Manual*, Dassault Systèmes, Providence, RI, USA, 2014.

[285] D. Silveira, H. Varum, A. Costa, T. Martins, H. Pereira, J. Almeida, "Mechanical Properties of Adobe Bricks in Ancient Constructions." *Construction and Building Materials*. 28 (2012) 36–44. https://doi.org/10.1016/j.conbuildmat.2011.08.046.

[286] H.B. Kaushik, D.C. Rai, S.K. Jain, "Stress-Strain Characteristics of Clay Brick Masonry under Uniaxial Compression." *Journal of Materials in Civil Engineering*. 19 (2007) 728–739. https://doi.org/10.1061/(ASCE)0899-1561(2007)19:9(728).

[287] J.P. Mercier, G. Zambelli, W. Kurz, *Introduction to Materials Science*, Elsevier, 2002. https://doi.org/10.1016/C2009-0-29148-3.

[288] L. Miccoli, U. Müller, P. Fontana, "Mechanical Behaviour of Earthen Materials: A

Comparison between Earth Block Masonry, Rammed Earth and Cob.” *Construction and Building Materials*. 61 (2014) 327–339. https://doi.org/10.1016/j.conbuildmat.2014.03.009.

[289] J.M. Nichols, Y.Z. Totoev, *Experimental Determination of the Dynamic Modulus of Elasticity of Masonry Units*, in: 15th Australian Conference on the Mechanics of Structures and Materials (ACMSM), Melbourne, Victoria, Australia, 1997.

[290] V.G. Kouznetsova, *Computational Homogenization for the Multi-Scale Analysis of Multi-Phase Materials*, Technische Universiteit Eindhoven, Eindhoven, The Netherlands, 2004. ISBN: 90-386-2734-3.

[291] ASTM International, *ASTM G115-10 Standard Guide for Measuring and Reporting Friction Coefficients*, in: ASTM Standards, ASTM International, West Conshohocken, PA, 2018. https://doi.org/https://doi.org/10.1520/G0115-10R18.

[292] ASTM International, *ASTM D1894-14 Standard Test Method for Static and Kinetic Coefficients of Friction of Plastic Film and Sheeting*, in: ASTM Standards, ASTM International, West Conshohocken, PA, 2014. www.astm.org.